Advanced Characterisation Methods for the Analysis of Nanoformulations and Extracellular Vesicles

Jelle Penders

IMPERIAL COLLEGE LONDON

Department of Materials

A thesis submitted for attaining the degree of

Doctor of Philosophy

2019

Declaration of originality

I, Jelle Penders, declare hereby that the work contained in this thesis is my own. Contributions and assistance by others has been clearly indicated where applicable in the text.

Copyright declaration

Acknowledgements

My PhD journey began on a cold day in early January 2016 when I received the enthusiastic phone call of Prof. Molly Stevens offering me a PhD position in her group, which I readily accepted and will never forget. I would like to express my sincere thanks to her for welcoming me in her group and setting standards to admire and aspire to, for research and the research environment.

It takes a village to raise a child and it turned out it takes a wonderfully friendly, helpful and supportive research group to conduct a PhD. I have been incredibly fortunate to do my PhD in the Stevens Group and it was a pleasure and a privilege to meet, work alongside and together with the brilliant minds that make up this group.

I would like to thank Dr. Isaac Pence for believing in the idea of a PhD student to build a whole new analysis system and tackling the problems with me on the way with such enthusiasm and creativity. It would certainly not have come so far without you and I hope it will have a bright future ahead of it. I am also very grateful to my other postdoc mentors Dr. Anika Nagelkerke, Dr. Ulrike Kauscher, and Dr. Mads Bergholt, who have formed me into the researcher I have become with great advice during our many many Wednesday morning coffee meetings and throughout my PhD. Despite having all moved on to bigger and better things, they found the time to continue with our papers and aid in proofreading this thesis, for which I express my gratitude.

There are too many people in the group to thank all individually, however a few need to be mentioned here by name. Conor Horgan, first of all you have become a great friend and I really enjoyed doing our PhD's together alongside in the NanoMed consortium and thanks for having the patience to teach me all your MATLAB tricks. Håkon Høgset, thanks for all the discussions and our board game nights and dinners and I hope we can continue some great research together in the future. I would like to thank Dr. Sahana Gopal and Dr. Natalie Reznikov for teaching me all the ins and outs of FIB-SEM and Dr. Hyejeong Seong for many afternoons together making me hone my FIB-SEM skills with her near inexhaustible amount of nanoneedle samples. Thanks to Dr. Jonathan Wojciechowski, Dr. Chris Wood and Dr. Adrian Najer for sharing your expert chemistry knowledge and creativity with which you practice your craft. To Dr. Ben Pierce, Sabrina Skeete, Alex Kirby, Melisse Chee, Sirli Treumuth, Brittany Rae, Dr. Chloe Stockford and Dr. Akemi Nogiwa Valdez thanks for supporting the group in many ways and always having the lab ready to go for amazing science. Thanks Dr. Stuart Higgins, Dr. Jennifer Puetzer and Dr. Adam Creamer for being my partners in crime organising epic group weekends, which, despite the occasional casualty, will sure be remembered in the group for a long time.

Last but not least I would like to thank my family for their never-ending support and their understanding of me living abroad. Bas, my dear twin brother, and his wife Eline, thank you for your interest in my work, your phone and skype calls and the many board games to unwind together. Thanks to my grandmother, Oma Marieke, for her love and attention and moral (and occasionally sustenance) support.

Thanks Mom and Dad for always providing a warm home to return to. You have always encouraged me in everything I do and I would never have come so far without it.

Abstract

Nanomedicine represents a challenging and highly multidisciplinary research field, concerned with the development and study of nanoformulations for diagnostic and/or therapeutic purposes. The nano-sized particles of interest are increasingly complex. Their translational potential has been hampered by difficulties in their thorough characterisation. On the nano scale, small variations in size and composition can have large implications for their pharmacodynamic and pharmacokinetic behaviour. More precise techniques are therefore required to address these challenges.

This thesis describes novel, advanced characterisation methods designed for the detailed study of single nanoparticles and their interaction and uptake behaviour with cells. A platform technology for Single Particle Automated Raman Trapping Analysis – SPARTA - was developed, capable of non-destructive, label-free and automated comprehensive single particle analysis. With the SPARTA system, the composition, functionalisation, size and dynamic reactions on the surface can be investigated in detail, of a wide variety of nanoparticles, through their Raman spectra.

A further improved, custom designed SPARTA 2.0 platform was built, optimised for the analysis of complex biological particles, such as EVs. EVs represent a high potential as biomarkers, studied here in the context of breast cancer. The SPARTA 2.0 platform was able to resolve compositional differences between non-cancerous and cancer cell-derived EVs with excellent sensitivity and specificity. This highlights the possibility for development of new minimally invasive diagnostic approaches.

In addition, a new imaging strategy for investigation of the EV-cellular interaction is presented, based on 3D Focused Ion Beam – Scanning Electron Microscopy (FIB-SEM). FIB-SEM allows the generation of 3D models of the subcellular structure and visualisation of the cellular trafficking of nanoparticles. This represents a powerful new approach for investigating EV uptake.

The methods developed in this thesis allow for the single particle-based analysis of a wide variety of nanoformulations and EVs, to aid in understanding their composition, applicability and cellular interactions.

Publications and Conference Presentations

First and co-first author publications

Single Particle Automated Raman Trapping Analysis

Jelle Penders, Isaac J. Pence, Conor C. Horgan, Mads S. Bergholt, Christopher S. Wood, Adrian Najer, Ulrike Kauscher, Anika Nagelkerke and Molly M. Stevens, *Nature Communications*, 9, 4256, 2018

Gold Nanocluster Extracellular Vesicle Supraparticles: Self-Assembled Nanostructures for 3D Uptake Visualization

Ulrike Kauscher, Jelle Penders, Anika Nagelkerke, Margaret N. Holme, Valeria Nele, Lucia Massi, Sahana Gopal, Thomas E. Whittaker and Molly M. Stevens, *Submitted.*

Single Particle Automated Raman Trapping Analysis of Breast Cancer Cell Derived Extracellular Vesicles

Jelle Penders, Anika Nagelkerke, Isaac J. Pence, Jonathan Wojciechowski, Daniel A. Richards, Sofiane J. El Kouarati, Seth Flaxman, Charlotte Ion, Julia So, Charles Coombes and Molly M. Stevens, *In preparation.*

Co-author publications

Porous Silicon Nanoneedles Modulate Endocytosis to Delivery Biological Payloads

Sahana Gopal, Ciro Chiappini, Jelle Penders, Vincent Leonardo, Hyejeong Seong, Stephen Rothery, Yuri Korchev, Andrew Shevchuk and Molly M. Stevens, *Advanced Materials,* 31, 12, 2019

In Vivo Biocompatibility and Immunogenicity of Metal-Phenolic Gelation

Mattias Björnmalm, Lok Man Wong, Jonathan Wojciechowski, Jelle Penders, Conor C. Horgan, Marsilea Booth, Nicholas Martin, Susanne Sattler and Molly Stevens, *Chemical Science,* 43, 2019.

Size-tuneable nanoneedle arrays for influencing stem cell morphology, gene expression and nuclear membrane curvature

Hyejeong Seong, Stuart G. Higgins, Jelle Penders, James P. K. Armstrong, Spencer W. Crowder, Axel C. Moore, Julia E. Sero, Michele Becce and Molly M. Stevens, *Submitted.*

Molecular Imaging of Extracellular Vesicles in vitro via Raman Metabolic Labelling

Conor C. Horgan, Anika Nagelkerke, Thomas E. Whittaker, Valeria Nele, Lucia Massi, Ulrike Kauscher, Jelle Penders, Mads S. Bergholt, Steve R. Hood and Molly M. Stevens, *Submitted.*

Conference presentations

SPIE Photonics West – BiOS – San Francisco: 1 - 6 February 2019 (Conference Talk)

Single Particle Automated Raman Trapping Analysis

Jelle Penders, Isaac J. Pence, Conor C. Horgan, Mads S. Bergholt, Christopher S. Wood, Adrian Najer, Ulrike Kauscher, Anika Nagelkerke and Molly M. Stevens

Gordon Research Seminar and Gordon Research Conference on Cancer Nanotechnology – 22 - 28 June 2019 (Poster)

Single Particle Automated Raman Trapping Analysis (SPARTA™) of Extracellular Vesicles as Cancer Biomarkers for Disease and Treatment Monitoring

Jelle Penders, Anika Nagelkerke, Isaac J. Pence, Charlotte Ion, Julia So and Charles Coombes and Molly M. Stevens

Materials Research Society – 25 - 30 November 2018 (Poster)

Si-based Nanoneedles to Guide and Regulate Stem Cell Behaviour

Hyejeong Seong, Stuart G. Higgins, Spencer W. Crowder, Julia E. Sero, Jelle Penders, Charlotte Lee-Reeves, James P.K. Armstrong and Molly M. Stevens.

Patent Application

Single Particle Automated Raman Trapping Analysis

Jelle Penders, Isaac J. Pence and Molly M. Stevens, application number 1810010.7.

Table of Contents

List of Figures

List of Tables

List of Abbreviations

APC	Antigen presenting cell
AuNC	Gold nanocluster
AuNP	Gold nanoparticle
CCD	Charge-coupled device
CCK	Cell counting kit
CIE	Commission Internationale de L'Eclairage
CuAAC	Copper catalysed azide-alkyne cycloaddition
CYY	Cysteine-Tyrosine-Tyrosine
DF	Dark-field
DIEA	Di-isopropyl ethylamine
DLS	Dynamic light scattering
DPPC	1,2-Dipalmitoyl-sn-glycero-3-phosphocholine
DRA	Dimensional reduction arrays
DTNB	5,5-Dithio-bis-2(-nitrobenzoic acid)
EDC	1-Ethyl-3-(3-dimethylaminopropyl) carbodiimide
EDX	Energy dispersive X-ray analysis
EM	Electron microscopy
ER	Oestrogen receptor
ESCRT	Endosomal sorting complex required for transport
EVs	Extracellular vesicles
FBS	Fetal bovine serum
FIB-SEM	Focused ion beam – scanning electron microscopy
FT-IR	Fourier-transform Infrared
GIS	Gas injection system
GUI	Graphical user interface
HAADF	High angle annular dark field

HBTU	Hexafluorophosphate benzotriazole tetramethyl uronium
HER2	Human epidermal growth factor receptor 2
HNFs	Holographic notch filters
HPLC	High-performance liquid chromatography
HR	High resolution
ILVs	Intraluminal vesicles
IR	Infrared
LBPA	Lyobisphosphatidic acid
LCMS	Liquid chromatography mass spectrometry
LV	Latent variable
miRNA	Micro ribonucleic acid
MS	Mass spectroscopy
MVB	Multivesicular body
MVs	Microvesicles
NA	Numerical aperture
NA	Nucleic acids (not to be confused with numerical aperture)
NEAA	Non-essential amino acids
NHS	N-hydroxy succinimide
NIR	Near infrared
NIST	National Institute of Standards and Technology
NTA	Nanoparticle tracking analysis
PBS	Phosphate buffered saline
PC	Principle component
PCA	Principle component analysis
PCT	Patent cooperation treaty
PDI	Polydispersity index
PDMS	Poly(dimethylsiloxane)
PFA	Paraformaldehyde

PLSDA	Partial least squares discriminate analysis
PMOXA	Poly(2-methyloxazoline)
PR	Progesterone receptor
PS	Polystyrene
RES	Reticuloendothelial system
RTM	Raman tweezers microscopy
SAAU	11-Acrylamidoundecanoate
SDS-PAGE	Sodium dodecyl sulphate – polyacrylamide gel electrophoresis
SEC	Size exclusion chromatography
SEM	Scanning electron microscopy
SERS	Surface enhanced Raman spectroscopy
SMVs	Shedding microvesicles
SNR	Signal-to-noise ratio
SPARTA	Single Particle Automated Raman Trapping Analysis
SSV	Serial surface view
STEM	Scanning transmission electron microscopy
TBS	Tris-buffered saline
TBS-T	Tris-buffered saline with 0.1% Tween 20
TCEP	Tris(2-carboxyethyl) phosphine
TEM	Transmission electron microscopy
TFA	Trifluoroacetic acid
TMV	Tobacco mosaic virus
UV-Vis	Ultraviolet – visible (spectroscopy)

Chapter 1

Introduction

'The application of nanotechnology to healthcare

– also called nanomedicine – requires the intersection

of many disciplines including biology, chemistry,

physics, chemical and mechanical engineering,

material science and clinical medicine.'

Omid C. Farokhzad and Robert Langer

Nanomedicine: Developing smarter therapeutic and diagnostic modalities

Advanced Drug Delivery Reviews, 58, 2006

1 Introduction

Here, the core concepts of this thesis are introduced, while each following chapter includes a dedicated, more in-depth introductory section. In the sections below, background information is given on the particle systems studied, nanoformulations and extracellular vesicles, as well as on several general techniques extensively used in this thesis, Raman spectroscopy and electron microscopy.

1.1 Nanomedicine and Nanoformulations

1.1.1 Background and relevance

Nanomedicine is a complex and highly active field, with as one of the core concepts being the design and formulation of nanoscopic delivery vehicles for therapeutics. On the one hand, the choice of the right design parameters of the capsule or matrix: the size, material and surface chemistry, depending on the desired mode of action, are critical. On the other hand, the study of their pharmacodynamics and pharmacokinetics, how they interact with the body and how the body interacts with them, are of great interest[1].

Nanomedicine finds its origins in the desire to design systems for the controlled, localised delivery of drugs, moving away from systemic injection or other bulk administration routes. The first controlled drug delivery systems were conceptualised in the 1960s, and in the last decades moved from macro implantable systems, through micro and finally to nanoscopic ones[2].

The main advantages for controlled drug delivery can be summed up as:

1. Control over drug delivery rate, allowing for sustained release over longer time periods as opposed to bulk release and strong fluctuations in drug exposure level[2,3].
2. Conveying targeting capabilities to the drug, using active or passive targeting approaches, increasing the drug efficiency and effectiveness at the site of interest[3,4].
3. Mitigation of adverse or side-effects of drugs caused by systemic delivery, such as those caused by chemotherapeutics[5,6].

While a thorough overview of the history and plethora of nano-sized drug delivery systems being developed is outside the scope of this thesis, two such systems will be discussed here in greater detail. These are liposomes and polymersomes as they are the basis of model systems studied in Chapter 2 of this thesis.

1.1.2 Liposomes

Liposomes are spherical vesicles consisting of a phospholipid bilayer membrane encapsulating an aqueous core. Phospholipids are amphiphiles, consisting of a hydrophilic headgroup and two hydrophobic tails. Due to the ratio between the hydrophilic headgroup size and hydrophobic tail lengths, these amphiphiles tend to assemble into a bilayer[7]. This bilayer formation minimises the free energy and is caused by the hydrophobic effect, minimising the fixed hydration shell around the hydrophobic tails. The hydrophobic tails are further held together by van der Waals forces between the hydrocarbon chains. The cone shape provided by the headgroup to tail size ratio, induces curvature in the membrane, which therefore assembles into a vesicle, encapsulating an aqueous core[7]. The structure of a liposome is schematically shown in Figure 1.1.a.

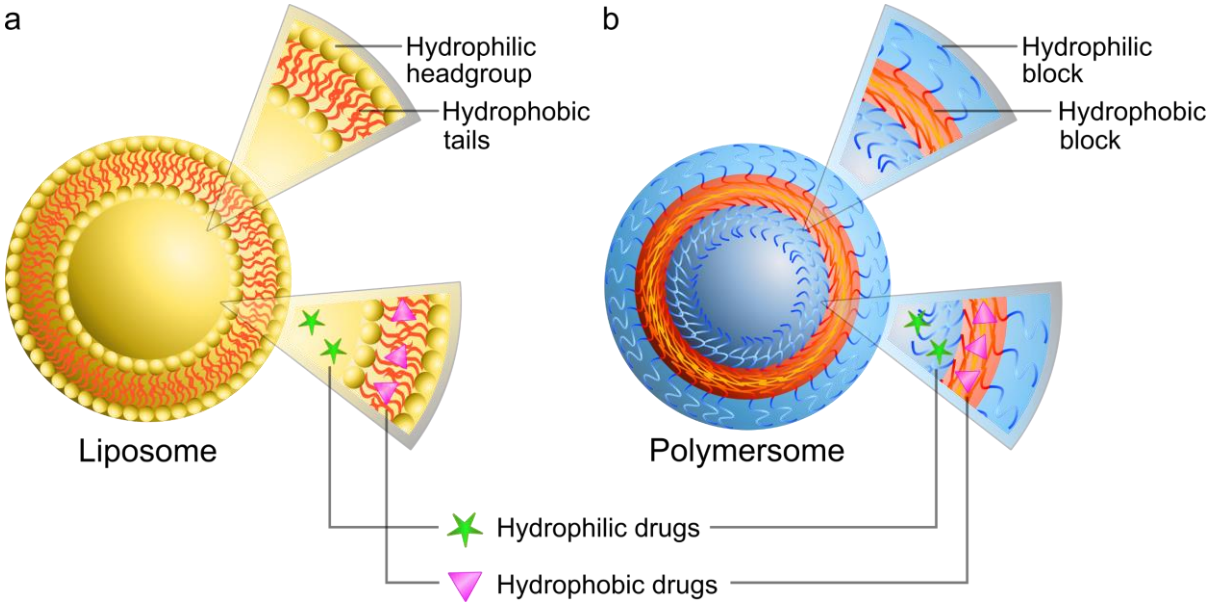

Figure 1.1 | Schematic representation of a liposome and a polymersome. (a) Liposomes consist of a bilayer membrane made up of amphiphilic lipid building blocks comprising of a hydrophilic headgroup with two hydrophobic tails. (b) A polymersome is built up from amphiphilic block co-polymers with a hydrophobic block sandwiched between two hydrophilic blocks. Drugs can be encapsulated within the hydrophobic membrane or the hydrophilic interior depending on their hydrophilicity.

Liposomes were first formed and studied in the mid-1960s by Bangham *et al.* during their work on swollen phospholipid phases[8,9]. The term 'liposomes' was first coined by Bangham, Sessa and Weissman a few years later[10]. While the methods for the preparations of liposomes were still being refined, their use as possible drug encapsulation and delivery vehicles was very quickly recognised[1,11].

Liposomes have been used to encapsulate both hydrophilic and hydrophobic drugs or molecules[12,13]. The aqueous core of liposomes can act as a reservoir for hydrophilic drugs, while hydrophobic drugs may reside in the bilayer membrane itself. The first successful nanomedicine formulation to pass through clinical trials and into commercialisation was Doxil®[6]. Doxil® consists of liposomes encapsulating doxorubicin, an effective chemotherapeutic for the treatment of certain cancers such as leukaemia and lymphomas. One of the main advantages of Doxil® over the direct systemic administration of doxorubicin, is mitigation of the severe cardiotoxicity of the drug[14].

Liposomes may be formed with various techniques; however the most common and straightforward method is thin film hydration followed by extrusion[15]. In this method, the lipids are dissolved in a solvent, such as chloroform, which is evaporated on the bottom of a flask or vial using a gas flow or evaporator to form a thin film. This thin film is subsequently hydrated with an aqueous solution. Agitation of the solution via stirring or sonication will initiate the formation of a mixture of multilamellar vesicles. This lipid dispersion may then be extruded numerous times through a membrane, with a mesh size in the nanometer range (~50-500 nm), to obtain a more homogeneous size distribution and unilamellarity[16]. A full description of liposome preparation may be found in section 2.2.4.

1.1.3 Polymersomes

Polymersomes are similar in structure as liposomes, in that they consist of an aqueous core and a membrane formed by amphiphiles. In the case of polymersomes, the amphiphiles most commonly consist of block co-polymers in (or assemble into) an A-B-A order, where A is a hydrophilic block and B a hydrophobic block[17,18]. These dual headed amphiphiles are also referred to as bola-amphiphiles[19]. By tuning the length ratios of the blocks, self-assembly into a vesicle structure can be obtained, as first described by Discher *et al.* in 1999[17]. A schematic representation of the basic polymersome structure can be seen in Figure 1.1.b. Compared to liposomes, polymersomes have certain advantageous characteristics. This is mostly taking advantage of the flexibility afforded by *ab initio* synthesis of the building blocks. The membrane thickness can be directly tuned by the size of the hydrophobic block in the block co-polymer and can therefore be made much thicker and stronger than in conventional liposomes[17].

As with liposomes, polymersomes have found significant application as drug delivery vesicles[20]. Hydrophilic drugs may be encapsulated in the aqueous core and hydrophobic drugs in the membrane. The high versatility of the polymer building blocks and the ease of modification, has led to numerous interesting modifications to create formulations that are stimuli-responsive[4].

When exposed to, for instance, a specific pH range, redox potential or temperature, the permeability of the polymersome can be increased or dissociation induced. Exploiting these characteristics can improve the targetability of drugs by localised, induced release of the loaded contents[4].

1.1.4 Nanoformulation analysis techniques

It is vital to adequately characterise nanoformulations, such as liposomes and polymersomes, as variances in their size, concentration and composition can have major impacts on their applicability, function and cytotoxicity. Two common techniques for determining size and concentration are dynamic light scattering (DLS) and nanoparticle tracking analysis (NTA), which will be introduced here. More advanced techniques, such as those based on spectroscopy and electron microscopy will be detailed in other sections and in subsequent chapters.

1.1.4.1 Dynamic Light Scattering

DLS is a common technique to rapidly determine the hydrodynamic size distribution of a colloidal solution. The particles in the solution are moving due to Brownian motion, which is described by the Stokes-Einstein equation:

$$D = \frac{k_b T}{6\pi\eta R_h}$$

with D the diffusion coefficient, k_b the Boltzmann constant, T the temperature, η the viscosity and R_h the hydrodynamic radius[21].

The Stokes-Einstein equation states that the diffusion coefficient is proportional to the temperature and inversely proportional to the viscosity of the solution and the hydrodynamic radius of the particles. By measurement of the diffusion coefficient the hydrodynamic radius can thus be calculated, as the other factors are all known and constant during the measurement. During a DLS measurement, a laser beam is shone through the solution in a cuvette and the photons scattered by particles in the solution are collected by a detector under a specific angle over time. Small particles will scatter with lower intensity, while larger particles will scatter more light. However, more importantly, smaller particles move faster which results in faster fluctuations of the scattering signal, compared to larger particles. Mathematically, these fluctuations can be converted into a correlation function, which describes how fast the intensity changes when the signal is compared to that shifted an arbitrary (small) time interval[22].

Fast fluctuations, thus small particles, will lead to a rapid decay of the correlation function over time, while larger particles will show correlation over a longer time interval. Fitting of the correlation function results in the diffusion coefficient, after which the hydrodynamic diameter is calculated through the Stokes-Einstein equation[21,22]. DLS is widely used due to its versatility and ease, to obtain size distributions of nanoformulations. In addition, it can be used to measure how certain processing steps or additions to the solution (*e.g.* salts) affect particle size[23]. A drawback is the need for *a priori* knowledge of the particle composition in order to achieve accurate measurements.

1.1.4.2 Nanoparticle Tracking Analysis

NTA is based on the same core principles as DLS, tracking the difference in Brownian motion to determine particle sizes. A particle solution sample is injected into a liquid flow cell and the sample is irradiated with a laser. The scattered light is collected by a camera, which allows the real time imaging of particle movement in the liquid cell[24]. Using image analysis algorithms, the movement of the particles in the imaging frame is tracked over time. For each particle a centre position is determined and its displacement in subsequent image frames is tracked. This results in diffusion coefficients for each of the particles, based on mean squared displacement over time. The hydrodynamic radius can subsequently be obtained again through the Stokes-Einstein equation[24].

The advantage of NTA when compared to DLS, is the direct observation of single particle traces, as opposed to the scattering fluctuations of multiple particles over time with DLS. This causes the NTA measurements to be less affected by samples with great dispersity in size. Where in DLS larger particles can, due to their strongly enhanced scattering intensity, overwhelm and obscure a population of smaller particles present, this issue is mitigated with the NTA approach[25]. In addition to size measurements, NTA can also reliably estimate the particle concentration, as the number of particles in the field of view is determined by the image analysis, which corresponds to a known volume in the flow cell[25].

1.2 Extracellular vesicles

1.2.1 Definition

Cells secrete a variety of vesicles, with a great diversity in size, origin, composition and function into the extracellular space[26]. The release of relatively large vesicles from cells undergoing apoptosis, called apoptotic bodies, has been known for decades[27]. In contrast, the fact that healthy or tumorous cells also shed numerous types of vesicles in the nanosize regime has become known and under intense scrutiny much more recently[28]. These vesicles, having in common a phospholipid bilayer membrane, are usually identified by their origin.

However, since the current methods do not allow separation of these vesicles with complete accuracy, they are generally referred to as a collective of cell derived vesicles called 'Extracellular Vesicles' or EVs, as proposed by Théry *et al.*[29]. The three main classes of EVs are exosomes, microvesicles and apoptotic bodies. The term exosome is reserved for the vesicles originating from within the cell, which are released after fusing of a multivesicular body (MVB) with the cell membrane. Exosomes vary in size but are usually within the range of 30-100 nm[28]. Microvesicles (MVs) are vesicles which directly bud from the cell membrane, also sometimes referred to as membrane vesicles or classified under cell released microparticles[26]. MVs are mostly bigger than exosomes, ranging from 100-1000 nm, although some smaller MVs have been reported, overlapping largely with the exosome fraction. Apoptotic blebs or bodies come from condensed remains of apoptotic cells and are bigger and are more heterogeneous in shape, ranging from 1-5 µm in diameter and are solely released from cells undergoing apoptosis. EVs were mostly thought of initially as a waste disposal mechanism of cells, a way to release excess proteins[30,31], however in particular for exosomes, strong indications have been found to indicate numerous more important functions, such as intercellular communication[31], transfer of genetic material[32], oncogens[33] or pathogens[34], promotion of angiogenesis[35] and immune response regulation[36].

In the experimental sections of this thesis, the term EVs is used for the combination of exosomes and microvesicles in the size range up to approximately 300 nm. This size range originates from the purification method used, based on size-exclusion chromatography, which will be further detailed in later sections. While in the literature review below, the terms 'exosomes', and 'microvesicles are used in concordance with the papers referenced, it should be noted that these are (more recently) experimentally found to be a mixed population, hence the classification as 'EVs' is deemed more appropriate. Efforts towards standardisation of the EV-field regarding nomenclature and reporting standard have been made, but are not yet universally accepted nor applied[37].

1.2.2 Biogenesis

Exosomes are a class of EVs which are derived from within the cell, as opposed to microvesicles which bud directly from the cell membrane. Exosomes were first classified by Trams *et al*.[38] in 1981 for exfoliated vesicles and soon after exosomes were isolated from reticulocytes by Johnstone *et al*[39,40]. Exosomes are formed by the inward budding of endosomal membranes which in turn leads to formation of intraluminal vesicles (ILVs) inside larger multivesicular bodies (MVBs). During the ILV formation certain proteins and lipids are sequestered from the endosomal membrane and incorporated into the ILVs[41]. The MVBs are also referred to as late endosomes, as they stem from the early-endosomes, where they gradually accumulate vesicles within (ILVs), maturing into late endosomes or MVBs.

The MVBs can then either fuse with a lysosome (degradative MVB) or with the plasma membrane (exocytic MVB)[42]. Fusion with lysosomes will lead to degradation of the contents and plasma membrane fusion will lead to release of the ILVs into the extracellular space, upon which they are called exosomes. Molecular analysis of purified exosomes has shown that their make-up is highly similar to the ILVs in MVBs, while not exhibiting the same plasma membrane marker make-up as seen for microvesicles, budding directly from the cell membrane[43,44].

This mechanism was first described by Johnstone when studying exosomes from reticulocytes during erythrocyte maturation[40] and was also seen for exosomes from B-lymphocytes by Raposo *et al*.[43] and a wide variety of cell types afterwards[45], leading to the definition of exosomes being tied to vesicles formed, according to the aforementioned mechanism. A schematic overview of the exosome formation mechanism can be seen in Figure 1.2.

Microvesicles (MVs), also sometimes referred to as shedding microvesicles (SMVs)[42], are EVs that are directly shed from the plasma membrane of a cell. The formation of these MVs occurs by formation of a small cytoplasmic protrusion which is then released from the plasma membrane upon fission of the ‘stalk’[46].

The MVs show a composition closer to that of the cell membrane than exosomes as they bud directly from the membrane, but various sorting mechanisms ensure the enrichment of the MV membrane with certain proteins such as metalloproteinases and integrins[46]. Another difference compared to exosomes is that the shedding of the MVs can be triggered for example by stimulation with Ca^{2+}, resulting in a burst emission of MVs from the cells, especially for dendritic cells[47].

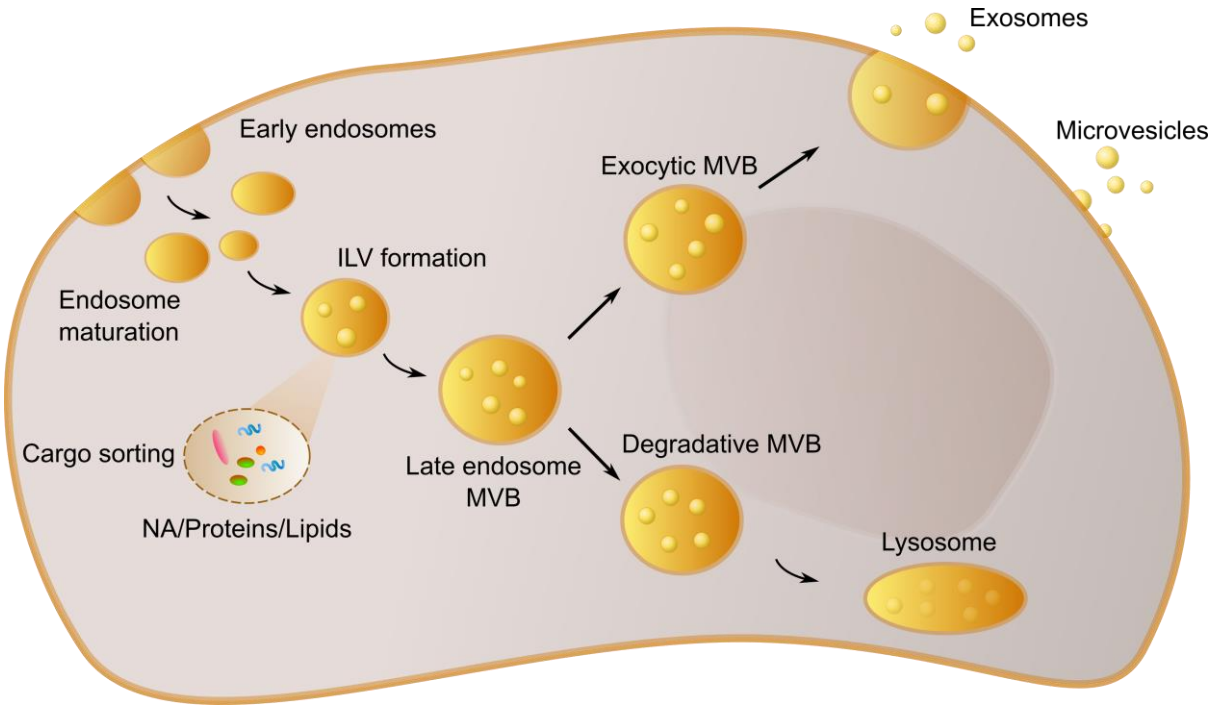

Figure 1.2 | Exosome and microvesicle biogenesis mechanism. Early endosomes mature and inward budding of the endosomal membrane results in formation of intraluminal vesicles (ILVs) to which the RNA/proteins/lipids are sorted as cargo. The late endosome or multivesicular body (MVB) can be digested in a lysosome (degradative MVB) or fuse with the outer cell membrane and release the ILVs as exosomes (exocytic MVB). Microvesicles bud directly from the cell membrane.

1.2.3 Isolation and purification

While cells have been shown to excrete the various types of EVs in natural culture conditions, the amount of EV secretion can vary greatly between cell types and cell specific conditions. Due to their rapid growth, cancerous cells are often used to isolate EVs, as they have increased EV secretion, particularly under stressed conditions[48]. In addition, external stimulation by Ca^{2+}, changes in pH, hypoxia and hypoglycaemia have all been shown to influence EV or exosome secretion in certain cell types[48,49]. The EVs can subsequently be isolated and purified from the conditioned media, usually after a few days of incubation.

It should be noted that that the addition of fetal bovine serum (FBS), commonly present in cell culture media, causes contamination of the cell derived EVs with bovine EVs present in the serum[50]. The most common ways around this are to use EV depleted FBS or, arguably a safer approach, is to culture the cells for a period on cell culture media devoid of FBS, called ‘starvation’. The starvation can also induce a change in EV secretion behaviour in the cells, and tumour cells are generally more resistant to these stressed conditions[48].

The isolation of the EVs from the conditioned medium is still a challenging aspect in the field[51] and numerous methods have been proposed to isolate the EVs from the other components of the culture media (such as high levels of free proteins) and to separate the EVs into exosomes, MVs and apoptotic bodies. The most common methods are differential ultracentrifugation and ultrafiltration, while more specialised methods are based on immunoaffinity adsorption[28,30].

Differential ultracentrifugation methods as described by Raposo *et al*.[43] are based on sequential centrifugation at increasing g. First the cells are removed via centrifugation at low speed and the EVs are retained in the last pellet after high g centrifugation. Further purification can be done by resuspension and repeated ultracentrifugation. Ultracentrifugation is often combined with a sucrose cushion to float the exosomes in the density range from 1.13 to 1.19 g/mL[51]. The drawbacks of this method are the long times of centrifugation required, the substantial losses, and the co-precipitation of proteins[45]. EVs can be damaged by the high forces involved or fusion and aggregation may occur. In addition, the smaller MVs have been shown to be similar in size and density as the exosomes and can thus not be completely separated.

Another purification method is based on size, using ultrafiltration techniques[52]. Ultrafiltration is in general less time consuming and uses much lower centrifugation speeds. Ultrafiltration is also more reliable to remove the bigger apoptotic bodies and MVs from the exosome fraction. However, this method also does not allow separation of exosomes and MVs of similar sizes. A combination of these techniques was adapted and scaled to a method for the preparation of clinical grade exosomes from dendritic cells[45]. Here, a first concentration of the media was achieved by ultrafiltration under high pressure and subsequent ultracentrifugation on sucrose/deuterium oxide cushions let to a highly enriched exosome fraction with up to 50% recovery and the possibility to purify up to 4 litres of cultured medium. Alternatively, size exclusion chromatography (SEC) may be employed as a single step EV isolation, or in combination with the above to separate EVs based on size[53,54]. An advantage of SEC is that it allows the separation of the majority of proteins from the EV fractions, in contrast to ultracentrifugation methods.

More advanced methods to isolate highly purified exosomes are based on immunoaffinity capture[30,55,56]. Here, magnetic beads are coated with specific antibodies to isolate exosomes from cancerous cell lines. While a specific exosome target antibody needs to be used, this method could possibly purify exosomes directly from the cultured media, without risking contamination by protein fractions or FBS exosomes. However, the drawback for these methods is the fact that the exosomes are physically bound to the beads and cannot be (easily) separated, hence serving only to detect the exosomes and not making them readily available for further studies.

In addition, it is yet unclear if the used antibodies can target all exosomes and exclusively exosomes, or only a specific subpopulation, as it is based on the assumption that EVs express the same markers and to the same extent.

This project will employ the latest isolation and purification protocols for EVs as established and optimised within the Stevens group (Whittaker, unpublished) and others[54]. These are based on ultrafiltration and SEC, to ensure optimum sample purity and reproducibility and controlled by a number of analysis methods such as NTA and protein quantification.

1.2.4 Standard characterisation methods

EVs are generally smaller than 200 nm[28], quite complex biological structures and in lower particle concentrations when comparing them to similarly sized liposomes or nanoparticles. Several methods have been proposed and developed for quantification of the number of EVs and their size, while analysing their (individual) composition is still a challenge.

To determine the size and concentration of EVs, DLS and standard flow-cytometry are unsuitable, as the limit of detection of flow-cytometry is generally around 300 nm and DLS is inaccurate towards smaller vesicles, especially in mixed-size samples causing the scattering of larger vesicles to overwhelm the signal of the smaller ones[57]. To overcome these limits NTA can be used instead to determine the size distribution and number of EVs, which is sensitive to particles larger than 50 nm[57]. With NTA, the number of EVs can be inferred from the number of particles observed correlated to the sample volume size[58,59]. In addition, high resolution flow-cytometry techniques have been developed which can accurately quantify and size EVs after fluorescent labelling[60,61]. In principle, this technique could also be used to phenotype the EVs after specific fluorescent antibody labelling of the EV population with known markers. However, since it is not yet possible to determine which markers specifically pertain to exosomes and to MVs and their subsequent heterogeneity within a sample, this has to be done with caution.

As EVs are too small to visualise in detail with light microscopy, electron microscopy studies have been performed to look at the EV morphology. Conventional TEM analysis of EVs ('whole-mount samples') show often a cup-shaped morphology[43] which was originally mistaken as a typical feature of exosomes, but is actually the result of membrane collapse during drying[28]. In contrast, with cryo-TEM it has been shown that the EVs are spherical in shape[62].

The evaluation of the composition of the EVs and of the sample purity with regard to contaminations or the separation of exosomes and MVs is not straightforward. Proteomic and lipodomic studies have been conducted based on sodium dodecyl sulphate-polyacrylamide gel electrophoresis (SDS-PAGE), immunoblotting and mass spectroscopy (MS) techniques and have identified numerous proteins and lipids specific or enriched in EVs or exosomes. However, the drawback of these techniques is that they are bulk analyses and can therefore not readily identify heterogeneity between EVs, nor separate exosomes from MVs.

To analyse EVs on a single particle basis to characterise their composition and purity, in addition to established bulk analysis methods, novel characterisation methods have been investigated in this thesis. These include EV trapping by confocal Raman spectroscopy, which is the main focus of Chapter 3.

1.2.5 Composition and functions

Exosomes, being membrane vesicles, show a distinct lipid and protein composition of their membrane, as well as being loaded with a specific hydrophilic cargo within the aqueous core of the vesicle. As methods for separating exosomes from, for example MVs are still being optimised, it is difficult to ascribe specific components only to exosomes or MVs. However, proteomic analysis of highly exosome enriched samples has shown that exosomes contain both a conserved set of proteins and cell specific proteins within their membranes[41,42]. The most common proteomic analysis techniques employed are mass spectroscopy (MS), Western Blotting, fluorescence activated cell sorting and immune electron microscopy[42].

Since exosomes originate from the ILVs formed by inward budding of a maturing endosome into an MVB, a common set of proteins is identified in almost all exosomes independent of cellular origin. These are membrane transport proteins and fusion proteins (GTPases, Annexins, flotillin), heat shock proteins (Hsc70 and Hsp90), proteins pertaining to MVB biogenesis (Alix and TSG101) and certain tetraspanins and integrins (CD63, CD81, CD82 and CD9)[30,31].

The proteins that are especially enriched in exosomes are CD63, Alix, flotillin and TSG101, and are therefore most used as specific markers for exosomes. Exosomes also contain cell specific proteins, such as A33 for exosomes derived from colon epithelial cells[55] and the presence of MHC class I and II complex peptides on exosomes from antigen presenting cells[63].

The lipid composition of exosomes, while less widely investigated, also shows both common and cell specific lipids present in the exosomes. The common lipids are mostly the 'raft-lipids', such as cholesterol and sphingomyelin, influencing the membrane stability and the ability of exosomes to fuse with other membranes[64]. Some lipids are involved in exosome biogenesis, such as lyobisphosphatidic acid (LBPA) which is important in the formation of ILVs,[65] and are also commonly found in exosomes.

The cargo of exosomes is a strong indicator of their prospective functions, this can vary greatly between cell lines. The 'endosomal sorting complex required for transport' (ESCRT) machinery in the cell is involved for the sorting of the endosomal cargo[31,66]. The enrichment of ESCRT related proteins in the exosome membrane is a strong indication of that[67]. Exosomes have also been shown to traffic mRNA and microRNA fragments as cargo[32], indicating their involvement in intercellular communication.

Major interest has been shown to elucidate the functions of EVs and exosomes in particular. This has been complicated by the difficulty in isolating pure fractions of exosomes from the other EV subclasses. Hence, some of the functions ascribed to exosomes could be pertaining most likely to MVs or other subclasses as well.

Originally EVs were thought of solely having a role in cell waste disposal, either by fusing inside a degradative MVB still as ILVs with a lysosome or fusing with the outer membrane to dispose of obsolete proteins. This is the case during reticulocyte maturation[68]. Later reports have shown that exosomes can have a distinct function and impact in intercellular communication, immune response regulation, cargo delivery and drug resistance[30].

Exosomes play a role in cell-cell communications in which the exosome can interact with the target cell in various ways[64]. The (transmembrane-) proteins present in the exosome membrane can interact directly with receptors in the target cell membrane, activating a signalling cascade. This is called juxtracrine interaction, or contact-dependent signalling, in a similar way to which two neighbouring cells could interact.

Alternatively, fragments of the exosomes can be released due to various enzymes in the extracellular environment close to the target cell, which in turn interact with the target cell receptors and activate a signalling cascade. The exosomes can also fully interact with the target cell membrane and release their cargo directly in to the cytoplasm, activating transcription pathways due to release of specific mRNA or microRNA fragments[32,42].

There are also numerous reports on the role of exosomes acting as activators in the immune system, by providing intercellular communication. It has been shown that exosomes secreted by antigen presenting cells (APCs) have a high degree of MHC complex peptides associated with their membrane[63].

Exosomes and their biogenesis mechanism may also be involved in the trafficking of viruses and they even exhibit remarkable similarities to certain viruses[69,70]. Following the endocytic uptake, the exosomes may fuse with the endosomal limiting membrane and subsequently release their cargo. This is highly similar to the uptake of viruses and subsequent release into the cytosol as for example described in the case of the influenza virus. Here, the viral envelope fuses with the endosomal membrane after uptake via endocytosis[71]. This is mediated by various fusion proteins, similar to CD9 which is also reported to be included in various exosomes[42,55].

1.2.6 Use of EVs as drug delivery vesicles

Despite the characterisation of EVs not being fully elucidated, various studies have been conducted on exploiting EVs and in particular exosomes for clinical use. EVs show promising properties as novel diagnostic markers, immunotherapeutic agents and drug delivery systems[30,72].

The discovery that EVs are present in all body fluids and excreted by a wide variety of cells, together with the emerging elucidation of their cell specific protein, lipid and cargo complement has posed them as a useful diagnostic marker. EVs can be isolated from patients with minimal or non-invasive diagnostics, such as collection of blood samples or even from urine or saliva. Particular interest has been shown for uses in early diagnosis of cancer, by analysing the microRNA (miRNA) carried by the exosomes, serving as a fingerprint for specific cancers[73] such as lung[74] and prostate cancer[75].

As stated, EVs from antigen presenting cells have been shown to play a role in activating the immune system due to the presence of a high degree of MHC complex peptides in their membranes. This property makes EVs potentially suitable in developing immunotherapy against cancers. Preliminary clinical trials show that administration of dendritic cell derived exosomes could be used to stimulate the immune system in an anti-cancer response[42,76,77].

From a drug delivery perspective, EVs naturally exhibit a range of highly desirable properties, which could make them excellent candidates for targeted drug delivery[78,79]. EVs, being excreted by cells from the patient's own body, will not elicit a strong foreign-body immune response or toxicity[76]. This being one of the main hurdles of artificial drug delivery systems which suffer often from rapid clearance from circulation by the reticuloendothelial system (RES)[2]. In addition, EVs naturally have a complement of cell targeting properties, directing specific uptake by components in their membranes such as integrins and fusion proteins[30].

The loading of EVs with a therapeutic cargo poses challenges of its own, with strategies being investigated either based on loading the EVs indirectly via the parent cells or after isolation, similarly as the loading of liposomes[79]. In the case of using small RNAs as the therapeutic cargo, the parent cells can be programmed via transfection-based approaches to overexpress these and subsequently release them into EVs[80]. However, the degree of loading seems dependent on the RNA fragment and the mechanisms of how the RNA gets incorporated into the EVs are still not fully understood. Post-isolation loading of EVs has been investigated using similar approaches as used for loading liposomes, including incubation (passive loading for hydrophobic drugs), electroporation, freeze-thaw cycles, sonication, saponification and extrusion[79]. All of these methods show advantages and disadvantages, indicating the incorporation of hydrophobic drugs into the membrane being easier achieved than hydrophilic drug incorporation into the core of the EVs.

Major challenges for clinical application of EVs in general, are the aforementioned issues regarding the purification and separation of various kinds of EV from co-isolated proteins and other particulates, especially regarding the stringent quality and safety controls from a pharmaceutical perspective.

Purification methods on a clinically relevant scale have been published by Lamparski *et al.*[45] for example, however still the different kinds of EV cannot be efficiently separated, the recovery is sub-optimal and the procedure is still quite intensive.

1.3 Raman Spectroscopy

1.3.1 Physical principles and instrument design

Raman spectroscopy is a spectroscopic analysis method based on the inelastic scattering of monochromatic laser light. When a sample is irradiated by the laser, the high majority of the light is elastically scattered, which is called Rayleigh scattering, where the scattered photons have the same energy as the incident ones. In addition, a small portion of the light, generally 1 in every 10^6-10^8 photons, is inelastically scattered by interacting with a molecule and elevating it shortly to a virtual energy state. The resulting photon can have a lower or a higher energy than the incoming photon. If the photon interacted with a molecule in the ground state the resulting scattered photon will have lower energy called Stokes Raman scattering, and the energy is transferred to the molecule leaving it in a higher energy state. If however, the photon interacted with a molecule already in an excited state, the scattered photon will have a higher energy, which is called anti-Stokes Raman scattering, taking up some of the vibrational energy from the molecule, as depicted in Figure 1.3. This shift in energy away from the Rayleigh line is what creates the Raman spectrum and correlates directly to the difference between the initial and final vibrational states of the molecule[81].

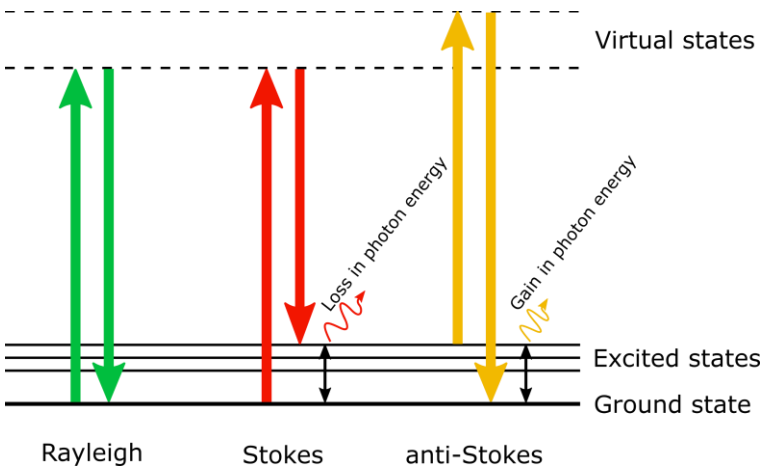

Figure 1.3 | Jablonski diagram depicting the physical principles of Raman spectroscopy. Diagram showing the differences between Rayleigh, Stokes and anti-Stokes Raman scattering. During Rayleigh scattering the energy of the incident and scattered photons is the same, while in Stokes Raman scattering energy is transferred from the photon to the molecule and in anti-Stokes Raman scattering energy is transferred from the molecule to the photon.

This is in contrast to infrared (IR) absorption spectroscopy where a range of wavelengths is used, and the energy of the absorbed photons matches the difference in energy between the ground and excited states of the molecules. For detection of spontaneous Raman, the Stokes Raman scattering is usually observed as it is stronger than the anti-Stokes scattering. This is due to fact that the population of molecules in an excited state at room temperature is much lower than that of molecules in the ground state.

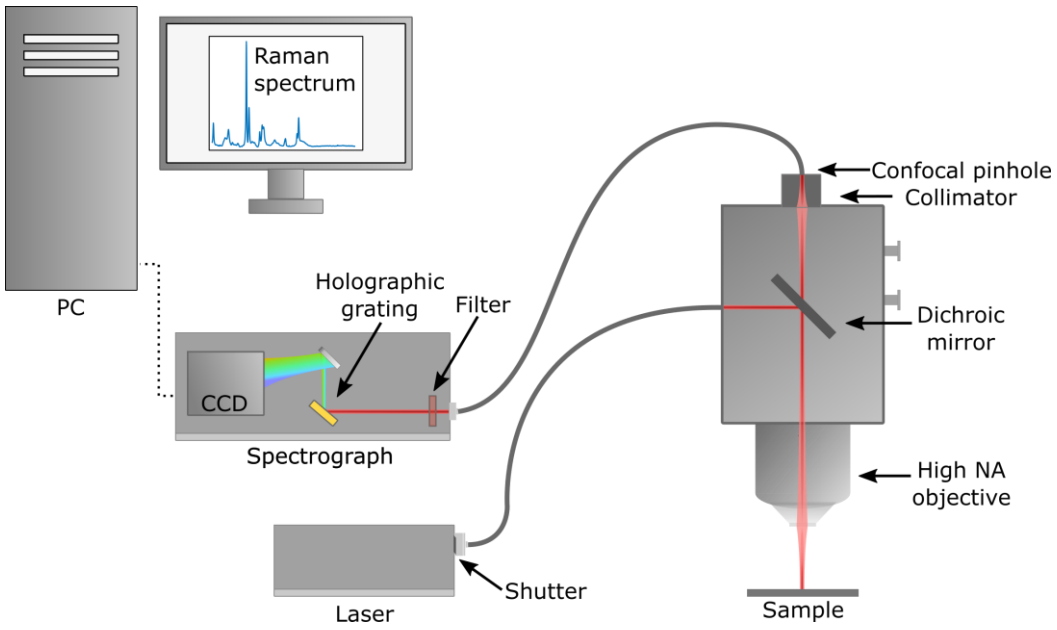

Figure 1.4 | Schematic representation of a confocal Raman microspectroscopic setup. A focused laser beam is guided through an optical fibre and directed through a high numerical aperture (NA) objective using a dichroic mirror onto the sample. The reflected light is collected back through the dichroic mirror and focused on a confocal pinhole using a collimator. An optical fibre guides the light to the spectrograph passing through a laser-line filter and projected by a holographic grating on a CCD detector which transfers the acquired data to the PC resulting in collection of a Raman spectrum.

1.3.2 Biological applications and imaging

Raman spectroscopy has numerous advantages over other spectroscopy techniques, such as IR absorption spectroscopy, when it comes to biological applications. From a practical perspective, IR spectroscopy is usually easier and faster than Raman as the instrumentation is more readily available and the signal to noise ratio is higher. However, the water peak dominates a great deal of the IR spectrum, while for Raman the water scattering is much lower and does not overlap with the signal from most biological components[82].

In addition, Raman spectroscopy has advantages over fluorescence or confocal microscopy as there is no need for the use of exogenous fluorophores or other tags and can be used on living cells in a non-destructive manner[82]. An optical microscope can be integrated in the setup resulting in Raman microspectroscopy.

A Raman spectrum can be acquired from whole cells or from small areas within a cell resulting in a generation of a 'fingerprint' of all the biochemical components within the measurement area. This fingerprint region ranges from around 600 to 1800 cm^{-1} and contains the signals obtained from the proteins, lipids, DNA and RNA present in the cell. Using libraries of signals of pure components[83] the resulting peaks can be assigned to specific components, taking into account possible overlap or interference.

A source of interference can be auto-fluorescence of certain components present, depending on the excitation laser used, and if so, can readily obscure the weaker Raman signal. The use of near infrared (NIR) laser can significantly reduce the background fluorescence, whilst also avoiding photo degradation of the cells and offering greater tissue penetration[82].

Using a more sophisticated setup, Raman microspectroscopy can be extended to allow confocal spectral acquisition and imaging. Depending on the set-up parameters such as the laser wavelength and the optics, a diffraction-limited resolution of around 300-500 nm can be reached. For imaging, a technique called hyper spectral mapping is employed in which the cell is scanned in a grid-like pattern and a spectrum is acquired in each pixel. The resolution is limited by the spot size of the laser, the accuracy of the stage movement and the time available. Complete 3D mapping of a cell with high resolution can exceed measurement times of 15 hours and is therefore not suitable for living cells. However, coarse mapping of a living cell or acquiring spectra on several locations for generation of a fingerprint is achievable. Distinguishing of different living cells based on their Raman fingerprint has been demonstrated[82,84,85]. This technique has been utilised in this thesis to investigate the biochemical similarities between EVs and their parent cells.

1.3.3 Data processing and analysis

Raman spectroscopic data consists of single or a series of spectra, which are intensity datapoints as read out by the CCD detector. The positions on the CCD can be calibrated to the spectrum of a known compound and the laser line, to obtain the corresponding Raman shift value at each intensity. The spectra thus obtained are termed 'raw' spectra and a variety of sequential processing steps can be applied to remove background signal and increase the signal-to-noise ratio (SNR) of the data[86], as shown schematically in Figure 1.5.

It should be noted that the type of processing steps applied can vary with regards to the intended application, as well as the manner in which they are executed[86].

The first step is removal of cosmic spikes, which are very high intensity narrow peaks arising from cosmic background radiation. These spikes can be easily identified and removed by plotting the second derivative of the spectrum, where the cosmic spikes will show up as a strong peak due to the sharp inflection of the slope over a high, narrow peak[87]. In contrast, the rest of the signal will be reduced to a rather narrow band. Using a threshold height, the spectra with cosmic speaks can be removed when they contain signal exceeding this threshold (Figure 1.5-I). More sophisticated algorithms have been developed for detection and removal of cosmic spikes. Examples of which are comparison of the contaminated spectrum to other spectra to correct the cosmic spike[88], or a moving window approach, where the spectrum is locally checked for abrupt intensity changes and the spike may be corrected by local linear fitting[89].

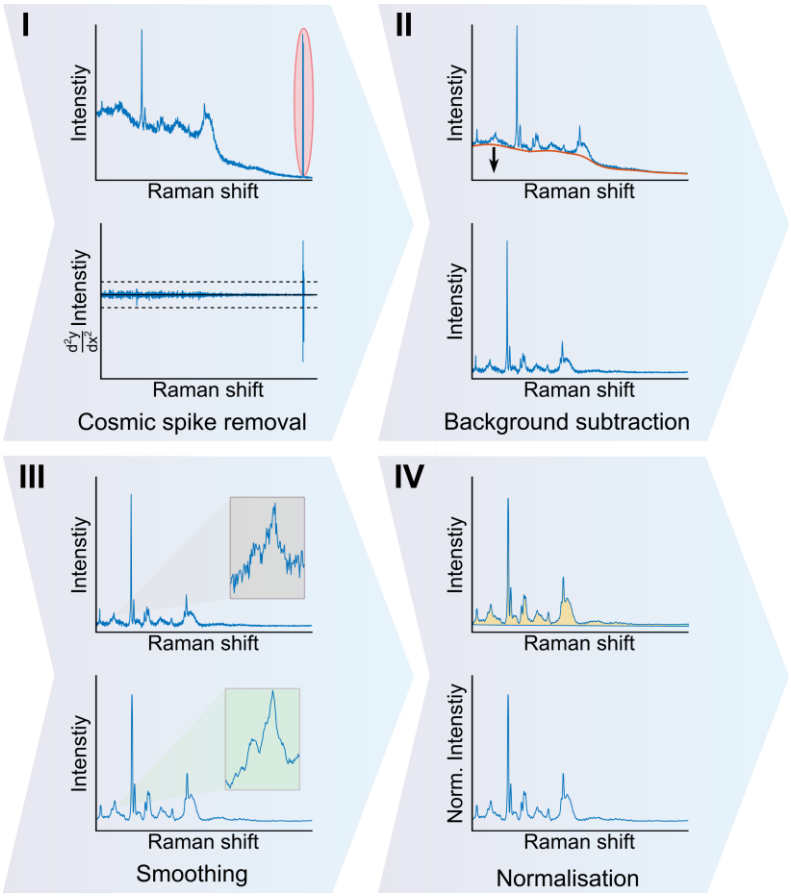

Figure 1.5 | Raman data processing steps. Standard processing of Raman spectra consists of (I) cosmic spike removal originating from cosmic background radiation, using a threshold to remove high intensity peaks in the second derivative, (II) background subtraction by fitting of a polynomial curve (red) to obtain a flat baseline of the spectrum, (III) Smoothing using a Savitsky-Golay filter by fitting sequential low order polynomials over a defined window size and (IV) normalisation by division of the intensity by the area under the curve.

Next, a polynomial curve may be fitted to remove the background of the spectrum, setting a flat baseline. The fitting of this curve can be achieved using a variety of approaches and constraints, one of which is minimising the least-squares distance with a non-negativity constraint, avoiding the creation of negative peaks[90,91] (Figure 1.5-II). The data can subsequently be smoothed, to remove some of the signal noise (Figure 1.5-III). A common smoothing algorithm is a Savitsky-Golay filter, where a line or polynomial is fitted through points in a specified window size[86]. Lower order polynomials and a wider window will lead to stronger smoothing of the data. The degree of smoothing should be carefully considered, as too much smoothing may lead to the overestimation of certain peaks or the loss of small peaks if the smoothing is particularly high.

Normalisation of the data is usually a final, optional processing step, where the total intensity is set to 1, commonly by division of the signal intensity by the area under the curve (Figure 1.5-IV)[86]. Normalisation is a requirement for multivariate statistical analyses, such as principle component analysis (PCA) and partial least squares discriminate analysis (PLSDA).

PCA is a basic multivariate statistical analysis technique[92], schematically illustrated in Figure 1.6. The Raman spectra are collected in a data matrix X, which can be expanded into a combination of matrixes M_1 through M_a, with the residuals collected in a matrix E (Figure 1.6-I). The matrixes M_1 through M_a can in turn be decomposed as orthogonal vectors p_1 to p_a and t_1 to t_a (Figure 1.6-II)[92]. The vectors p_i are the loading vectors which describe the multidimensional space and t_i the corresponding score vectors, representing the location coordinates in that space for each sample. This location thus represents how similar a given sample spectrum is to the PCA component pseudo-spectra given by the loading vectors (Figure 1.6-III). This approach is particularly useful for spectral unmixing, as samples with different spectra will group together in the space described by the principle components. Using a subsequent clustering analysis, these groups can be statistically distinguished and quantified, as further detailed in Chapters 2 and 3.

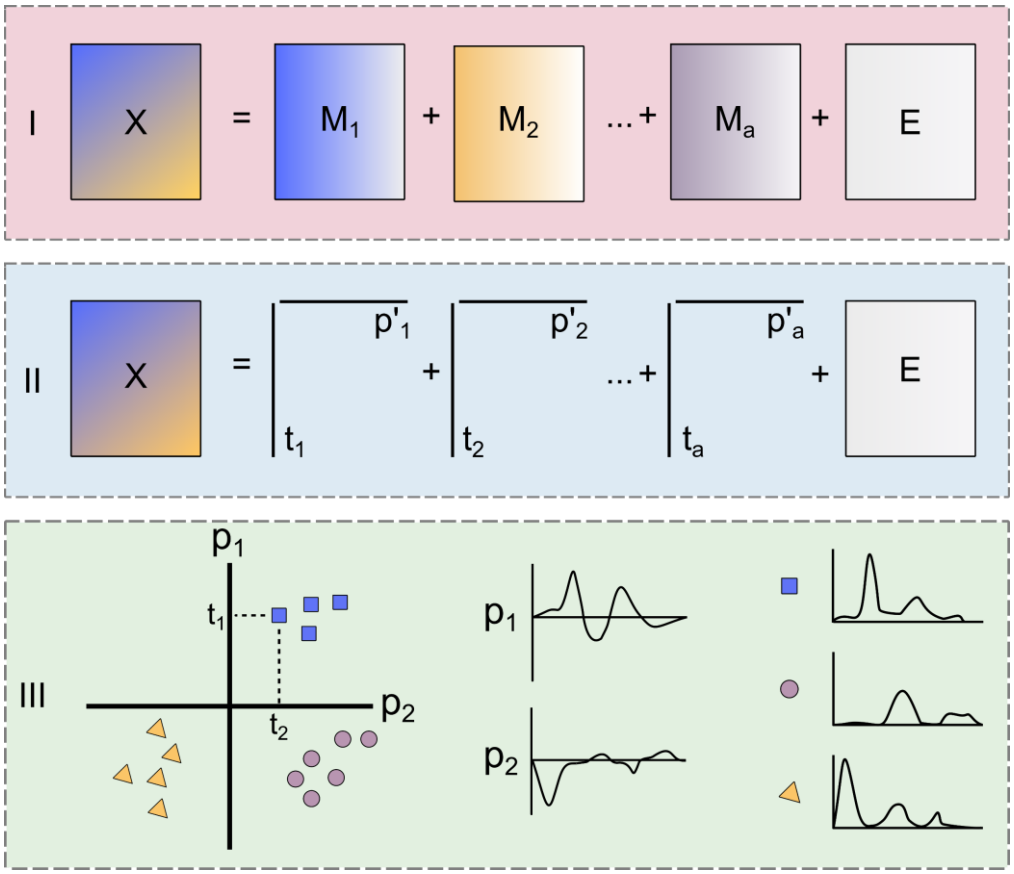

Figure 1.6 | Schematic representation of PCA. (I) A data matrix *X* can be represented as a combination of matrixes M_1 through M_a and a residual matrix *E*. (II) *X* can be projected on a combination of orthogonal vectors p_1 and t_1 through p_a and t_a, where t_i are the score vectors and p_i the loading vectors. (III) the vectors p_i can be plotted with the corresponding scores t_i for each spectrum (p_1 and p_2 shown). This results in a plot where each spectrum is in a location in the spot representing its relative similarity to the PCA component pseudo-spectra. (I), (II) adapted from *Wold*[92].

1.4 Electron Microscopy

This section is aimed to provide an overview and working principles of the various electron microscopy imaging techniques used in this thesis, as well as describing their uses in biological systems and the associated sample preparation considerations. Specific methods and applications used are detailed in Chapter 4, a comparison overview can be seen in Table 1.1.

1.4.1 Imaging techniques

1.4.1.1 TEM/STEM

Transmission Electron Microscopy (TEM) is a high-resolution imaging technique, in modern systems and on certain samples even resulting in atomic resolution. A sample is placed in a high vacuum column and irradiated with a focused beam of electrons[93,94]. The electrons that pass through the sample (hence 'transmission') fall on a fluorescent plate or camera detector, generating the image. To allow for the transmission of electrons, samples are limited to a certain thickness (~100 nm)[95], depending on the material used. An addition to a conventional TEM system is Scanning Transmission Electron Microscopy (STEM) where instead the beam is scanned in a grid pattern across the sample. STEM can provide higher contrast and resolution when paired with Dark-Field (DF) or High Angle Annual Dark Field (HAADF) detectors and is particularly used in EM tomography, where a 3D image of the sample can be obtained by collecting a high number of images under a range of angles[96,97]. TEM and STEM are commonly used to study nanoparticle morphology and are excellent to measure accurate size distributions. In addition, high resolution imaging in combination with electron diffraction allows for detailed studies of the lattice or crystal structure[93].

TEM can also be performed at liquid nitrogen temperatures in a cryo-TEM setup. Here, the samples and the holder are kept in liquid nitrogen to reach a temperature of approximately -165°C to -180°C during imaging[98]. This ensures that the samples, prepared by rapid freezing techniques, such as plunge freezing or high-pressure freezing, are kept in vitrified ice. The preparation and imaging of samples with this method allows the preservation of the samples' native, hydrated structure. This is particularly important in the imaging of biological particles such as EVs[99], which will be detailed below.

1.4.1.2 SEM

Scanning Electron Microscopy (SEM) is a widely used EM technique particularly suited to study surfaces and surface topography[100]. While the resolution does not quite match that of TEM, still, depending on the sample and system, a resolution of 5-10 nm can be readily achieved[101]. SEM is based on the principle of scanning an electron beam across the surface of the sample and collecting the electrons that are either elastically or inelastically scattered with a variety of detectors. Most commonly, secondary electron images are obtained, consisting of detecting the electrons emitted from sample atoms after interaction with the primary electron beam. These electrons are collected by a detector using a slight positive voltage bias (*e.g.* Everhart-Thornley detector) and mounted under an angle, affording a characteristically increased edge contrast. This makes secondary electron SEM imaging ideal to investigate (nano-sized) topographical structure. The detection of elastically scattered primary electrons, termed back-scattered electrons, affords a powerful tool for generating elemental contrast images, as the signal intensity is proportionally increased with increasing atomic number[94].

1.4.1.3 FIB-SEM

Focused Ion Beam – Scanning Electron Microscopy (FIB-SEM) is the addition of a focused ion beam into a conventional SEM system. The ion beam, in most cases Ga^+, is positioned in the microscope under an angle to the electron beam. The sample can be imaged as in a conventional SEM (perpendicular to the beam) after which it is tilted to 52 or 54°, depending on the construction, to be perpendicular to the FIB instead. In this position, the sample can be milled from the top, while viewed in SEM mode from the side. By milling trenches with the FIB, a new interface can be exposed and subsequently studied. The FIB can be operated with a high degree of precision from milling rough trenches to nanometre range thinning. A schematic overview can be seen in Figure 1.7.

In addition to imaging of the inner structures of a sample, the FIB can also be used to slice a sample in sequential sections down to 5 nm thin[101]. Taking images after each slice, results in an image stack that can be reconstructed into a 3D image of the cell using a dedicated software package. This procedure is called ‘slice-and-view’ or ‘serial surface view’ (SSV)[102], which will be discussed in detail in Chapter 4.

A FIB image taken during the slice-and-view process of a cell is shown on the right of Figure 1.7, with the SEM imaging direction indicated by the orange wedge and the direction of milling by the blue arrow. A cross-shaped fiducial can be seen on the top right, this can be used by the FIB-SEM to automatically correct for any drifting movement during imaging.

Depending on the sample, preparation and staining the imaging and slicing resolution of the FIB-SEM is around 5-10 nm[103].

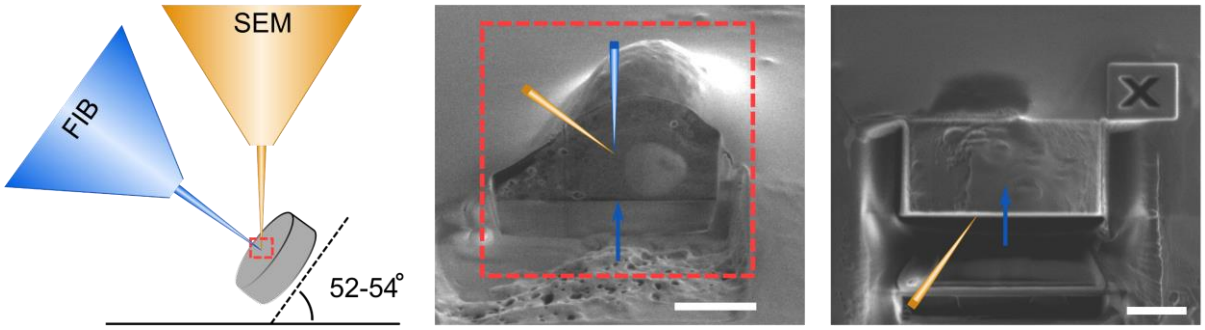

Figure 1.7 | Schematic illustrating the setup of a FIB-SEM. Depending on the machine architecture, the sample is tilted 52 to 54° to be perpendicular to the FIB. In the middle an SEM image can be seen of a cell, with the directions of the FIB and electron beams (SEM) indicated by blue and orange wedges respectively. A trench is milled in front of the region of interest to expose the interior. On the right a FIB image can be seen during slice-and-view, with the slicing direction indicated by the arrow. Scale bars 5 µm.

1.4.2 Biological applications

Electron microscopy techniques are inherently more suitable for the study of inorganic materials rather than biological ones, as ultra-high vacuum conditions are required, and no water can be tolerated. In addition, since the image is constructed by irradiation of the samples by a high energy electron beam, biological samples can suffer rapidly from electron beam induced degradation[104]. However, the enormous potential of the (sub) nanometre resolution than can be attained with the various EM methods has sparked the development of specialised techniques to allow analysis of biological matter such as cells[95,105,106]. A key requirement is careful sample preparation, which will be detailed in the sections below.

TEM has been used extensively both to analyse biological (i.e. non-metallic) nanoparticles, as well as high resolution imaging of tissue and cell sections obtained via embedding and subsequent microtoming of bulk samples. While metal nanoparticles are inherently compatible with the high-vacuum conditions of EM imaging, for biological particles such as liposomes and EVs alternative methods are required to ensure compatibility, such as cryo-TEM[62,98].

SEM and FIB-SEM have been applied to investigate the structure and sub-cellular components of cells. Following EM preparation, detailed images can be obtained of the cellular morphology[107], uptake of particles[108], as well as studying the interaction with substrates[95,109].

1.4.3 Sample preparation

Sample preparation is critical in EM analysis especially for biological samples, due to the delicate nature and often high initial water content. The preparation routes for sample preparation can roughly be divided in two classes: room temperature and cryo preparation. A detailed method description may be found in sections 4.2.4 and 4.2.6.

1.4.3.1 Room temperature preparation

Room temperature preparation, as the name implies, occurs fully at room temperature. There are several stages in preparing a sample, for example cells on a coverslip, before imaging can commence. The sample first needs to be fixed, in a similar way as for immunofluorescence imaging with paraformaldehyde and glutaraldehyde[105]. Care has to be taken to use EM-grade quality of the chemicals as they can otherwise contain small contaminations by polymer particles, which will introduce artefacts into the samples. Next, the sample needs to be stained in order to provide contrast during imaging. Since the contrast in EM is generated by the differential electron opacity and a biological sample consists almost exclusively of light atoms, there is very little inherent contrast. By adding heavy metal stains that bind selectively to the proteins and lipids in a sample, a high degree of contrast can be achieved, after which membranes and organelles can be clearly visible during imaging. Common heavy metal based stains are osmium tetroxide, uranyl compounds and lead-based compounds[103].

After fixation and staining the water has to be removed from the samples by a dehydration process, commonly in an ethanol gradient. By increasing the amount of ethanol to water in the solution gradually to 100% the water in the sample is carefully removed. By infiltrating a resin (also in a gradient composition) and subsequent curing, the samples may be stabilised and preserved before imaging at room temperature for long periods (>months).

1.4.3.2 Cryo preparation

Cryo preparation of EM samples is a way to better preserve the ultra-structure of the samples by fixing the samples primarily in a physical way, rather than chemically. This is achieved by very rapid freezing of the samples to fix the structure, but also to avoid crystallization of the present water[98]. For cryo-TEM, a drop of sample is placed on a grid, which is blotted and very rapidly plunged into liquid ethane. Due to the thinness of the sample and rapid transfer, the ice and sample is vitrified, rather than crystallised. This amorphous ice enables imaging of the physically stabilised hydrated structure of the sample[98]. The samples are subsequently transferred to liquid nitrogen for storage prior to imaging under cryogenic conditions.

Table 1.1 | Comparison of electron microscopy techniques. *Note the categories for comparison are additionally depended on the exact type of sample and instrument used.*

	TEM	SEM	FIB-SEM
Resolution	<1 nm	5-10 nm	5-10 nm
Sample preparation	Staining, dehydration and embedding	Dehydration	Staining, dehydration and embedding
Sample restrictions	Requires thin sections (<100 nm)	Requires visibility of object of interest on the surface	Sample must be minimally embedded in resin to allow orientation and visualisation
Biological application	Microtomed thin sections of embedded cells or tissue	Cellular surface interaction	*In situ* milled cells or tissue
Main advantage	Superior resolution, post slicing (immuno) staining possible	Rapid screening of a large surface	Superior slicing fidelity and thickness down to 5 nm, full 3D cellular reconstruction
Main disadvantage	Microtoming artefacts, high manual handling of slices	Only the surface is accessible for imaging	Low throughput due to slower milling *in situ* and long image acquisition times

1.5 Limitations and challenges

The highlighted nanoparticles, from drug delivery formulations based on liposomes and polymers to complex biological particles like EVs, have great promise in numerous diagnostic and therapeutic applications. However, challenges remain and in particular those pertaining to the limitations of current analysis techniques are of interest here.

While size and concentration of particle solutions can usually be readily obtained by techniques, such as DLS and NTA, the thorough characterisation of their composition remains difficult. Small differences in size and composition of nanoformulations can significantly alter their *in vivo* behaviour[110,111]. For EVs, the complex, fine variations in their composition between and within populations remains to be full elucidated. This is paramount for the understanding of their biological role, as well as their useful application as diagnostic or therapeutic agents.

In the following chapters, the techniques introduced, based on Raman spectroscopy and electron microscopy, have been used to develop novel analysis methods for the single particle characterisation of nanoformulations and EVs, as well as track their *in vitro* uptake in great detail.

1.6 Scope of the thesis

This thesis aims to present newly developed analysis and imaging techniques for the characterisation of nanoformulations and extracellular vesicles, to study their composition and cellular interaction.

Chapter 2 describes the development of SPARTA – Single Particle Automated Raman Trapping Analysis, a novel approach for the label-free automated analysis of a wide variety of nanoparticles. The setup and capabilities of the SPARTA analytical platform are described in detail and several model systems based on common types of nanoformulations; liposomes, polymersomes and polymer beads are analysed.

Chapter 3 discusses the augmentation of the first-generation SPARTA system into a dedicated SPARTA 2.0 analytical platform technology, following six improvement factors based on signal enhancement, system accuracy and stability. This improved system was applied to the analysis of EVs, in the context of breast cancer biomarkers. The detailed Raman spectral compositional analysis of EVs is discussed and a panel of 11 breast (cancer) cell line derived EVs is analysed. The ability of the SPARTA system for the classification and separation between EVs of cancerous and non-cancerous origin is demonstrated.

Chapter 4 concerns the study of breast cancer EV - cell interactions by development of a novel 3D imaging approach. Gold nanocluster-based EV hybrid structures, called AuNC EV supraparticles, are prepared and their uptake into breast cancer cells is imaged across different time points using FIB-SEM. The resulting 3D models allow detailed tracking of the uptake of AuNC EV supraparticles, from cell membrane interactions to lysosomal degradation

Chapter 5 includes overall conclusions and discusses future studies and applications of the developed technologies and approaches. In addition, the results of this work are placed into context in the current field.

Chapter 2

Single Particle Automated Raman Trapping Analysis

– SPARTA –

Development and Validation

‘As we shall see, the unique characteristics of this technique are having a major impact on the many subfields of physics, chemistry, and biology where small particles play a role.’

Arthur Ashkin

History of Optical Trapping and Manipulation of Small-Neutral Particle, Atoms, and Molecules, IEEE, 2000

2 Single Particle Automated Raman Trapping Analysis – SPARTA – Development and Validation

Parts of this chapter were published in Penders J. *et al*., Single Particle Automated Raman Trapping Analysis, *Nature Communications,* 9, 4256, 2018[112].

2.1 Introduction

2.1.1 Aims

This chapter details the development and validation of a comprehensive platform for the characterisation of individual nanoparticles and nanoformulations. The platform, which is named Single Particle Automated Raman Trapping Analysis (SPARTA), is founded on Raman spectroscopy for compositional analysis of a sample through optical interrogation and combined with single laser optical trapping, to position a single nanoparticle for analysis.

Nanoparticles and nanoformulations physically encompass the great promise of nanomedicine as new vectors for targeted delivery of a wide variety of therapies and have been made with an abundance of innovative chemistries. However, as this promise has unfortunately been lacking on delivering its expected return[113,114], there is a need to look in much greater detail at the underlying issues, which could be the root cause for this underperformance. One of the causes identified is the heterogeneity of nanoformulations[110]. As small differences in size, composition and surface chemistry can cause major differences in pharmacokinetic behaviour on the nanoscale, conventional bulk analysis of nanoformulations is not sufficient to successfully predict and interpolate their individual performance. Particle sizing and compositional analysis is typically achieved by combining a range of laser-based diffraction and spectroscopic techniques. Dynamic Light Scattering (DLS) and Nanoparticle Tracking Analysis (NTA) are generally employed to determine the particle population size distribution,[25,59,115] whereas compositional analysis can be conducted using Mass Spectrometry (MS) techniques as well as (Fourier-transform)-Infrared (FT-IR) spectroscopy[116–118] among others, depending on the type and size of particles. The reliance on multiple techniques for sizing and composition analysis, brings the drawback that these methods vary in sample requirements, such as concentration, preparation, and sensitivity. For nanoparticles in particular, population heterogeneity can severely affect their function and applicability, which cannot be resolved with these conventional bulk analysis techniques[110,111].

Enabling concurrent, high throughput analysis of single nanoparticles would greatly increase the capacity to study size, composition and inter- and intra-particle population variance, and therefore, aid in a more precise characterisation and a more robust preparation of nanoformulations. This ensures that in the development stage the uniformity of the formulations can be verified, which would be beneficial to their performance down the line. Therefore, SPARTA is developed and presented here as a comprehensive platform, able to integrally analyse nanoparticles ranging from synthetic polymer particles to liposomes without any modification. With the developed highly controlled automated trapping process, single nanoparticles are analysed with high throughput and sensitivity to resolve particle mixtures, obtain detailed compositional spectra of complex particles, track sequential functionalisations, derive particle sizes and monitor the dynamic reactions occurring on the nanoparticle surface. The SPARTA platform opens-up a wide range of new avenues for nanoparticle research through label-free integral high-throughput single particle analysis, overcoming key limitations in sensitivity and specificity of existing bulk analysis methods.

2.1.2 Optical trapping

In order to efficiently interrogate single nanoparticles with Raman spectroscopy, the single laser used to excite Stokes Raman scattering from the molecules in the sample is simultaneously employed as a single laser optical trap, holding the particle in place for analysis. Below the origins and physical principles of optical trapping are detailed, as well as a variety of applications leading-up to the first examples of Raman nanoparticle analysis as the foundation on which the SPARTA system is built.

2.1.2.1 Physical principles

Optical trapping, often used in conjunction with the term optical tweezers, is the manipulation of objects using lasers. The origins of the concept of light as an optical force can be retraced in history to the 17th century, where Johannes Kepler posed the concept of radiation pressure by the light of the sun as explanation for his observation of Halley's comet's tail pointing always away from the sun. The physical fact that light can transfer momentum to an object was theoretically stipulated by Maxwell and Bartoli in the late 19th century and experimentally proven by Lebedew in 1901[119]. From the calculations and experiments it was shown that the radiation pressure, at least that which is exerted by the sun was exceedingly small, and thus, without direct practical use.

This changed dramatically with the development of lasers in the 1960s, allowing the use of very highly powered and focused beams of light, which could be made to exert a physically relevant and utilisable force. A strong pioneer of this new field was Arthur Ashkin and he was awarded the Nobel prize in physics in 2018 for his contributions. Ashkin's seminal paper in 1970[120] showed that by using a laser, polystyrene micron-sized spheres could be drawn into the laser beam path and accelerated in the direction of the light. It was shown that this is due to the difference in refractive index, with the particle having a higher index of refraction than the surrounding media (in this case water). The resulting Fresnel reflection and deflections of the light through the particle lead to a net force towards the beam centre (highest intensity) and along the beam propagation axis, as shown schematically in Figure 2.1.a. This force is termed the intensity gradient force, as the rays of stronger intensity, closer to the beam axis generate a stronger force towards the beam axis than the opposite force generated by weaker rays on the opposite side of the particle[121]. A direct postulation was the use of two facing laser beams to construct an optical well, able to stably trap a particle in the symmetry point. A displacement of the particle was shown to lead directly to a correcting force towards the highest power density, ensuring stable trapping in the centre.

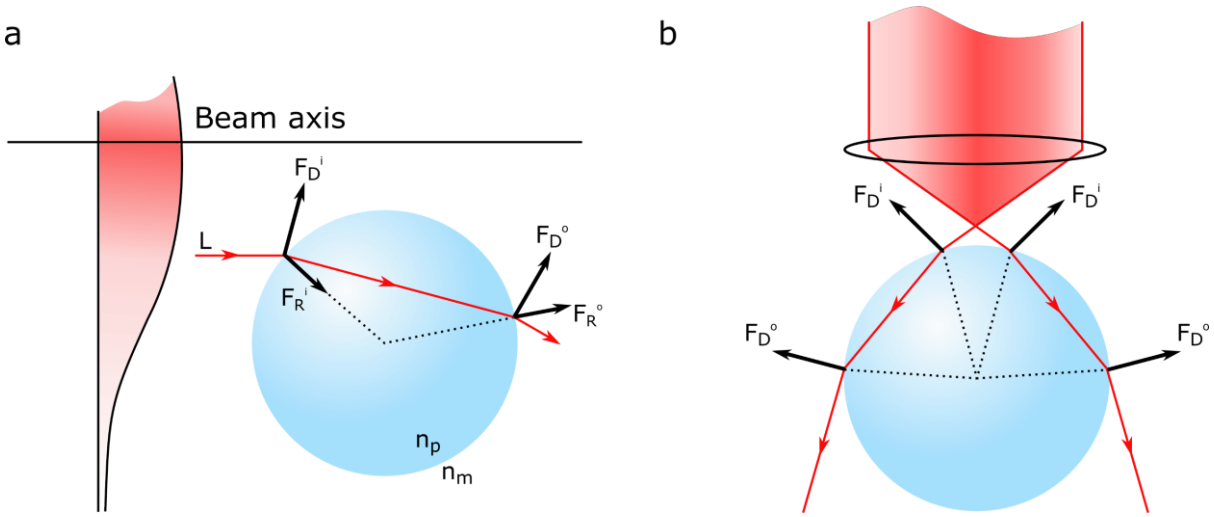

Figure 2.1 | Schematic representation of the origin of optical trapping forces. (a) Interaction of a light ray (L) with a dielectric polystyrene bead resulting in incident and output deflection (F_D) and reflection (F_R) forces with a net force towards and along the beam axis when the refractive index of the particle is larger than the media ($n_p > n_m$). (b) Single laser trapping using a diffractive focused beam resulting in a net force towards the point of maximum power density. These representations hold for Mie particles ($d > \lambda$). Adapted from *Ashkin et al.*[120,122]

In a subsequent pivotal paper by Ashkin in 1986[122], the theoretical and experimental proofs were demonstrated for using a single laser to stably trap particles in solution. The main change was the introduction of a high numerical aperture (NA) lens to tightly focus the beam in the solution. This generated a negative radiation pressure, or backwards force on a particle below the focal point of maximum power density, as illustrated schematically in Figure 2.1.b. Combination of the above shown diagrams illustrate the self-correcting or guiding trapping nature of the optical trap, by exhibiting a force towards the beam axis if the particle is not in the centre as well as a negative radiation pressure on a particle below the focal point.

It should be noted that the nature and strength of these forces are strongly dependent on the size range of the particle compared to the incident wavelength. The ray optics diagrams of Figure 2.1 are valid representations for particles in the Mie range[123], where the diameter (d) is large compared to the wavelength of the light (λ). However, trapping was observed well into the Rayleigh range where $d << \lambda$, due to a difference in origin of the forces contributing to the overall trapping force. In the Mie range the trapping forces on those particles mainly arise from differences in refractive index between the particle and medium, while for particles in the Rayleigh range the interaction path length through the particle is so small that this does not lead to a significant momentum on the particle itself. For particles that are small compared to the incident wavelength, the main force of consideration is the (dipole) gradient force arising from a difference in polarizability of the particle compared to the surrounding medium. This force, proportional to the polarizability (α), derives from the gradient of free energy which is lowered significantly when the particle is trapped and displaces water from the optical trap[122]. The dipole gradient force scales with the laser intensity and particles with lower polarizability can thus be trapped by using higher laser intensity and vice versa.

An important additional consideration is the fact that these models are based on the assumption of trapping solid particles. When considering hollow particles, such as liposomes or other vesicles, the apparent optical interaction diameter is not necessarily the particle diameter but that of the particle membrane or shell. Therefore, even for micron sized particles in the Mie range, the Rayleigh regime trapping forces can be more applicable[124,125]. This will be elaborated on in future sections concerning the trapping of non-solid particles.

2.1.2.2 Applications

The foundation of optical trapping laid by Ashkin and his colleagues led to a wide variety of applications of optical trapping. Two previous Nobel prizes were awarded for breakthroughs in physics, having optical trapping at their origins.

In 1997, the prize was awarded to Chu[126], Cohen-Tannoudji[127] and Philips for the development of methods of using laser light to cool and trap atoms[128129], and in 2001 it was awarded to Cornell, Ketterle and Wieman for their achievements in making Bose-Einstein condensates[130]. Both applications rely on a laser to trap, in this case atoms, and use the optical forces to slow them down and therefore achieve extreme cooling[121]. Within life sciences, the applications are somewhat closer to the concepts and scales directly following Ashkin's experiments, but with no less impressive results. The applications can be roughly divided into two, the direct manipulation and analysis of a trapped object of interest or the manipulation of a particle or bead to study a secondary interaction. An overview of the major applications of optical trapping can be seen in Figure 2.2.

The first applications of optical traps in life sciences were also pioneered by Ashkin when studying tobacco mosaic viruses (TMV). He demonstrated for the first time that individual biological entities could be trapped and manipulated by the light of laser traps, and thus that optical trapping as a technique was compatible with life[131]. A serendipitous observation was made when analysing viral solutions that were left open to the atmosphere for several days. Noticing that the bacterial growth that occurred in the solution interfered with the measurements, lead to the observation that bacteria themselves could be stably trapped, as well when reducing the trapping power significantly to avoid optical damaging. Conversely, increasing the power was sufficient to kill the bacterium directly within the optical trap, observing a release of the bacterial contents into the trap volume. The next important step in the development of optical trapping for life sciences, was the switch from conventional visible light range argon-based lasers (around 515 nm), to near infrared (NIR) and infrared (IR) light sources, which was shown to significantly reduce the optical damage[132]. These IR optical traps could provide higher trapping powers and increased manipulation, while maintaining a damage free environment to study for instance bacteria, yeast cells and red blood cells. By moving back to two laser systems, optical tweezers were developed which could manipulate with greater accuracy the trapped cells and could be used to probe cellular and subcellular properties such as the viscoelastic behaviour of the cell cytoplasm[133].

More recent applications of optical traps in life science include the probing of properties and interactions down to a molecular scale in the field of single molecule biophysics. By using a particle, such as latex bead as a proxy, molecular scale interactions can be probed by holding the bead inside an optical trap. Making use of surface functionalisation on the bead to design a system for single molecular interactions, capable of measuring forces down to the piconewton scale. A key example was shown in the study of elasticity of single DNA strands by Smith *et al.*[134], schematically shown in Figure 2.2 (top right).

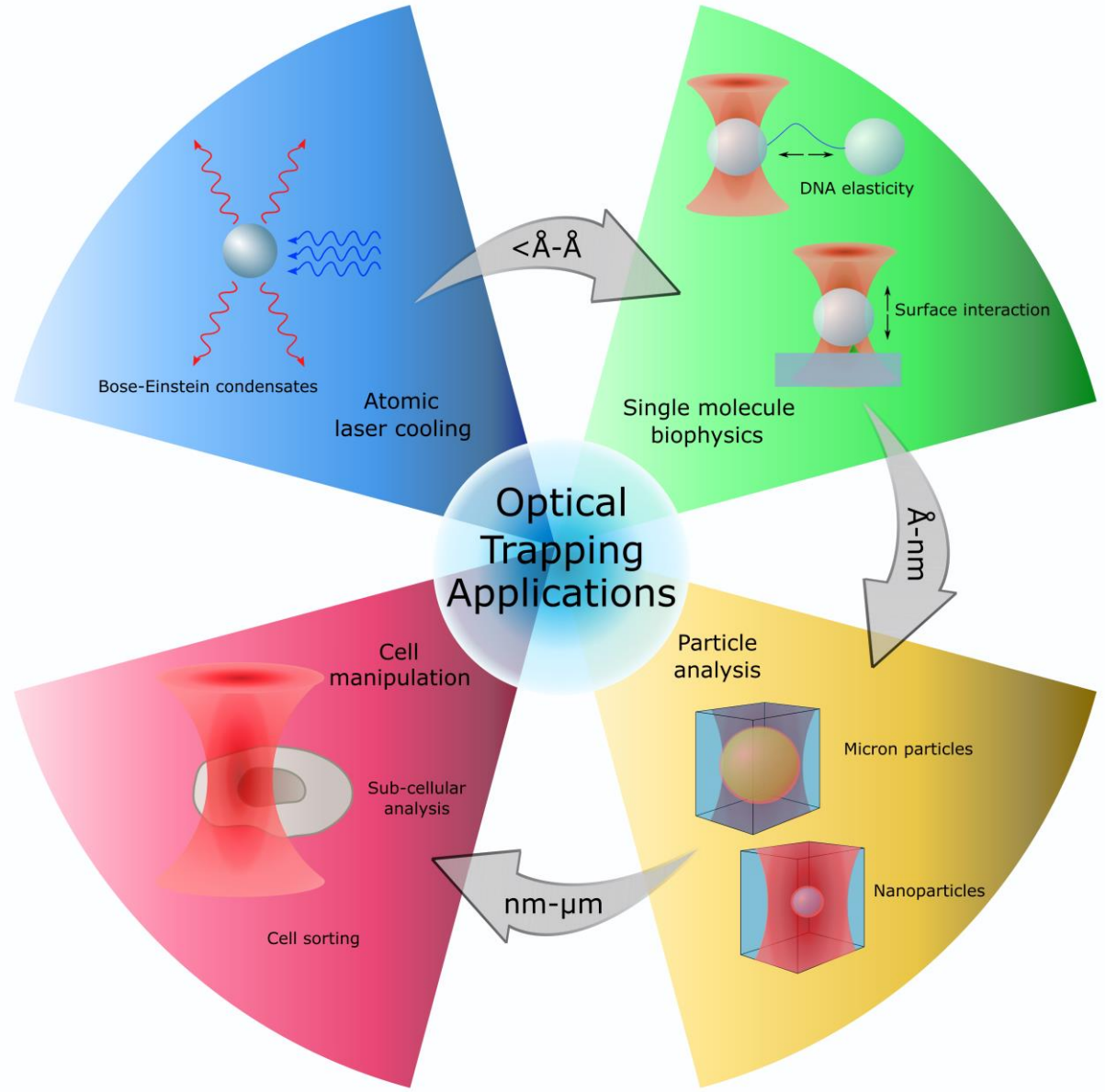

Figure 2.2 | Applications of optical trapping. Optical trapping has applications across multiple length scales. At the atomic scale optical trapping has been used in different kind of atomic trapping and laser cooling, for instance, the formation of Bose-Einstein condensates. At the molecular scale, optical trapping has been used to investigate single molecule biophysics, such as measuring the elasticity of DNA and molecular surface interactions. At the nanometre to micron scale, it can be used to trap, manipulate and analyse particles, as well as cells, bacteria and viruses.

In the study, latex beads were attached to both ends of a DNA strand and one was kept stationary by a micropipette while the other bead was trapped in an optical trap. The length and elasticity of the strand could thus be probed by moving the bead held by the micropipette and measurement of the displacement force on the bead inside the optical trap.

Another active field of study is that of the mechanics of single molecular motors, such as kinesins and DNA polymerases. These proteins can move along microtubules or DNA, respectively, to perform long range intracellular transport or ensure correct DNA replication. By attaching such a single molecular motor to a silica bead and guiding it to its substrate by a laser trap, the motion of the motors could be studied in great detail[135]. This revealed, for instance, the characteristic stepping motion of kinesins, by a combination of optical trapping and laser interferometry[136].

2.1.3 Combining optical trapping with Raman spectroscopy

2.1.3.1 Development and initial studies

The capabilities to hold and manipulate nano- and micro-sized particles in an optical trap also fuelled the avenue of research into the analysis of the trapped particle itself. Around the same time as Ashkin's first experiments on optical trapping, advances in Raman microspectroscopy led to the use of lasers for Raman excitation[137] and the possibility to excite Raman signals from microparticles was demonstrated[138]. Thurn and Kiefer were the first to show that in order to remove the interference of the substrate when analysing microparticles with Raman, the particle could be suspended in an optical trap[139], as demonstrated by Ashkin and Dziedzic some years earlier[120,140]. While this approach was not yet employing the highly focused single laser trapping in solution[122], rather the particles were levitated in air with a laser, the key idea was to take advantage of the fact that optical trapping can position a single particle in the focal point of the laser, which can simultaneously be leveraged to generate Raman scattering from the same particle to study its composition. As Raman scattering intensity is highest at the highest laser intensity, this places the particle in the ideal position for analysis during optical trapping. This led to a wide variety of uses and advances from analysing aerosols[141] to the study of microparticles and liquid droplets in solution[142]. Of interest here is that the compositional analysis by Raman scattering was not limited to static analysis of the particle in question, or the contents of a liquid droplet, but that of key interest was the study of reactions on the particle surface or inside the trapped droplet[143].

As noticed with the optical trapping of bacteria by Ashkin[131], the use of visible light lasers could lead to significant optical damaging and the use of NIR or IR lasers was proposed. This was successfully experimentally verified and able to induce high powered traps while avoiding optical damaging of biological components[132]. Similarly, for the simultaneous trapping and Raman analysis the use of NIR lasers was brought about by Ajito[144], overcoming technical challenges by using a new generation of holographic notch filters (HNFs).

This reduced sufficiently the Rayleigh scattered light of the laser line, to observe the Raman scattering from trapped droplets. In addition to less optical damage, the shift to a NIR laser significantly reduced the interference from fluorescence of organic compounds in the Raman spectrum, increasing the sensitivity. NIR laser Raman trapping paved the way for further detailed studies on micron and nano particles while avoiding optical beam damage[145] (detailed below) and the simultaneous manipulation as well as the characterisation of cells[146] and organelles[147], which will be further elaborated on in Chapter 3 of this thesis.

2.1.3.2 Micro- and nano particle analysis – state of the art

Visible and NIR laser Raman trapping has been explored as a valuable tool for the structural and compositional study of micro- and nanoparticles. Of particular interest is the use of Raman spectroscopy to analyse the composition and heterogeneity of vesicular structures posed for drug delivery systems, such as liposomes[124,148] and polymersomes[4,149]. These particles can be made from a wide range of amphiphilic molecules, to obtain vesicles with a variety of compositions, size ranges and physical properties[17,148].

The first detailed studies on the Raman spectroscopic analysis of (large) unilamellar liposomes were almost simultaneously performed by Cherney *et al*.[150] and Sanderson *et al*.[148], trapping liposomes of around one micron in diameter and obtaining spectra from the lipid membrane components, such as DMPC, DOPC and cholesterol. A first attempt was made to estimate, from the spectra of single liposomes, their compositional mixture ratio and comparing it to the intended bulk mixture. Interestingly, a strong discrepancy was found in this ratio for the single liposomes, highlighting the value of single particle analysis. In addition, the effect of variance in particle size was observed, where an initial increase in Raman scattering was observed for increasing particle size, until a maximum was reached after which the signal decreased. This can be explained by relation to the focal spot size, where upon exceeding this spot size, even though more material is available to elicit Raman scattering, the liposomal membrane was forced to move further away from the highest intensity point upon increase of the size, leading to a reduction in overall Raman scattering intensity.

Raman optical trapping was also used to study in detail the effect of trapping forces on liposomes[124]. As stated in 2.1.2.1, due to the nature of liposomal particles having a 5-10 nm thick membrane, physically, they behave and interact with the optical trap as particles in the Rayleigh regime, rather than the Mie regime, as would be the case for solid micron-sized particles. The effects of optical forces on these liposomes can be studied by addition of a solution marker, such as perchlorate ions to the solution, which have been shown to be impermeable to lipid membranes[150].

By careful analysis of the amount of perchlorate signal present in the confocal volume, the trapping configuration and the degree of membrane deformation of the liposome could be inferred[124].

In addition to particle compositional analysis, studies have shown the possibility of investigating dynamic events or reactions occurring on the particle surface, by monitoring the spectrum of optically trapped particles over an extended time. Examples include observation of polymerization reactions[151,152], solid phase particle assisted peptide synthesis[153] or measurements of analyte concentrations in liposomes[154]. The Raman spectroscopic analysis of single optically trapped particles is a valuable technique to study these processes due to the advantage that Raman can be performed in a label-free manner without directly disturbing the chemical system, as well as the fact that the droplets or particles are suspended in solution, thus avoiding the influence of surface transport phenomena and closer mimicking of the bulk process. An exemplary study of these capabilities was performed by Schaefer *et al*.[152] the radical polymerization of 11-acrylamidoundecanoate (SAAU) was tracked through trapping of the emulsion droplets forming prior to radical initiation, resulting in direct measurements of the polymerization kinetics. In addition, they studied the structure of the polymeric particles post formation and the accumulation of a model compound into these particles to obtain their loading capacity and uptake and release kinetics.

Despite recent advances, the use of Raman spectroscopy for single particle analysis suffers from a major limitation, namely the fact that the particles need to be manually trapped inside the laser or lifted from a substrate[155,156]. This significantly limits the number of particles that can be analysed as the process is both slow and labour-intensive. The very limited particle throughput also obstructs any investigation of composition heterogeneity with sufficient statistical power.

To address the imperative need for large scale integral size and composition characterisation of single nanoparticles, a novel platform for Single Particle Automated Raman Trapping Analysis (SPARTA) was developed. SPARTA enables high throughput, routine analysis of individual nanoparticles in solution without any need for particle labelling or modification. A thorough analysis of the composition of liposomes and polymersome systems is demonstrated, as well as the ability to resolve mixtures and investigate particle heterogeneity using the SPARTA platform. In addition to particle compositional analysis, the SPARTA platform is ideally suited for monitoring sequential functionalisation of nanoparticles, as well as tracking the dynamics of a click reaction on the particle surface. Lastly, by taking advantage of the high-throughput measurement capability, a method is demonstrated showing that perchlorate addition can be used in a radical new way, to allow single particle sizing of the trapped particles.

SPARTA opens up a plethora of exciting new applications to analyse inter and intra sample heterogeneity, complex mixtures, on-line reaction monitoring and integrated simultaneous sizing of single particles in high detail.

2.2 Materials and Methods

2.2.1 SPARTA Raman microspectroscopy system

Confocal Raman spectral acquisition was performed on a Raman micro-spectroscope (alpha300R+, WITec, Ulm, Germany). The light source used was a 785 nm laser (Toptica XTRA II) with a 63×/1.0 NA water immersion microscope objective lens (W Plan-Apochromat, Zeiss, Oberkochen, Germany). The scattered light was collected via a 100 µm fibre with a 600 g mm^{-1} grating spectrograph (UHTS 300, WITec, Ulm, Germany) and spectra were acquired using a thermoelectrically cooled back-illuminated CCD camera (iDus DU401-DD, Andor, Belfast, UK) with a spectral resolution of 3 cm^{-1} and 85 mW laser power at the sample. Laser control was performed remotely controlled via a serial connection and custom MATLAB (2016b, The Mathworks, MA, USA) scripts. Dr. Isaac Pence was instrumental in the development, writing and optimisation of the scripts.

2.2.2 SPARTA standard sample preparation

For SPARTA analysis typically 200 µL of particle solution was required, of which approximately half was routinely recovered, depending on the measurement time. Ideal particle concentrations were determined to be between 1×10^{10} – 1×10^{12} particles per millilitre or around 0.1-0.01 % solids for polystyrene particles. Sample solutions were placed on a 22 mm coverslip, affixed to a standard microscopy slide with a drop of phosphate buffered saline (PBS). The sample was placed under the water immersion objective for measurement.

2.2.3 SPARTA standard data analysis

The following pre-processing procedure was applied to all spectra acquired with the SPARTA platform. The spectral centre during acquisition was standard set at 1000 cm^{-1} and the raw data was truncated to the range of 350 – 1825 cm^{-1} to omit the excitation signal. For the measurements including the alkyne modification, the spectra centre was shifted to 1500 cm^{-1} resulting in a measurement range of 606 – 2254 cm^{-1}.

An automated script based on peak amplitude and 2nd derivative was employed for cosmic spike removal, followed by a manual visual check. Spectral background was subtracted via curve fitting (Whittaker filter, λ=100,000) and noise smoothed using a Savitzky-Golay filter (3 points, first order). The resulting spectra were normalised via area under the curve, except for the SPARTA sizing analysis as this is incorporated via the perchlorate ratio calculation. Subsequent statistical analyses (hierarchical cluster analysis, principal component analysis, multivariate curve regression, partial least-squares discriminant analysis) were implemented using PLS Toolbox (Eigenvector Research, Inc. WA, USA).

2.2.4 DPPC and d-DPPC liposomes preparation

Liposomes were prepared according to the following standard procedure. 5 mg mL^{-1} stock solutions of each of the following compounds were made in chloroform and stored at -20 °C under Argon prior to use: lipid (1,2-dipalmitoyl-sn-glycero-3-phosphocholine (DPPC) and 1,2-dipalmitoyl-d62-sn-glycero-3-phosphocholine (DPPC-d62, referred here to as d-DPPC), (Avanti Polar Lipids Inc. AL, USA), 17-octadecynoic acid (Cambridge Bioscience, UK) and cholesterol (Sigma-Aldrich, UK). For DPPC liposomes a lipid film was made by adding 500 µL DPPC stock and 43 µL of cholesterol stock solution in a 10 mL round bottom flask, resulting in a mol ratio of 85: 15 mol% DPPC: cholesterol. For d-DPPC liposomes 250 µL DPPC stock and 250 µL d-DPPC stock was used, resulting in a ratio of 42.5: 42.5: 15 mol% // DPPC: d-DPPC: cholesterol. For 17-octadecyonic acid DPPC liposomes the DPPC/17-octadecynoic acid/Cholesterol stocks were mixed to obtain molar ratios of 50:40:10 mol % respectively. The chloroform was evaporated under nitrogen flow to form a thin lipid film. Lipid films were lyophilised overnight in a freeze dryer (Labconco, MO, USA) prior to rehydration. The films were hydrated with 1 mL PBS, shaken for 1 minute and sonicated for 1 minute. The solutions were then extruded 31 times through a polycarbonate membrane (Avanti Polar Lipids Inc. AL, USA) with a mesh size of 200 nm at 60 °C. Liposome size distribution and particle concentration were determined via NTA. The liposomes were prepared with aid of Mr. Conor Horgan.

2.2.5 DPPC liposome photostability

A 100 times dilution in PBS of the liposome solution as described above, was made and a liposome was trapped and held in the laser beam (785 nm, 85 mW) of the SPARTA system. Spectra of 10 second integration time were acquired with a 1 second interval between measurements.

A spectral series of 5 minutes was identified as having one particle stable in the trap consisting of 26 consecutive measurements. The mean and standard deviation of the raw truncated spectra were determined with OriginPro 2016 (OriginLab Corporation, MA, USA). A surface plot of the raw truncated data was obtained with MATLAB (2016b).

2.2.6 Polymersome preparation

PMOXA-b-PDMS-b-PMOXA polymersomes (denoted further as ABA) were prepared from the poly(2-methyloxazoline-b-dimethylsiloxane-b-2-methyloxazoline) (Mn · 103 = 0.5-b-4.8-b-0.5) triblock copolymer (P18140D-MOXZDMSMOXZ, Polymer Source Inc., Quebec, Canada). 1 mL of a 6 mg mL^{-1} stock solution of the triblock copolymer in ethanol was added to a 5 mL round bottom flask. ABA-heparin polymersomes were made by mixing in 25 wt. % PDMS-b-heparin (Mw = 5kDa-b-11kDa) block copolymer synthesised as previously described by Najer *et al*.[18] Briefly, commercial heparin sodium salt (15 kDa, Merck, KGaA, Germany) was ion-exchanged to tetrabutylammonium salt and reacted in DCM with an excess of commercial diamino-PDMS (5 kDa, ABCR GmbH, Germany) via reductive amination using 2-picoline borane (Sigma-Aldrich GmbH, Germany) as reducing agent. The reaction was stirred for 7 days at RT with two more additions of 2-picoline borane on day three and five. The product was dried, washed in diethyl ether, dried, dissolved in ethanol, purified by repeated precipitation in cold diethyl ether and dried. 1 mL of 6 mg mL^{-1} ABA stock was combined with 0.5 mL 4 mg mL^{-1} stock of PDMS-b-heparin block copolymer in ethanol in a 5 mL round bottom flask. The polymer solutions were dried on a rotary evaporator at 50 °C and 20 mbar for approximately 15 minutes. Subsequently, the polymer films were rehydrated in 1.2 mL PBS for 72 hours under vigorous stirring. The polymer solutions were filtered through a 0.45 µm syringe filter (Millex-HV 13 mm PVDF, Merck KGaA, Germany) and extruded 5 times through a polycarbonate membrane (Avanti Polar Lipids Inc. AL, USA) with a mesh size of 200 nm and subsequently 31 times through a polycarbonate membrane with a mesh size of 100 nm. The polymersomes were further purified by (SEC) (10×300 mm column packed with Sepharose 2B (Sigma-Aldrich, UK)) in PBS, collecting 1 mL fractions. Polymersome size distributions were analysed by DLS and NTA. The polymersomes were prepared by Dr. Adrian Najer.

2.2.7 Nanoparticle Tracking Analysis (NTA)

Nanoparticle Tracking Analysis (NS300, 532 nm laser, Malvern, UK) was performed by acquisition of 3 times 30 second videos of a 1 mL sample in PBS.

The camera level was kept between 13 and 14, with a screen gain of 1 and detection threshold set at 5. The samples were diluted to within the optimum measurement range of 1×10^8 – 1×10^9 particles per millilitre for measurement. The measurements were analysed using the Nanosight NTA 3.0 software (Malvern, UK, 2014).

2.2.8 Dynamic light scattering (DLS)

Dynamic light scattering (ZEN3600 Zetasizer, Malvern, UK) was performed within disposable semi-micro cuvettes (Brand GMBH, Germany) with 400 µL solution, through acquisition and averaging of 3 measurements (each of 10-15 acquisitions) by NIBS at 173° scattering angle. The measurements were acquired using the Zetasizer Software v.7.02 (Malvern, UK, 2013). The number distributions were used to verify and compare particle size distributions.

2.2.9 Preparation of Cysteine-Tyrosine-Tyrosine (CYY) tripeptide

CYY tripeptide was synthesised by standard solid phase peptide synthesis using Fmoc protecting group chemistry on Rink-amide MBHA resin and protected Cysteine and Tyrosine amino acids (AGTC Bioproducts Ltd.). Briefly, Fmoc deprotection was performed with 20 v% piperidine in DMF for 10 minutes, followed by two washes with DMF and DCM. Amino acid couplings were carried out with Fmoc-protected amino acids (4 equivalents), HBTU (3.75 equivalents), and DIEA (6 equivalents) in DMF for 2 hours and the process repeated as per the sequence. The peptide was cleaved from the resin and deprotected with 95% trifluoroacetic acid (TFA), 2.5% tri-isopropylsilane, and 2.5% water for 4 hours. The TFA was removed using rotary evaporation, and the peptide was precipitated and washed with cold diethyl ether 200 mL and 2 × 50 mL. For purification, the peptide was dissolved in a solution of 4.9% ACN in ultrapure water with 0.1% TFA and purified using reverse-phase preparative high-performance liquid chromatography (HPLC; Shimadzu, Japan) with a C18 Gemini 150 × 21.2 mm column (Phenomenex, CA, USA) with a 5 µm pore size and a 100 Å particle size. The mobile phase was ultrapure water containing 0.1% TFA at 15 mL min^{-1} and during the 15-minute run the concentration of ACN containing 0.1% TFA in the mobile phase changed was 0% 0-3 minutes, 0-100% 3 - 12 minutes, 100% 12 - 13 minutes and 0% 13-15 minutes. The HPLC fractions were checked for the correct mass using Liquid Chromatography-Mass Spectrometry (LCMS, Agilent, CA, USA) (Observed MW = 447.2, Predicted [CYY] H+ = 447.16), and the pure peptide fractions were combined, rotary evaporated to remove ACN and lyophilised by freeze drying (Labconco, MO, USA). Preparation of the CYY tripeptide was performed by Dr. Christopher Wood.

2.2.10 Serial functionalisation of polystyrene particles

Amine functionalised 0.2 µm polystyrene particles (Polybead Amino 0.20 µm, Polysciences Inc.) were further functionalised with 2-iminothiolane. A reaction buffer of 2 mmol EDTA in PBS was made and adjusted to pH 8 with 2 M NaOH, from which a 6 mg mL^{-1} solution of 2-iminothiolane was prepared. For functionalisation 780 µL of reaction buffer was combined with 200 µL of 0.20 µm polystyrene particles (2.6% solids (w/v)) and 20 µL 2-iminothiolane solution and left to react overnight at room temperature. This resulted in a 0.5 % solids (w/v) solution of sulfhydryl functionalised particles, which were further diluted 10 times in PBS and purified. Unless otherwise stated, purification was performed by centrifugation for 10 minutes at 14,000 rcf, after which the pellet was redispersed in PBS. Redispersion was aided by vortexing for 30 seconds and ultrasonication for 1 minute, obtaining a clear solution. After each purification step DLS measurements were performed to verify the absence of aggregation, prior to SPARTA. A minimum of 100 successful trapping spectra were acquired with the SPARTA experimental parameters set to 1 second iteration acquisition time, 10 seconds high SNR acquisition times and 1 second laser disabling time. The particles were further treated with 10 mg of 5,5-dithio-bis-(2-nitrobenzoic acid (DTNB), forming a disulphide bond between the sulfhydryl functionalisation and the TNB anion. The particles were purified, and SPARTA was performed to verify disulphide bond formation. The tripeptide functionalisation was obtained by treating the TNB functionalised particles with 2 mg of CYY (Mw = 446.16 g mol^{-1}, 4.5 mM). SPARTA was performed after purification to observe the tripeptide functionalisation. To demonstrate the reversibility of the functionalisation, 100 µL of tris(2-carboxyethyl) phosphine (TCEP, 0.5 M, neutral pH Bond-Breaker™, Thermo Fischer Scientific, UK) was added to the TNB functionalised particles, turning the solution bright yellow indicating cleavage of the disulphide bonds. Similarly, the disulphide bonds between the particle and the tripeptide were cleaved. After purification the recovery of the sulfhydryl functionalisation was verified by SPARTA.

2.2.11 Dynamic click reactions on polystyrene particles

Carboxyl functionalised 0.2 µm polystyrene particles (Polybead carboxylate 0.20 µm, Polysciences Inc.) were functionalised with propargyl amine using EDC-NHS coupling. Solutions were made of 20 mg mL^{-1} 1-ethyl-3-(3-dimethylaminopropyl) carbodiimide and 20 mg mL^{-1} N-hydroxysuccinimide in PBS and 40 µL of each was added to 200 µL of polystyrene particles (2.6% solids) and 800 µL of PBS. The solution was shaken on a thermomixer at room temperature and 20 µL of neat propargylamine was added after 30 minutes. The reaction was allowed to proceed under continuous shaking overnight.

The synthesis solution was diluted 10 times and purified. Purification was performed by centrifugation for 10 minutes at 14,000 rcf, after which the pellet was redispersed in PBS. Redispersion was aided by vortexing for 30 seconds and ultrasonication for 1 minute. After purification, DLS traces were obtained to verify the absence of aggregation, prior to SPARTA. Solutions were made of 100 mM of copper sulphate, 100 mM of sodium ascorbate and 0.5 M of potassium bicarbonate in PBS. Azido acetate was made by addition of a 1 M solution of sodium hydroxide in a molar equivalent to 2-azidoacetic acid (Sigma-Aldrich, UK). The population click reaction was carried out by formation of the triazole by addition of 2.88 µL 100 mM of sodium ascorbate, 1.80 µL 100 mM of copper sulphate and 0.5 µL neat azido acetic acid to 200 µl of alkyne functionalised polystyrene particles, diluted 100 times in PBS. Droplets of a 0.5 M solution of $KHCO_3$ were applied to adjust the pH to 7. The single particle hold click reaction was performed with addition of 7.46 µL azido acetate (equalling 0.5 µL neat azido acetic acid), with no further pH adjustment necessary.

2.2.12 Click reaction monitoring by UV-Vis analysis

3-Azido-7-hydroxycoumarin (Jena Bioscience GmbH, Germany) was used to validate whether a CuAAC reaction[157,158] would occur on the alkyne functionalised polystyrene nanoparticles. To do this the fluorescence of the resulting triazole product (Absorption/Emission = 404/477 nm) was monitored by UV-Vis spectroscopy. In a 96 well plate 200 µL of a 1000 times dilution of the purified alkyne functionalised polystyrene particles in PBS was combined with 2.88 µL 100 mM sodium ascorbate, 1.80 µL 100 mM copper sulphate and 5 µL 3-Azido-7-hydroxycoumarin 1 µM in water. As controls, the measurements were performed at the same time with exclusion of 3-Azido-7-hydroxycoumarin or copper sulphate. The fluorescence was monitored over 30 minutes and measured at 15 second intervals.

2.3 Results and Discussion

2.3.1 SPARTA system development

The first issue considered in development of the SPARTA system, was the manner of sample interfacing with the Raman microspectroscopy system, a schematic setup of which can be seen in Figure 1.4. In order to achieve a tight confocal volume and ensuring optimum focusing of the laser, a 63× 1.0 NA objective was chosen, interfacing directly with the sample solution. A water immersion objective has the added advantages of allowing a higher magnification, and thus, tighter focusing of the laser[122,159], as well as avoiding a refracting air-water interface between the objective and the sample. In order to interface the objective directly with the solution, a compact droplet is preferred, to minimise the amount of sample solution required for analysis. It was observed that when placing a droplet on a standard glass microscopy slide, the glass is too hydrophilic and the drop has a strong tendency to spread, especially upon light manipulation (*e.g.* due to sample transfer), schematically shown in Figure 2.3.a. This was resolved by adhering a coverslip (16-22 mm in diameter) to the microscopy slide by approximately 2 µL of water, ensuring the top of the coverslip is not wetted while adhering to the slide. Pipetting a drop of sample solution on the coverslip ensures the formation of a stable and compact drop, which can be interfaced efficiently with the immersion objective (Figure 2.3.b). The ideal droplet size was found to be between 150-200 µL, ensuring sufficient volume to be able to retract the objective away from the surface to ensure the focal point is within the solution and allowing measurement times of around 2-3 hours before evaporation of the droplet cause loss of drop interfacing with the objective.

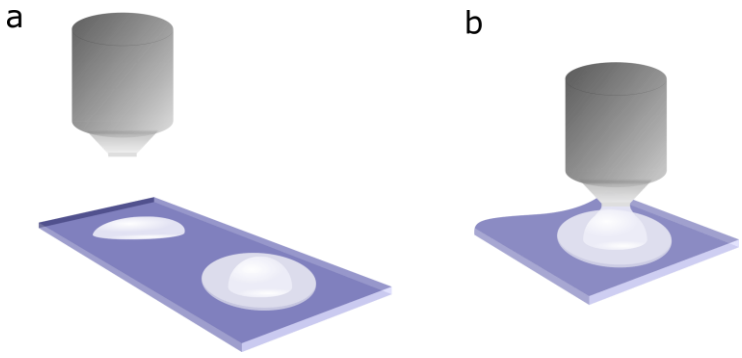

Figure 2.3 | Schematic Raman trapping sample interfacing. Droplets of 150-200 µL of solution can be interfaced with a water-immersion objective. Due to the system confocality, standard glass slides can be used. (a) Placing a drop directly on a slide will not form a stable drop while placing it on a coverslip will form a tight stable drop. (b) The water immersion objective is brought in contact with the drop and retracted to ensure the focal point is in the solution.

As has been alluded to, the use of confocal optics is a key requirement for the SPARTA system for two main reasons. First, a confocal system is necessary to enable the use of standard microscopy slides and coverslips to interface the sample droplet with the system. As the confocality ensures only the spectral information from a defined axial depth is collected (~1 µm), the high background signal that would arise from the glass substrate is eliminated when the distance to the substrate is sufficiently large. The second reason that necessitates a confocal system is the requirement and aim to only collect signal from a single particle in the solution, the one that is held in the optical trap. A tight confocal volume therefore ensures that the signal collected above and below the particle of interest, possibly from surrounding particles, in minimised.

Prior to developing an automated particle trapping and analysis system, the confocal Raman system in place was tested for its capabilities for single laser optical trapping, as this had not been attempted before. As a model system, DPPC liposomes were made labelled with 17-octadecynoic acid, which would contribute an alkyne moiety to be observed in the Raman silent region in addition to the lipid signatures of DPPC. The liposome solution was interfaced with the water immersion objective (Figure 2.4.a) and a continuous acquisition of Raman spectra was initiated at 10 seconds acquisition and a 1 second interval time. Trapping was observed within a few seconds by appearance of lipid signature peaks (*e.g.* CH_2 vibration at 1450 cm^{-1}). 10-15 spectra were collected of the trapped particle (Figure 2.4.b, green time frames), after which the optical trap was manually disabled for a few seconds by manipulation of the shutter on the laser head (Figure 2.4.b, red time frames).

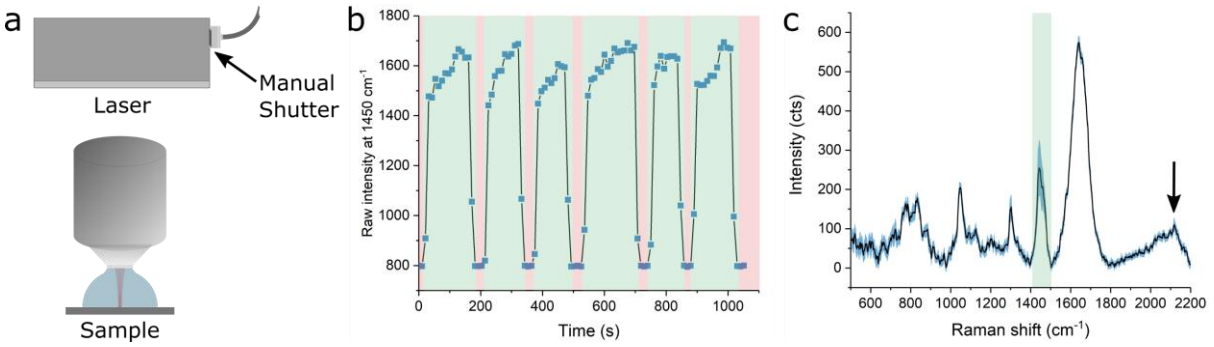

Figure 2.4 | Manual trapping of liposomes. DPPC liposomes labelled with 17-octadecynoic acid were manually trapped using a time series acquisition series of 10 seconds with 1 second intervals. (a) Schematic of laser showing manual shutter on laser head and objective sample interfacing. (b) Raw intensity at 1450 cm^{-1} over time with shutter open time blocks in green and closed shutter times in red. Shutter was kept open to collect 10-15 spectra of a trapped particle. (c) Mean ± s.d. of background subtracted DPPC liposome spectrum (n=13) of the first trap shown in b, arrow indicates a small alkyne peak at 2120 cm^{-1}.

The average collected spectrum (mean ± s.d.) can be seen in Figure 2.4.c, with the arrow indicating the presence of a small amount of signal arising from the alkyne moiety of 17-octadecynoic acid. This initial experiment indicated the base suitability of the confocal Raman microspectroscopic setup for single particle trapping.

In the next sections the design and validation of the completed SPARTA platform is described, including a variety of model systems developed to demonstrate its three distinctive modes for single nanoparticle characterisation.

2.3.2 SPARTA system design and validation

The SPARTA system is based on a high-end confocal Raman spectroscopy setup where the laser, camera and spectroscope are simultaneously controlled via custom, in-house MATLAB scripts, for automated single particle trapping and Raman spectral acquisition. To enable the application of SPARTA for comprehensive particle analysis, three distinct modes of operation were developed (Figure 2.5).

The first mode comprises the functionalisation and composition analysis (Figure 2.5-I) by acquisition of high quality Raman spectra for single particles in solution, allowing investigation of their composition and verification of the presence of specific functionalisations. The SPARTA system has the key advantage of enabling automated analysis of hundreds of particles, compared to existing systems only capable of analysing in the range of tens of particles. The automation and up scaling of the number of particles analysed enables a means to analyse particle variance both on a single particle basis and at population level for complex mixtures of particles.

The second mode of the SPARTA platform (Figure 2.5-II) is solution marker mediated sizing analysis. By combining the high throughput single particle analysis with a perchlorate ion standard, it is demonstrated here that the size of the particle in the trap can be estimated simultaneously when acquiring its compositional information. A particle entering the trap displaces its volume of perchlorate ion solution from the trap. By measuring the decrease in perchlorate signal in the Raman spectrum (at 938 cm^{-1}), relative to trapping particles of known size, a calibration curve can be obtained to relate the perchlorate signal in the spectrum to the size of the particle in the trap, provided it is smaller than the confocal volume. This enables particle sizing on a single particle basis with the simultaneous collection of compositional data, allowing direct acquisition and correlation of particle size and composition, where hitherto a combination of several analysis techniques had to be used and size and composition could not be compared on a per particle basis.

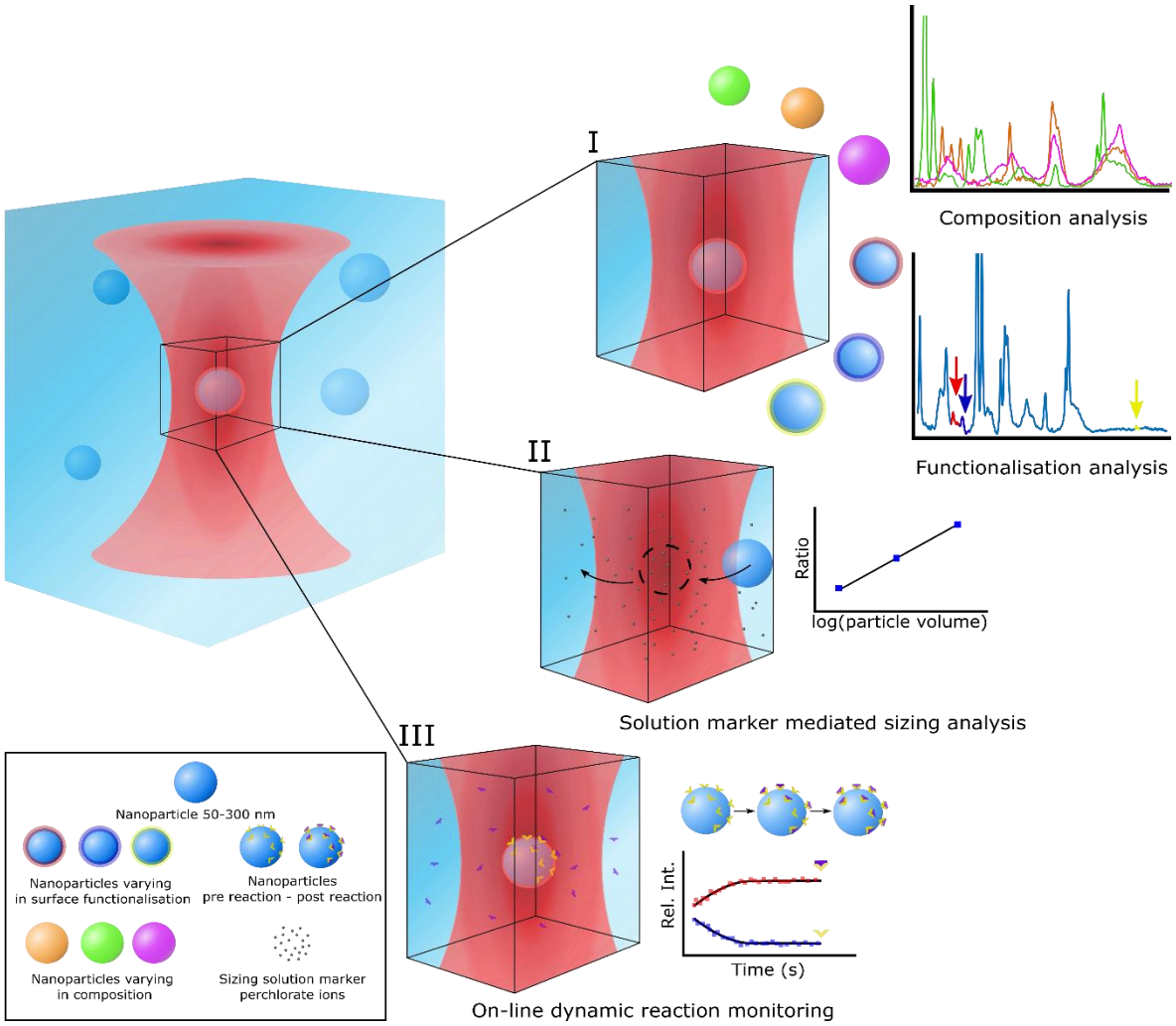

Figure 2.5 | Schematic overview of the functionalities of the SPARTA platform. The capacity to trap nanoparticles in the size range of 50 – 300 nm automatically and with a high degree of control allows the analysis of the particles in three distinct, complimentary modes: (I) the first mode is functionalisation and composition analysis, which provides the Raman spectrum of single particles in solution to verify functionalisation and provide detailed analysis of their composition. This also enables the analysis of the heterogeneity of single particles within a uniform population or complex mixtures. (II) The second mode is solution marker mediated sizing analysis, allowing the estimation of the size of a trapped particle by measuring the relative displacement of perchlorate ions from the confocal volume. (III) The third mode is on-line dynamic reaction monitoring, which allows the tracking of the progress of a reaction occurring on the surface of the particle, either on a single particle for the duration of the reaction or a different single particle at distinct time points. *Figure originally published in* Penders J. *et al.*, *Nature Communications,* 9, 4256, 2018[112].

The third mode of the SPARTA platform is on-line dynamic reaction monitoring (Figure 2.5-III); tracking the progress of a dynamic event on single particles. This can be achieved by either holding a single particle in the trap for the duration of the reaction, or by trapping a new particle at subsequent time points to compare reaction progress on a particle by particle basis. The single particle sampling aspect of this technique permits investigation of reaction kinetics, identifying if the reaction occurs simultaneously at the same rate on each particle, or on specific single particles at any one time, as would be the case for reactions limited by catalyst availability. These results can further be correlated to bulk dynamics, which can be tracked with conventional methods.

To facilitate the aforementioned areas of application, extensive control is required over the trapping process, detailed in the SPARTA process flow (Figure 2.6.a). The core concept of the automated trapping process is the alternation between short acquisitions, called iterations, and longer acquisitions for high signal-to-noise ratio (SNR) spectra. To allow for automated trap recognition, an initial particle is trapped and a characteristic peak in the spectrum is selected, along with its (approximate) middle height as a threshold (Figure 2.6.a II). This results in the recognition of a successful trap, if the chosen peak is above the threshold intensity during an iteration acquisition. Next, the acquisition iteration loop is initiated (Figure 2.6.a-III IV). If the thresholding peak is not above threshold intensity in the iteration spectrum (Figure 2.6.a-IV), a maximum of 10 iterations is performed. If the peak signal fails to exceed the selected threshold during any of these iterations, the trap is registered as unsuccessful and the laser is momentarily disabled. When a successful particle trap is recognised (Figure 2.6.a-V), a longer acquisition is taken to obtain a high SNR spectrum of the trapped particle (Figure 2.6.a-VI). Lastly, the trap is momentarily disabled by turning off the laser to allow the particle to diffuse away. This iteration process allows for a much higher turnover of trapping attempts and acquisitions, since it only permits the acquisition of longer, high SNR spectra when trapping is successful. The automated determination of a successful particle trap obviates the need to record data from iterations without sufficient signal relative to the threshold as can be seen by the comparison of the spectral lineshape for a successful polystyrene particle trap (Figure 2.6.a-V) *versus* a trapping iteration containing only the fluid medium (Figure 2.6.a-IV).

An adequate laser disabling time ensures momentary disengaging of the trap to allow the particle to diffuse away and is essential for avoiding duplicate analysis of the particle. If the disabling time is too short (Figure 2.6.b), *e.g.* only blinking the laser, it results in more than 90% of the successful traps occurring at the first iteration, thus with a high likelihood that the same particle is repeatedly trapped before it can diffuse away.

However, a laser disabling time between 0.5 and 1 second is sufficient to ensure <1% trapping at the first iteration number (Figure 2.6.c), which is in agreement with diffusion speeds reported in literature[160]. In addition, it was verified that the iteration number at which a spectrum is acquired does not affect the peak intensity of the spectrum, for instance due to fluctuations in the laser power.

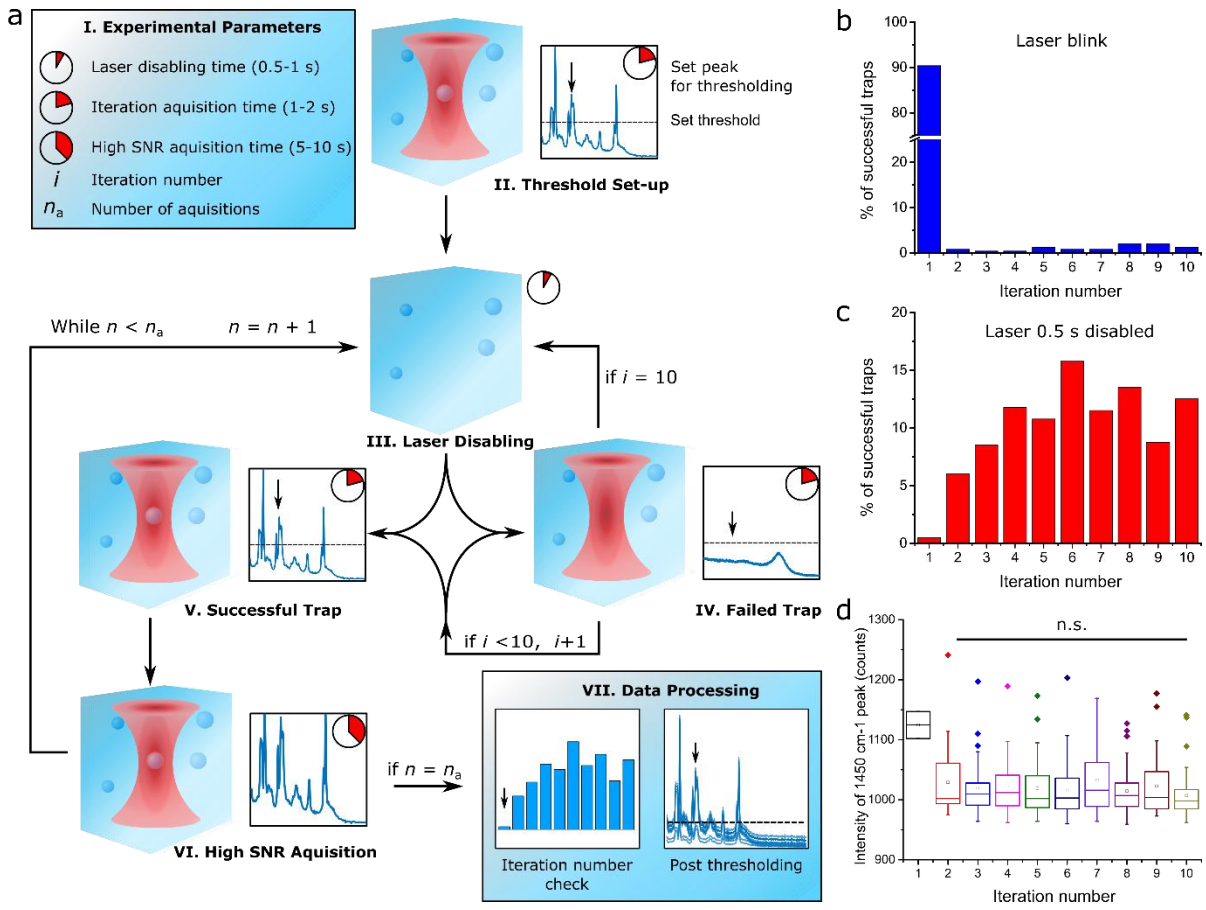

Figure 2.6 | Overview of the SPARTA process flow and trapping control validation. (a) Process flow starting with the set-up of the acquisition parameters (I) and thresholding based on the signal obtained from an initial particle trap to set the peak position and height used to determine a successful particle trap (II). Next, the acquisition loop is initiated (III-IV) where quick scans are iterated until a trap is recognised (V) after which a high SNR acquisition is taken and saved (VI). The laser is disabled (III) to allow the particle to diffuse away and the process is repeated. After n_a acquisitions the data can be processed (VII) for further analysis. (b) Iteration number distribution when rapidly blinking the laser after each trap. (c) Iteration number distribution when turning the laser off for 0.5 seconds. (d) Box and whisker plot showing the signal intensity distribution for a characteristic peak *versus* the iteration number of the trap, no significant influence was found between any of the iteration numbers > 1. One-way ANOVA, with holm corrected multiple comparisons test, n = 355 combined traps. Indicated are the median (horizontal line inside the box), mean (□), minimum and maximum values as the ends of the whiskers and outliers (♦). *Figure originally published in* Penders J. *et al.*, *Nature Communications,* 9, 4256, 2018[112].

As shown in (Figure 2.6.d) for a characteristic peak at 1450 cm^{-1} (CH_2 vibration), the peak intensity is not significantly altered by the iteration number of a successful trap, with the notable exception of particles trapped at iteration 1.

The parameters as indicated (Figure 2.6.a-l), such as the number of acquisitions (n_a), and the times for iteration, high SNR acquisition and laser disabling between each trap can be set prior to starting the measurements through a custom developed Graphical User Interface (GUI) as can be seen in Figure 2.7. This interface allows for a user-friendly adjustment of the desired acquisition parameters, enhancing the flexibility of the system for use to analyse a wide variety of particles and experiments. For example, shorter or longer acquisition times may be desired dependent on the intensity of Raman scattering of the components in the particle, or a higher number of acquisitions may be necessary if the variance between particles in the solution is expected to be large. Other options in the GUI include the setting of an email address for automated notification of completion of the measurement (Figure 2.7-V), as well as receiving a warning message upon 20 consecutive failed trapping attempts, indicating a possible need to check the system or solution for errors. Lastly, a desired project name for the measurement run can be set, as well as the file path to save the data in a specific directory (Figure 2.7-VII, VIII respectively).

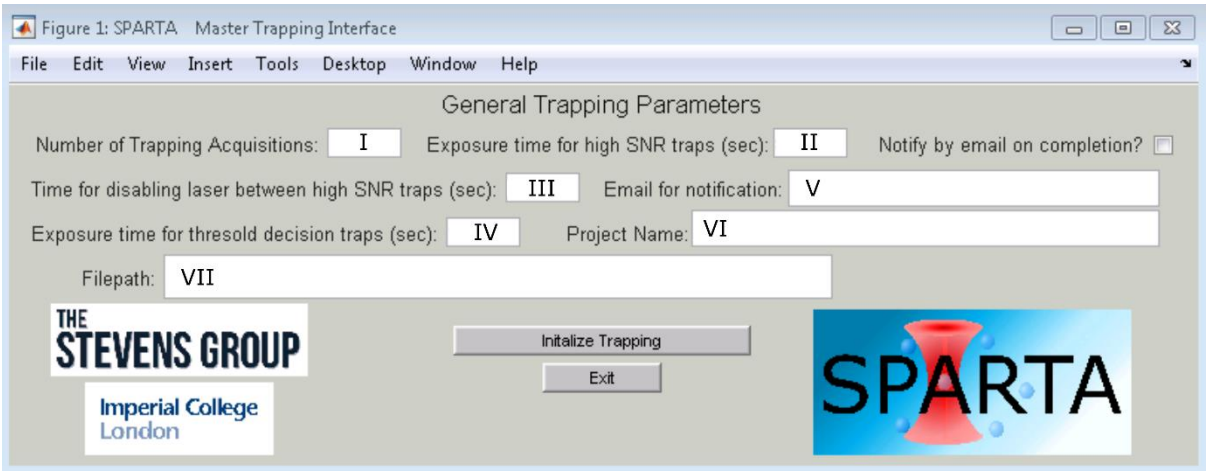

Figure 2.7 | SPARTA trapping interface (GUI). The SPARTA Master Trapping Interface is a menu for setting all the relevant acquisition parameters prior to the SPARTA measurements. The user can set the desired number of trapping acquisitions (I), the times for high SNR acquisition (II), laser disabling (III) and iteration threshold decision traps (IV), enable and set email notification upon completion (V) and set the name (VI) and file path (VII) for saving the data. *This GUI was designed by Dr. Isaac Pence.*

For each successful particle trap, the acquisition parameters, time and iteration number are recorded in a trapping log file alongside the high SNR spectral data, to be used for verification and post processing (Figure 2.6.a-VII). The iteration number is used to verify an adequate laser disabling time in an iteration number check.

The spectra can also be put through post thresholding to pick out any 'false positive' traps if the thresholding intensity was initially set too low. Conventional Raman spectral processing can be performed afterwards, including cosmic spike removal, baseline subtraction and normalisation.

While it has been previously shown that NIR lasers do not induce significant photodamage on trapped particles,[160–162] this was further verified by trapping and holding a 1,2-dipalmitoyl-sn-glycero-3-phosphocholine (DPPC) liposome for 5 minutes in the laser and taking spectra at regular intervals. The standard deviation of the mean spectrum is low and does not show appreciable peak changes indicative of photodamage (Figure 2.8.a), nor does the surface plot indicate spectral changes over time (Figure 2.8.b) apart from small overall intensity changes attributable to the slight fluctuations in laser power.

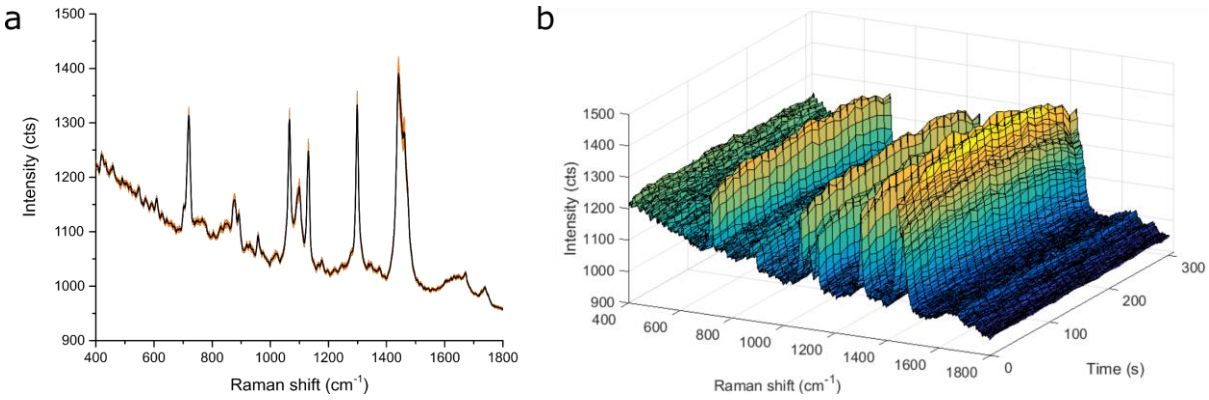

Figure 2.8 | DPPC liposome photostability over time. DPPC liposome held in the optical trap for 5 minutes. (a) Averaged Raman spectra (mean ± s.d., n = 26), (b) surface plot of Raman spectra over time, showing minimal variation over time in the spectrum indicative of photostability. *Figure originally published in* Penders J. *et al*., *Nature Communications,* 9, 4256, 2018[112].

2.3.3 Functionalisation and composition analysis

The primary mode of operation for the SPARTA system is single particle functionalisation and composition analysis. Here, either particles of varying composition, or particles with the same main composition, but varying surface functionalisations are analysed.

This was demonstrated by trapping commonly used model liposomes made of DPPC and d-DPPC liposomes, the latter of which were prepared containing 50% deuterated DPPC (d-DPPC). In the Raman spectra of the two samples (Figure 2.9.a) a clear *C-D* signal can be observed around 2105 cm^{-1} in the spectrum for the d-DPPC liposomes, which is absent for the DPPC liposomes. Due to the high-throughput automated operation, mixtures of particles can be analysed and resolved.

To demonstrate this, a 50-50 v/v % mixture of DPPC liposomes and d-DPPC liposomes was made. With SPARTA, hundreds of particles were trapped, and the spectra were analysed by a Gaussian mixture analysis based on the histogram of the intensity of the *C-D* vibration at 2105 cm^{-1}. This resulted in a clear bimodal distribution of the histogram (Figure 2.9.b) covering 44 and 56% of the traps for DPPC and d-DPPC, respectively, showing that the mixture can be clearly resolved. Alternatively, the mixture can be resolved by cluster analysis, as can be seen in the Ward's dendrogram (Figure 2.9.c), showing two main clusters of spectra relating to the non-deuterated and deuterated populations. A small deuterium signal was observed in the non-deuterated classed spectra, which possibly resulted from lipid exchange between deuterated and non-deuterated liposomes. As deuterium containing molecules are very strong Raman scatterers[163], only a small percentage of deuterated molecules are required to generate a detectable Raman signal. The small discrepancy between the mixing ratio (50-50 v/v%) and the detected ratio (44-56%) may be explained by a slight liposome concentration difference in the stock solutions.

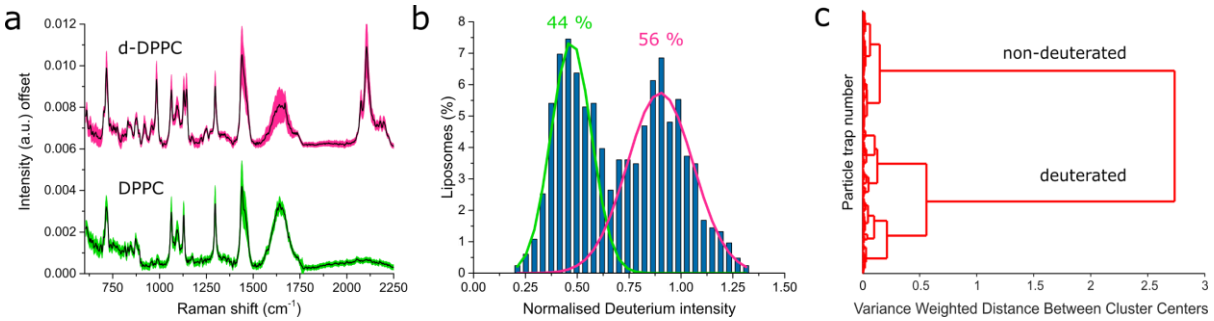

Figure 2.9 | SPARTA composition analysis of liposomes. (a) Offset averaged Raman spectra of DPPC liposomes (green mean ± s.d., n = 649) and 50% d-DPPC liposomes (magenta mean ± s.d., n = 340). (b) Gaussian 2 component mixture analysis based on expectation maximisation; bimodal histogram of the CCD counts at the *C-D* peak position (2105 cm^{-1}) of a 50-50 v/v % mixture of DPPC and d-DPPC liposomes (n = 828) with 44% classed as DPPC and 56% as d-DPPC. (c) Ward's clustering dendogram of a 50-50 v/v % mixture of DPPC and d-DPPC liposomes (n = 828). *The liposomes were prepared with Mr. Conor Horgan. Figure originally published in* Penders J. *et al.*, *Nature Communications,* 9, 4256, 2018[112].

With SPARTA, more subtle differences in composition can also be detected, which is of high relevance in nanoparticle analysis, particularly in the field of nanomedicine, where an exact definition of the composition of nanomaterials is of the utmost importance, yet often elusive. To demonstrate this, two formulations of model polymersomes were made, one from poly(2-methyloxazoline-b-dimethylsiloxane-b-2-methyloxazoline), (PMOXA-b-PDMS-b-PMOXA) denoted further as ABA and the other of ABA supplemented with 25 wt. % PDMS-b-heparin, prepared as described by Najer *et al*.[18], and termed ABA-heparin polymersomes. SPARTA analysis of the particles (Figure 2.10.a) showed characteristic peaks that can be attributed to PDMS (Table 2.1) for both preparations.

Table 2.1 | Raman peak vibration assignment

Figure	Vibration	Raman shift (cm^{-1})	Reference
Figure 2.9.a	*C-D* stretch	2105	[163]
Figure 2.10.a	*Si-O-Si* stretch	490	[164]
Figure 2.10.a	*Si-C* sym. stretch	709	[164]
Figure 2.10.a	*C-C* stretch glucose/saccharide	930	[83]
Figure 2.10.a	Glucose/saccharide	1070	[83]
Figure 2.11.b,c	*S-S* stretch	452, 512	[165,166]
Figure 2.11.b,c	*S-H* bend	936	[166]
Figure 2.11.b,c	*C=C* ring breathing (Tyrosine)	840, 860	[83]
Figure 2.12	*Cl-O* stretch (Perchlorate)	938	[124]
Figure 2.14.b,c,d	*C≡C* stretch (Alkyne)	2129	[163]
Figure 2.14.b,c,d	*N≡N* stretch (Azide)	2116	[163]
Figure 2.14.b,c,d	Triazole ring stretch	1331	[83,165]

In the spectra obtained from the ABA-heparin polymersomes, additional peaks can be seen and assigned to the saccharide units of heparin, as indicated by the arrows in the inset. In addition, the average area under the curve for the normalised spectra of the PDMS peaks at 490 and 709 cm^{-1} (Table 2.1) is lower for the ABA-heparin polymersomes, with a ratio compared to the ABA polymersomes of 1:0.898.

This is in excellent agreement with the theoretical ratio of 1:0.843, corresponding to 83 and 70 wt. % PDMS respectively for the ABA and ABA-heparin polymersomes, as calculated from the molecular weights and quantities added of the PMOXA-b-PDMS-b-PMOXA and PDMS-b-heparin block copolymers.

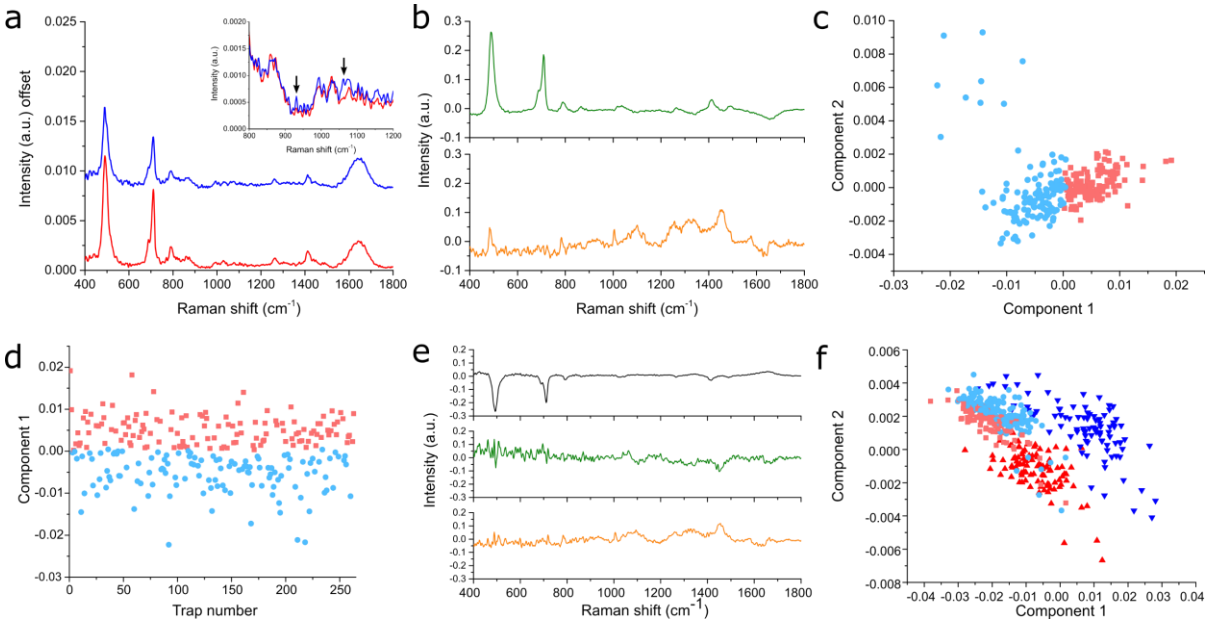

Figure 2.10 | SPARTA composition analysis of polymersomes. (a) Offset averaged Raman spectra of ABA polymersomes (red, n = 99) and ABA-heparin polymersomes (blue, n = 98), inset showing a close-up of the region with arrows denoting heparin signals around 930 and 1070 cm^{-1}. (b) 2 component PCA decomposition analysis of a 50-50 v/v % mixture of ABA and ABA-heparin polymersomes (n = 263), component 1 (top) and component 2 (bottom). (c) PCA scores post Ward's clustering (light red ABA-like, light blue ABA-heparin-like). (d) Classification *versus* trap number. PCA component 1 against the trap number of a 50-50 v/v % mixture of ABA and ABA-heparin polymersomes (n = 263), classified by PCA based Ward's clustering into ABA (red) and ABA-heparin (blue) populations. Plot shows a random distribution of trapping of both particles over time. (e-f) 3 component PLSDA classification analysis of a 50-50 v/v % mixture of ABA and ABA-heparin polymersomes (n = 263). (e) PLSDA components 1, 2 and 3 (top to bottom), (f) PLSDA scores of component 1 and 2 and classification of ABA (light red) and ABA-heparin (light blue) like polymersomes, modelled using pure ABA (red, n = 99) and ABA-heparin (blue, n = 98) trapping runs. *The polymersomes were prepared by Dr. Adrian Najer. Figure originally published in* Penders J. *et al*., *Nature Communications,* 9, 4256, 2018[112].

Next, a 50-50 v/v % mixture of ABA and ABA-heparin polymersomes was made and analysed with SPARTA. These mixtures can be resolved by either an unsupervised classification, such as PCA or a supervised method, PLSDA.

With a PLSDA model the data from the pure populations is used to build a model and subsequently applied to classify the spectra obtained from the particles in the mixture. A 2 component PCA model (Figure 2.10.b) shows clear distinction into two clusters, mainly based on variance in PDMS composition. With PCA based Ward's clustering, 49% of the spectra were classified as ABA-like polymersomes, 47% as ABA-heparin-like polymersomes and 4% were not classified as belonging to either of those clusters (Figure 2.10.c). PLSDA classified 38% of the acquired spectra as ABA polymersomes and 62 % as ABA-heparin polymersomes (Figure 2.10.e-f), based on a model of pure particles that achieved 100% sensitivity and 97.9% specificity for ABA polymersomes by venetian blinds cross validation (10 splits). To verify that either type of polymersome was trapped in a random manner, without time dependence, the scores for PCA component 1 were plotted against the trap number, resulting in a random distribution of polymersome classes over time, proving no bias over time for either composition (Figure 2.10.d).

In addition to vesicular systems, the composition and sizing of a wide variety of solid nanoparticles is critically important in a range of applications from drug delivery to catalysis[167,168]. To validate the use of the SPARTA platform for analysis and verification of successful nanoparticle functionalisation, a model system was devised based on the sequential functionalisation of polystyrene (PS) nanoparticles via disulphide exchange (Figure 2.11.a). At each step the size distribution of the particles was measured by DLS. While the intrinsic size variation of the commercially obtained particles obscured the slight size differences occurring during functionalisation, it was used in verifying particle stability during the sequential functionalisation and purification (Figure 2.11.b). Amine functionalised PS particles with an average size of 200 nm were sulfhydryl functionalised by addition of 2-iminothiolane. After purification by centrifugation and resuspension, the particles were analysed with the SPARTA platform which verified the presence of sulfhydryl, as seen from the signals in the spectra arising from the *S-H* bend vibration around 936 cm^{-1} (Table 2.1) (black, Figure 2.11.c). Next, an excess of 5,5'-dithio-bis-(2-nitrobenzoic acid) (DTNB) was added, which reacted with the sulfhydryl functionalised particles to form disulphide bonds. After further purification, the Raman spectra (magenta, Figure 2.11.c) showed the clear presence of disulphide bonds. These bonds are dynamic covalent bonds and can thus be exchanged upon addition of another moiety containing a sulfhydryl functionality. This was demonstrated by addition of a tripeptide, consisting of cysteine and two tyrosines (CYY), with the cysteine affording the sulfhydryl functionality and the tyrosines an enhanced Raman signature, due to their aromatic rings. In addition a peptide functionalisation of nanoparticles is a desirable and widely used strategy, especially in the field of drug delivery[169,170].

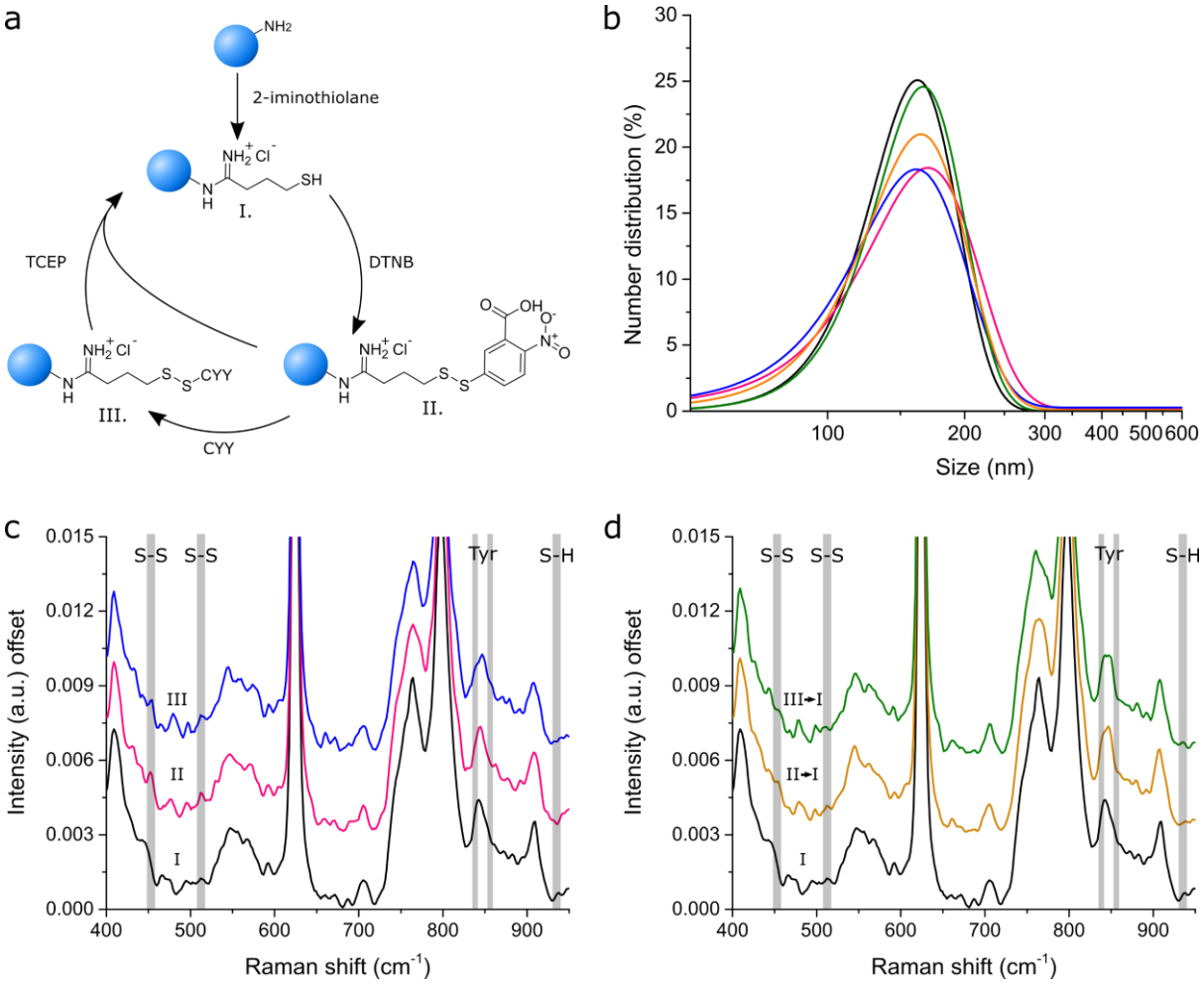

Figure 2.11 | SPARTA functionalisation analysis of PS nanoparticles. (a) Schematic overview of the PS nanoparticle (blue sphere) functionalisation path. Amine functionalised particles are treated with 2-iminothiolane (Traut's reagent) leading to sulfhydryl functionalised particles (I). Addition of 5,5'-dithio-bis-(2-nitrobenzoic acid) (DTNB) leads to disulphide bond formation (II), which can be exchanged by the tripeptide consisting of cysteine-tyrosine-tyrosine (CYY) (III). Addition of Tris(2-carboxyethyl) phosphine (TCEP) to a disulphide containing particle returns the sulfhydryl functionalisation. (b) DLS number distributions of polystyrene particles during serial functionalisation. Gaussian fits of DLS number distributions for PS particles with sulfhydryl functionalisation (mean ± s.d.) (black, 157.5 ± 34.9 nm), disulphide and nitrobenzoic acid (red, 166.1 ± 46.6 nm) and disulphide and CYY functionalised particles (blue, 156.6 ± 43.5 nm), recovery of sulfhydryl after addition of TCEP to disulphide and nitrobenzoic acid functionalisation (orange, 162.1 ± 36.6 nm), and to CYY functionalisation (green, 160.3 ± 40.9 nm). (c) Averaged offset Raman spectra of trapped PS particles with sulfhydryl functionalisation (black, n = 201), disulphide and nitrobenzoic acid (magenta, n = 119) and disulphide and CYY functionalised particles (blue, n = 122). Bands indicating the characteristic *S-S* stretch (452, 512 cm^{-1}), tyrosine ring breathing (*C=C* 840, 860 cm^{-1}) and *S-H* bend (936 cm^{-1}) vibrations. (d) Averaged offset Raman spectra of trapped PS particles with sulfhydryl functionalisation (black, n = 201) recovery of sulfhydryl after addition of TCEP to disulphide and nitrobenzoic acid functionalisation (orange, n = 119), and to CYY functionalisation (green, n = 115). *The CYY peptide was prepared by Dr. Christopher Wood. Figure originally published in* Penders J. *et al*., *Nature Communications,* 9, 4256, 2018[112].

The cysteine residue provides a sulfhydryl functionality and the tyrosines exhibit a characteristic Raman peak, due to the aromatic *C=C* bonds. Upon addition of the peptide to the purified particles, the solution turned characteristically yellow, demonstrating that the 2-nitro-5-thiobenzoate dianion ($TNB2^-$) was formed.

This indicated that disulphide exchange had occurred and confirmed the specific conjugation of the tripeptide to the particle. After purification, Raman spectra were acquired of the particles, showing the presence of characteristic tyrosine peaks (blue, Figure 2.11.c). To complete the cycle, Tris(2-carboxyethyl) phosphine (TCEP) can be added to either disulphide-containing particle solution to recover the sulfhydryl functionalisation (Figure 2.11.d).

2.3.4 Solution marker mediated sizing analysis

The second mode of the SPARTA system allows for simultaneous estimation of the particle size inside the trap, alongside the acquisition of a high SNR compositional spectrum. As illustrated (Figure 2.5.b), a particle entering the trap displaces the same volume as itself out of the surrounding solution from the confocal volume, leading to a decrease in the perchlorate signal in the measured spectrum. Perchlorate is particularly suitable for this application as it has a single sharp Raman peak around 938 cm^{-1} (Figure 2.12).

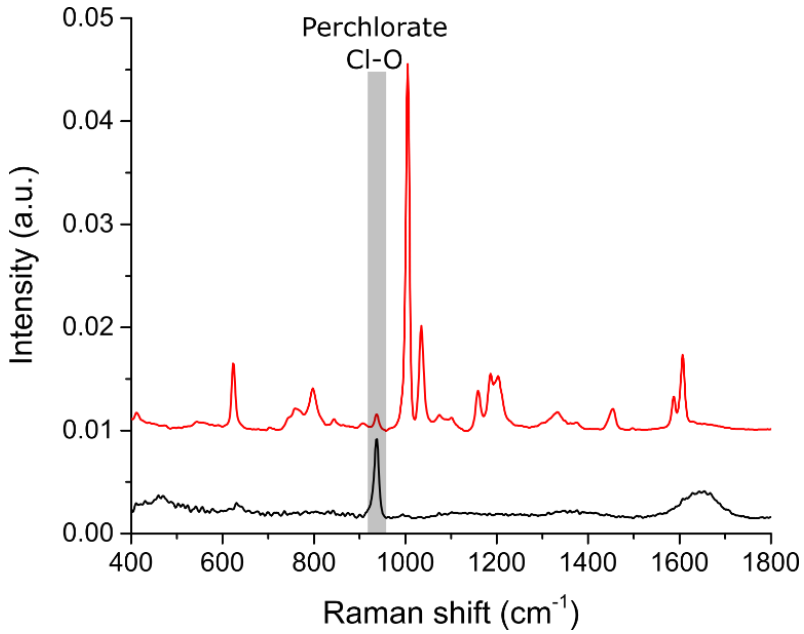

Figure 2.12 | Perchlorate Raman spectra. Averaged Raman spectra of PBS (black, n = 234) and 200 nm polystyrene beads (red, n = 300), each supplemented with 50 mM sodium perchlorate. The perchlorate gives a single, clear solution marker peak at 938 cm^{-1}. *Figure originally published in* Penders J. *et al*., *Nature Communications,* 9, 4256, 2018[112].

As the polystyrene signal also increases upon increasing particle size inside the confocal volume, the perchlorate signal is best quantified by a ratio contribution to the spectrum according to (eq. 1):

$$\text{Perchlorate ratio} = \frac{A_t - A_p}{A_p} \qquad \text{(eq. 1)}$$

where, A_t is the total area under the curve of the spectrum and A_p the area for the perchlorate peak. The ratio will increase when A_p approaches zero (particle completely fills the trap) and go to zero (no particle) once A_p approaches A_t. As a model system, polystyrene particles were analysed of 200, 100 and 50 nm (mean size as commercially obtained) with the SPARTA platform upon addition of 50 mM of sodium perchlorate to the solution. It was found that the perchlorate ratio was distinct between the various sizes and are within bandwidths with minimal overlap (Figure 2.13.a). The average ratios can be plotted against the log particle volume (calculated from the size provided by the manufacturer) resulting in an excellent linear correlation (R^2 = 0.99) (Figure 2.13.b).

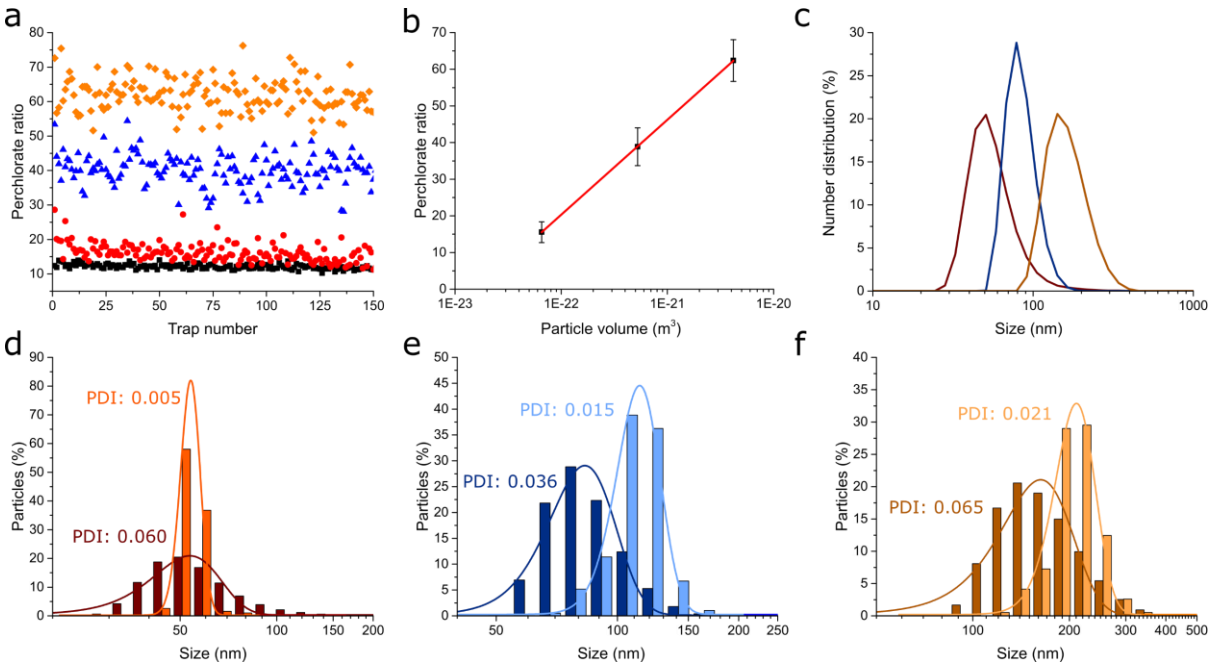

Figure 2.13 | SPARTA solution marker mediated sizing analysis. (a) Scatterplot of the perchlorate ratio for 150 traps of 50 nm (red circles), 100 nm (blue triangles) and 200 nm (orange diamonds) polystyrene particles and PBS background (black squares) containing 50 mM of sodium perchlorate in the solution. (b) Average perchlorate ratio (mean ± s.d.) *versus* the log particle volume, a linear fit (R^2 = 0.99) is shown in red. (c) DLS number distributions of polystyrene particles (mean ± s.d.) , 50 nm (red, 53.6 ± 13.1 nm), 100 nm (blue, 83.0 ± 15.7 nm) and 200 nm (orange, 162.8 ± 41.5 nm). (d-f) Histogram of particle sizes measured by DLS (dark) and calculated from the calibration curve from the Raman spectra (light), including respective Gaussian fits of (d) 50 nm, (e) 100 nm and (f) 200 nm polystyrene particles. *Figure originally published in* Penders J. *et al.*, *Nature Communications,* 9, 4256, 2018[112].

The linear fit of the calibration curve can be used to estimate the particle size of the individual particles trapped with the SPARTA system. These sizes were binned identically to the corresponding DLS number distributions of the particles (Figure 2.13.c) to yield a histogram of the size distribution (Figure 2.13.d-f). The main means of comparison between the DLS and SPARTA size measurements is the distribution broadness. This can be characterised by the polydispersity index (PDI), which is the square of the quotient of the standard deviation (σ) and the mean (μ). For each particle size, the PDI obtained by the SPARTA solution marker-mediated sizing analysis was significantly lower than measured by DLS, demonstrating the ability of SPARTA for accurate single particle sizing analysis.

2.3.5 On-line dynamic reaction monitoring

The third application of the SPARTA platform is the capability for on-line dynamic reaction monitoring, either on a single particle during the timescale of the reaction, or via continuous sampling of different single particles from the population. This allows the distinction between two different reaction scenarios, where the reaction proceeds uniformly throughout the whole population simultaneously, or where the reaction is initiated on different particles sequentially.

A model system was used to investigate the dynamics of the copper catalysed azide-alkyne cycloaddition (CuAAC) reaction, a type of click reaction which is frequently employed for nanoparticle functionalisations[171,172]. Polystyrene particles with an alkyne functionality were obtained via the EDC-NHS mediated coupling of propargyl amine to carboxylated PS particles with an average size of 200 nm. This alkyne was subsequently reacted, in the presence of a copper catalyst, with an azide-containing moiety resulting in the formation of a triazole ring (Figure 2.14.a). Verification of the successful alkyne functionalisation of the polystyrene particles was achieved by SPARTA (Figure 2.14.b), showing a characteristic Raman peak at 2129 cm^{-1}.

The CuAAC reaction was subsequently conducted while trapping single particles sequentially or holding a single particle continuously in the trap. Both the alkyne and azide signals of the reactants show a clear decrease over time, with the peak intensity of the triazole product increasing in an inverse trend (Figure 2.14.c). Reaction completion was observed after approximately 8 minutes. Adapting the system to instead hold a single particle in the trap and monitor the spectral changes continuously for the duration of the reaction resulted in a similar trend of reaction (Figure 2.14.d), albeit showing reaction completion within 2 minutes, taking into account an additional lead time between activation of the catalyst and acquisition of the first spectrum of approximately 30 – 60 seconds.

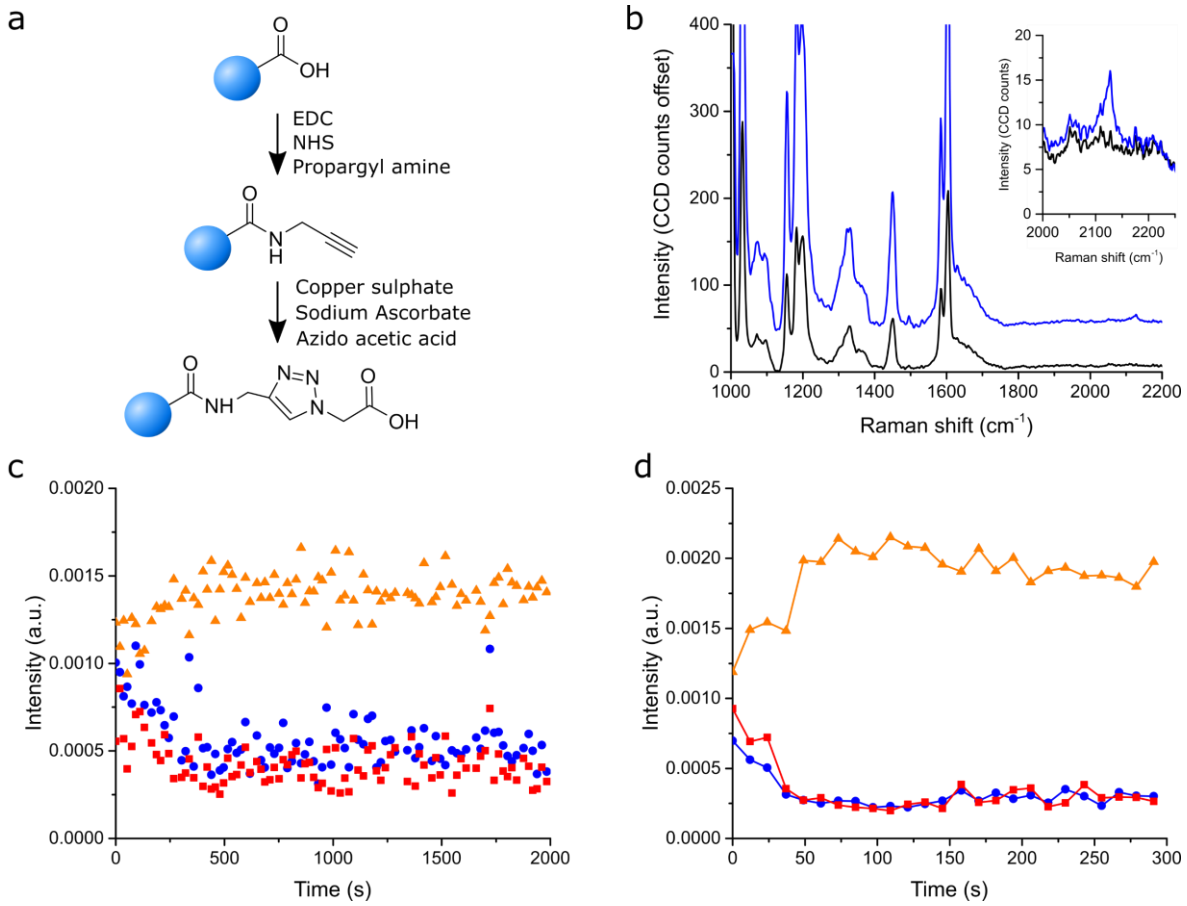

Figure 2.14 | SPARTA on-line dynamic reaction monitoring. (a) Schematic overview of the functionalisation of PS nanoparticles with an alkyne moiety via EDC-NHS coupling with propargyl amine and subsequent CuAAC reaction with azido acetic acid to form the triazole product. (b) Offset averaged Raman spectra of trapped PS particles with carboxylic acid functionalisation (black, n = 100) and after alkyne functionalisation (blue, n = 100). Inset showing a close-up of the alkyne peak region, with a clear alkyne peak visible after functionalisation with a maximum at 2129 cm^{-1}. (c) Dynamic trace over time of the alkyne peak intensity (blue spheres, 2129 cm^{-1}), azide peak intensity (red squares, 2116 cm^{-1}) and triazole product (yellow triangles, 1331 cm^{-1}) for single particle trapped population dynamics and (d) single particle dynamics. *Figure originally published in* Penders J. *et al.*, *Nature Communications,* 9, 4256, 2018[112].

In addition, to verify the successful reaction on the alkyne functionalised particles, the reaction of 3-Azido-7-hydroxycoumarin with the particles was monitored by UV-Vis fluorescence, as the triazole product of 3-Azido-7-hydroxycoumarin results in a characteristic fluorescent emission (Absorption/Emission = 404/477 nm). In the presence of the dye and reaction conditions, the fluorescence increased gradually and starts to level off within 30 minutes (Figure 2.15).

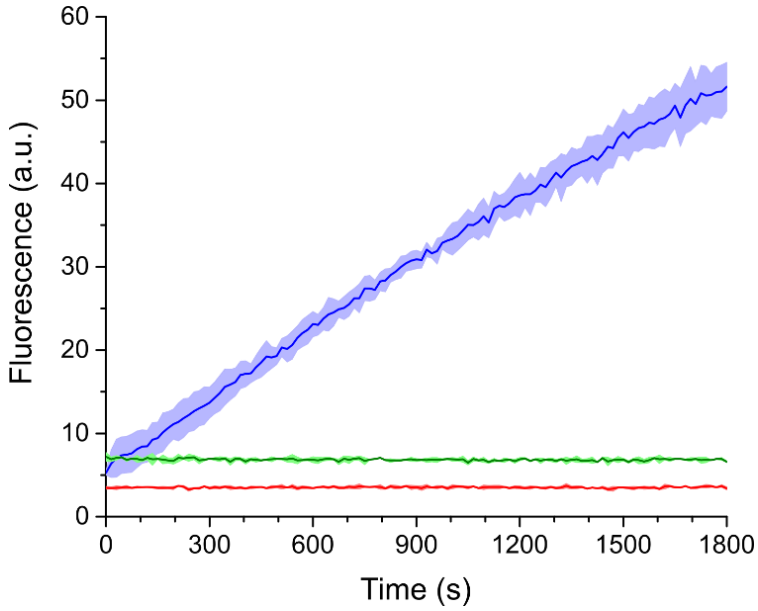

Figure 2.15 | Fluorescence analysis of coumarin dye clicking. Copper catalysed click reaction of 3-azido-7-hydroxycoumarin (Excitation/Emission = 404/477 nm) to 200 nm polystyrene particles functionalised with propargyl amine resulting in fluorescence when forming the triazole product, (n = 3, mean ± s.d.) clicking conditions (blue), no change in fluorescence in absence of dye (red) or absence of copper sulphate (green). *Figure originally published in* Penders J. *et al.*, *Nature Communications,* 9, 4256, 2018[112].

2.3.6 Intellectual Property

The SPARTA platform as presented shows significant advances in the field of single nanoparticle characterisation and its main innovation lies in the automation of the analysis due to implementation of the developed trapping algorithms. Hereto, applications were filed in cooperation with Imperial Innovations, the valorisation platform of Imperial College London, to trademark the name 'SPARTA' (application number UK00003308379), as well as for a patent: *Single Particle Automated Raman Trapping Analysis*, J. Penders, I.J. Pence and M.M. Stevens (application number 1810010.7). The patent application has progressed to the European Patent Cooperation Treaty (PCT) filing stage as of 18th of June 2019.

2.3.7 Conclusions

The SPARTA platform enables concurrent label-free multi-parameter, non-destructive characterisation of particles smaller than the diffraction limit. It combines the efficiency of optical trapping with the established sensitivity of Raman spectroscopy for measuring composition and functionalisation at high-throughput via automation.

Demonstrating efficient trapping and spectral analysis for multiple nanoparticle formulations, including different liposome and polymersome compositions, and serial chemical functionalisation of polystyrene particles.

Simultaneously, for the first time the particle size and distribution were evaluated based solely on Raman scattering of single particles, through addition of perchlorate as an example solution marker. Furthermore, the temporal analysis capabilities of this platform were demonstrated by monitoring a copper catalysed click reaction as it occurs on the surface of either a population sample or an individual nanoparticle. The automated evaluation of large samples of these particles can provide new insights into the heterogeneity of nanoparticle systems, investigate subpopulations, and monitor dynamic composition changes for myriad sample designs.

The SPARTA platform represents the first automated system to study chemical composition, functionalisation, and size for nanoparticles within a single modality with the label-free chemical and temporal resolution to track on-particle dynamic processes. The SPARTA platform is ideally suited to polymer and lipid systems, but can be extended to a wide range of particle formulations with unique vibrational spectra. The technology described here is limited by fundamental properties; it is particularly well suited to samples with low turbidity to generate the particle trapping force gradient, compositions with non-overlapping spectral features, dynamic processes that occur over the course of minutes up to a few hours, and sample concentrations low enough such that no low-level background is contributed to the trapped particle measurement. Furthermore, each target particle system will have unique optical properties that must be further assessed for potential photothermal or other photo-induced processes that can occur during trapping. Each of these considerations can be mitigated by careful selection and preparation of nanoparticle systems for evaluation.

The deployment of the SPARTA platform for complex nanoparticles provides multiplexed information regarding the intricate composition, size, and dynamic processes of these systems and to improve fundamental understanding. Indeed, the SPARTA platform provides, in an automated fashion, feature rich Raman spectra from hundreds of individually trapped particles in a single experiment. In summary, the complimentary information obtained from the multifaceted SPARTA platform, regarding particle composition, functionalisation, size and dynamics, has enormous potential to critically impact fields including drug development and delivery, materials science, and cellular biology.

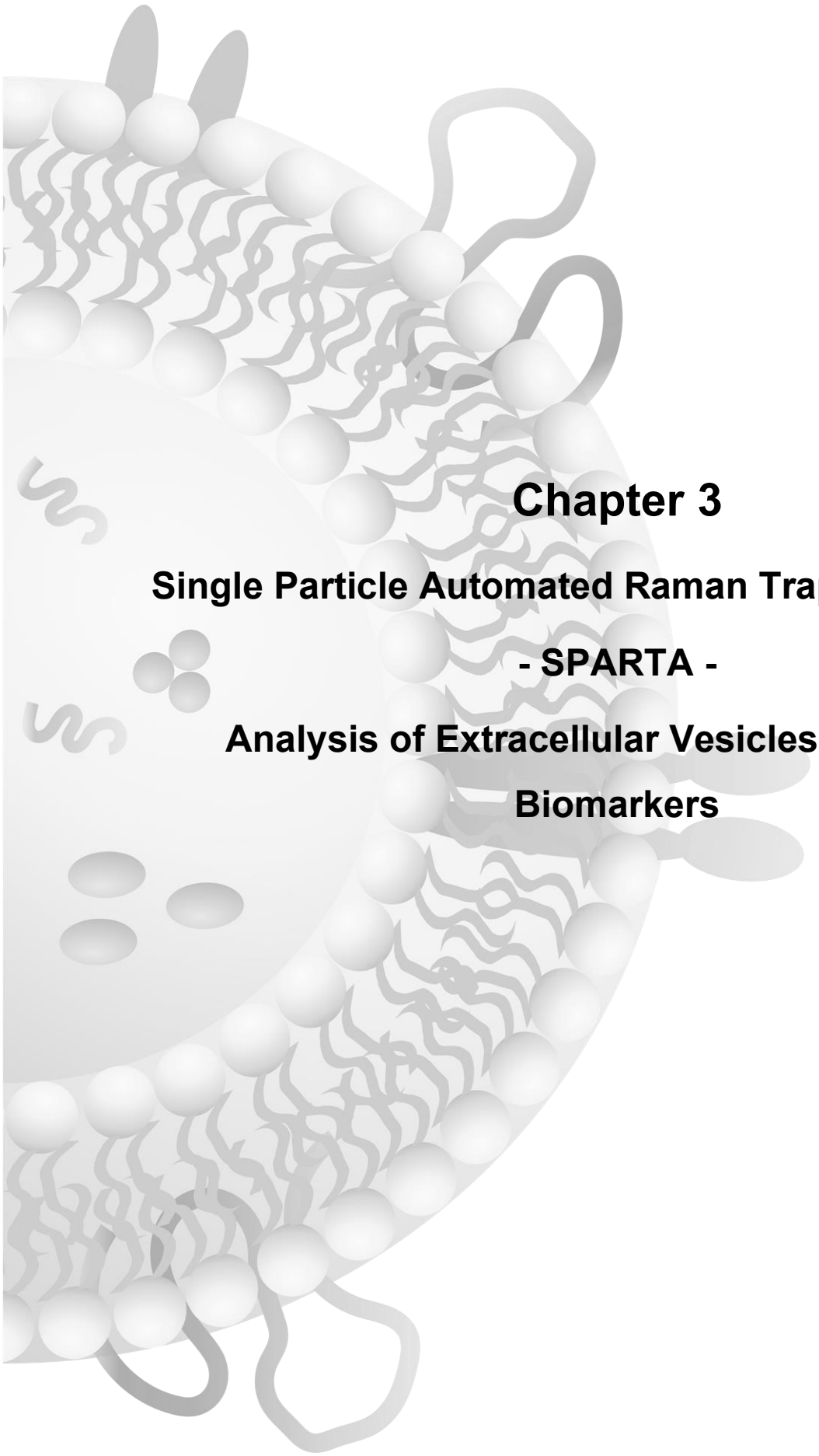

Chapter 3

Single Particle Automated Raman Trapping Analysis

- SPARTA -

Analysis of Extracellular Vesicles as Cancer Biomarkers

‘*It lives desperately, inventively, fiercely, territorially,*

cannily, and defensively - at times, as if teaching us how to survive.

To confront cancer is to encounter a parallel species,

one perhaps more adapted to survival than even we are.’

Siddhartha Mukherjee

The Emperor of All Maladies, a Biography of Cancer

Scribner, 2010.

3 Single Particle Automated Raman Trapping Analysis – SPARTA – Analysis of Extracellular Vesicles as Cancer Biomarkers

Parts of this chapter are being prepared for a publication to be submitted by J. Penders, A. Nagelkerke, I. Pence *et al*. with as preliminary title: Single Particle Automated Raman Trapping Analysis of Breast Cancer Cell Derived Extracellular Vesicles.

Part of the data on Raman spectroscopic cell-EV comparison was collected within the MSc. Thesis project of Ms. Julia So, co-supervised by J. Penders and A. Nagelkerke.

3.1 Introduction

3.1.1 Aims

Extracellular vesicles (EVs), secreted by virtually all cell types, are increasingly recognised for their strong potential as biomarkers in a variety of diseases, chief among which is cancer[173–175]. Secreted EVs are thought to reflect the composition of their parent cells and it is therefore posed that they could be used as a proxy to discover and elucidate a disease state. Raman spectroscopy has an impressive track record for the analysis of cancerous cells and tissues and has been used successfully for clinical disease detection[176,177]. While it is currently mostly used for accessible tumours, such as skin cancer[178,179], it shows a strong potential for the analysis of liquid biopsies, such as to detect cancer cell derived EVs[175].

In this chapter, the potential of EVs as biomarkers in breast cancer is investigated, taking advantage of the previously developed high throughput Single Particle Automated Raman Trapping Analysis (SPARTA) platform. The primary aim was the continued development of SPARTA into a platform for compositional analysis of single EVs, towards comprehensive characterisation of EVs as cancer biomarkers. Several improvements to the SPARTA system were realised, resulting in increased accuracy, stability and flexibility of the system. These improvements optimised the system for EV analysis, resulting in a dedicated setup, SPARTA 2.0. Efficient trapping of EVs derived from healthy cell lines and breast cancer cell lines was demonstrated, resulting in the acquisition of comprehensive compositional information. EV spectra obtained by SPARTA were compared to spectra obtained through Raman imaging of the parental cell lines, demonstrating a close agreement.

A full panel of EVs derived from 11 cell lines was constructed, reflecting a variety of origins (healthy / ductal carcinoma / adenocarcinoma) and receptor status (Human epidermal growth factor receptor 2 (HER2+) / oestrogen receptor (ER+) / triple negative).

Multivariate statistical analysis was applied to identify compositional differences based on single EV spectra and cancerous/non-cancerous classification was achieved with high specificity and sensitivity. A novel Raman spectral visualisation approach, dubbed a Dimensional Reduction Array was utilised to aid the presentation and interpretation of complex Raman data sets. SPARTA 2.0 represents a powerful and versatile approach to the investigation and realisation of EVs as biomarkers in cancer.

3.1.2 Breast cancer

3.1.2.1 Classification

Breast cancer is one of the most commonly diagnosed types of cancer, and the most common type of cancer in women. Over 2 million new cases were identified worldwide in 2018 by the Global Cancer Observatory, part of the WHO[180]. Breast cancer is characterised by a strong degree of heterogeneity, which critically impacts both treatment options and survival[181]. Primary classification of breast cancer is based on the site and tissue of origin of the primary tumour. The major classes of breast cancer include ductal carcinoma, originating in the epithelial tissue of the ducts of the mammary gland, and adenocarcinoma, a carcinoma directly originating in the gland[181].

In addition to the site of origin, breast cancer cells and tumours are often classified according to their receptor status. These receptors used for classification are the oestrogen (ER) and progesterone (PR) hormonal receptors, and human epidermal growth factor receptor 2 (HER2)[181]. A cell line or tumour that expresses none of these receptors is termed a ‘triple negative’ breast cancer. The receptor status is of major importance for prognosis and in determining an effective treatment strategy. Cells that express the hormonal ER and PR receptors are particularly susceptible to hormonal treatment strategies, where starvation from these hormones may lead to significant tumour growth suppression. Conversely, hormonal treatment strategies are not effective when administrated to patients with tumours of cells not expressing these receptors. Similarly, the HER2 receptor, when overexpressed, provides another handle for treatments based on blocking this receptor with an antibody-based drug called trastuzumab or by its brand name Herceptin®[182]. Conversely, in the case of triple negative breast cancers, hormonal or Herceptin treatment strategies are not effective, due to the absence of the expression of ER or HER2 receptors.

The treatment of triple negative breast cancers is therefore more complicated and these often aggressive cancers have a poorer prognosis for survival[181].

3.1.2.2 Diagnosis – state of the art

The current, most prevalent mode of breast cancer diagnosis is based on a combination of three techniques: physical examination, imaging and, in the case of suspected malignancy, a biopsy followed by histopathological screening. Physical examination, as well as X-ray mammography are routinely incorporated in preventative screening programs prevalent across the (Western) world since the 1980s[183]. Preventative screening is usually performed only on women over 50, as numerous clinical trials have shown minimal benefits for younger age groups[183]. An exception to this is women in high risk categories, such as those having mutations in the BRCA 1 and 2 genes[184], implicating a strong genetic predisposition for the development of breast cancer. X-ray mammography may reveal a suspected tumour, based on image analysis of local contrast differences. In this case, further diagnosis may be performed by analysing a tissue sample, obtained via excisional biopsy or fine needle aspirates. The tissue sample is then screened using histopathological techniques, to indicate the presence of a tumour, as well as being used to type and stage the cancer if present. Immunohistological assays have been developed to determine the presence of abnormal receptor statuses of the tumour, such as ER+, HER2+ and triple negative, and are integral to determining treatment options and strategies[181].

While considerable success has been achieved using this combination of diagnostic techniques, several drawbacks and limitations exist. A primary concern is the invasiveness of the current methods, in particular the biopsy. In addition to the invasive nature of the procedure, biopsies may be prone to sampling error, both in accuracy of the sampling position as the amount of tissue extracted. Thirdly, both X-ray screening and histopathological assessment depend strongly on the individual judgement of trained specialists, with variations between individuals and laboratories being recognised as a drawback of this approach[185]. These limitations stress the need for the development of novel approaches, focusing on non- and minimal invasiveness, as well as the reduction of interpretation variability and bias.

3.1.2.3 Raman spectroscopy in (breast) cancer

Raman spectroscopy has been demonstrated, over the last several years, of having high potential clinical value as a diagnostic tool for aiding in the diagnosis of different types of cancer[186]. Raman spectroscopy has several key advantages which would allow its transition into clinical practice.

Intrinsically, being a light-based technique, Raman spectroscopy is non-invasive and non-destructive, making it possible to directly measure samples *ex* or *in vivo.* In addition, it provides compositional spectral information in a label-free manner, which has been applied to directly distinguish between benign and cancerous lesions[187]. This is in contrast to existing diagnostic techniques for breast cancer, which are invasive and rely on a combination of multiple techniques to reach a diagnostic decision. Moreover, Raman spectroscopy has a high potential for automation, both in terms of data acquisition and analysis, with the capability to largely eliminate user bias and involvement.

Numerous Raman spectroscopy studies have been conducted on cell lines, primary cells and tissue originating from various types of breast cancer[176,186]. Healthy tissues undergo significant biochemical changes during tumoral transition, which can be attributed to the uncontrolled, rapid growth of the cells. Raman spectroscopy studies have demonstrated a disruption of the healthy ('normal') lipid and protein distributions, with cancerous tissue generally showing lipid depletion and protein enrichment[176,188]. Interestingly, when individual cells are analysed, such as from several established breast cancer cell lines, an overall increase of the lipid content is found in abnormal cells[189,190]. This, it has been suggested, is a hallmark of the tendency for cell migration and invasiveness. The distinction between healthy and cancerous tissues and cells, through analysis of the obtained Raman spectra, has generally been conducted by chemometric analysis. This involves the construction of mathematical models, based on multivariate statistical analysis techniques such as PCA and PLSDA. The resulting models have been able to attain a high level of sensitivity and specificity, depending on the exact type of tissue, cell line or level of intrinsic biological difference[186].

3.1.3 Extracellular vesicles in cancer

3.1.3.1 Metastasis and EVs

Ever since the late 1800s cancer researchers have been trying to identify the mechanisms and patterns governing cancer metastasis, as it is the leading cause of cancer morbidity and mortality. Paget observed in 1889, by comparing numerous necropsies of fatal cases of breast cancer, that secondary growths had a significant predisposition towards the liver over for example the spleen, kidneys and lungs[191]. In addition, it was noted that metastasis towards the bones showed a predisposition to establish in the femur, humerus and cranium, while the tibia and hands and feet, for example, were mostly unaffected.

This led to the so called 'seed-and-soil' hypothesis, stating that in metastasis the cancerous 'seeds' will have a predisposition towards specific organs and places in the body as their environment ('soil') is most suitable for further growth. This predisposition of metastasis towards certain organs is called 'metastatic organotropism', with the formation of a receptive environment termed the pre-metastatic niche[192,193].

In recent years a novel potential key player of metastatic organotropism and pre-metastatic niche formation has been identified, namely tumour derived EVs, and in particular exosomes[194,195]. EVs can be considered one of the tumour secreted factors inducing inflammation, vascular leakiness and recruitment of bone marrow progenitor cells, aiding in forming the pre-metastatic niche.

EVs have been shown to contain various types of DNA and RNA[32], which can be actively translated into recipient cells after EV uptake. Together with their stability in circulation, EVs show the innate ability to effect changes in remote microenvironments leading to pre-metastatic niche formation. In particular, the Lyden group has performed several studies, indicating a strong involvement of EVs in pre-metastatic niche formation and directing metastatic organotropism[192,194,195].

This potential key role of EVs in cancer metastasis is an example of why, while a major challenge, the thorough study and analysis of EVs is recognised as being of increasing importance. This could have major implications both for the study of cancer biology and disease progression, as in novel approaches for disease detection and monitoring.

3.1.3.2 Raman analysis of extracellular vesicles – state of the art

Several initial studies have been performed to apply Raman spectroscopy for the analysis of EVs, with a strong focus on EVs from cancerous origin. The concepts of laser tweezers and optical trapping in combination with Raman spectroscopy, have been recognised as a potential powerful tool for the biochemical study of the composition of EVs.

The first study using optical trapping in combination with Raman spectroscopy for the analysis of EVs was conducted by Tatischeff *et al.*[62]. EVs from *D. discoideum* (amoebae) and exosomes isolated from urine were analysed. Their study shows the feasibility of trapping EVs and the acquisition of a fingerprint spectrum showing peaks pertaining to nucleic acids, lipids and proteins. A study by Smith *et al.*[156] showed very promising results on the analysis of EVs from various cancerous and non-cancerous cell lines using Raman trapping. This work indicated that the spectra from EVs from various cell lines are markedly different and that subpopulations of EVs within the total EV population from a cell line could be distinguished. However, there are several significant limitations to the above studies.

Firstly, the EV sample purity in each of these studies cannot be guaranteed due to their reliance on ultracentrifugation-based techniques for EV isolation. As has more recently been shown, this is inadequate for the isolation of EVs from cellular proteins and debris[54]. Indeed, as mentioned by Smith *et al.*, the presence of protein or other aggregates contaminating the measurements cannot be excluded. Notably, in both cases a non-confocal Raman spectroscopy system was employed for the EV measurements. As such acquired spectral information was not limited to a confocal volume, increasing the potential for contaminants to influence the resultant spectra.

Most recently, three further studies were published on the use of Raman tweezers for EV analysis, stressing the potential for Raman-based EV characterisation[175,196,197]. However, all studies exhibit severe limitations in terms of the ability to capture and analyse single EVs in a high throughput manner. Lee *et al.*[175] analysed EVs derived from prostate cancer cell lines, and from red blood cell and platelets as a healthy cell control. Their approach resulted in high classification between these EVs with accuracies up to 98%, however the spectral classification was not based on single-EV spectra and the comparison to normal prostate cell EVs was omitted. The study by Carney *et al.*[196] investigated the presence of a subpopulation of EVs from mesenchymal stromal cells containing a specific protein surface marker (CD9). While demonstrating the interesting combination of fluorescent antibodies to reveal this CD9+ subpopulation, only very few vesicles (‘at least 10 vesicles’) were analysed and had to be manually trapped. This low amount of EVs analysed makes any claims regarding population characteristics tenuous. Kruglik *et al.*[197] investigated EVs from human urine and rat hepatocytes, using a Raman tweezers microspectroscopy (RTM) approach. Due to limitations in their setup and sensitivity, mostly small groups of EVs were analysed with spectral acquisition necessary in the order of minutes. In addition, a semi-confocal system was used resulting in non-single particle spectral acquisition and probably contribution to the Raman spectra by surrounding constituents, possibly present due to use of an ultra-centrifugation-based isolation approach.

A moderately different approach to Raman-based EV analysis was shown recently by Stremersch *et al.*[155], in which surface enhanced Raman spectroscopy (SERS) was employed in an effort to decrease the measurement time needed thus increase the population sampling. With SERS, the Raman signal can be enhanced up to 10^{15} times by plasmon excitation of typically gold or silver nanostructures, which enhances the incident and scattered electromagnetic field. This results in a strong enhancement of the biological signatures from the components in direct contact with these particles. To this end EVs were coated with 10 nm gold nanoparticles, resulting in a reduction in measurement time to around 0.5 seconds per EV.

However using SERS also has numerous disadvantages. Most significantly, the need to coat the EVs fully in gold nanoparticles removes one of the key advantages of using Raman, namely label-free characterisation. Since the core EV fraction is on the order of 50-200 nm, the coating with hundreds of 10 nm particles will have a significant impact on their behaviour in solution or interaction. In addition, the SERS signal is strongly enhanced close to the gold nanoparticles, while the signal from moieties not in direct contact with these particles may be obscured and relative quantification of the components within the EV is not feasible.

In addition to the direct incorporation or interaction with SERS enhancing nanoparticles, several recent studies have focused on developing SERS active substrates aim at EV analysis[198]. An noteworthy example is the recent study by Yan *et al.*[199], where smart pattern design of the SERS substrate allowed analysis of single EVs. However, the EVs in this study were dried on top the substrate, which hinders the analysis of EVs in a high-throughput fashion in their native state. While SERS may strongly reduce the required measurement times, the complications introduced may also hamper truthful characterisation of single EVs.

The concept of being able to trap and analyse single EVs without the need for labelling is highly interesting for further development into a robust high-throughput analysis method. This is aimed to be achieved by use of careful purification methods, a confocal Raman system for high data specificity and automation of laser exposure and data acquisition, overcoming key limitations of the above-mentioned studies. The accurate distinction between EVs derived from cancerous and non-cancerous origin is a key step in the design of a minimal invasive cancer diagnosis approach, based on EVs as cancer biomarkers.

3.2 Materials and Methods

3.2.1 SPARTA 2.0 system

A custom Raman microspectroscopic system was built, dubbed SPARTA 2.0. The basic microscope setup was built with the Cerna® platform (Throlabs, UK). A spectrograph (HoloSpec-F/1.8-NIR, Andor, UK) was coupled with an iDus 416A-LDC-DD (Andor, UK) thermoelectrically cooled (-60 °C) back-illuminated CCD camera. For optical trapping and simultaneous Raman excitation, a 200 mW 785 nm laser (Cheetah, Sacher Laser Technik, Germany) was used, temperature controlled through a laser diode control box (PilotPZ 0500, Sacher Laser Technik, Germany). A 50 µm optical fibre was used as confocal pinhole and to collect the scattered light. Measurements were conducted at 375 mA laser diode current resulting in 135 mW before the objective and 100 mW post objective output power. An in-line shutter (SHB05T, Thorlabs, UK) and controller were used to enable and disable the optical trap when required. The samples were interfaced with a 63× 1.0 NA water immersion objective (W Plan Apochromat, Zeiss, Germany). The sample slide was supported by a Zaber automated lift-stage (X-VSR40A, Zaber Technologies Inc. Canada) controlled through a custom joystick button controller (Laser 2000, UK). The spectrograph, camera, shutter and stage were controlled through custom MATLAB 2016b scripts (MathWorks). The SPARTA 2.0 system was designed and built together with Dr. Isaac Pence.

3.2.2 Signal intensity comparison

For signal intensity comparison between the SPARTA 1.0 system and SPARTA 2.0 system a sample of MDA-MB-231 EVs was taken and analysed with both systems, using an acquisition time of 20 seconds. The spectra processed for cosmic spike removal and the spectral background was subtracted using a Whittaker baseline filter.

3.2.3 EV isolation of the breast cancer cell line panel

A breast cancer cell line panel (see Table 3.1) was compiled consisting of MCF7, HCC1937, HCC1964, Hs578T, JIMT1, MDA-MB-231, MDA-MB-436, MDA-MB-468 and T47D cancer cells and the non-cancerous HuMEC and MCF10A cells. Cells were cultured to confluence at 37 °C and 5% CO_2.

HuMEC cells were cultured on HuMEC Ready Medium (HuMEC Basal Serum-Free Medium (12753018) supplemented with HuMEC Supplement kit (12755013, Thermo-Fisher, UK). MCF10A cells were cultured on DMEM/F12 media supplemented with 5% (v/v) horse serum (Invitrogen), 20 ng/mL EGF (Peprotech), 0.5 µg/mL hydrocortisone (Sigma), 100 ng/mL cholera toxin (Sigma), 10 µg/mL insulin (Sigma) and 1× penicillin/streptomycin (Gibco, UK). All other cell lines were cultured on high glucose DMEM supplemented with 10% (v/v) FBS, 20 mM HEPES, 1× non-essential amino acids (NEAA, Gibco) and 1× penicillin/streptomycin (Gibco, UK), with media changes every 2 days. All cells were obtained from the ATCC with the exception of JIMT1 and HuMEC cells which were obtained from the DSMZ and Life Technologies (Thermo-Fisher) respectively.

For EV isolation, cells were cultured to ~90% confluence, after which cell culture media were changed for serum-free equivalents. Cells were cultured for a further 3 days, after which the conditioned medium was collected, centrifuged at 300 rcf for 5 minutes and the supernatant passed through a bottle top filter with a 0.45 µm pore size (VWR, UK). The media was concentrated to approximately 500 µL by ultrafiltration (Amicon Ultra-15, 100 kDa) and further purified by size exclusion chromatography over a Sepharose CL-2B (Sigma Aldrich, UK) column of 30 × 1 cm. 1 mL fractions were collected and the EV containing fractions, as verified by NTA (Malvern, UK), were pooled. The EVs were stored frozen at -80 °C and kept in an ice bath prior to Raman spectroscopic analysis. The culture and EV isolation of the breast cancer panel was performed by Dr. Anika Nagelkerke, as well as aiding with part of the SPARTA 2.0 measurements.

3.2.4 EV composition analysis

EV samples isolated from the breast cancer panel were thawed on ice and 200 µL of solution was placed on a 22 mm coverslip fixed on a standard microscopy slide. Using the SPARTA 2.0 system, 200 acquisitions of 20 seconds were initialised and the spectra of the successfully trapped EVs acquired and processed as described above. The mean spectra ± s.d. were calculated in MATLAB and plotted in OriginPro 2017. PCA and PLSDA Multivariate statistical modelling was performed using the PLS Toolbox 8.1.1 (Eigenvector Research Inc.).

3.2.5 SPARTA 2.0 spectral processing

The Raman spectra were imported into MATLAB and processed using custom made analysis scripts. Cosmic spikes were removed from the data based on peak amplitude and a threshold on the 2nd derivate.

A spectral response correction was applied based on measurement of standardised samples supplied by the NIST (National Institute of Standards and Technology, US).

Minimum and maximum post-thresholding was conducted if applicable, by manual threshold decision to remove background solution spectra or spectra of clearly non-single particle origin (*e.g.* aggregates). A primary background subtraction was performed by subtraction of 85% intensity of 20 averaged spectra of PBS, followed by a Whittaker baseline subtraction. Smoothing of the spectra was conducted by application of a first order Savitsky-Golay smoothing filter with a frame size of 7, and normalisation of the data was applied were applicable by division by the area under the curve.

3.2.6 Raman imaging of breast cancer cells

HuMEC, MDA-MB-436 and T47D cells were cultured below confluence on MgF_2 slides to avoid significant glass background during imaging. Cells were fixed in 4% paraformaldehyde for 15 min at 37 °C and washed three times in PBS. Cells were kept submerged in PBS in the fridge prior to imaging. Raman spectral imaging of cells was performed on a confocal Raman microspectroscope (alpha300R+, WITec, Germany). A brightfield image was acquired prior to Raman imaging at the same position, scanning in a grid pattern and performing spectral acquisition every 1.5 µm. A 785 nm laser (Toptica XTRA II) with a 63x /1.0 NA water immersion microscope objective lens (W Plan-Apochromat, Zeiss, Oberkochen, Germany) was used for Raman excitation, with 85 mW laser power at the sample. The scattered light was collected via a 100 µm fibre with a 600 g mm^{-1} grating spectrograph (UHTS 300, WITec, Ulm, Germany). The spectrograph was equipped with a thermoelectrically cooled back-illuminated CCD camera (iDus DU401-DD, Andor, Belfast, UK). Spectral analysis and processing was performed using the Project FOUR 4.1 (WITec, Germany) software package and MATLAB 2016b. Cells were cultured by Dr. Anika Nagelkerke and Ms. Julia So for Raman spectral imaging.

3.2.7 Dimensional Reduction Array (DRA) construction

Dimensional Reduction Arrays (DRA) were constructed based on the processed, averaged Raman spectra of the breast cancer cell panel derived EVs. A custom MATLAB script and function were made consisting of truncating the data to the desired spectral range. A set block size of 10 cm^{-1} chosen for dimensional reduction and the CCD positions of the data were matched with the correct wavenumber positions (Raman shift). The reduced spectra were plotted on a colormap based on the MATLAB ‘perula’ preset for uniform intensity presentation.

3.3 Results and Discussion

The first part of the results and discussion will concern the development of SPARTA 2.0, a dedicated system for SPARTA. The SPARTA 2.0 system features numerous improvements to the system as presented in Chapter 2, referred to here as SPARTA 1.0.

The second part will focus on the analysis of breast cancer cell derived EVs with the improved SPARTA 2.0 system.

3.3.1 SPARTA 2.0 development

The SPARTA system described in Chapter 2 was developed by modification of an existing confocal Raman microspectroscope (alpha300R+, WITec, Germany), through the addition of an automated laser control system. While this system functioned well for the analysis of nanoformulations, such as liposomes and polymersomes, further optimisation of the system was preferred for the analysis of EVs. As EVs are highly complex vesicles, both in composition and in intrinsic biological variability, a high number of traps and samples is required for their comprehensive analysis with the SPARTA system. Therefore, six factors were identified which could be improved upon, to design a dedicated SPARTA system from the ground up, dubbed SPARTA 2.0. The system as described in Chapter 2, will therefore be referred to here as SPARTA 1.0.

The six areas of improvement are schematically shown in Figure 3.1. A primary factor of improvement was the increase of the signal intensity and signal-to-noise ratio of the acquired Raman spectra. From a system point of view, the signal intensity is mainly dependent on acquisition time, laser intensity and detector sensitivity. As increasing the acquisition time would slow down the measurements, improvement of the other two parameters was the focus in the design of the SPARTA 2.0 system. A spectrograph with higher sensitivity was acquired, as well as a 785 nm laser with up to 30% more output power, up to 110 mW. This led to an increase in signal intensity for a typical EV sample of up to 15-30 times (Figure 3.1-I).

The second improvement factor was the spectral range of acquisition. This range is dependent on the grating structure and position in the detector. In the SPARTA 1.0 system, the grating could be tuned to capture a range of around 1800 wavenumbers. While this allowed capturing down to very low wavenumbers, including the laser line, simultaneous collection of the full fingerprint region and silent regions was not possible.

For the SPARTA 2.0 system a fixed grating was chosen with a wider range, capturing 2060 wavenumbers in the range form 572-2632 cm^{-1} (Figure 3.1-II). In addition to this 14% range increase, the number of data points captured over this range was almost doubled from 1024 to 2000.

Thirdly, the confocality of the system was improved. This was achieved by switching to a smaller confocal pinhole fibre, from 100 µm internal fibre diameter in SPARTA 1.0 to 50 µm in the SPARTA 2.0 setup. While this led to a significant reduction in the potential signal gain achieved through the improvements of factor I, as less light reaches the detector, the smaller confocal volume ensures the signal is more specific to the particle trapped (Figure 3.1-III). Therefore, this should result in reduced signal acquisition from other particles in close proximity to the particle in the trap. In addition, this made the system more sensitive to smaller particles, as the EV size ranges extends down to the lower range identified for the SPARTA system. It should be noted that the 15-30 times increase in signal intensity, as mentioned for the first improvement factor, was achieved with the increased confocality in place.

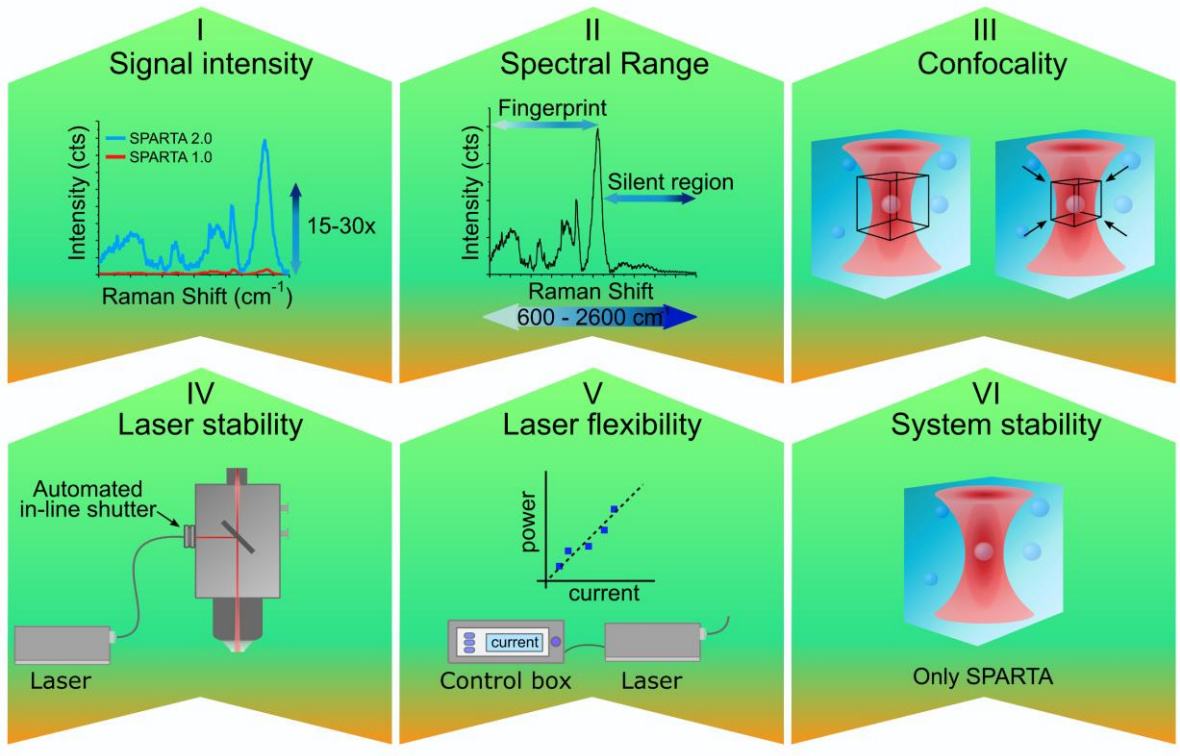

Figure 3.1 | SPARTA 2.0 system improvements. (I) Signal intensity improved by 15-30 times in comparison to SPARTA 1.0, (II) spectra range extended to 2600 cm^{-1} for simultaneous fingerprint and silent region acquisition, (III) increased confocality due to shift from a 100 to 50 µm pinhole, (IV) increased laser stability due to an automated in-line shutter, (V) improved laser flexibility, the laser diode current can be controlled via a control box and is linearly proportional to the output power, (VI) increased system stability as it is dedicated for SPARTA measurements only.

The fourth factor of improvement was an increase in laser stability. In the SPARTA 1.0 system, trapping automation was achieved by controlling the laser through MATLAB scripts. This resulted effectively in turning the laser off and on between traps, to achieve temporary trap disablement. Apart from possibly negatively impacting the longevity of the laser diode, by continuous on and off switching, this resulted in fluctuations in the output power during the measurements. By introducing an automated in-line shutter in the beam path in the SPARTA 2.0 setup, the laser could be permanently left on during measurements (Figure 3.1-IV). The in-line shutter was automated with a MATLAB script and could therefore physically, temporarily, block the laser beam in between traps.

The fifth, factor to improve on the SPARTA 1.0 system, was the introduction of flexibility in the laser output power. The laser for the SPARTA 2.0 system is controlled through a control box. Using the control box, the current to the laser diode can be easily modulated, which is linearly proportional to the output laser power (Figure 3.1-V). This flexibility is convenient when samples with sensitivity to the laser beam would be analysed, or to specifically investigate the signal intensity gain upon increasing the laser power.

Lastly, the overall system stability was improved as the final, sixth improvement to the SPARTA 1.0 system. As the SPARTA 1.0 system was a modification on an existing Raman microspectroscopy setup, this system was alternatively used for confocal Raman imaging when not set-up for SPARTA. This resulted in necessary changes to laser wavelength, alignments and switching of collection fibres when switching back and forth between SPARTA and Raman imaging modes. The SPARTA 2.0 system was constructed as a dedicated system for SPARTA measurements (Figure 3.1-VI). This eliminated measurement variability arising from re-configuration of the system prior to each measurement and improved ease of use.

Taking a closer look at the improvement in signal intensity with the SPARTA 2.0 system, a sample of MDA-MB-231 breast cancer cell-derived EVs was measured on both systems at an acquisition time of 20 seconds (Figure 3.2). As can be seen, the overall spectral profile is similar, taking into account some biological variance and system dependent variation in the spectral background. However, the intensity of the signal post baseline subtraction is around 15 times higher for the SPARTA 2.0 measurement, compared to the spectra measured with SPARTA 1.0. This gain in signal intensity can be dramatically seen when both curves are plotted on the same intensity scale axis, as shown in Figure 3.2.b. For this comparison, the background signal of the PBS solution was not subtracted, only a polynomial based baseline subtraction was applied.

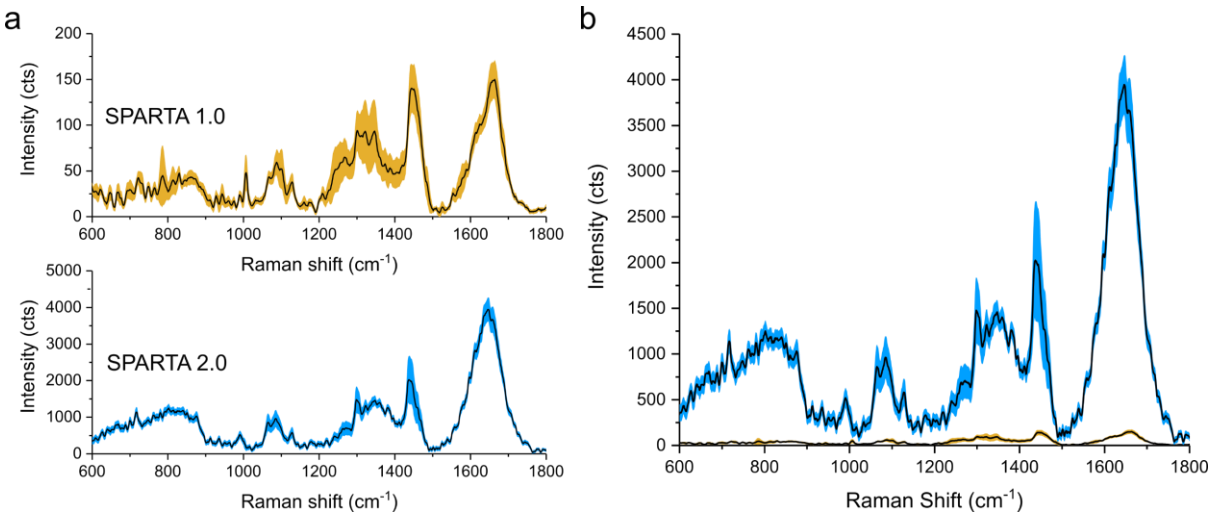

Figure 3.2 | SPARTA systems signal comparison. MDA-MB-231 EVs were analysed with the SPARTA 1.0 system (orange) and SPARTA 2.0 system (blue). (a) Mean ± s.d., dedicated intensity scale (b) Mean ± s.d, overlay spectra on the SPARTA 2.0 intensity scale. *Note that for these spectra the PBS background was not subtracted, however baseline subtraction was applied.*

The six aforementioned improvements were incorporated in the SPARTA 2.0 system configuration, which is schematically shown in Figure 3.3. Compared to a standard confocal Raman microspectroscopic setup (Figure 1.4), a number of additional components can be seen. The laser is connected to a control box which regulates the diode current, and thus, the power output of the laser. Through this control box, the laser current is kept stable during measurements due to the integrated temperature stabilisation. The laser light is directed *via* an optical fibre through an automated in-line shutter. This physical shutter is controlled via a shutter control box, which can be manually operated, but during SPARTA measurements is controlled via a custom MATLAB script. The automated shutter disengages the trap when necessary, without the need for manual shuttering or disabling the laser itself.

The light is reflected by a dichroic mirror through a high NA objective onto the sample, as is the case with the SPARTA 1.0 system. The sample is held in place by a sample holder supported by an automated stage. Since the SPARTA 1.0 system had an automated stage as well, this is not directly counted as one of the system improvements, however through the stage control box this stage can be integrated and controlled by custom MATLAB scripts as well, the importance of which will be stressed in sections below. The scattered light is collected back through the dichroic mirror and focused by the collimator on the 50 µm optical fibre acting as confocal pinhole. The optical fibre directs the light to the improved spectrograph, which converts the Raman scattered light into the spectral information, as read out by the PC.

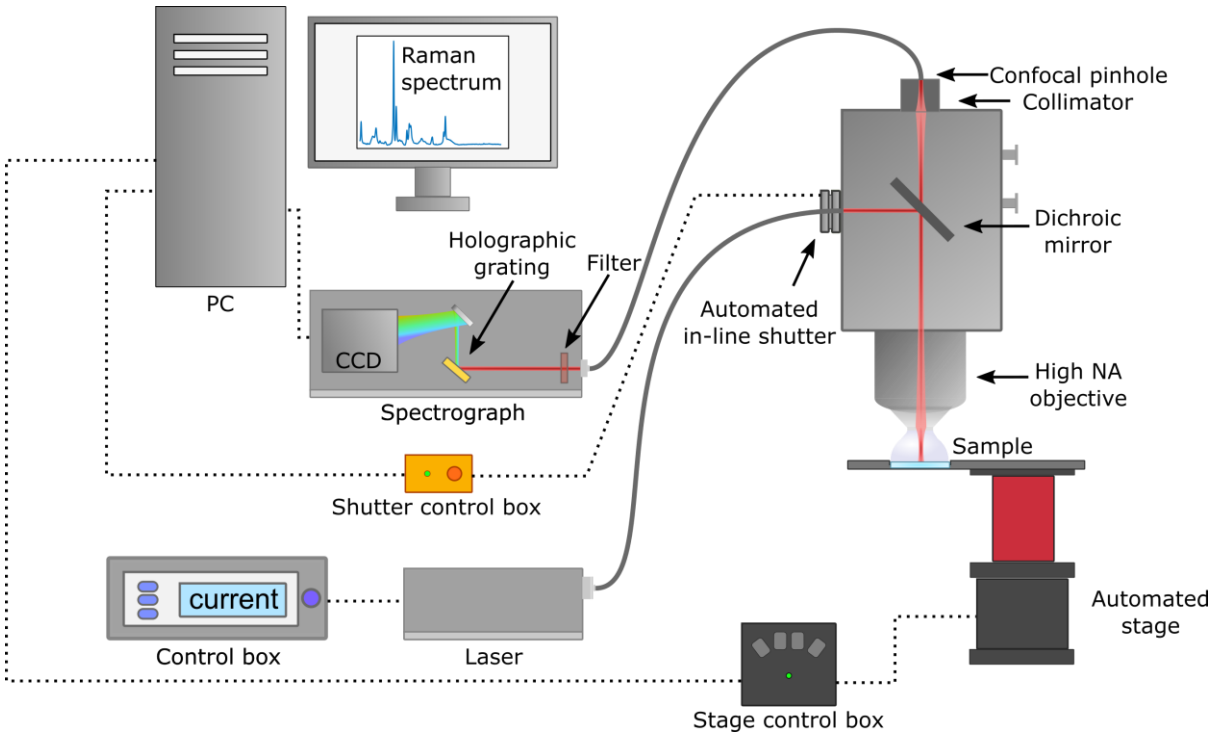

Figure 3.3 | SPARTA 2.0 System configuration. Schematic overview showing the system setup for SPARTA 2.0. A 785 nm laser is controlled via a control box (dotted line). The laser light is guided through an optical fibre (solid grey) to the main microscope part, through an automated in-line shutter, controlled via a shutter control box. The light is reflected by a dichroic mirror through a high NA objective on to the sample. The sample is held by an automated stage and controlled through a stage control box. The scattered light is reflected through the dichroic mirror and collimated on a confocal pinhole. An optical fibre guides the light to the spectrograph where the Rayleigh scattered light is filtered out and the Raman scattered light projected by a holographic grating on a CCD. The CCD signal is collected and processed on a PC, which controls the whole trapping process through custom MATLAB scripts. *A standard confocal Raman microspectroscopic setup is shown in Figure 1.4.*

3.3.2 SPARTA 2.0 operation and ease of use

To establish the SPARTA platform as a comprehensive nanoparticle analysis technique, it was deemed paramount to take ease of use and operation into careful consideration. Therefore, a process flow was developed focusing on automation, as well as on clear user input and feedback. A schematic representation of this process flow is shown in Figure 3.4.

The first step in this process is initialisation of the system, by powering on all components, such as the PC, spectrograph, stage, shutter and the laser. Once powered up, all components are connected via the PC through MATLAB scripts and the automated control over the shutter and stage are initialised. As a final step of start-up, the detector CCD is cooled down to -60 °C, to minimise thermal noise.

The second step is a calibration of the system, to verify all components are working properly. Using a dedicated calibration script, the user is guided through the process using MATLAB dialog boxes. A spectrum is taken under dry conditions of a paracetamol tablet, as well as from polystyrene under immersion, originating from the bottom of a polystyrene dish filled with PBS. These standards were chosen for their clear and stable Raman signatures, making them suitable for this calibration purpose. These spectra are verified to have a minimal threshold intensity to check proper configuration and alignment of the system. Using automated control over the stage, the calibration standards are positioned close to the ideal measurement position by the calibration script, improving both ease and speed of the calibration procedure.

Once the system is initialised and calibrated, the acquisition parameters for the desired measurements can be set using the SPARTA graphical user interface (GUI). As shown in Figure 2.7, the custom MATLAB code operating the system (jointly written with Dr. Isaac Pence) includes a GUI, to allow facile access to and adaptation of the main acquisition parameters. Before sample measurement, as the fourth step of operation, spectra are taken of the solution background in which the particles to be analysed are present. This background may be used during SPARTA analysis to subtract it from the sample measurements. Additionally, this is to help identify if the acquisition of non-particle containing traps occurred during measurements, possibly due to a too low trapping threshold.

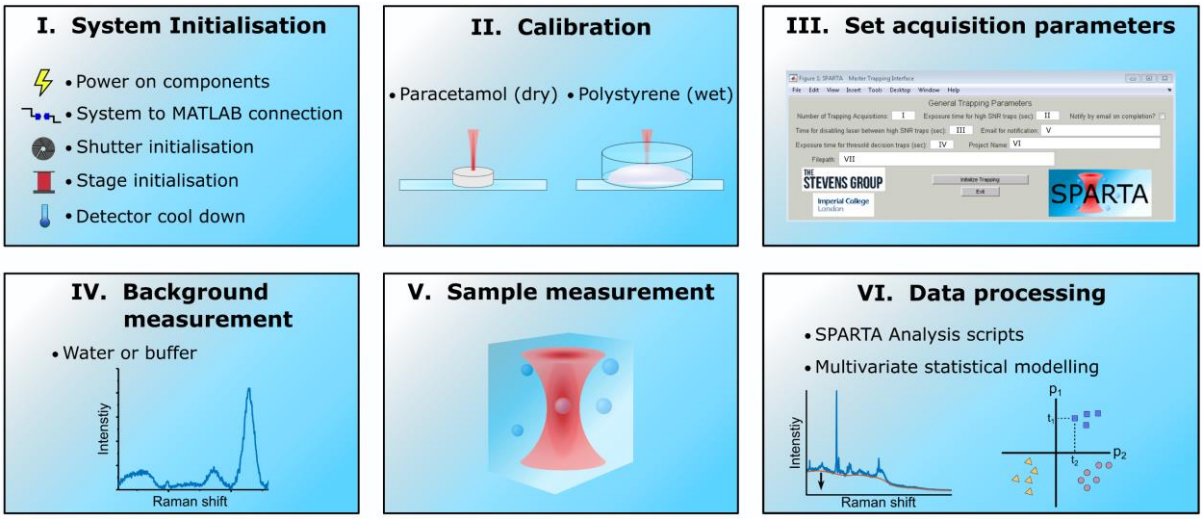

Figure 3.4 | SPARTA 2.0 operation process flow. (I) The system is initialised by powering on and initialisation of the components, connection to MATLAB and cooling down of the detector. (II) The system is calibrated by acquisition of a spectrum of paracetamol (dry) and of a polystyrene dish (wet). (III) The acquisition parameters are set through the SPARTA GUI. (IV). A background measurement of the solution is conducted at the same acquisition conditions as the prospected sample. (V) SPARTA sample runs are conducted. (VI) The acquired data is processed through analysis scripts and can be used for multivariate statistical modelling.

For an experienced user, this process takes about 10-15 minutes, depending on the number of background measurements. In principle, this initialisation and calibration procedure is only carried out once per day. However, additional background measurements would be needed if different acquisition parameters are used (specifically acquisition time and laser power) or particles are to be measured in a different solution.

Post acquisition, the data is analysed using custom developed analysis scripts, guiding the user through applying sequential processing steps, such as those shown in Figure 1.5. In addition, a number of extra steps have been included in the analysis of the data acquired by SPARTA 2.0. A spectral response correction is carried out on the raw data, which corrects for any changes in sensitivity of the detector over the acquisition range. The spectral response calibration is carried out by the measurement of standards as set and provided by the National Institute of Standards and Technology (NIST)[200].

Another step specifically developed for SPARTA, is post-threshold checking. All spectra are plotted in an overlay to be able to visually identify spectra that should be excluded from the analysis. A minimum post-threshold check checks for spectra where the signal is too low. These spectra, mostly representing the solution background, may have resulted from setting a threshold intensity during measurements that was too low. Conversely, the maximum post-threshold check allows for the exclusion of spectra which, if present, may result from aggregates in the solution giving a spectrum of several times the intensity normally obtained for single particles. While these post-threshold checks introduce some degree of user bias in the analysis, it allows for salvaging the part of the data that is useful and representative of the particles. The inclusion of aggregate or background spectra can cause misrepresentative mean spectra, as well as hamper meaningful multivariate statistical modelling. However, their presence can be informative regarding the heterogeneity and stability of the sample.

The final processing steps of the spectra include the background and baseline subtraction. For EV analysis the background signal of PBS is subtracted, as the EVs are purified in PBS. The one-to-one subtraction of PBS often results in the generation of some negative peaks in the water region. This may be explained by the slight difference in density of the EV solution compared to pure PBS and the displacement of some of the PBS in the trap when an EV is present. Hereto, the intensities of the PBS spectrum are multiplied by a factor of 0.85 and this 15% reduced intensity spectrum is subtracted from the EV spectra. A subsequent polynomial curve fit baseline subtraction algorithm removes the rest of the background from the spectra. Lastly, the spectra are smoothed and, optionally, normalised as indicated in Figure 1.5.

3.3.3 SPARTA breast cancer EV analysis

Using the SPARTA 2.0 system, EVs derived from a panel of breast cancer cells were analysed for their composition and their inter cell line differences were modelled using multivariate statistical techniques. This cell line panel was carefully selected to reflect various types of breast carcinoma and adenocarcinoma, as well as metastatic cell lines originating directly from metastases and not the primary tumour. In addition, a mixture of receptor status expression profiles was selected from ER+ and HER2+ to triple negative cell lines. Two types of non-cancerous breast epithelial cell lines were also included as controls (Table 3.1).

In the sections below, first a detailed analysis of an EV spectrum is discussed, highlighting the biological components that can be identified using Raman spectroscopy. Secondly, the spectra of a selection of EVs is compared to those obtained by Raman confocal imaging of their parent cells, illustrating spectral similarities and differences. Next, the spectra of the full panel of breast cancer cell derived EVs are compared and modelled using multivariate statistical analysis such as PCA and PLSDA to discover the spectral features that allow separation of different classes of EVs.

Table 3.1 | Breast cancer cell panel for EV analysis. *The panel was composed by Dr. Anika Nagelkerke.*

Cell line	Disease state	Receptor expression
HuMEC	Non-cancerous, primary	-
MCF10A	Non-cancerous, immortalised	-
MCF7	Metastatic adenocarcinoma	ER+
HCC1937	Primary ductal carcinoma (stage IIB), BRCA mutated	Triple negative
HCC1954	Ductal carcinoma (stage IIA)	HER2+
Hs578T	Ductal carcinoma	Triple negative
JIMT1	Metastatic ductal breast carcinoma	HER2+
MDA-MB-231	Metastatic adenocarcinoma	Triple negative
MDA-MB-436	Metastatic adenocarcinoma, BRCA mutated	Triple negative
MDA-MB-468	Metastatic adenocarcinoma	Triple negative
T47D	Ductal carcinoma	ER+

3.3.3.1 EV composition analysis

As stated in Chapter 2, the primary mode of application of the developed SPARTA system, is the analysis of the composition of a trapped nanoparticle, through acquisition of the Raman spectrum of said particle. As a model EV for detailed composition analysis MDA-MB-436 EVs were chosen, from a metastatic triple negative adenocarcinoma cell line. The mean spectrum ± s.d. is shown in Figure 3.5. The compositional analysis of the spectrum is indicated by highlighting spectral regions with coloured bands, pertaining to the main class of biological compounds having Raman vibrations in that region. As seen, the EV spectrum is composed of a range of lipid, protein and nucleic acid (NA) signals, as well as some lipoproteins and glycans (saccharides).

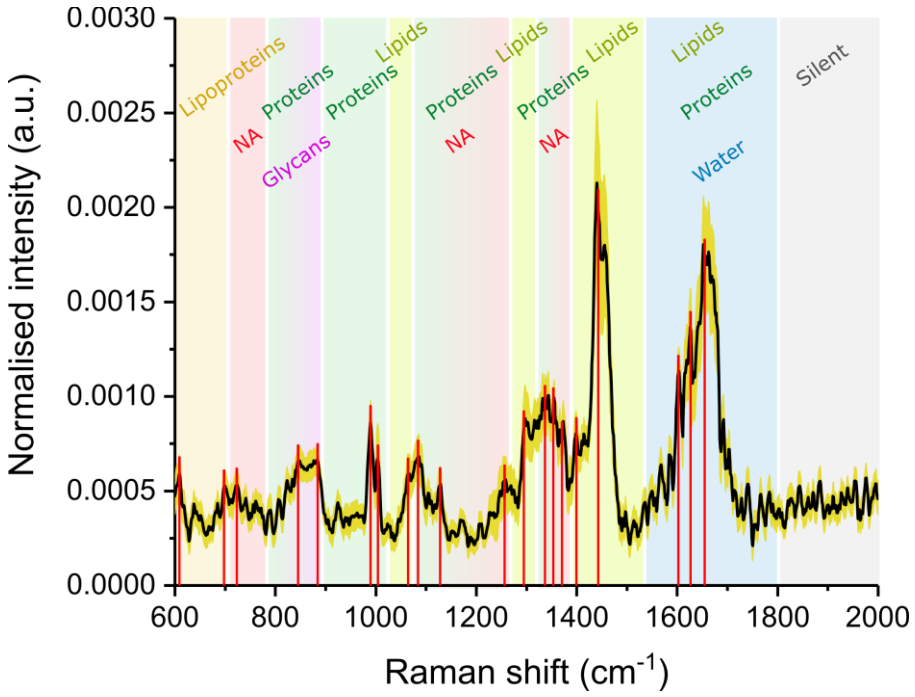

Figure 3.5 | SPARTA EV compositional analysis. Compositional analysis of MDA-MB-436 breast cancer EVs, mean ± s.d. (n = 87). Spectral regions pertaining to various signals of biological origin indicated as shown. MDA-MB-436 EVs contain moderate protein and nucleic acid (NA) signal, strong phenylalanine signal (1004 cm^{-1}) and strong lipid signals. *See Table 3.2 for peak assignments.*

A detailed assignment of the main peaks present in the spectrum is tabulated in Table 3.2. It should be noted that the Raman shifts pertain to the peak centre, with the peaks often spanning a spectral range between 10-100 cm^{-1}.

Table 3.2 | EV composition Raman peak assignment. *Peaks assigned by the compendium tabulated by Movasaghi et al.*[83]

Band	Vibration/Compound	Raman shift (cm^{-1})
Lipoprotein	*Cholesterol*	609
Lipoprotein	*Cholesterol*	698
NA	*DNA ring breathing modes*	723
Proteins/Glycans	*Tyrosine, Glycans*	845
Proteins/Glycans	*Tryptophan, Glycans*	884
Proteins	*C-C stretch protein β-sheet*	989
Proteins	*Phenylalanine*	1004
Lipids	*C-C stretch lipids*	1064
Proteins/NA	*C-N stretch proteins, PO_2^- stretch DNA backbone*	1084
Proteins/NA	*C-N stretch proteins*	1128
Proteins/NA	*Amide-III proteins, DNA ring breathing modes*	1256
Lipids	*CH_2 twist lipids*	1295
Proteins/NA	*Amide-II proteins, DNA ring breathing modes*	1337
Proteins/NA	*Guanine, Tryptophan*	1354
Proteins/NA	*DNA ring breathing modes*	1371
Lipids	*C=O stretch, CH_2 lipids*	1399
Lipids	*CH_2 bend lipids*	1442
Lipids/Proteins/Water	*C=C bend proteins*	1603
Lipids/Proteins/Water	*Amide-I proteins*	1626
Lipids/Proteins/Water	*Amide-I proteins*	1654

The lipoprotein signals observed around 609 and 698 cm^{-1} may be attributed to the presence of cholesterol in the EV membrane[41,42,201]. Several peaks (723, 1256, 1337, 1354 and 1371 cm^{-1}) can be assigned to the presence of nucleic acids in the EVs, resulting from ring breathing modes of the nucleotide bases of DNA or RNA. Additionally, the *PO_2^- stretch* vibration of the DNA backbone can be observed around 1084 cm^{-1}, with overlap expected with the *C-N stretch* vibration present in proteins. The signal present around 845 and 884 cm^{-1} indicates the presence of glycans, such as those of glycoproteins, a class of EV components more recently discovered as important compositional markers[202,203]. The EV membrane has been shown to be rich in a variety of (transmembrane) proteins[42,201], which can be identified in the Raman spectra by several bands. Specific amino acids have an enhanced Raman signature due to their aromatic ring structure, such as phenylalanine, tyrosine and tryptophan, in a similar way as the nucleotide bases in DNA. Phenylalanine has a characteristic Raman peak around 1004 cm^{-1}. The signals for tyrosine around 845 cm^{-1} and tryptophan 884 at cm^{-1} overlap with those of the glycans, with a second peak for tryptophan at 1354 cm^{-1} overlapping with the nucleic acid peak of guanine. Other protein peaks visible can be related to the *C-C stretch* vibration in the protein β-sheet structure at 989 cm^{-1} and the aforementioned *C-N stretch* vibrations around 1084 and 1128 cm^{-1}. Additionally the primary (1626, 1654 cm^{-1}), secondary (1337 cm^{-1}) and tertiary (1256 cm^{-1}) amide bonds can be observed. Lastly, a number of strong peaks can be seen originating from the lipids present in the EV membrane. These include several alkane chain vibrations such as *C-C stretch* (1064 cm^{-1}), *CH_2 twist* (1295 cm^{-1}), *C=O stretch* and *CH_2 bend* (1399 and 1442 cm^{-1}).

As shown, using SPARTA, the complex composition of EVs may be revealed, resulting in a detailed fingerprint spectrum. From the perspective of using EVs as cancer biomarkers, this can be used to investigate the presence of significant biological compositional differences between EVs from cancerous and non-cancerous origin, thus enabling disease detection.

3.3.3.2 EV to EV and cellular comparison

A sub section of the breast cell line panel, as shown in Table 3.1, was made of three cell lines, consisting of one non-cancerous (HuMEC) and two cancerous (MDA-MB-436 and T47D) lines. For this subset, the cells were cultured and EVs extracted, purified and analysed by SPARTA. In addition, cells were cultured on magnesium fluoride windows for Raman imaging, to enable Raman spectroscopic imaging, as a comparison to the EV Raman spectra obtained by SPARTA. The averaged spectra obtained for the analysed EVs can be seen in Figure 3.6.a.

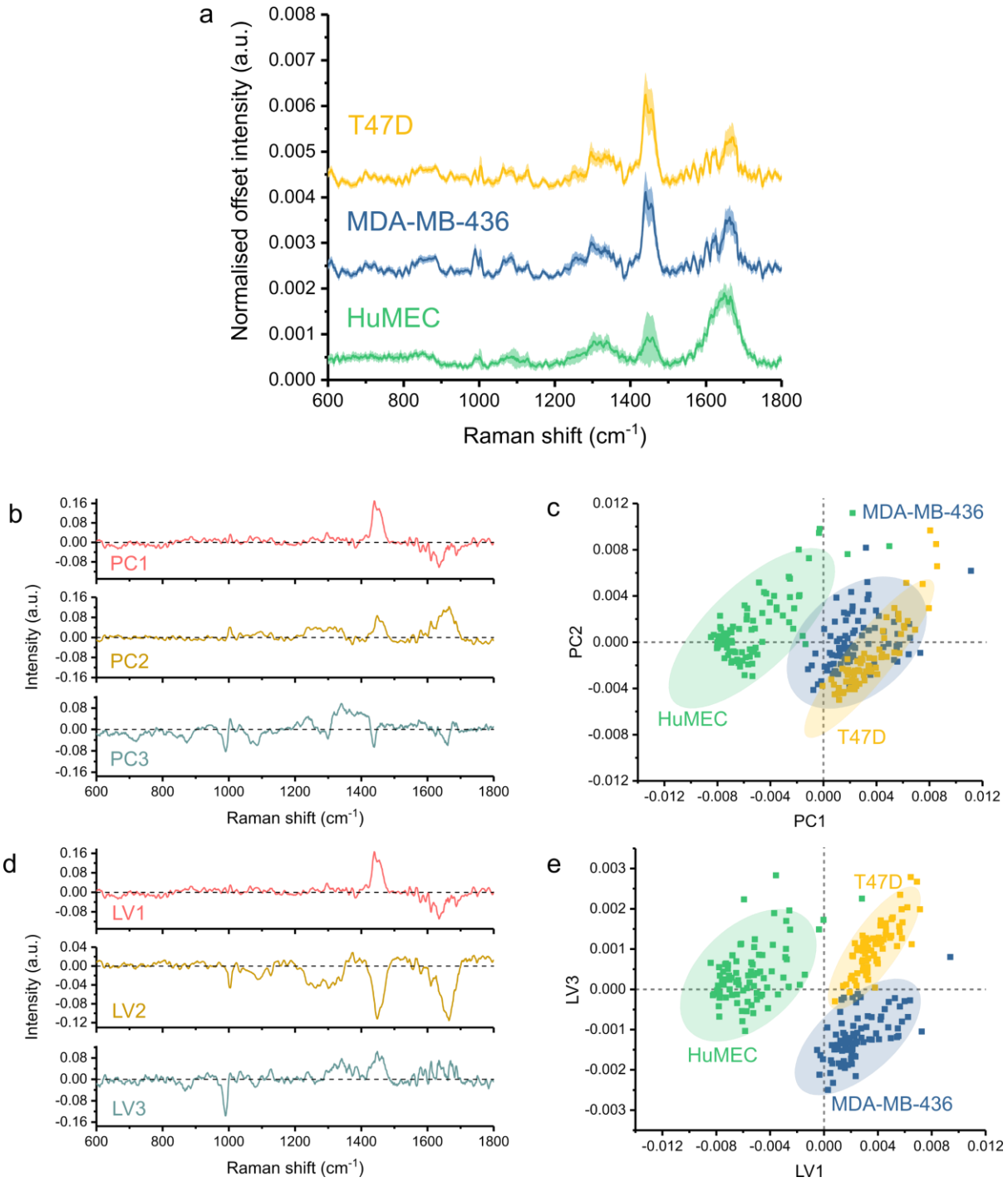

Figure 3.6 | PCA and PLSDA modelling of a 3-EV panel. (a) Mean ± s.d. SPARTA spectra of HuMEC (n = 88), MDA-MB-436 (n = 87) and T47D (n = 72) EVs. (b-c) PCA modelling showing the pseudo-spectra of the first three principle components (PC1 50%, PC2 18%, PC3 2% variance captured) (b) and the corresponding score plot of PC1 against PC2, including 95% confidence ellipses (c). (d-e) PLSDA modelling showing the latent variable pseudo-spectra (LV1 49%, LV2 18%, LV3 3% variance captured). (d) and the corresponding score plots of LV1 against LV3, including 95% confidence ellipses.

While the overall spectral profile for the EVs from the different cell lines appears very similar at first glance, some distinct differences can be seen in certain protein and lipid signatures. The main lipid signature intensity of the CH_2-bend vibration around 1450 cm^{-1} is reduced for the HuMEC EVs as compared to those obtained for MDA-MB-436 and T47D EVs. Additionally the protein signal for the MDA-MB-436 EVs around 1000 cm^{-1}, arising from phenylalanine appears enhanced in comparison.

The spectral differences were further analysed by application of multivariate statistical techniques. This was performed to identify if there is sufficient statistical difference between the EV signatures, to be able to reliably distinguish the EVs of different cellular origin. A first model was constructed using PCA. The first three principle components (PCs) are shown in Figure 3.6.b. PC1 mainly shows the CH_2-bend vibration around 1450 cm^{-1} and as seen in the scores plot in Figure 3.6.c, this is the main classifier between the EV subtypes. Viewed along PC1, the HuMEC EVs (green) are very well clustered and classified away from the other subtypes with MDA-MB-436 shown in blue and T47D in yellow. As shown, the cluster of HuMEC EVs scores negatively on PC1, indicating a negative contribution of the pseudo-spectrum of PC1, thus a relatively lower signal present around 1450 cm^{-1}. This indicates a lower lipid content in the HuMEC EVs, as representative of a non-cancerous origin, with conversely a higher relative lipid content in the cancerous cell line derived MDA-MB-436 and T47D EVs. The PCA model does show moderate overlap between the MDA-MB-436 and T47D EVs, especially when viewing the 95% confidence ellipses. Some difference can be seen when viewed along the axis of PC2, indicating a more positive contribution of PC2 in the MDA-MB-436 EV spectra.

In an attempt to resolve classification between the cancerous subgroups, another model was constructed based on PLSDA. In contrast to PCA, PLSDA is a supervised method, where *a priori* knowledge of the origin of the EVs is used in the construction of the model. The resulting latent variables (LVs) are therefore constructed as those best describing the differences between the EV classes. From the LVs shown in Figure 3.6.d. it can be seen that LV1 and PC1 are near identical, confirming that the difference in lipid (CH_2-*bend*) signal is a major source of variance between the spectra of the different EVs. The resulting scores plot (Figure 3.6.e) indicates a very high degree of classification power between the three EV classes, both between the non-cancerous and cancerous subtypes as between the two cancerous ones. Interestingly, the MDA-MB-436 and T47D EVs can now be separated based on their scores on LV3. The MDA-MB-436 cluster scores negatively on LV3, with LV3 showing a significant negative peak around 1000 cm^{-1}.

Therefore, an increase of the signal around 1000 cm^{-1} for the MDA-MB-436 EVs results in classification between the MDA-MB-436 and T47D EVs, as previously indicated from comparison of the spectra in Figure 3.6.a. In addition, the presence of a (smaller) positive peak around 1450 cm^{-1}, indicates a lower lipid content for the MDA-MB-436 EVs compared to those of T47D. The classification sensitivity and specificity with the PLSDA model was calculated to be both 100% when using a venetian blinds cross validation (10 splits).

Taking these observed changes between the EV compositions, Raman spectral imaging of the parental cell lines was performed, to see if these EV differences are originating within conserved compositional variation of the cells themselves. Using the confocal Raman microspectroscopy system of the first-generation SPARTA, in imaging rather than trapping mode, Raman spectra were acquired by scanning in a grid-pattern across cells. The cells were cultured and imaged on MgF_2 coverslips, as these are Raman transparent and do not contribute to a significant background signal, as is the case for glass coverslips. Spectra were acquired every 1.5 µm and the spectra containing the highest 10% of signal intensity at the 1450 cm^{-1} peak were selected for further analysis. This was done to attempt to select a set of spectra, which closer reflects the cellular membrane and closer relates to the EV composition. The mean spectra and s.d. are shown in Figure 3.7.a. Visually, these spectra show a close resemblance to each other, with small variations visible around 700 - 750 cm^{-1}, 1050 cm^{-1} and 1300 cm^{-1}. A heatmap was generated from the spectra of the 1450 cm^{-1} peak intensity, visualising the main lipid distribution in the cells *by proxy* of the CH_2-*bend* vibration. The Raman heatmaps were overlaid with the brightfield image for clarity, which can be seen in Figure 3.7.b.

Similar to the EVs, closer analysis of the cellular spectral subset was performed by multivariate modelling, using both PCA and PLSDA. The principal components and scores plots can be seen in Figure 3.7.c-d, respectively. The scores plot indicates a clear separation between the non-cancerous HuMEC cell spectra and the cancerous MDA-MB-436 and T47D clusters, while the latter overlap to some degree with each other. The main classification vector between the cancerous- and non-cancerous sets was PC2, indicating an increase in peaks at 715, 1270 and 1442 cm^{-1}. The 715 cm^{-1} vibration may be assigned to the *C-N* bond of the headgroup of some of the membrane phospholipids[83]. The increase in signal at 1270 cm^{-1} corresponds to the tertiary amide bond in (membrane) proteins and the aforementioned 1442 cm^{-1} peak to the CH_2-bend vibration[83]. Overall, this reflects an increase in lipid content in the membrane of cancerous cells, compared to non-cancerous (HuMEC) cells, in line with recent findings by others[189,190].

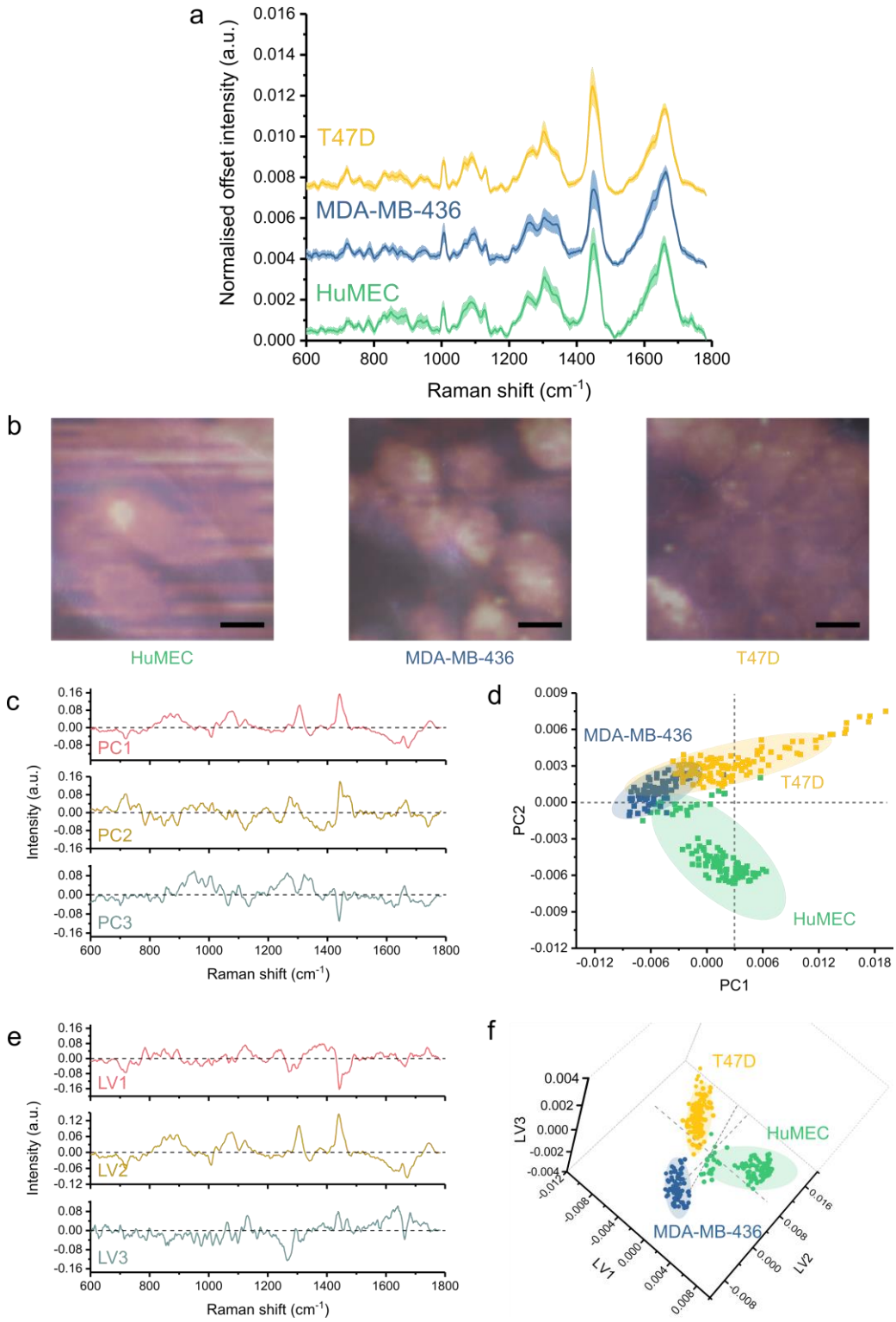

Figure 3.7 | PCA and PLSDA modelling of a 3-cell panel. (a) Mean ± s.d. Raman spectra of HuMEC (n = 102), MDA-MB-436 (n = 74) and T47D (n = 120) cell imaging, spectra with the highest 10% signal at 1450 cm^{-1}. (b) Raman imaging heatmaps at 1450 cm^{-1} overlaid with BF image (c-d) PCA modelling, showing the pseudo-spectra of the first three principle components (PC1 42%, PC2 25%, PC3 5% variance captured) (c) and the corresponding score plot of PC1 against PC2, including 95% confidence ellipses (d). (e-f) PLSDA modelling showing the latent variable pseudo-spectra (LV1 26%, LV2 41%, LV3 4% variance captured) (e) and the corresponding score plots of LV1 against LV2 and LV3, including 95% confidence ellipses (f).

Further modelling was performed using PLSDA, with the latent variables and scores shown in Figure 3.7.e-f, respectively. The PLSDA model performed very well, both in respect to sensitivity and specificity with sensitivities of 97.9, 98.6 and 100% and specificities of 100, 99.5 and 98.8% for HuMEC, MDA-MB-436 and T47D predictions respectively.

As shown in Figure 3.7.f, the separation between the three cell lines was best achieved using three latent variables, resulting in the 3D scores plot. The main separation between the HuMEC cells and the cancerous ones was achieved by LV1, with a strong negative peak around 1450 cm^{-1} and negative scores for the cancerous MDA-MB-436 and T47D spectra, again indicating a higher lipid content being the main classifier. Between MDA-MB-436 and T47D separation was achieved by an overall negative score on LV2 for MDA-MB-436 and positive score on LV3 by T47D. This indicates a lower lipid content for the MDA-MB-436 cell spectra compared to T47D, but a lower *C-N* headgroup signal for T47D.

Comparison between the EV spectra as obtained by SPARTA and the cell spectral subset from the Raman imaging, reveals an overall agreement in the lower lipid content of the EV and cell (membrane) for the non-cancerous HuMEC cell line. This results in the main classifier between cancerous and non-cancerous EVs being the CH_2*-bend* signal around 1450 cm^{-1}. The classification between MDA-MB-436 and T47D is more subtle for both the EVs and cells, with agreement on the lower lipid content for MDA-MB-436 EV and cell spectra, placing it intermediate between HuMEC and T47D. The increase in phenylalanine signal for the MDA-MB-436 EVs as revealed by PLSDA modelling of the EVs (Figure 3.6.d-e), is not clearly reflected in the cell measurements, although a small negative peak in the 1000 cm^{-1} region can be seen in LV2 with a corresponding negative overall score on LV2 for the MDA-MB-436 cell spectra.

In summary, using the above exemplary cell lines and derived EVs, excellent distinction was achieved between the Raman spectra of cancerous and non-cancerous origin, with sensitivities and specificities close to and up to 100%. Comparison between EVs and their parental cell lines was attained resulting in an overall agreement in the compositional variance, illustrating the difference between cancerous and non-cancerous origin.

3.3.3.3 Analysing and modelling of a 11-cell line derived EV panel

Following successful analysis and classification of three exemplar cell lines, the SPARTA analysis was expanded to the full 11-cell line panel as shown in Table 3.1. Expansion to such a large panel resulted in challenges in data representation and comparison. Analysis and visual comparison of averaged spectra of the EVs, as shown in Figure 3.8.a, does not allow for clear distinction of the spectral, and thus, compositional differences.

Hereto, a novel data representation approach was developed, inspired by heat maps conventionally used to represent up and down regulation of gene expression or lipid composition clustering for a high number of analytes and samples[204]. This representation, dubbed a 'dimensional reduction array' or DRA, reduces the dimension of the data by taking the average intensity over a predetermined block size (here 10 cm^{-1}) and showing this intensity as a colour on a heat map.

A custom MATLAB function was designed to this effect, where the block size and spectral range can be easily adapted. It also corrects for the dimensional mismatch between the CCD collection axis of the spectrograph and the true Raman shift axis in wavenumbers. This procedure was applied on the averaged EV spectra of the 11-EV panel, the result of which is shown in Figure 3.8.b.

In contrast to the spectra of Figure 3.8.a, the DRA allows clear, direct visualisation of the spectral regions, contributing to the difference between a large number of EV samples. For example, the HuMEC EVs exhibit a distinct lower intensity signal at the 1450 cm^{-1} region, as previously shown with PCA and PLSDA modelling. The EVs with the highest lipid signal can be identified from the DRA in Figure 3.8.b as being those derived from the HCC1954, JIMT1, MCF7 and MDA-MB-468 cell lines.

To visualise the changes in the lower wavenumber range of the fingerprint region in more detail, an additional DRA was constructed over the range of 600-1200 cm^{-1}, shown in Figure 3.8.c. Here, smaller intensity differences can be seen due to the more sensitive scaling, by cropping of the strong signatures around 1450 cm^{-1}. Protein peak intensity differences can be observed between the EV spectra around 900, 1000-1050 and around 1100 cm^{-1}, as well as more subtle differences in NA content indicated by differences in intensity around 750 cm^{-1}.

A key factor in the design of these DRA's was the choice of colormap to display the intensity differences. While the commonly used 'rainbow' gradient may highlight the intensity differences stronger than the blue-green-orange-yellow gradient as shown, the rainbow scale is not a perceptually uniform gradient. The perceptual ordering of the colours of the rainbow gradient are abrupt and could introduce so-called 'phantom features' by introducing artificial, additional contrast between features of neighbouring intensity[205,206]. The DRA's as shown, were therefore constructed using a perceptually uniform gradient dubbed 'parula' in MATLAB[206]. The parula colour map is based on the CIELAB colour space, as set by the International Commission on Illumination (CIE, Commission Internationale de l'Eclairage) for uniform data representation[207].

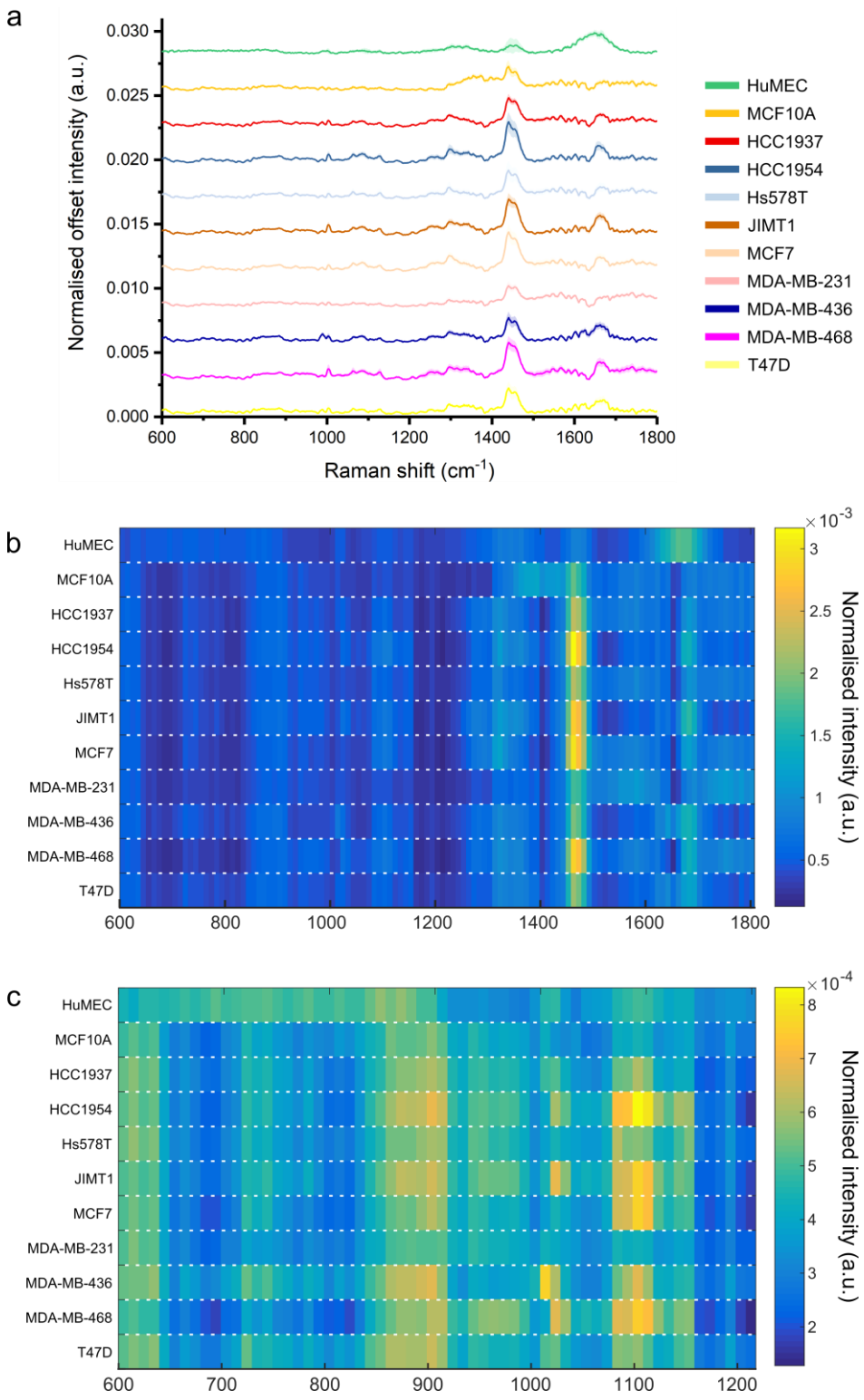

Figure 3.8 | SPARTA analysis of an 11-EV panel. (a) Mean ± s.d. Raman spectra of HuMEC (n = 88), MCF10A (n = 113), HCC1937 (n = 188), HCC1954 (n = 196), Hs578T (n = 69), JIMT1 (n = 163), MCF7 (n = 154), MDA-MB-231 (n = 79), MDA-MB-436 (n = 87), MDA-MB-468 (n = 88) and T47D (n = 72) EVs (n = 1297 total). (b-c) Dimensional reduction arrays representation of the mean spectra as shown in (a) with a block size of 10 cm^{-1}. (b) full fingerprint spectra 600-1800 cm^{-1}. (c) spectral subsection 600-1200 cm^{-1}.

The obtained spectral data sets for the 11-EV panel, were further analysed for the significance of the spectral differences between the EV types. The main goal was observing the difference between EVs from healthy cell lines and those from cancerous origin for the extended panel. In addition the extend of similarity or differentiation between the spectra of EVs from various types of cancer cell lines was of interest. To this end a PLSDA classification model was constructed, a 3D plot of the loadings of a total of 1297 single EV spectra, each belonging to one of the aforementioned 11 cell line classes, can be seen in Figure 3.9.a. The model was cross-validated by venetian blinds (10 splits).
A 5-LV PLSDA model was constructed with the loadings and scores of the primary three LVs plotted. While this representation of 11 clusters is inherently crowded, clear clusters were identified, in particular those belonging to the two non-cancerous cell line derived EVs, HuMEC (green) and MCF10A (yellow).

The corresponding LV pseudo spectra (Figure 3.9.b) show a clear negative peak in LV1 for the *CH_2-bend* vibration around 1450 cm^{-1}, with clear protein-related peaks in LV2 around 1000 cm^{-1} (phenylalanine, 1004 cm^{-1}) and a broad Amide-III band around 1600 cm^{-1}. LV3 mainly consists of a broad lipid feature between 1350-1500 cm^{-1}.

To assess the classification power and accuracy of the PLSDA model, a confusion matrix was constructed, as shown in Figure 3.9.c. This matrix shows the actual class (assigned) *versus* the predicted class by the model. All values not on the diagonal highlighted in green, were therefore misclassified by the model. Primarily, classification between non-cancerous (HuMEC, class 1, and MCF10A, class 2) and cancerous EVs was excellent. A very small number of cancerous EVs were classified in either class 1 or 2, and none of the non-cancerous EVs in any of the classes belonging to the cancerous EVs (classes 3-11). This resulted in a specificity and sensitivity of 100% and 99.5%, respectively, for cancerous/non-cancerous classification, as well as perfect separation between the two non-cancerous sub-groups. However, the classification between the cancerous classes was not perfect, with three main misclassification groups highlighted in red in Figure 3.9.c. Of the HCC1954 EVs 23% was wrongly classified in the JIMT1 class (6), 45% of the Hs578T EVs were classified as HCC1937 (3) and 36% of the T47D EVs as belonging to the MDA-MB-436 class (9). The reason for the misclassification by the model for part of the cancerous EVs in other classes, may be found in the apparent compositional similarity between those EV types, as measured by SPARTA. Looking at the receptor status subtypes, as shown in Table 3.1 for the parental cell lines, this similarity can largely be explained. Both HCC1954 and JIMT1 cell lines are HER2+ and both Hs578T and HCC1937 cell lines are triple negative lines of ductal carcinoma origin. It stands therefore to reason that the EVs from these lines could exhibit extensive compositional similarity.

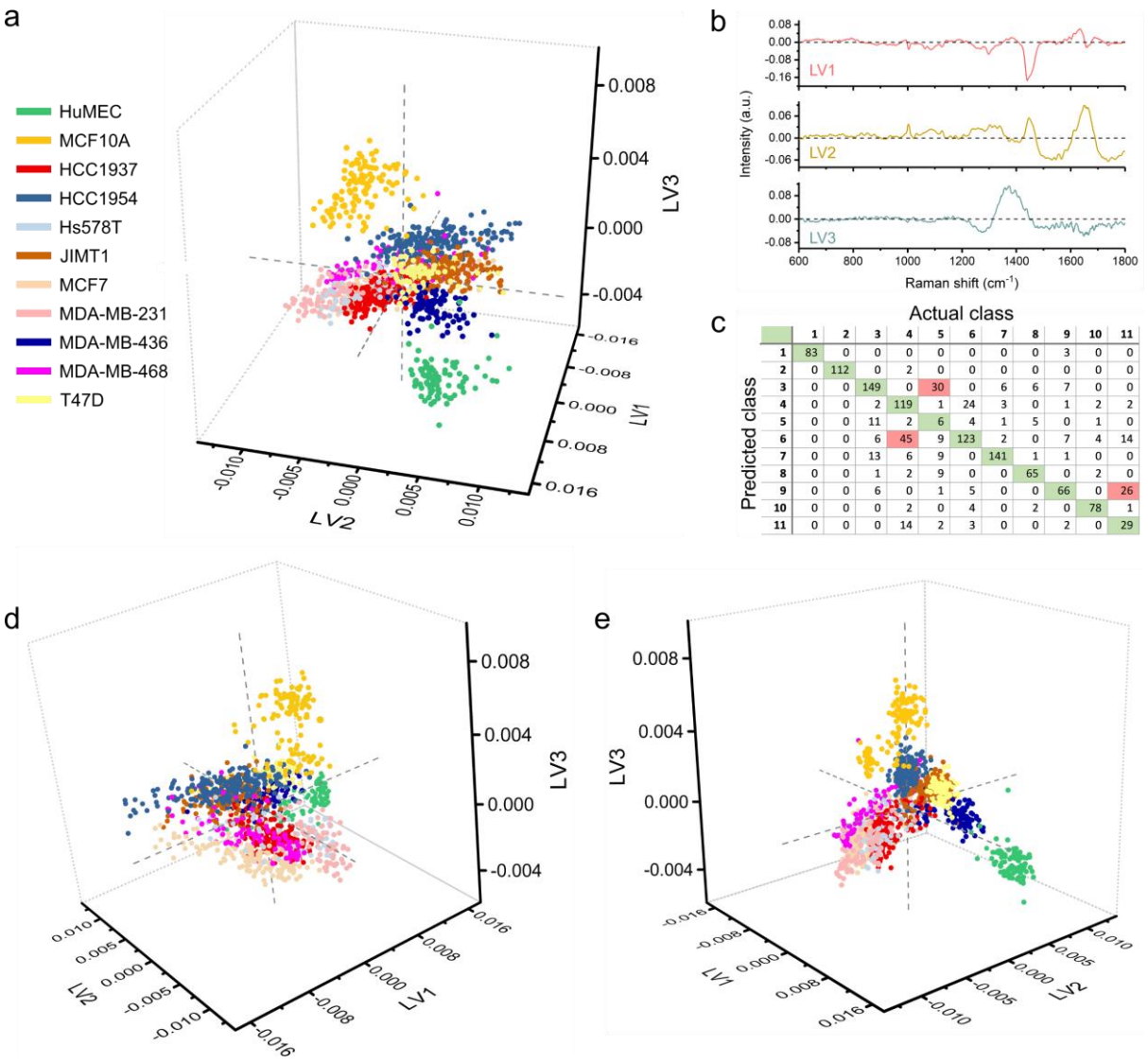

	1	2	3	4	5	6	7	8	9	10	11
1	83	0	0	0	0	0	0	0	3	0	0
2	0	112	0	2	0	0	0	0	0	0	0
3	0	0	149	0	30	0	6	6	7	0	0
4	0	0	2	119	1	24	3	0	1	2	2
5	0	0	11	2	6	4	1	5	0	1	0
6	0	0	6	45	9	123	2	0	7	4	14
7	0	0	13	6	9	0	141	1	1	0	0
8	0	0	1	2	9	0	0	65	0	2	0
9	0	0	6	0	1	5	0	0	66	0	26
10	0	0	0	2	0	4	0	2	0	78	1
11	0	0	0	14	2	3	0	0	2	0	29

Figure 3.9 | PLSDA modelling of an 11-EV panel. (a) PLSDA score plot for a panel of 11 EVs for LV1 against LV2 and LV3. HuMEC (n = 88), MCF10A (n = 113), HCC1937 (n = 188), HCC1954 (n = 196), Hs578T (n = 69), JIMT1 (n = 163), MCF7 (n = 154), MDA-MB-231 (n = 79), MDA-MB-436 (n = 87), MDA-MB-468 (n = 88) and T47D (n = 72), (n = 1297 total, 1283 included in the model, outliers excluded based on Q residuals and Hotelling T^2). (b) LV pseudo-spectra of the PLSDA model (LV1 39%, LV2 29%, LV3 8% variance captured). (c) PLSDA model cross-validated confusion matrix for a 5 LV PLSDA model showing actual *versus* model predicted classes, correct predictions along the diagonal shown in green with substantial miss classifiers indicated in red. (d-e) Different projections of the PLSDA score plot of (a).

For clarity and further visual assessment of the PLSDA classification model, additional projections of the model are shown in Figure 3.9.d-e. An interesting comparison can be made between the EVs of the three triple negative MDA-MB cell lines: MDA-MB-231 (pink), MDA-MB-436 (dark blue) and MDA-MB-468 (magenta). The scoring of the respective clusters is summed up being positive (+) negative (-) or neutral (+/-) overall in Table 3.3. Comparing these scores to the LV pseudo spectra, as shown in Figure 3.9.b and the DRA's shown in Figure 3.8.b-c. reveals the compositional differences between the EVs overall derived from these cell lines.

Table 3.3 | MDA-MB cell line derived EVs PLSDA LV scoring

Parental cell line	LV1	LV2
MDA-MB-231	+/-	-
MDA-MB-436	+	+
MDA-MB-468	-	-

The pseudo-spectrum of LV1 reflects mostly a strong negative peak around 1450 cm^{-1}, indicating a lower lipid content for clusters scoring positive on LV1, such as MDA-MB-436, and conversely a higher lipid content for clusters scoring negative on LV1, such as MDA-MB-468. This would order the MDA-MB EV classes in order of descending lipid content as MDA-MB-468 > MDA-MB-231 > MDA-MB-436. Looking at LV2, mainly containing protein-related peaks around 1000 cm^{-1} (phenylalanine, 1004 cm^{-1}) and a broad Amide-III band around 1600 cm^{-1}, this indicates a higher protein content for the MDA-MB-436 EVs, as was seen previously for the 3-EV panel in Figure 3.6.

Overall, the modelling of the 11-EV panel reveals accurate classification between most cancerous EV subclasses, with the overlap largely explained by EVs being of very similar origin. In addition, the high sensitivity and specificity achieved between cancerous and non-cancerous EVs is encouraging for the future diagnostic potential of the method.

3.4 Conclusions

An upgraded, dedicated SPARTA 2.0 system was developed, expanding on the original system as described in Chapter 2 with six key improvements. These improvements included a 15-30 times increase in signal intensity, extension of the spectral acquisition range and increase of the confocality of the system. This resulted in a smaller, more specific volume of Raman spectral acquisition. In addition, the laser stability was improved by decoupling of the trap disablement from the laser output, by introducing an automated in-line shutter. The laser flexibility was enhanced by the capability to easily tune the output power. Finally, the overall system stability was significantly improved, by reserving the 2.0 system only for SPARTA measurements. These improvements, while advantageous for all types of aforementioned nanoparticle analysis, were primarily conducted to enable comprehensive compositional analysis of EVs. Due to their complex makeup of proteins, lipids and nucleic acids, the obtained SPARTA 2.0 system enhancements were of key importance to enable their accurate analysis.

The in-depth compositional analysis of Raman spectra obtained from MDA-MB-436 cell line derived EVs revealed the presence of many constituents, such as (lipo)proteins, glycans, lipids and nucleic acids.

Of major interest was the comparison of these compositional Raman signatures between EVs derived from healthy or cancerous cell lines. A panel of 11 breast cell lines (and their EVs) was constructed consisting of a mix between healthy (primary and immortalised) and cancerous (ER+, HER2+, Triple negative) origin. A preliminary study of 3 exemplary EVs revealed the capability to distinguish between EVs from healthy *vs*. cancerous origin and between two cancerous subtypes with a high degree of specificity and sensitivity. Similar results were obtained by analysis of the Raman spectra obtained through imaging of the parental cell lines. Comparison between the cell and EV Raman spectra revealed the increased lipid content for cancerous EVs (and cells) to be the main classifier.

Analysis of the full 11-EV panel was enabled by employing a novel visualisation approach, representing the Raman spectra as heat maps, dubbed dimensional reduction arrays (DRA's). DRA's facilitated the direct visual inspection and comparison between spectra. This was combined with multivariate statistical modelling, revealing excellent separation between EVs from cancerous and non-cancerous origin with sensitivities and specificities close to 100%. Overlap, thus compositional similarity, between the EVs of certain cancer cell lines were attributed to the similarity of their cellular origin and receptor status subtype. Overall, the lipid content difference between the EVs from cancerous and non-cancerous origin was revealed as the major source of compositional difference.

In addition, more subtle differences in protein content, based on the Raman signatures of phenylalanine and amide bonds, contributed to the differentiation between EVs of various cancerous origin.

Several limitations to the SPARTA 2.0 system should be noted, as indicated in section 2.3.7, some fundamental restrictions apply to the samples to be analysed with SPARTA in general. For instance, a too high turbidity of the sample would break up the trap and an optimal particle concentration has to be found where efficient trapping is achieved, but signal from particles in too close proximity to each other is minimised. From the perspective of EV analysis as cancer biomarkers, the throughput is reduced due to the need for longer acquisitions per particle, to be able to capture the more subtle differences between complex particles, as compared to more straightforward analysis of synthetic particles. The impact of these limitations will be mitigated with future improvement strategies, based on optimisation of the sample interfacing and the trade-off between throughput and spectral information required.

As demonstrated, the improved SPARTA 2.0 system can be a powerful tool for the automated, label-free single particle-based analysis of EVs and has the potential to be further developed into an approach for minimally invasive disease detection, as explored here for breast cancer.

Chapter 4

Electron Microscopical Methods for the Analysis of Extracellular Vesicles uptake in Cancer Cells

'These new particles are poised to become

the 'atoms' and 'molecules' of tomorrows materials

if they can be successfully assembled into useful structures'

Sharon C. Glotzer, Michael J. Solomon

Anisotropy of building blocks and their assembly into complex structures

Nature Materials, Vol 6, 2007

4 Electron Microscopical Methods for the Analysis of Extracellular Vesicles Uptake in Cancer Cells

Parts of this chapter were prepared in a publication submitted by U. Kauscher*, J. Penders* *et al*. with as title: Gold Nanocluster Extracellular Vesicle Supraparticles: Self-Assembled Nanostructures for 3D Uptake Visualisation. **co-first authors*

4.1 Introduction

4.1.1 Aims

Extracellular vesicles (EVs) are secreted by the vast majority of cells and are being intensively studied due to their emerging involvement in a variety of cellular communication processes. However, the study of their cellular uptake and fate has been hampered by difficulty in imaging EVs against the cellular background. In this chapter the transition is made from the analysis of particles in and off themselves, as with SPARTA, to the detailed study of their interaction with cells. Here, the combination of EVs with hydrophobic gold nanoclusters (AuNC) is explored, which can self-assemble into supraparticles, dubbed AuNC EV supraparticles. These particles offer an excellent labelling strategy for high resolution electron microscopic imaging *in vitro.* The self-assembly process of hydrophobic gold nanoclusters (AuNCs) and EVs into supraparticles is visualised via cryo-TEM imaging, as well as through characterisation of the components via size analysis (DLS, NTA and TEM imaging), UV-Vis spectroscopy and protein quantification assays. The cell compatibility is demonstrated by supraparticle toxicity assays prior to tracking the re-uptake of the supraparticles into breast cancer cells in detail. Using Focused Ion Beam – Scanning Electron Microscopy (FIB-SEM), detailed 3D reconstructions of cells were created for the direct visualisation of the intracellular uptake and distribution of the self-assembled biomaterial. The presence of gold within the uptaken EVs and in lysosomes, was confirmed *in situ* via lift-out and DF-STEM EDX analysis. This is the first study on the formation of these highly complex self-assembled AuNC EV supraparticles and the first in depth study and 3D visualisation of EV uptake into cells via FIB-SEM. The self-assembled AuNC EV supraparticles demonstrate a way to bring together the best of two worlds: the biocompatibility of EVs and the versatility of metal nanoparticles. The demonstrated formation of AuNC EV supraparticles will facilitate future applications in EV imaging as well as EV-assisted cellular delivery of AuNCs.

4.1.2 AuNPs and AuNC supraparticles

Gold nanoparticles (AuNPs) have been extensively used as a tool in nanotechnology and are arguably one of the most ubiquitous, due to their excellent optical and electrical properties and facile surface modification, most commonly through thiol based chemistry[208,209]. In contrast, gold nanoclusters (AuNCs) have only recently emerged as a distinct novel material with extremely promising properties[210]. AuNCs, sometimes referred to as gold nanodots or simply, but somewhat confusingly, as small gold nanoparticles, are particles that contain so few atoms (typically less than 200-300) that it causes quantum confinement effects on the electrons present[211]. This leads to discrete energy levels emerging, as opposed to a continuous energy band in larger particles or bulk materials. As a result AuNCs exhibit unique photochemical characteristics, since they occupy the space between molecules and nanoparticles[210]. The atomic packing, electronic structure, magnetism, electrochemical and charge transport properties of AuNCs differ vastly from those of larger gold nanoparticles. AuNCs are a powerful tool in diagnostic applications. In addition to being traceable using a variety of imaging modes, they also have therapeutic potential due to their photothermal properties[212,213].

Analogous to how molecules can be (self-)assembled into larger structures in the field of supramolecular chemistry, so can AuNCs self-assemble into larger defined structures, which are termed supraparticles. The seminal paper by Glotzer and Solomon[214] describes the fundamental ideas behind tuning the inter particle interactions as well as particle sizes and shapes (anisotropy specifically), to allow the creation of hierarchical, structural assemblies of nanoparticles under carefully controlled conditions. The main goal here is to achieve mesoscale structures while retaining the unique properties of the nanocluster or nanoparticle dimensions, afforded by the building blocks[215]. There is a clear distinction between agglomerates and aggregates to supraparticles. The former two are a random, and in the case of aggregates, irreversible collection of nanoparticles, whereas supraparticles exhibit an ordered structure arising from the complex interplay of inter-particle forces dependent on the formation conditions. As the nanocluster or nanoparticle building blocks pre-exist as colloidally stable entities, the key in the formation of supraparticles lies in overcoming the repulsive forces between the particles to allow assembly to occur. This is a delicate balance, as complete disruption of these forces would inevitably lead to uncontrolled aggregation.

There are several approaches to the formation of supraparticles, based usually either on confined formation or bulk formation[215,216]. In confined formation methods, the nano building blocks are templated into supraparticles by confining them into droplets of liquid-liquid emulsions. Evaporation or otherwise depletion of the disperse phase will force the particles closer together which may lead to the formation of supraparticles[217].

In bulk formation methods the electrostatic repulsion can be tuned to induce supraparticle formation by changing the pH or ion concentrations or by addition of a mutually attractive species, such as amphiphiles or surfactants[218,219]. When the conditions are very well controlled, the bulk formation approach gives self-limited self-assembly behaviour due to a thermodynamic equilibrium being reached where the repulsive forces between the supraparticles and the nanoparticle or nanocluster precursors equal the attractive forces[220]. This results in greater control over the size dispersity compared to confined formation using templating methods, as those exhibit kinetic rather than thermodynamic control[221]. While in a kintically controlled approach the state with the lowest energy barrier is reached, under thermodynamic control the most stable state is reached, thus limiting the size dispersity.

The advances on several fronts of supraparticle formation, both in synthesis of building blocks, as in understanding of formation mechanisms[215,216] has given rise to recent applications in medicine and biology. Examples of these are the use of iron-oxide based supraparticles for theranostic applications, enabling deep tissue imaging and photothermal treatment of cancer[222] and AuNC and AuNP assemblies for radiosensitisation and photothermal treatment through plasmonic effects[223,224].

4.1.3 AuNC synthesis

To synthesise AuNCs ranging from clusters of a few atoms to several hundreds, specific reaction conditions are required to prevent formation of larger AuNPs alongside the clusters. Most commonly, a gold (III) precursor salt, usually $HAuCl_4$, is reduced by a strong reducing agent, such as $NaBH_4$. This results in a single controlled spontaneous nucleation event, with slower and diffusion limited growth of the clusters to the desired size, while preventing any secondary nucleation. Apart from the ratio between the gold precursor and the reducing agent, the type and quantity of stabilising ligand present for the gold surface and cluster is critical. Well controlled synthesis methods for small AuNCs have been reported using phosphine ligands[225,226]. However phosphine ligand stabilised AuNCs have the critical drawback that these clusters decompose within several days. Using the well-established strong chemical interaction between thiols and gold, with alkyl- or aryl thiols as ligands[227,228], led to the formation of highly (long-term) stable AuNCs

For certain applications, such as in optics or catalysis[229,230] precise control over the number of gold atoms in the cluster is highly important, as a few atoms difference can cause clearly observable differences in their photochemical characteristics or electrical structure. These clusters are denoted Au_n where *n* is the number of gold atoms in the core, such as Au_{11} and Au_{39}.

While the separation of a disperse synthesised gold nanocluster mixture is certainly non-trivial[231,232], recent advances in synthesis methods allow, under very carefully chosen and controlled conditions, the near exclusive formation of certain cluster sizes. An example of such a method is a kinetically controlled two-phase approach. In the first phase the gold (III) precursor is reacted with the alkyl- or aryl thiols to form reduced intermediated Au(I):SR complexes, which are subsequently reacted to the Au(0) clusters by a strong reducing agent in the second phase, commonly $NaBH_4$[233], as schematically shown in Figure 4.1. It has been shown that precise control over the reaction temperature can also significantly increase the specificity of cluster size formation. The work by Zhu *et al.*[233] demonstrates that kinetic control, over the Au(I):SR intermediate aggregates sizes, due to a low reaction temperature (0 °C), critically impacts the final cluster sizes. It should be noted, that the exclusive formation of specific cluster sizes, despite recent advances, is still a capricious process. Many, in other reactions considered more circumstantial factors such as stirring speed, can cause disperse sizes of clusters to form instead.

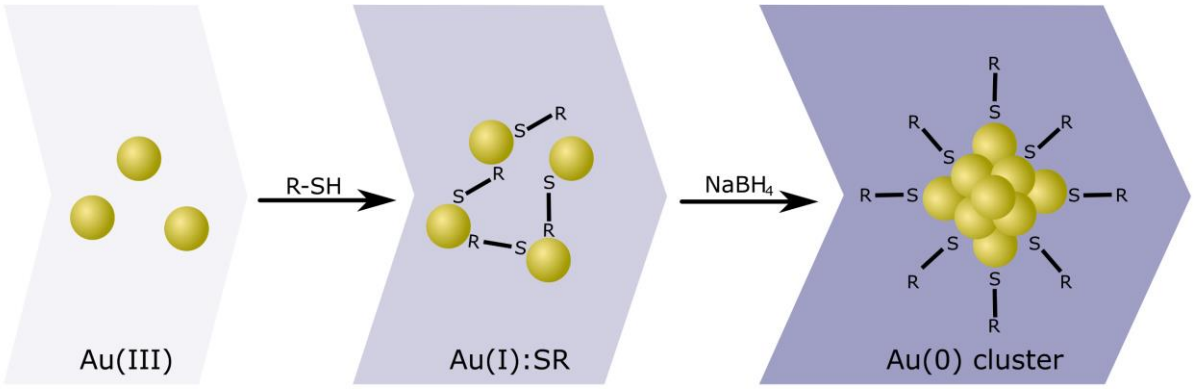

Figure 4.1. | Schematic representation of two-phase AuNC synthesis. Au(III) from a gold salt precursor (*e.g.* $HAuCl_4$) is reduced and forms a Au(I):SR complex upon addition of alkyl- or aryl thiols (R-SH). Upon addition of $NaBH_4$ the gold is reduced to Au(0) and forms a stable ligand capped cluster.

The size distribution of the synthesised gold nanoclusters can be assessed by conventional or high resolution (HR-) TEM imaging and analysis. In addition, the absence of a plasmon resonance peak is a hallmark of gold nanoclusters, which is typically reported and measured via UV-Vis spectroscopy[231,233].

4.1.4 AuNC and AuNPs for electron microscopy

Due to their high contrast to biological tissues, metal, and specifically gold nanoparticles, have been used extensively to track and label specific subcellular components or pathways in cells where aimed at imaging using electron microscopy techniques[208]. Particle sizes commonly used are between 5-50 nm[208,234], depending on the trafficking pathway of interest and the resolution of the specific imaging technique. In TEM these gold nanoparticles appear as black dots in the cells due to the inability of the electrons to transmit through the particles, thus creating dark areas on the fluorescent screen or camera images. In dark-field mode, such as in DF-STEM imaging, the contrast is inverted, and the gold nanoparticles appear as bright spots instead. In (FIB-)SEM imaging the contrast afforded by gold nanoparticles is usually best observed using a backscattered electron detector, as this will detect the increased elastically scattered electrons by the heavy gold atoms in the gold nanoparticles. This increased scattering is observed as an increase in signal and the gold nanoparticles therefore appear as bright spots in the backscattered electron images.

There are three main and distinct applications of AuNCs and AuNPs in EM imaging within tissues and the inter- and intra cellular environment:

1. The imaging of the AuNPs in and of themselves, to observe their uptake and trafficking dependent on their shape, size and composition, for example, as theranostic or cytotoxic agents.
2. The use of AuNPs to illuminate a change in trafficking response in tissues or cells, in the presence of specific surface chemistries or modifications.
3. The use of AuNPs or AuNCs to label inter- or intra cellular components for identification during imaging, such as immunogold approaches.

In the first instance, a variety of AuNPs have been studied for their cytotoxic[235,236], anti-bacterial[237,238] or theranostic capabilities[239,240] and their trafficking into cells has been visualised by TEM. These studies indicate the uptake and trafficking of AuNPs within cells through the endo-lysosomal system, which can be of use when investigating their pharmacokinetics.

The second use of AuNPs is the visualisation of trafficking pathways, here the surface of the gold nanoparticles can be modified with a target compound to observe a change in trafficking response to the surface modification, the AuNP core is thus used to provide a high contrast during imaging[208,241].

The third application is arguable the most versatile and widely applicable approach, where antibody conjugated AuNPs or AuNCs are used to bind to and identify specific cell surface or subcellular components in cells. This approach, usually called 'immunogold staining' was introduced by Faulk and Taylor in 1971[242] and has since seen widespread use as a labelling strategy against cellular antigens[243,244]. There are two methods for introducing the immunogold label into the cells, pre-embedding and post-embedding. The difference is based on whether the label is added before the heavy metal staining of the cells and embedding into resin (pre-embedding) or after thin sections are obtained via microtoming methods[245]. With post-embedding larger AuNPs, usually up to 30 nm can be used, while for pre-embedding significant surfactant based permeabilisation would be required in order to get the nanoparticles into the cells. Since the loading density and specificity for pre-embedding is significantly higher, AuNC immunogold strategies are developed where AuNCs usually less than 3 nm are coupled to the antibodies to minimize the need for permeabilisation, which can cause damage to the ultrastructure of the cells, hampering high resolution imaging[106,246].

4.1.5 Serial sectioning and 3D reconstruction

The visualisation of gold nanoparticles in cells is usually achieved after EM preparation (see section 1.4.3) using a combination of microtoming, to achieve ultra-thin sections (<100 nm thickness), and TEM imaging. While this method can give very high ultrastructural resolution in biological samples of around 2 nm[97], it will only give a 2D snapshot of a cell or tissue at a specific location. The imaging of a number of sequential sections is possible, but not practical for larger volumes and associated with a high risk for loss of intermediate sections due to physical limitations and aberrations introduced by microtoming embedded samples. For small (thin) subsections of cells or tissues TEM-tomography can be used to obtain a 3D image, where a sample section of around 300 nm can be rotated and imaged under various angles to compute a tomogram[247]. While this can be extended to sections up to 1 µm thick using Scanning Transmission Electron Microscopy (STEM) tomography[248], it still does not allow complete cell 3D imaging in high resolution.

Focused Ion Beam Scanning Electron Microscopy (FIB-SEM) is an alternative EM technique where an ion beam, most commonly gallium-based, is used to cut sections of a cell or tissue *in-situ* with a thickness down to about 5 nm. Subsequent SEM imaging of the newly exposed cross section, results in cellular imaging approaching TEM resolution (~5-10 nm)[101]. The sequential cutting and imaging, termed serial sectioning or 'slice-and-view', allows for the collection of an image stack that can be rendered into a 3D reconstruction of the cell or tissue section being imaged[95,102].

When the imaging resolution is matched to the slicing thickness, isotropic voxels are obtained, resulting in equal dimensions of the pixels in the imaging and slicing planes. This allows for digital re-slicing of the cell in any arbitrary direction without the loss of resolution. While this is physically possible, the sectioning and imaging time for larger volumes would be excessive and a lower z-resolution (in the slicing direction) is usually chosen to cut the processing time for a single cell down to several hours.

To obtain a 3D reconstruction of a FIB-SEM image stack, several processing steps are performed: automated and manual image registration, component segmentation and rendering. Dedicated software packages have been developed to assist with these steps and while some parts can be partly fulfilled by computer-based algorithms, there is still significant manual work involved. During registration, the images are aligned to each other to correct for drift during acquisition. This can be coarsely done by an algorithm (automated registration), while fine tuning of this alignment is done by hand afterwards (manual registration). For the segmentation, the contrast difference-based assignment of pixels to subcellular components, this is still superior when performed by eye, rather than using algorithms. However, recent advances using deep- and machine learning approaches are showing great future promise in this field[249,250]. A detailed description of a FIB-SEM workflow to achieve 3D cellular reconstructions will be provided in section 4.3.7.2.

4.1.6 EV uptake studies

After release of the EVs into the extracellular space, the EVs can interact with the surrounding cells to exert their physiological functions. EV uptake has been shown by various techniques, for example, by fluorescently labelling the EVs and studying their uptake into cells by confocal microscopy or flow cytometry of the cells[251]. In addition, EV mediated delivery of various RNA fragments and subsequent transcription has been observed, demonstrating uptake of the EV and its contents into the cell cytoplasm[32]. It has been shown in several studies that EVs from a certain cell line have preferential interaction with similar cells or specific target cells, depending on the expression of various targeting molecules or receptors on their membranes[28]. For example, dendritic cell derived vesicles with a high expression of MHC complex peptides show preferential uptake by T-cells[41,252].

Most methods so far being discussed in literature will call for EV functionalisation, for example, via the immobilisation of fluorescent molecules on their membrane surface. One needs to carefully evaluate how these surface functionalisations will affect the mechanism and quantity of uptake of the EVs[251]. In addition, these fluorescent tags can leach from the EVs into the membrane of the cells, confounding the measurement of uptake of the EVs.

Most studies also rely on quantification of the uptake by fluorescence microscopy, which cannot distinguish the individual EVs due to limitation in resolution and can thus only give an estimation of the EV uptake. However, accounting for these issues, various studies have shown a wide range of uptake mechanisms involved, depending on the protein composition of the EV and the recipient cells and the cellular environment[251]. As the proteomic analysis of EVs progresses, several proteins particularly enriched on the EV membranes have been identified, which also serve to mediate specific uptake pathways. Tetraspanins such as CD63, CD9 and CD81 and integrins, such as α_v and β_3, are abundantly present on the EV membrane[30], which mediate cell adhesion and membrane fusion. Blocking of these markers shows reduced EV uptake in the target cells[251]. In addition, the uptake of EVs has been directly visualised via labelling of the vesicles with 5 to 10 nm immunogold against exosomal markers and subsequent immune-electron microscopy (TEM) of ultra-thin cell sections sections[253]. Co-localisation of the gold nanoparticles with the EVs in the TEM micrograph can elucidate the presence of exosomes and their interactions with the cells[28]. This technique is however hampered by the delivery of the immunogold particles into the cells during staining and the specificity of the targets, leading to significant off-target or aspecific labelling[99,245].

The possible uptake pathways are direct fusion with the cell plasma membrane or endocytic pathways[251]. Clathrin-dependent endocytosis and clathrin-independent endocytic pathways as macro pinocytosis[253,254], phagocytosis[255], caveolin-mediated and lipid raft mediated uptake have been observed[256]. Direct fusion of the EV membrane with the recipient cell has been observed for exosomes from melanoma cells by confocal microscopy and mediated by an acidic pH[257]. This is potentially simulating the environment in endosomes and fusion of the EVs with the endosomal membrane has also been shown. However, most EV uptake studies suggest various endocytic pathways as the main uptake route, where the type of endocytic uptake observed varies for types of EVs and recipient cells[251,255]. It is speculated that the EV uptake may involve very specific routes for certain recipient cells or specific types of EVs, while for others it could be an aspecific uptake by various routes depending on cell conditions or environment[251]. The presence of certain receptors and targets on both the EV surface, and the recipient cell membrane have a key role in regulating the uptake of EVs. Specifically with regards to metastasis, integrins on cancer derived EVs were shown to direct EV uptake preferentially to certain sites *in vivo*[192].

This intricate interplay of EV-cell interaction and uptake heralds the need for novel strategies to study these phenomena. Alternative labelling and tracking approaches combined with high resolution and high content visualisation methods as presented here, are posed as an important building block towards understanding the complex EV-cell biology.

4.2 Materials and Methods

4.2.1 Cell culture and EV extraction

MDA-MB-231 breast cancer cells were obtained from the ATCC (Manassas, VA, USA) and maintained in DMEM supplemented with 10% (v/v) FBS, 20 mM HEPES and penicillin/streptomycin (all Gibco). To maximise production of EVs they were adapted to non-adherent culture to allow high-density growth. The cells were cultured at 37 °C and 5% CO_2 and their medium was changed every 2 days. To obtain EVs, cells were cultured to a concentration of approximately $1 \cdot 10^6$ cells/mL. Cells were pelleted *via* centrifugation at 300 rcf. The cells were resuspended in DMEM supplemented only with 20 mM HEPES and penicillin/streptomycin and incubated for 2 days. Afterwards, the conditioned medium was collected by centrifugation of cell suspensions at 1500 rcf for 5 minutes. The medium was then filtered over a bottle top filter with 0.45 µm pore size (VWR, UK) and concentrated, using ultrafiltration (Amicon Ultra-15, 100kDa). The concentrated medium was purified by size exclusion chromatography. 500 µL of the concentrated medium was loaded on a 30 cm long, 1 cm diameter column containing Sepharose CL-2B (Sigma Aldrich, UK). 1 mL fractions were collected, and the EV-containing fractions were determined *via* data correlation of a BCA assay (Thermo Fisher, UK) and NTA (Malvern, UK). EVs were snap frozen and stored at -80 °C until further use. The EV extraction and isolation performed using the methods optimised by Dr. Thomas E. Whittaker and some of the batches used were isolated by Dr. Anika Nagelkerke.

4.2.2 AuNC synthesis

All chemicals were obtained from Sigma Aldrich UK and of the highest purity unless otherwise stated. $HAuCl_4 \cdot 2H_2O$ (0.1576 g, 0.40 mmol) was dissolved in 5 mL Milli-Q water. TOAB (0.2558 g, 0.47 mmol) was dissolved in 10 mL toluene. Both solutions were combined in a 25 mL round bottom flask and stirred at 1100 rpm for 15 minutes. By this time the bottom phase became clear in colour due to the gold salt transferring into the toluene phase. The bottom phase was removed with a syringe. The toluene phase was cooled to 0 °C and purged with nitrogen for 30 minutes. Octanethiol (0.2 mL, 1.20 mmol) was added and stirring was reduced to 30 rpm. Reduction in stirring speed results in higher yield of smaller clusters[233]. The solutions turned yellow over a period of 5 minutes and turned clear after 1 hour.

Stirring speed was increased to 1100 rpm and freshly-prepared $NaBH_4$ solution was added immediately and all at once. To prepare the $NaBH_4$-solution, $NaBH_4$ (0.1550 g, 4 mmol) was added to 7 mL of ice cold Milli Q water. The reaction was stirred overnight under N_2-atmosphere at 0 °C. Afterwards the water phase was removed with a syringe and the reaction vessel was flushed with 5 mL of toluene to bring all AuNCs to the bottom of the vessel. The toluene phase was removed by vacuum distillation using a dry ice cooler under gentle stirring and using a heat gun to gently heat the mixture to aid distillation. After removal of the toluene the vessel was kept under vacuum for a further 10 minutes to dry. The AuNCs were resuspended in 20 mL of ethanol, filtered over cotton, and washed a further three times on cotton with ethanol. The clusters were removed from the cotton by flushing with toluene and further dried by vacuum distillation as above. The clusters were further dried overnight on vacuum and the clusters were analysed by TEM (JEM JEOL 2100F, FEI TITAN) for their size distribution. The AuNC synthesis was performed together with Dr. Ulrike Kauscher.

4.2.3 Supraparticle formation

Supraparticles containing EVs were synthesised using 500 µL of purified EVs in PBS in a glass vial. The concentration of EVs ranged from 7×10^{11} - 2×10^{12} particles per mL. 40 µL of a saponin stock solution (3.5 mg/mL) in Milli-Q water was added to the EV suspension. Afterwards, 40 µL of an AuNC solution (10 mg/mL) in THF was added. This mixture was then added to a commercially available size exclusion chromatography column (qEV, Izon Sciences Ltd.). 500 µL of the suspension was added to a qEV column and the entire grey band was collected from the column. Typically, the supraparticles would elute in fractions 7-8 when collecting 500 µL fractions. Supraparticles without EVs were synthesised using the same protocol, but instead using 500 µL of PBS rather than 500 µL EVs in PBS. The supraparticle formation process was developed by Dr. Ulrike Kauscher and part of the batches used were prepared by her.

4.2.4 Cell incubation with supraparticles and preparation for FIB-SEM

10 mm glass coverslips (VWR, UK) were sterilised by washing in 70% ethanol, washed twice in PBS and placed in a 24-well plate. Coverslips were pre-coated in full cell culture medium for 1 hour at 37 °C, 5% CO_2. MDA-MB-231 cells grown to 80% confluency in a T75 culture flask were harvested. Cells were seeded at 15000 cells/cm^2 and allowed to adhere overnight.

AuNC EV and EV-free supraparticles at 0.4 - 1 × 10^{11} p/mL were sterile-filtered using a 0.45 µm syringe filter. 120 µL was added to each well (PBS only for controls) containing 1 mL of complete medium. The cells and particles were incubated for 1, 2, 4 or 6 hours, respectively. The experiment was performed in duplicate, only a 6-hour time point was used for the controls without particles. At each time point, cultures were washed with PBS and fixed in 4% EM grade PFA (Electron Microscopy Sciences) for 15 minutes at 37 °C, 5% CO_2. After fixing, the slides were washed a further three times in PBS and kept overnight covered in PBS in the fridge.

For FIB-SEM preparation the samples were washed 2 × 5 minutes in 0.1 M of cacodylate buffer (Electron Microscopy Sciences, 0.2 M stock) in dH_2O. The samples were post fixed for 1 hour in 2.5% EM grade glutaraldehyde (Electron Microscopy Sciences, 16% stock) in 0.1 M of cacodylate buffer. After further washing for 2 × 5 minutes in 0.1 M cacodylate the samples were stained for 1 hour in 1% OsO_4 (Electron Microscopy Sciences, 4% stock) in 0.1 M of cacodylate and washed 2 × 5 minutes in dH_2O. Further staining was performed by 1 hour in 1% of Tannic acid (0.2 µm syringe filtered) and 2.5 hours in Uranyl Acetate (0.2 µm syringe filtered) in dH_2O with 2 × 5-minute washes in dH_2O in between. The samples were serially dehydrated using an ethanol/water gradient of 20, 30, 50 and 70% ethanol for 2 × 5 minutes each and kept on 70% ethanol overnight at room temperature.

The samples were further dehydrated by 2 × 5 minutes washes in 80 and 90% ethanol and 4 × 5 minutes in 100% ethanol. Next the samples were resin embedded by gradient infiltration of 2.5 hours each of 3:1, 2:1, 1:1 (v/v) ethanol and epoxy resin (Epoxy embedding medium kit, Sigma Aldrich UK) and 1:2 overnight, covered at room temperature. The next day, the resin infiltration was finalised by 2 × 2.5-hour incubation in full resin and removal of excess resin by rapid ethanol spraying and blotting on paper for minimal resin embedding. The coverslips were transferred to PDMS mats and cured for 72 hours in an oven at 60 °C. Prior to imaging the coverslips were mounted on standard SEM stubs using double sided carbon tape and sputter coated with 20 nm of chromium (Quorum Q150T S). The staining protocol used here was optimised by Dr. Sahana Gopal and published in Gopal *et al*.[95]

4.2.5 FIB-SEM imaging and 3D reconstruction

Cells were imaged using an Auriga Zeiss Crossbeam and a sample tilt of 54° with 36° image tilt correction and 5 mm working distance. Coarse FIB milling was performed at 2 nA:30 kV and fine milling for serial sectioning at 1 nA:30 kV. SEM images were taken at 1.6 kV accelerating voltage using a back scattered electron detector.

For 3D reconstruction serial images stacks were taken with 90 nm interval and automatically aligned using Fiji (ImageJ, StackReg plugin) and further manually aligned and segmented using Amira 5.3.2 (FEI).

4.2.6 TEM and cryo-TEM

Copper Grids (CF200-Cu, Electron Microscopy Sciences) and Holey Carbon Grids (HC200-Cu, Electron Microscopy Sciences) were plasma treated (15 s, O_2/H_2) on a Gatan Solaris Plasma Cleaner. Samples for TEM were prepared by adding 4 µL sample to the grid and incubation for 30 seconds after which excess solution was blotted off with filter paper and the sample was dried overnight. Samples for cryo-TEM were prepared with a Leica EM GP automatic plunge freezer. 4 µL of sample was added onto a grid in an environmental chamber (relative humidity: 90%, temperature 20 °C). Excess suspension was blotted on filter paper and the obtained film was vitrified in liquid ethane. Samples were stored in liquid nitrogen until the day of use.

TEM Samples were imaged on a JEOL 2100F or JEOL 2100Plus using 200 kV while Cryo-TEM samples were imaged only on the JEOL 2100Plus using 200 kV using the Minimum Dose System. Cryo-TEM samples were imaged at -170 °C on a Gatan914 Cryo-holder for Cryo-TEM imaging. Micrographs were taken using the Gatan Orius SC1000 camera at a magnification of either 30k or 15k. Cryo-TEM imaging was performed by Dr. Ulrike Kauscher with assistance of Dr. Lucia Massi and Ms. Valeria Nele.

4.2.7 Lift-out preparation and STEM/EDX

Lamellae of MDA-MB-231 cells incubated with supraparticles prepared with or without EVs were prepared using FIB-SEM lift-out for further analysis by TEM/STEM and EDX using a Helios Nanolab 600 (FEI) system equipped with a micromanipulator (Omniprobe, Oxford Instruments plc, UK). The samples were imaged by SEM at 0.17nA:2 kV and lamellae were prepared using 30 kV FIB milling at various currents from 28 pA to 2.8 nA. A trench was milled in the cell until a region of interest was observed in SEM imaging. A second trench was milled behind the region of interest until a lamella of 1-1.5 µm thickness remained. Platinum was deposited using a gallium ion assisted gas injection system (GIS, 93-0.28nA) on top of the lamella to a thickness of 1-2 µm. The lamella was freed by further milling on either side, except the base and a micromanipulator needle was attached to a corner by further platinum deposition.

The base of the lamella was cut, the lamella gently lifted out using the micromanipulator and guided to a three-pronged lift-out grid (Omniprobe, EM sciences). The lamella was attached to one of the posts by platinum deposition and the needle cut loose. By FIB polishing down to 5 kV and 8 pA the lamella was thinned to electron transparency, 100-120 nm, using SEM imaging to ensure the region of interest was conserved within the lamella.

The lift-out grid was transferred to a JEOL 2100F 200 kV TEM where the lamella was observed and further imaged using STEM mode and a dark field detector at 15° sample tilt. EDX was performed in STEM mode using the INCA software (Oxford Instruments). Peaks were assigned using the Bruker X-ray energies table (Bruker, Berlin, Germany). For the verification of the presence of gold in the AuNC EV supraparticles the acquisition time was 30 seconds. To assess the presence of gold in lysosomes for the EV-free AuNC supraparticles sample an acquisition time of 60 seconds was used.

4.2.8 Histogram analysis

For equalisation and comparison of the lysosomal brightness in the backscattered electron SEM images, the images were cropped to the cell boundaries and imported into MATLAB (R2016B). A 1-hour AuNC EV supraparticle image was taken as reference and the histograms of the other images were matched using the built-in 'imhistmatch' function. The equalised images were imported back in Fiji (ImageJ) and cropped to the lysosomes, for 5 lysosomes per condition except for the 2-hour AuNC EV sample were 10 lysosomes were analysed due to the large observed variance. A histogram was calculated of the centre area of a lysosome at each time point and particle type and the means and standard deviations of the histograms plotted in Origin (Origin Pro 2017). Welch's corrected t-tests were performed in Origin between particle types for means comparison and a Welch's Anova with Games-Howell post hoc test in SPSS (SPSS 25, IBM) to compare means over time for the AuNC EVs, both taking into account unequal variance and unequal sample size.

4.2.9 NTA measurements

EV particle concentrations and size distribution were measured on a Nanosight NS300 (Malvern) equipped with a 532 nm laser and a sCMOS camera. Samples were diluted 1000 times in PBS to yield a concentration of 10^8-10^9 particles/mL. Three 30 second videos were recorded per sample, using NTA software V3.0 with camera level set to 15 and detection threshold set to 5.

4.2.10 BCA assay

A BCA protein quantification assay kit (Thermo Fisher UK) was used according to the manufacturer's instructions to quantify the amount of protein in each of the 26 sequential 1 mL elution fractions of the size exclusion chromatographic purification of MDA-MB-231 EVs. An 8-point BSA calibration curve was made between 0 - 2 mg/mL and measured in duplicate and used to quantify the amount of protein in the sample fractions (mean of n = 2) upon read out of the assay absorbance at 562 nm using a UV-Vis plate reader (SpectraMax M5, Molecular Devices).

4.2.11 CCK8 assay

To test potential cytotoxicity of the EVs or supraparticles a CCK-8 (Sigma Aldrich, UK) cell viability assay was performed. MDA-MB-231 cells were cultured to 80% confluency in a T75 culture flask, trypsinised and seeded at 10,000 cells/well in a 96-well tissue culture plate and incubated overnight. A stock of MDA-MB-231 EVs at 7×10^{11} particles/mL was used to prepare AuNC EV supraparticles and AuNC supraparticles. The particles were sterile-filtered using a 0.45 µm Millex PVDF mini syringe filter and premixed with complete media (around 3.5×10^{11} particles/mL due to qEV column dilution, corrected for native EVs), equivalent to the FIB-SEM assays. The particles were further diluted 2 and 10-fold to assess potential differences in cytotoxicity. Cells with complete media and cells in complete media with an equivalent of PBS were used as controls. The cells were incubated for 6 hours, washed once in PBS and incubated for a further three days before assessing viability using the CCK-8 assay. 10 µL of substrate in 190 µL of complete media was added to each well (premixed for all wells), including wells with a CCK-8 background control (no cells). The endpoint absorbance was read using a UV-VIS plate reader (SpectraMax M5, Molecular Devices) at 450 nm after 3-hour incubation. The assay was performed with three technical and biological replicates.

4.2.12 Dot blots

A stock of MDA-MB-231 EVs of 7×10^{11} particles/mL was used to prepare AuNC EV supraparticles as described above and EV samples from the same batch were used as a control, diluted 2× in PBS to match the dilution from the qEV column used to purify the AuNC EV supraparticles. AuNC supraparticles were prepared in a similar way using PBS instead of the EV stock. A nitrocellulose membrane (0.45 µm, Bio-Rad) was soaked in 1× TBS (tris-buffered saline, 20× stock diluted in Milli Q water, Bio-Rad) for 10 minutes.

The BioDot apparatus (Bio-Rad) was assembled according to the manufacturer's instructions and 200 µL was loaded per sample and per antibody target in triplicate, adding TBS to the remaining empty wells. The wells were allowed to drain for 1-2 hours after which the wells were washed 3× with TBS and drained by vacuum. The membrane was retrieved from the apparatus, marked with pencil and cut into strips pertaining to each antibody target. The membranes were blocked in a 5% skimmed milk in TBS-T (1× TBS with 0.1% of Tween 20) solution for 1 hour at RT. After blocking, the membranes were washed 3 times in TBS-T for 10 minutes at RT and incubated overnight at 4 °C while shaken with the respective primary antibody. The primary antibodies used were anti-CD63 (Invitrogen, 10628D), anti-CD81 (Invitrogen, 10630D) and anti-CD9 (Invitrogen, 10626D), respectively, diluted 1:1000 in 5% BSA (w/v) in TBS-T. The next day, the membranes were washed 3× in TBS-T for 10 minutes at RT and incubated for 1 hour at RT with the secondary antibody (IRDye® 800CW Donkey anti-Mouse IgG, Li-Cor) 1:10000 in 5% (w/v) BSA in TBS-T. The membranes were finally washed 3 times in TBS-T for 10 minutes at RT before imaging using the Li-Cor imaging system. The dot blots were performed with assistance of Dr. Colleen Loynachan.

.

4.3 Results and Discussion

4.3.1 Overview of the AuNC EV supraparticle formation process

The AuNC EV supraparticle formation process can be depicted in three phases, as shown schematically in Figure 4.2. The first phase consists of the formation and isolation of the core building blocks, the AuNCs and the EVs. The AuNC synthesis concerns the formation of hydrophobic nanoclusters between 1 and 3 nm in diameter. The EVs are produced by MDA-MB-231 breast cancer cells in a high-density culture and isolated and purified by a combination of ultrafiltration and size exclusion chromatography processes. After obtaining the building blocks, a small amount of AuNCs are dissolved in THF and spiked under quick agitation into the EV solution containing saponin, a mild plant-derived surfactant that can transiently permeabilise the EV membrane[72,258]. A resulting homogeneous grey solution signifies supramolecular self-assembly of the AuNCs and the EVs in to AuNC EV supraparticles. The third phase concerns a purification step via size exclusion chromatography to make sure no unbound AuNCs are present in the solution. The steps involved in the phases shown will be discussed in greater detail in the sections below.

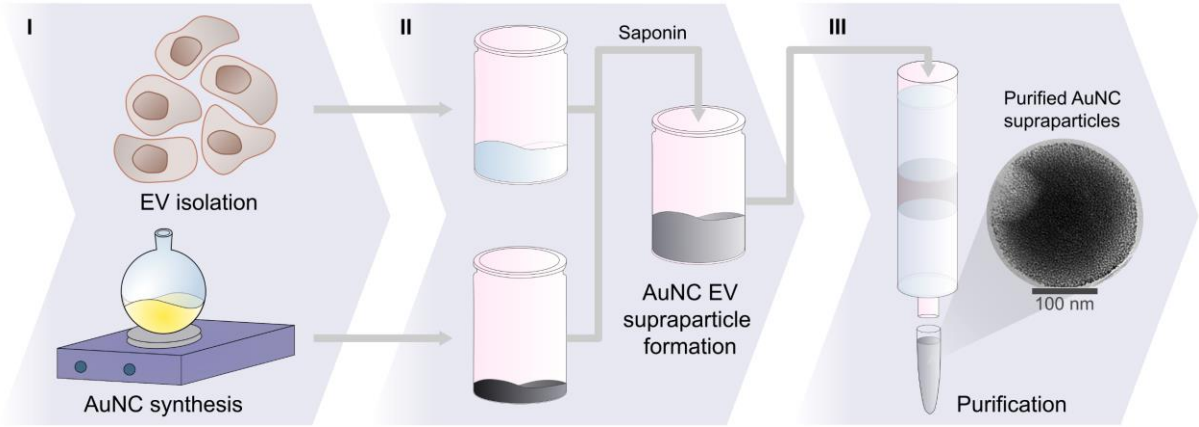

Figure 4.2 | Formation process of AuNC EV supraparticles. Hydrophobic alkyl-capped AuNCs around 2 nm in diameter and synthesised and combined with MDA-MB-231 breast cancer cell derived EVs (I) in a saponin assisted self-assembly processes (II), and purified using size exclusion chromatography (III) to obtained AuNC EV supraparticles.

4.3.2 Gold nanoclusters synthesis and characterisation

AuNCs were synthesised *via* the adaptation of a kinetically controlled two-phase method by Zhu *et al.* at around 4 °C [233]. In short, Gold(III) salts were reduced *via* addition of an octanethiol to an intermediate Au(I)-SR-complex and further reduced to Au(0) by the strong reducing agent $NaBH_4$. The particles were analysed *via* UV-Vis-spectroscopy and TEM as seen in Figure 4.3.a-c. The spectra obtained *via* UV-Vis spectroscopy do not show any distinctive plasmon resonance signals, indicating that the particles are small AuNCs predominantly less than 3 nm in size. Further analysis of the particles was carried out *via* Transmission Electron Microscopy (TEM). Small spherical particles were observed with a size of 1.7 nm ± 0.5 nm (mean ± s.d.).

4.3.3 Extracellular vesicles isolation and characterisation

EVs were isolated from an adenocarcinoma breast epithelial cell line (MDA-MB-231), chosen for its capability for high density culture and resulting high EV production. Cells were cultured for 48 hours in serum-free conditions to prevent contamination with serum vesicles. The conditioned media was harvested from the cells and then concentrated *via* spin-filtration and purified *via* SEC. The obtained vesicles were analysed with BCA protein quantification assays, NTA and cryo-TEM (Figure 4.3.d-f). The BCA quantification assay was carried out on each 1mL fraction of the 24 mL of eluent after SEC (Figure 4.3.e). The column trace shows a smaller peak for fraction 6-12 and a larger one for 16-24. The EVs are eluted in the fractions 6-12 and the signal is due to EV proteins, while the larger signal at fraction 16-24 originates from soluble extracellular proteins not associated with EVs. Cryo-TEM images of fractions 6-12 show spherical particles with a membrane thickness of 5 nm and a diameter in the range from 30 to 500 nm (Figure 4.3.f). The size range is confirmed by the NTA measurements (Figure 4.3.d). The large polydispersity is characteristic for EVs, as they consist of a heterogenic population of exosomes (approximately 30-100 nm) and microvesicles (up to 1000 nm). Due to overlap of size and marker proteins, separation of the two populations is not readily achievable.

4.3.4 AuNC EV supraparticle formation and analysis

AuNC EV Supraparticles were prepared and analysed as a new self-assembled hybrid between an inorganic material (AuNCs) and a natural building block (EVs) *via* a saponin-assisted encapsulation procedure (Figure 4.2).

Saponin is a plant-derived amphiphilic glycoside that self assembles with cholesterol in bilayer membranes and can permeabilise membrane bilayers. Saponin has previously been used to permeabilise EVs for loading of small molecules in drug delivery applications[258]. The use of saponin is advantageous over other methods, such as electroporation as it does not alter size distribution or zeta-potential.

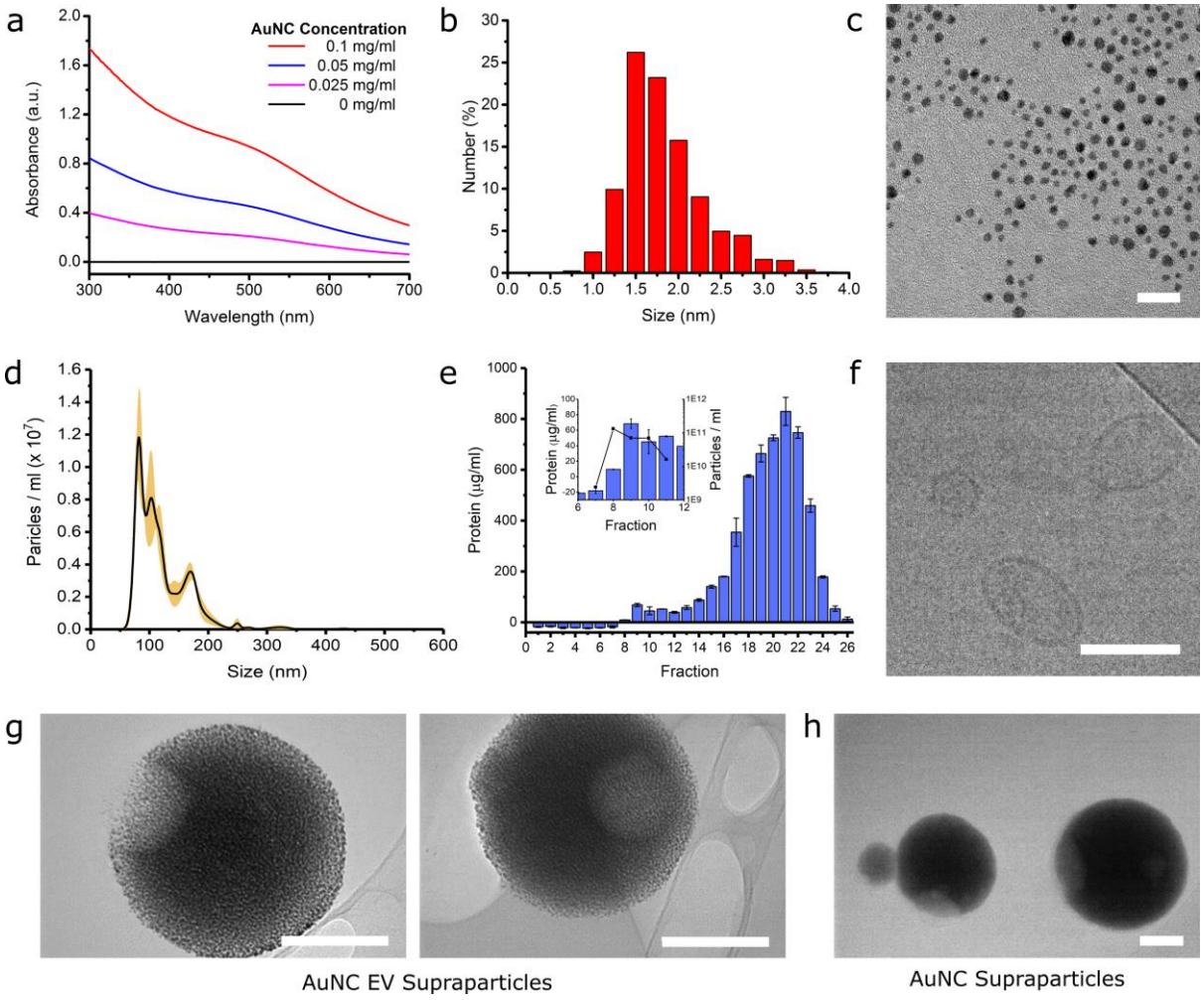

Figure 4.3 | Characterisation of AuNCs, EVs and supraparticles. (a) UV-Vis spectroscopy of [AuNC] = 0.0 - 0.1 mg/mL in $CHCl_3$. (b) Size distribution histogram based on TEM imaging, 1.7 nm ± 0.5 nm (mean ± s.d. n = 805). (c) TEM representative micrograph of AuNCs, scale bar 10 nm. (d) NTA analysis of native MDA-MB-231 EVs (mean ± s.e.) 1000 times dilution in PBS, n = 3, (e) BCA protein quantification of size exclusion chromatography fractions and NTA particle analysis of EV-fractions, n = 2, (f-h) Cryo-TEM representative micrographs of (f) native EVs (g) AuNC EV supraparticles, (h) AuNC supraparticles, scale bars 100 nm. *Cryo-TEM imaging performed by Dr. Ulrike Kauscher.*

Here, addition of saponin and AuNCs to a solution of EVs resulted in supraparticles - large self-assembled entities consisting of small particles and EVs in the size regime of the parent EVs. The challenge of creating supraparticles lies in overcoming the repulsive forces between the nanoparticles, which has been previously achieved by diverse methods[215]. Surfactant-based procedures are commonly-used to form supraparticles in aqueous environments, and the surfactant concentration and type can even be used to affect the supraparticle structure[259]. While surfactants have previously been used to form supraparticles with AuNCs, this is the first time saponin has been used for this task.

After the assembly process, AuNC EV supraparticles were purified using a SEC column. The purification can be observed by the naked eye as the supraparticles run down the column as a grey band (Figure 4.4.a). The fractions containing self-assembled supraparticles, identified by their characteristic colour, were collected. After addition of 500 µL sample solution to the column, roughly 1 mL of eluate was collected, resulting in an approximate two-fold dilution.

Supraparticles can also be formed without EVs, by self-assembly of the AuNCs in the presence of saponin. The so formed EV-free AuNC supraparticles are employed as a control system to monitor the difference in supraparticle-cell interaction behaviour with and without the EV building block. However, these AuNC supraparticles proved to be quite unstable and successful formation was not always readily achieved. A homogenous grey liquid evidences successful supraparticle formation (Figure 4.4.b).

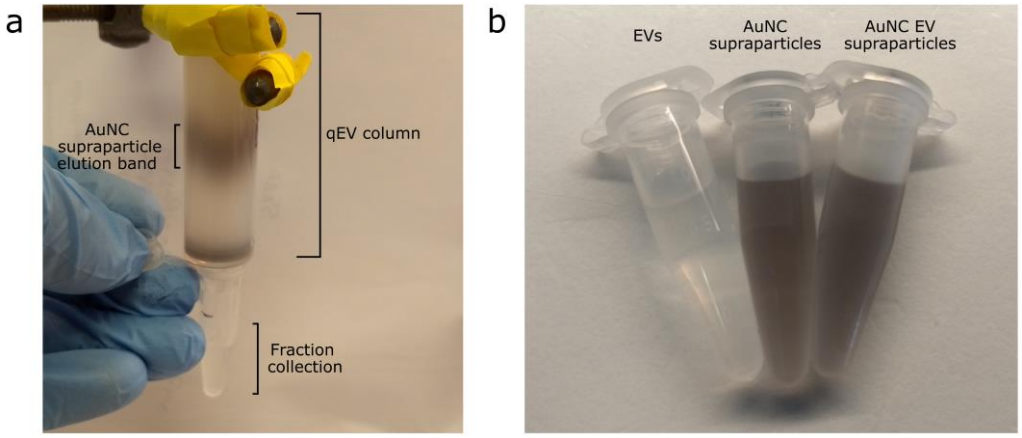

Figure 4.4 | AuNC supraparticle and AuNC EV supraparticle formation. (a) qEV column purification of the supraparticles gives a clear grey band running down the column, collected in fraction 7-8 (500 µL fractions). (b) Native EV solution, AuNC supraparticles and AuNC EV supraparticles after purification.

Occasionally the supraparticles precipitate after the formation process or during column purification, resulting in particle aggregates visible to the naked eye. The lesser stability against aggregation is hypothesised to be due to the type of amphiphiles present (saponin only *vs.* a mixture of phospholipids and other bilayer forming amphiphiles) and the higher ratio of hydrophobic particles to amphiphiles.

The self-assembled structures were visualised by cryo-TEM, a technique that allows EM imaging in vitrified ice. This is beneficial compared to conventional TEM as the samples are not dried and self-assembled structures can therefore be visualised in their native hydration state. The images revealed the presence of spherical structures that visibly consist of small 1-3 nm AuNCs for both types of self-assembled supraparticles, with and without EVs (Figure 4.3.g-h).

Both types of supraparticles were analysed *via* Dot Blot, Cryo-TEM and FIB-SEM after cell uptake. Dot Blots were performed to confirm that the EV AuNC particles still contained EV proteins after AuNC labelling and purification. The expression of CD63, CD81 and CD9, well-established EV markers [28,45], was assessed and found to be abundant in native EVs, with preservation of some of the signal for AuNC EV supraparticles, while no signal was seen for the EV-free supraparticles control (Figure 4.5).

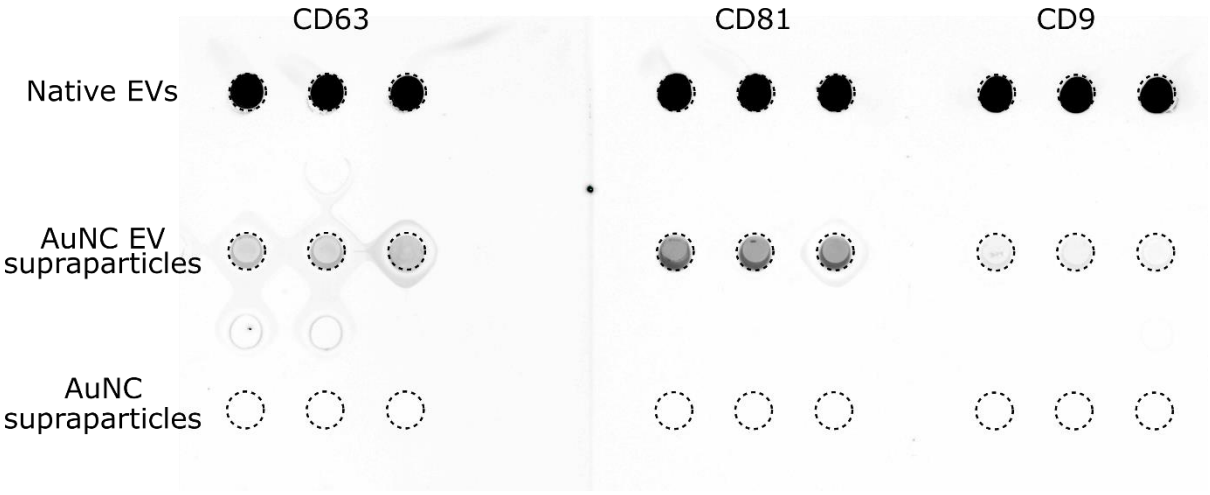

Figure 4.5 | Dot blot EV marker screening. Native EVs, AuNC EV supraparticles and AuNC supraparticles (top to bottom) were screened using dot blots against the presence of known EV makers CD63, CD81 and CD9 (left to right). Signal is absent in AuNC supraparticles while a moderate signal is observed in the AuNC EV supraparticles, with a strong signal in native EVs. (n = 3). *The dot blots were performed with assistance of Dr. Colleen Loynachan.*

Intriguingly, both supraparticle assemblies showed a smaller spherical area within them that was free of AuNCs (Figure 4.3). To make sure that this area was not just remaining THF solvent from the stock solution of AuNCs, the formed supraparticle solutions were incubated in a drying oven over a period of 1 hour to evaporate remaining solvent. However, the inner empty sphere remained and was not different to that of the supraparticles formed without this drying process (Figure 4.6.a). An alternative drying process was also tested by adding the supraparticle solutions into a rotation evaporator at a pressure of 20 mbar for 30 minutes, but the Cryo-TEM images showed again this characteristic spherical area (Figure 4.6.b).

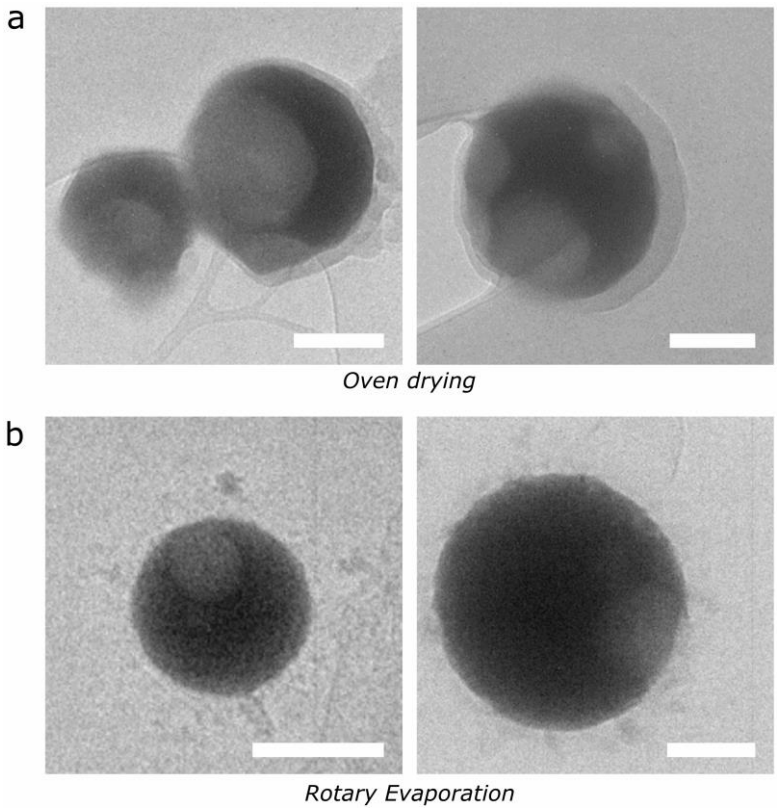

Figure 4.6 | Oven and rotary evaporation drying of AuNC EV supraparticles. Cryo-TEM micrographs of AuNC EV supraparticles (a) after drying in oven at 60 °C for 1 hour, (b) after rotary evaporation at 20 mbar for 30 minutes. Scale bars 100 nm. *Cryo-TEM imaging performed by Dr. Ulrike Kauscher.*

4.3.5 Overview of cell uptake, preparation and analysis

AuNC based supraparticles are a powerful tool for *in vitro* detection as they are easily visualised with electron microscopy, and thus, provide a handle to track the uptake process over time within cells. MDA-MB-231 cells were incubated with purified and *via* filtration sterilised AuNC EV supraparticles and AuNC supraparticles and their uptake was analysed. An overview of this process is shown in Figure 4.7. In the first phase the cells were incubated with media supplemented with the AuNC EV supraparticles or AuNC supraparticles for 1, 2, 4 or 6 hours and fixed at their respective end time point using EM-grade paraformaldehyde (PFA). The second phase concerns the processing of the cells to prepare them for FIB-SEM imaging. A secondary fixation step with glutaraldehyde ensured full stability and cross-linking of the subcellular components after which a combination of heavy metal stains was used to provide contrast during EM imaging. The cells were first incubated with osmium tetroxide (OsO_4), a highly reactive compound, reacting in an oxidative manner with lipids and proteins primarily in the cell membranes forming osmium complexes which provide membrane contrast during EM imaging.

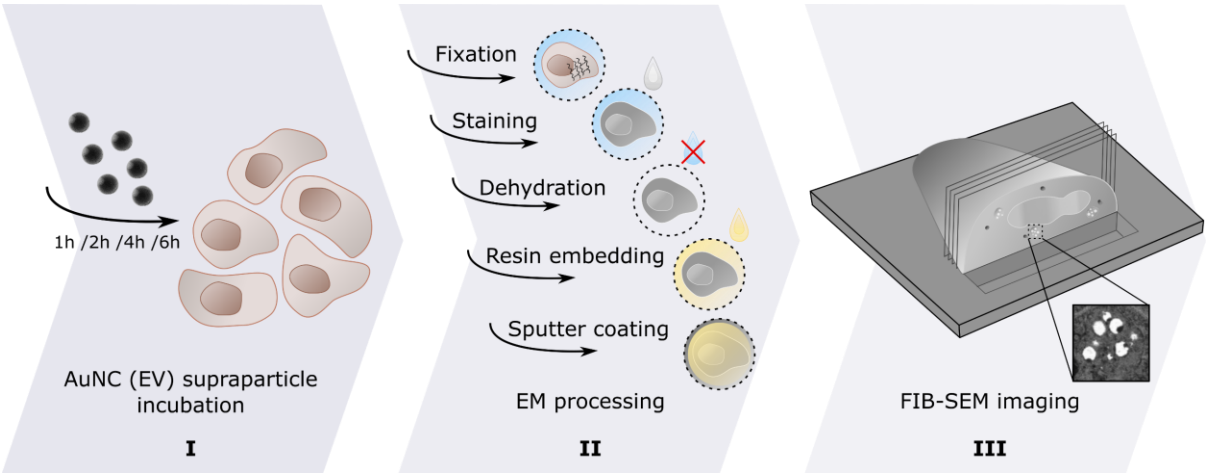

Figure 4.7 | Process of cellular uptake study of AuNC (EV) supraparticles. AuNC EV and AuNC supraparticles were incubated with MDA-MB-231 breast cancer cells for 1, 2, 4 and 6 hours (I). To process the cells for EM imaging the cells were fixed, stained, dehydrated, resin embedded, and sputter coated (III). FIB-SEM imaging was performed by cutting a trench and revealing the inner structure of the cell, following serial sectioning and imaging to obtain 3D image stacks.

Next, an incubation with tannic acid was performed, which acts as a mordant to improve binding of the next heavy metal stain, uranyl acetate, acting in a complementary manner and enhancing the nuclear staining primarily as well as subcellular membranes. The cells were then dehydrated to ensure compatibility with the (ultra) high vacuum conditions required for FIB-SEM operation and imaging, using an ethanol serial dehydration (against water) to slowly extract water from the cells.

The cells were slowly re-infiltrated with a gradient (against ethanol) of epoxy resin solutions providing stability to the cells, as well as acting as a matrix for stable FIB milling as empty pockets would cause uneven processing. Before curing the epoxy resin, the majority of the resin was removed by quick ethanol spraying and blotting to achieve only a thin (~100 - 500 nm) layer of resin on top of the cells[95,260]. This ensured that the cell shape and position was clearly visible in SEM and FIB-SEM imaging, whilst still conveying the necessary stability. The last processing step involved mounting the cells on their coverslips onto SEM imaging stubs using conductive carbon tape and sputter coating the sample with a 15 - 20 nm layer of chromium to ensure conductivity of the sample during imaging. Note that chromium was chosen for this on purpose, as opposed to the more stable and ubiquitous gold coating, to avoid the introduction of any additional gold to the samples, besides that derived from the AuNCs. The third phase concerns the FIB-SEM imaging of the samples, were a cell of interest was localised in SEM mode and tilted within the coincidence point of the electron and ion beams to 54° to achieve perpendicular FIB cutting. A trench was cut to expose the inner surface and serial sections were cut and imaged to obtain image stacks detailing the cellular ultrastructure and revealing the particle uptake behaviour.

4.3.6 Cell viability assay

A first requirement for uptake studies is demonstrating a non-negative impact on the cell viability by the particles themselves, thus not confounding the uptake results by the excessive triggering of cell apoptosis. The cell viability impact was evaluated using a Cell Counting Kit (CCK)-8 based assay. No significant negative impact on cell viability was observed up to 6 hours post incubation with both supraparticles with and without EVs, compared to the native EV or PBS controls (Figure 4.8). It should be noted that the viability was assessed by removal of the particle containing media 6 hours post incubation and culturing of the cells for a further three days prior to the CCK-8 assay.

As the CCK-8 assay is based on the metabolic conversion of a tetrazolium salt to produce a coloured product, formazan, performing the assay directly post incubation with the particles would only result in revealing any metabolomic impact to the cells rather than true cytotoxicity. The true cytotoxicity therefore is revealed when the assay is performed several days post exposure to the particles.

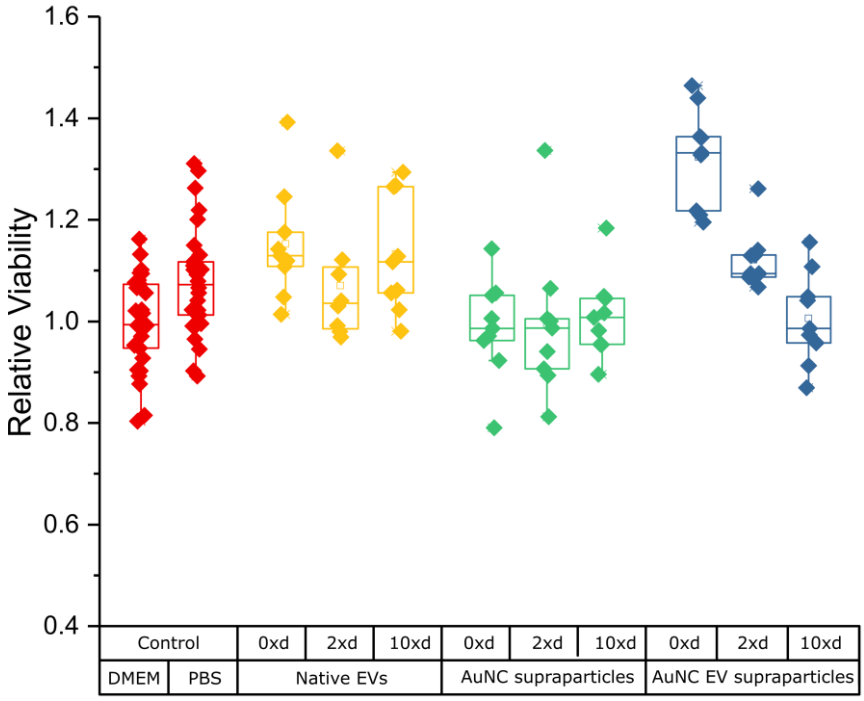

Figure 4.8 | CCK-8 viability assay. MDA-MB-231 cells treated for 6 hours with native EVs, AuNC EV supraparticles and EV-free AuNC supraparticles at various dilutions, 0xd corresponds to used concentration for cell uptake experiments. As control an equivalent amount of PBS to the particles was added. (n = 3, N = 3).

4.3.7 FIB-SEM uptake studies of AuNC- and AuNC EV supraparticles

4.3.7.1 AuNC EV- and AuNC supraparticle uptake comparison

The two particle types were incubated with cells for different periods of time (1, 2, 4 and 6 hours) to investigate and compare their uptake behaviour over time, after which the cells were washed and fixed. Following heavy metal staining, dehydration and resin embedding, the samples were imaged using Focused Ion Beam – Scanning Electron Microscopy (FIB-SEM). With FIB-SEM, slices of resin-embedded cells can be cut down to 5-10 nm thickness and imaged sequentially *in situ*. The resulting image stack can be aligned, and following manual segmentation a detailed 3D model is obtained of the subcellular structures[103,261].

The inner structure of the cells was segmented and visualised in high detail to track the uptake behaviour of the supraparticles. A strikingly different uptake behaviour was detected when AuNC EV supraparticles and AuNC supraparticles were compared, showing that the EVs strongly influenced how these complex structures were recognised and taken up by cells. An overview of the uptake between 1 and 6 hours of the AuNC EV supraparticles in MDA-MB-231 cells is shown in Figure 4.9.a-d and for the AuNC supraparticles in Figure 4.9.e-h.

Cells were milled perpendicular to the cell surface to expose and image the inner structure of the cells using a backscattered electron detector in SEM mode. The cell cytoplasm, nucleus, AuNC EV supraparticles, endosomes and lysosomes can be seen as indicated by the arrows and Roman numerals I-V, respectively. Within the cells, clear uptake of AuNC EV supraparticles is confirmed, as the gold labelling provides a very bright elemental contrast in the backscattered electron images. An example is indicated with an arrow (III) in Figure 4.9.c. In contrast, no intact uptake was observed at any of the time points when the cells were incubated with AuNC supraparticles (Figure 4.9.e-h). This indicates that the AuNC supraparticles are not taken-up by the cells while remaining intact or degrade very rapidly upon uptake.

Another clear difference for the comparison of EV-free and EV-containing supraparticle uptake studies was observed regarding the appearance of the lysosomes. Already after 1 hour of incubation with AuNC supraparticles without EVs, numerous very bright lysosomes (identified by their size and dense staining) can be seen inside the cell (Figure 4.9.e). This implies the presence of AuNCs (or their aggregates) inside the lysosomes due to their high brightness in the backscattered electron images. This difference in lysosomal brightness is observed between the AuNC EV supraparticle and AuNC supraparticles uptake across the different time points (Figure 4.10.a-b respectively) during FIB-SEM imaging.

To be able to compare the lysosomal brightness of these two experimental sets quantitatively, the histograms of the cell images were equalised using MATLAB to correct for differences in brightness and contrast imaging settings during acquisitions. After equalisation, the images were cropped to the lysosomes and a local histogram was calculated from the centre area of each lysosome for comparison. In addition, the cells and time-points compared were all from the same experimental preparation batch, to avoid differences in staining (thus resulting brightness and contrast) influencing the analysis. The resulting brightness of the lysosomes after incubation with AuNC supraparticles is high from the 1-hour incubation time point onward, remaining more or less constant up to the final 6-hour time point. A quantitative assessment of this can be seen in Figure 4.10.c. However, for the AuNC EV supraparticles the brightness of the lysosomes is significantly lower after 1-hour incubation, with an increase in variability at 2-hour time point and finally similar accumulation into the lysosomes at 4 and 6 hours.

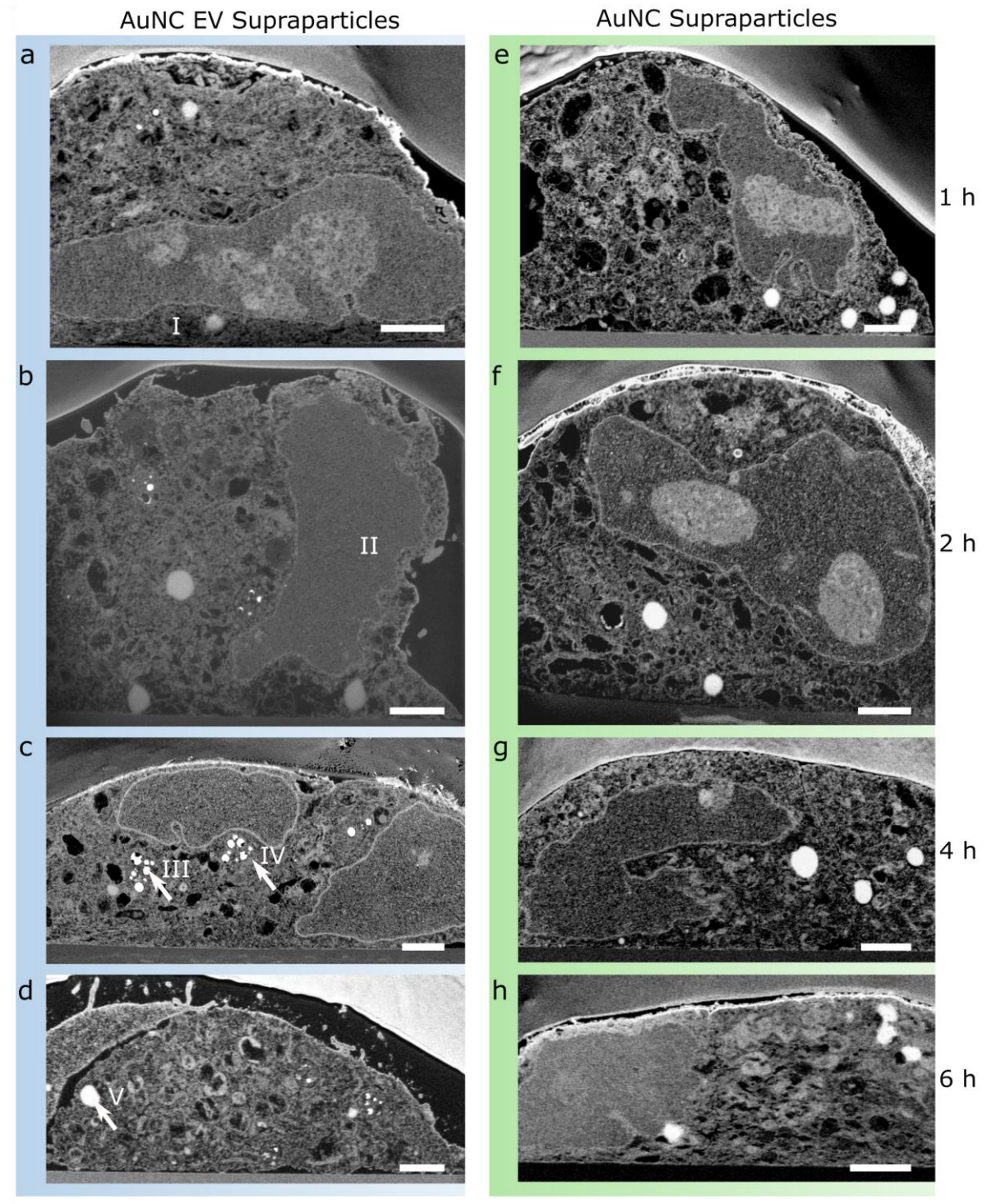

Figure 4.9 | FIB-SEM imaging of uptake comparison in MDA-MB-231 cells. (a-d) AuNC EV supraparticles, (e-f) AuNC supraparticles, top to bottom 1, 2, 4- and 6-hours incubation, scale bars 2 µm. Roman numerals and arrows indicate exemplar structures of cytoplasm (I), nucleus (II), AuNC EV supraparticles (III), endosome (IV) and lysosome (V).

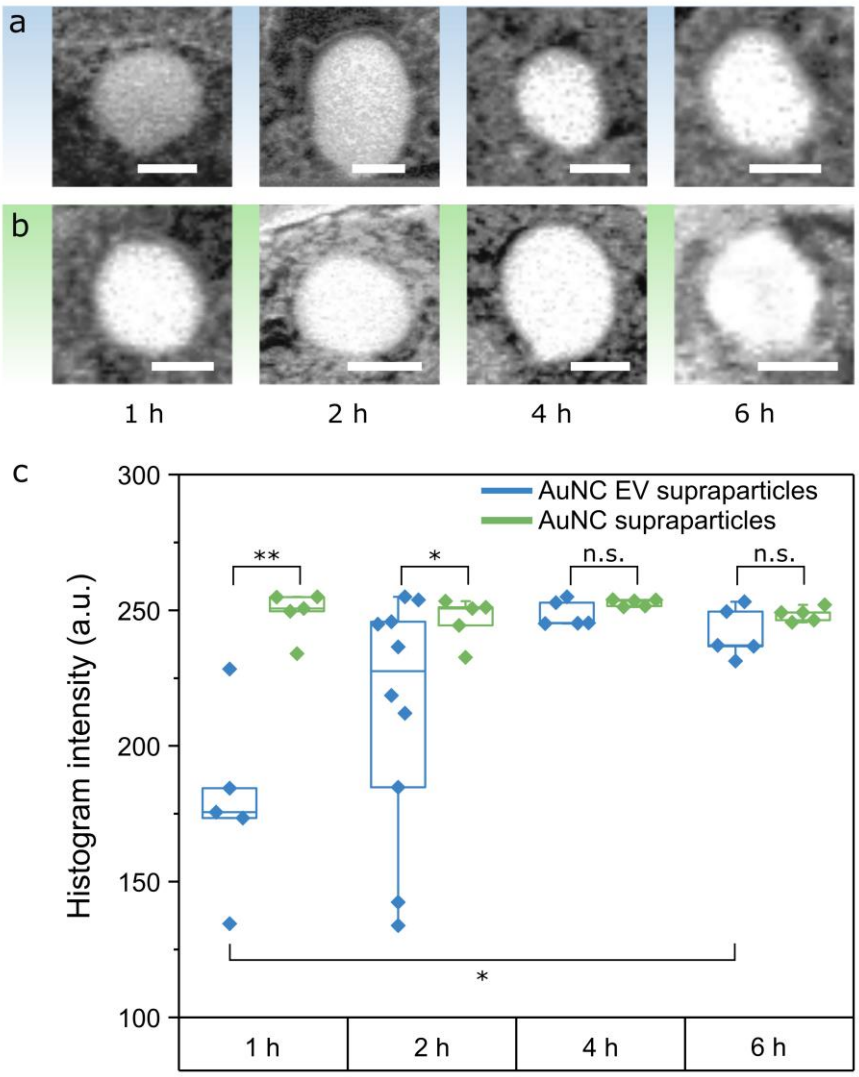

Figure 4.10 | Lysosomal brightness analysis. (a-b) close-up of lysosomes, 1, 2, 4 and 6 hours for (a) AuNC EV supraparticles and (b) AuNC supraparticles, scale bars 500 nm. (c) Brightness analysis from centre histograms mean ± s.d. (n = 5, 2 hours EVs n = 10), *p<0.05, ** p<0.01, Welch's corrected t-test between particle types, Welch's Anova with Games-Howell post-hoc test for AuNC EVs over time. Histograms of all cell images are equalised to the 1-hour AuNC EV supraparticles image prior to close-up cropping.

In summary, this indicates that a large number of AuNCs of the AuNC-supraparticles without EVs can be found inside the lysosome from the earliest time point of 1 hour onward, while for the AuNC EV supraparticles there is a more gradual trafficking to the lysosomes. This is indicated by the lower brightness at 1 hour, increasing over 2-4 hours to a similar end point as compared to the AuNC supraparticles.

4.3.7.2 3D reconstruction and visualisation

To visualise the structure and uptake of the supraparticles in greater detail, the image stacks obtained were processed to obtain 3D cellular reconstructions. As mentioned in section 4.1.5, the workflow to obtain 3D reconstructions consists of automated and manual image registration, component segmentation and rendering. A schematic overview of this process is shown in Figure 4.11. Careful image registration is a critical first step, where the images in the stack were aligned to each other, correcting for any imaging drift occurred during serial sectioning. This was achieved by a first, coarse, automated registration using the Fiji (ImageJ) StackReg plugin. Next, the image stacks were imported into a dedicated software package (Amira 5.3.2., FEI) for fine, manual, adjustment of the stack alignment. By overlaying two sequential images at 50% transparency and inverting the contrast on one of them, alignment was achieved by observing a minimal contrast difference, as two identical, perfectly aligned images would give a uniform grey field.

The next step is manual component segmentation, where pixels were labelled as belonging to any of the desired subcellular components for the final 3D reconstruction, in this case cytoplasm (green), nucleus (purple), lysosomes (red), endosomes (orange) and AuNC EV supraparticles (yellow). Once the pixel volumes for the components were assigned in each slice, a 3D reconstruction of the cell was rendered and analysed.

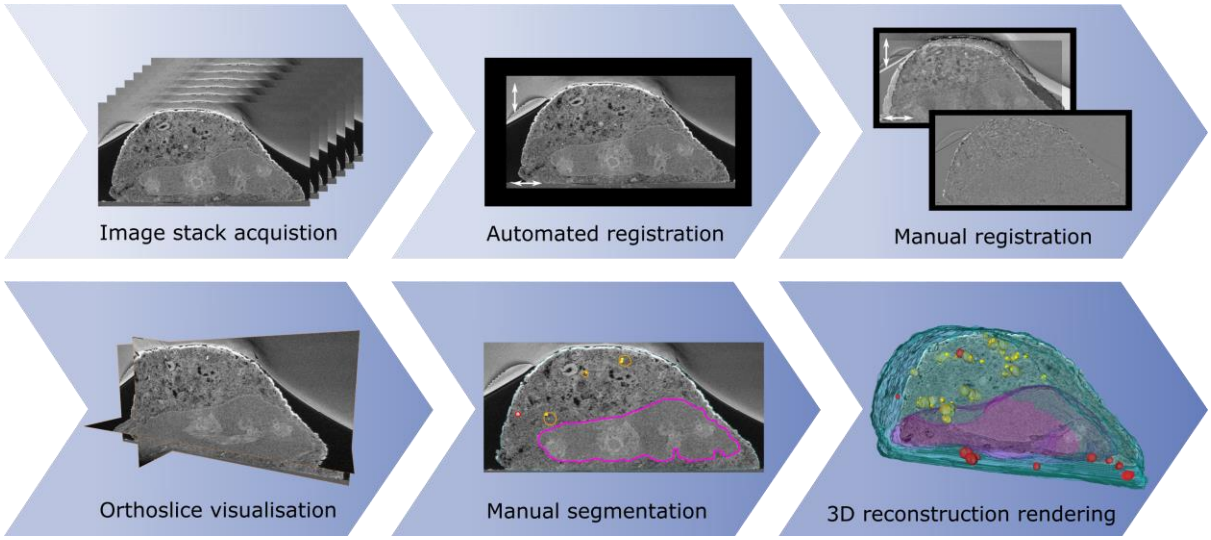

Figure 4.11 | FIB-SEM 3D reconstruction workflow. A FIB-SEM image stack is acquired and coarsely aligned using automated image registration. Fine manual registration is performed based on minimising visual contrast difference of sequential inverted transparent slices. The aligned image stack can be visualised and digitally resliced using orthoslice visualisation. Pixel areas belonging to specific subcellular components are manually selected: cytoplasm (green), nucleus (purple), lysosomes (red), endosomes (orange) and AuNC EV supraparticles (yellow) in each slice and a 3D reconstruction is rendered.

Here, image stacks were taken with a 90 nm spacing between slices for cells incubated 1, 2, 4 and 6 hours with AuNC EV supraparticles, the result of which can be seen in Figure 4.12 (a-d for 1, 2, 4 and 6 hours, respectively) and Supplementary movies 1-4.

Significant endosomal uptake was already observed for the 1-hour incubation time point with the AuNC EV supraparticles. Moreover, a few AuNC EV supraparticles can be seen in the cytoplasm and near the cell membrane. At 2- and 4-hour time point clear localisation of AuNC EV supraparticles in the endosomes is observed, as well as several lysosomes visible within the cells, while at the 6-hour time point both endosomes and lysosomes can be seen in high numbers as seen in Figure 4.12.d.

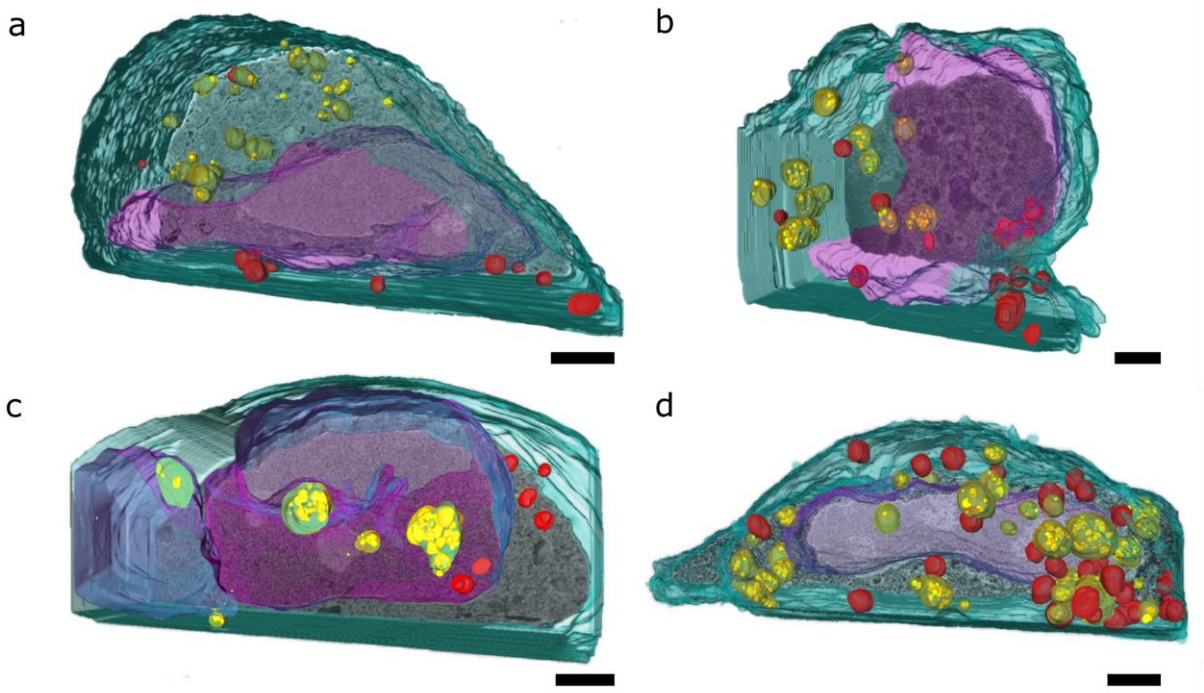

Figure 4.12 | 3D reconstructions of AuNC EV supraparticle uptake. (a) 1 hour, (b) 2 hours, (c) 4 hours, (d) 6 hours, segmentation in the 3D reconstructions shows the cytoplasm (green), nucleus (purple), lysosomes (red), endosomes (orange) and AuNC EV supraparticles (yellow). Endosomal uptake of the particles can be seen over time with an increase in lysosome presence, scale bars 2 µm.

4.3.7.3 Early- and endosomal uptake of AuNC EV supraparticles

Looking further into the early uptake of AuNC EV supraparticles, at the 1-hour time point, multiple cells were imaged, paying close attention to the presence of AuNC EV supraparticles close to the cell membrane.

Due to the high number of washes involved in the preparation before FIB-SEM imaging, only AuNC EV supraparticles actually in the process of uptake will have been retained, while those that may be adsorbed or otherwise associated with the membrane would most likely have been removed. Some of these uptake events are visualised in Figure 4.13. These images all show AuNC EV supraparticles in very close proximity to the cell membrane with membrane wrapping around the particles, which indicates macropinocytosis as one of the uptake mechanisms[251].

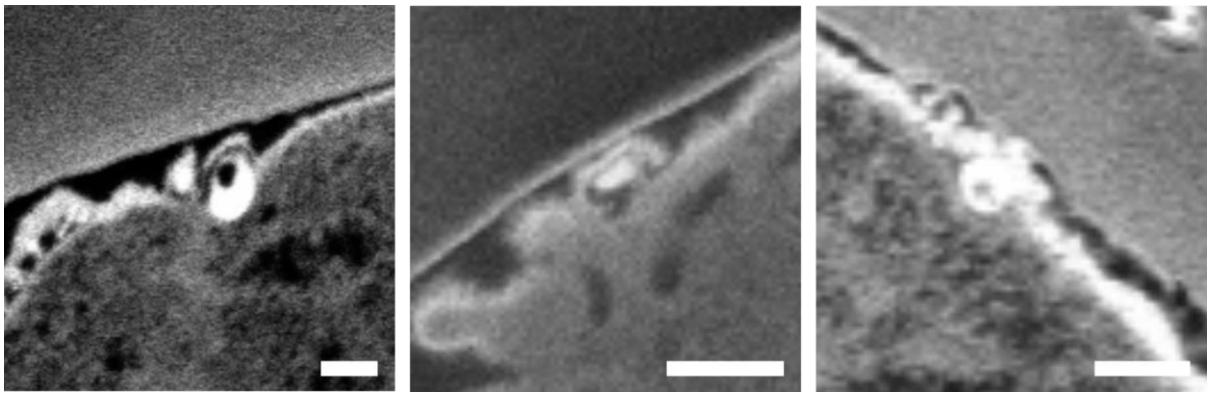

Figure 4.13 | 1-hour uptake of AuNC EV supraparticles. Close-up FIB-SEM imaging of 1-hour uptake of AuNC EV supraparticles into MDA-MB-231 breast cancer cells. Uptake events visible in three different cells. Scale bars 500 nm.

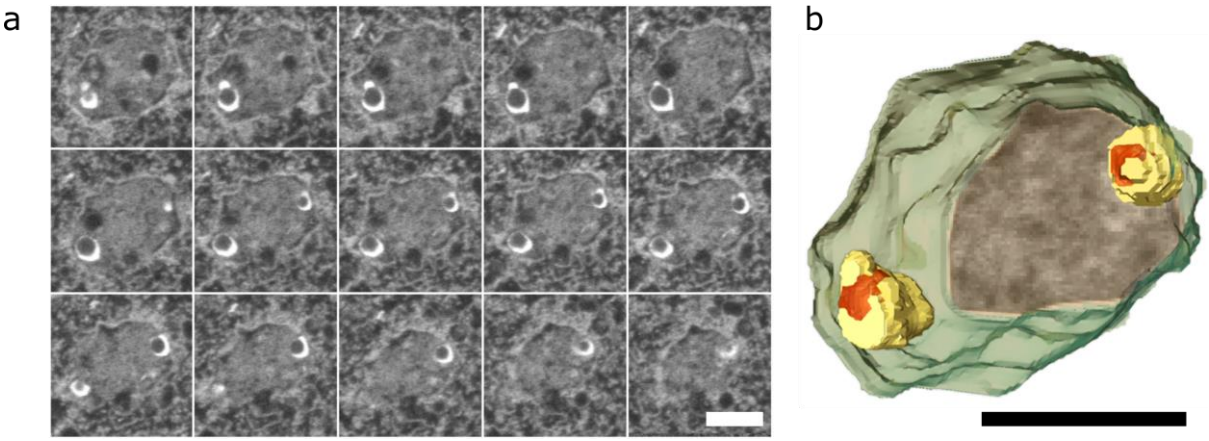

Figure 4.14 | Endosomal uptake of AuNC EV supraparticles. 2-hour incubation of MDA-MB-231 breast cancer cells with AuNC EV supraparticles visible within an endosomal membrane, (a) image stack left-to-right, top-to-bottom with a 20 nm slice thickness. (b) 3D reconstruction of the endosome stack in a, showing endosomal compartment in orange, AuNC shell in yellow and the supraparticle centres in red. Scale bars 500 nm.

The endosomal uptake was additionally visualised in greater detail, as shown in Figure 4.14.a-b. The image stack montage in Figure 4.14.a shows a serial sectioning performed on an endosome with AuNC EV supraparticles inside using a fine sectioning of 20 nm between slices. Here, it was observed that the AuNCs form a shell surrounding an inner lumen, similar to the EV membrane around its inner compartment. A 3D reconstruction of this endosome can be seen in Figure 4.14.b with the endosomal compartment in orange, AuNC shell in yellow and the particle interior in red.

4.3.8 FIB lift-out and *in situ* elemental analysis

To confirm the presence of gold within the AuNC EV supraparticles *in situ* and the presence of AuNC at the 1-hour incubation time point in lysosomes for AuNC supraparticles, FIB lift-out sections of MDA-MB-231 cells incubated with the particles were prepared. Due to the small amount of gold present, EDX analysis in the bulk cell sample during FIB-SEM would not have been accurate. Additionally, a high accelerating voltage is needed to excite the $L\alpha_1$ shell of gold, which would result in a large X-ray generation volume in a bulk sample.

Therefore, lamellae were prepared by FIB lift-out to allow TEM and DF-STEM imaging and high-resolution EDX analysis, in a similar procedure to one recently described by the Stevens Group[95]. The lamella preparation steps are depicted in Figure 4.15. A cell is imaged using serial sectioning until a region of interest is observed (Figure 4.15.a), whereupon large trenches are milled before and after the region of interest, leaving a lamella of approximately 1 µm thickness remaining (Figure 4.15.b). In addition a thick layer (~200-300 nm) of platinum is deposited on top of the lamella for stability, using a platinum vapor gas injection system (GIS). Next, the sample is tilted to observe the backside of the lamella and the left connecting edge of the lamella is cut loose with the FIB (Figure 4.15.c).

This exposes a clear attachment point for a micromanipulator needle, which is very carefully guided to the top left corner of the lamella and attached using localised platinum deposition. The bottom and right side of the lamella are then cut loose to de-attach the lamella from the sample completely (Figure 4.15.d). The micromanipulator needle with the lamella attached is very carefully retracted and moved to one of the pillars of a TEM lift-out grid (Figure 4.15.e-f). Using further platinum deposition the lamella is attached with the right edge to the lift-out grid and the needle is de-attached by milling away the attachment point using the FIB. Using further localised FIB milling while tilting the lamella back and forth, the lamella is thinned to approximately 100 nm, making it electron transparent for subsequent TEM imaging (Figure 4.15.g-h).

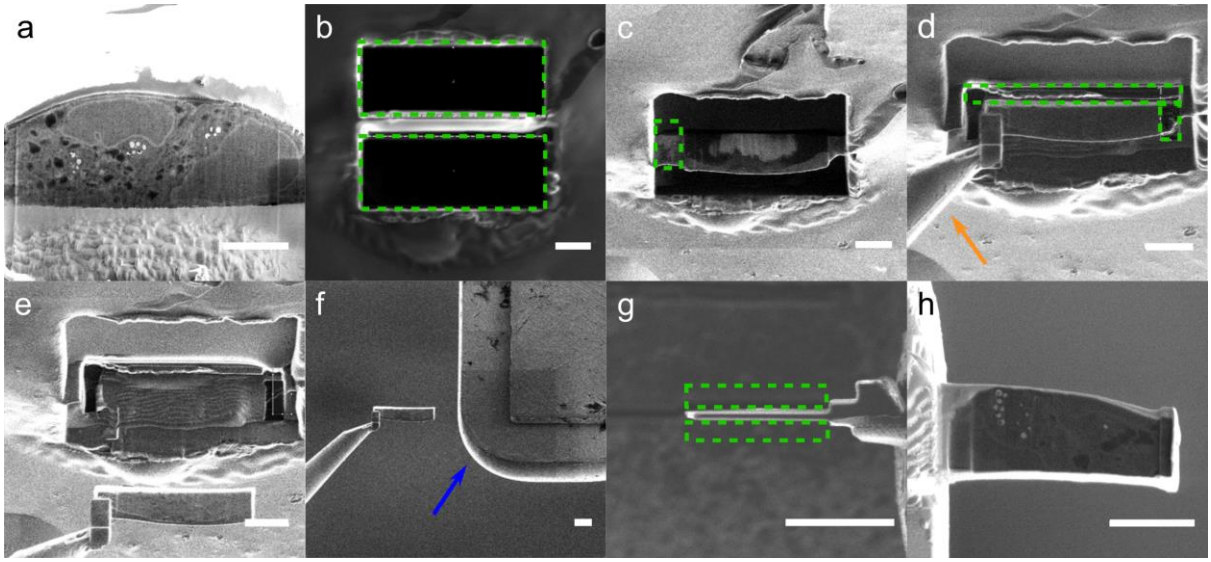

Figure 4.15 | Steps illustrating FIB-SEM lift-out to prepare cell lamellae. The cell is milled and imaged up to a region of interest (a) after which deep trenches are milled in front and the back of the cell to expose a lamella (b, c). A micromanipulator needle is attached (orange arrow), and the lamella milled free on the bottom and sides using the ion beam (d). The needle with lamella is retracted (e) and attached to a lift-out grid (bue arrow) and the needle released (f). The lamella is thinned to electron transparency (g, h) and polished for subsequent TEM imaging. Milling areas are indicated with green dashed boxes. Scale bars 5 µm.

These lamellae were imaged using DF-STEM (Figure 4.16.a,c) and the presence of gold was confirmed within the AuNC EV supraparticles with EDX analysis, as well as small amounts of gold within the lysosomes after 1-hour incubation with AuNC supraparticles, as shown in Figure 4.16. Spectra 1-3 in Figure 4.16.b show that the gold signal increases with particle size, while no gold is detected away from the particles (shown in spectra 4 and 5 in Figure 4.16.c). A notable increase in the Uranium elemental signal is observed when collecting a spectrum on a membranous structure in the cytoplasm (spectrum 4), due to the heavy metal staining protocol, which illustrates the high resolution of the EDX acquisition.

As shown in Figure 4.16.e, a lamella was prepared after a 1-hour incubation with AuNC supraparticles, isolating a region of interest containing numerous bright lysosomes. EDX analysis confirmed the presence of a small amount of gold within these lysosomes, confirming the early uptake, as shown in Figure 4.10.c.

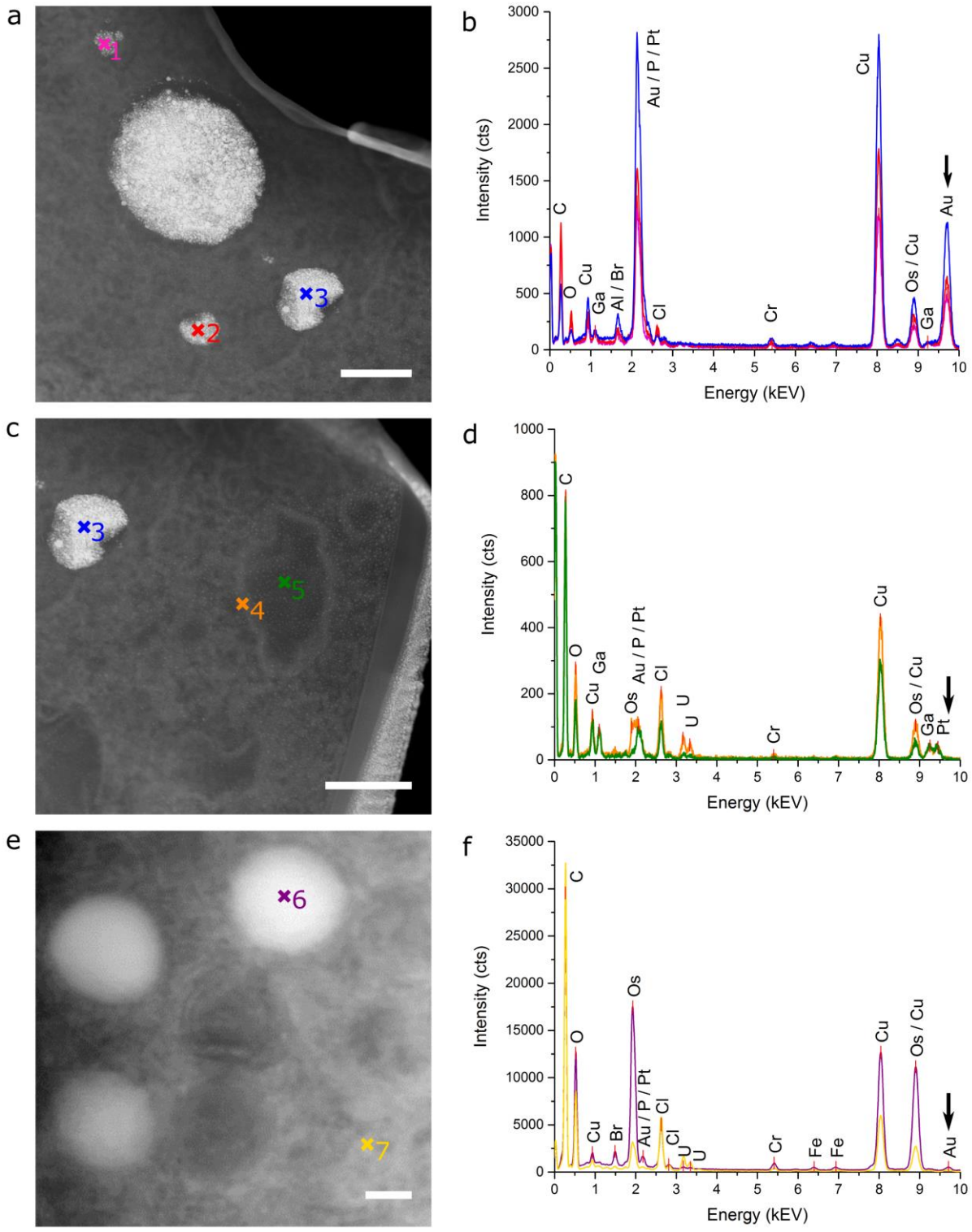

Figure 4.16 | DF-STEM imaging and EDX analysis of FIB lift-out lamellae. (a, c) DF-STEM imaging at 4 hours incubation with AuNC EV supraparticles, a and c show a close-up of AuNC EV supraparticles within the cell with increasing detection of gold in the EDX spectra (b, 1-3) and no detectable gold away from the particles (d, 4-5). (e) DF-STEM imaging at 1-hour incubation with AuNC supraparticles showing bright lysosomes with a small amount of gold detectable within the lysosome by EDX (f, 6-7). Scale bars 250 nm.

4.4 Conclusions

This work demonstrates the first method for the self-assembly of supraparticles with breast cancer cell-derived EVs and hydrophobic AuNCs. These were characterised by cryo-TEM and their cellular uptake was analysed *via* FIB-SEM and 3D reconstructions. Clustering of the AuNC EV supraparticles in endosomes was shown and later degradation in lysosomes. Isolation of cell lamellas *via* FIB lift-out and subsequent DF-STEM imaging and EDX analysis showed the presence of gold in the AuNC EV supraparticles inside the cell. In comparison, AuNC supraparticles (formed without the natural EV component) were not sufficiently stable for cellular uptake tracking. No intact AuNC supraparticles were observed within the cells, but the presence of gold was detectable in the lysosomes within 1 hour.

In summary, the role that EVs can play in making a difference to the cellular uptake of nanoparticles was demonstrated. While exceeding the scope of this study, the demonstrated easily accessible route for combination of nanoparticles with EVs is also a potential route to combine theranostic functionality of different nanoparticles with EVs. It was also shown that the assembly of AuNCs with EVs allows detailed tracking and visualisation within cells *via* FIB-SEM imaging and this method may be instrumental in a variety of future applications, such as mechanistic uptake studies of EV-based diagnostic and therapeutic technologies. This is the first proof-of-concept of EV-based AuNC supraparticles and exemplifies the powerful combination of complex biological entities with the versatility of nanoparticles.

4.5 Supplementary movies

Movies showing the full SEM image stacks obtained during FIB-SEM serial acquisition (exemplary images in Figure 4.9.a-d) and the 3D reconstruction visualised as in Figure 4.12.a-d.

Supplementary Movie 1: 1-hour uptake of AuNC EV supraparticles

Supplementary Movie 2: 2-hour uptake of AuNC EV supraparticles

Supplementary Movie 3: 3-hour uptake of AuNC EV supraparticles

Supplementary Movie 4: 4-hour uptake of AuNC EV supraparticles

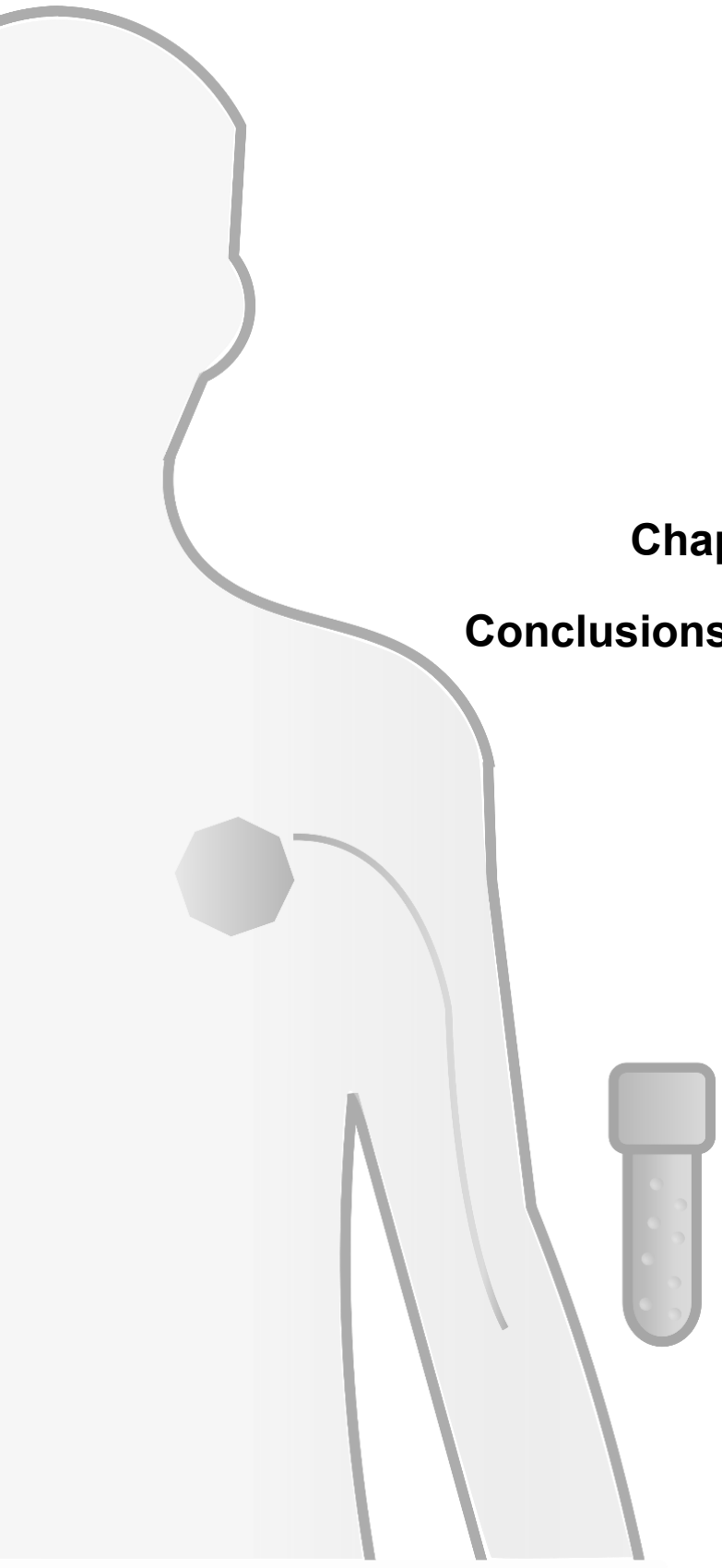

Chapter 5

Conclusions and Outlook

‘Connecting the dots is not possible looking forward

but is possible only looking backward.’

Kinam Park

Controlled drug delivery systems: Past forward and future back

Journal of Controlled Release, 190, 2014

5 Conclusions and Outlook

The concept of nano-sized entities being able to transport and deliver drugs or interact in unique ways on a (sub)-cellular level, has enraptured the field of nanomedicine since its inception. From the humble beginnings of simple liposomes, great strides have been made to develop ever more intricate particles, based on a combination of natural and purely synthetic components. In addition, in recent years the recognition of various types of extracellular vesicles, being excreted by virtually every cell type, has led to a true explosion of research into their composition, biological function and possible applications.

Methods to analyse these increasingly complex particles and their cellular interactions are of critical importance to their successful translation and future clinical application. As such, a novel, comprehensive nanoparticle analysis platform was the scope of this thesis, to allow automated label-free characterisation of these particles. For nanoformulations this is key, due to the major impact compositional and size heterogeneity can have on their functionality. In addition, EVs intrinsically encompass strong biological heterogeneity. This demands individual characterisation, in order to extract accurate information and unlock their potential as disease biomarkers or drug delivery vesicles.

In the sections below, the key findings of this thesis are summarised and placed into context of the state-of-the-art of the field. In addition, several future research directions are discussed based on the current and other preliminary studies conducted.

5.1 SPARTA – nano formulations

In chapter 2 the design and validation of SPARTA was discussed, and the successful development of a system was achieved that is capable of accurate single particle analysis with the following key advantages:

1. The SPARTA system is based on Raman spectroscopy, making it a non-destructive and label-free technique.
2. The system is automated through a custom MATLAB-based trapping algorithm. The algorithm detects the presence of a nanoparticle in the trap and regulates efficient spectral acquisition by switching between short and long acquisition measurements.
3. SPARTA is a comprehensive nanoparticle analysis technique able to perform composition and functionalisation analysis, solution marker mediated sizing and on-line dynamic reaction monitoring.

Based on the principles of optical trapping of particles using a tightly focused laser, as conceived by Ashkin[122,139] and others, the SPARTA system at its core is a combination and automation of single laser trapping and Raman spectroscopy. This powerful union allows for the precise interrogation of single particles and the generation of their Raman spectrum, to primarily obtain compositional information, in a label-free manner. The capability to analyse single particles, as opposed to bulk measurements, is an advantage, which cannot be underestimated, especially in the field of nanomedicine. The studies by Adjei *et al.*[110] and Mullen *et al.*[111] illustrate clearly that the heterogeneity of nanoformulations can be much greater than expected. This can critically impact their pharmacokinetic and pharmacodynamic behaviour and thus clinical applicability. Simply put, when devising, for example, a polymersome system made of two types of block-copolymers in a 50-50 wt.% ratio in the particles, a bulk compositional analysis will likely just reveal this input ratio (disregarding solvability issues or aggregation). However, it may very well be that in truth several subpopulations are formed containing highly variable degrees of these components. A compositional analysis based on single particles will be able to uncover this phenomenon, while it would be overlooked by bulk analysis. In addition, this ability becomes especially important when looking at the loading of nanoformulations with active components, such as drugs. A highly variable loading in the particles may lead to undesirable effects and produce uncontrolled results upon administration[110,262].

The use of optical trapping and Raman spectroscopy for the study of drug delivery vesicles, such as liposomes and polymersomes, has been recognised and demonstrated in studies, as described by Cherney *et al.*[124,150] and Sanderson *et al.*[148]. However, the fact that these particles need to be individually, manually trapped or lifted from a substrate[155,156] severely limits this approach as a means to study nanoparticles, on a single particle basis in a (statistically) meaningful way.

The development of the SPARTA system, with as key advantage being the automation of single particle trapping, addresses therefore this critical shortfall and thereby opens-up a multitude of applications of particle investigation hereto unavailable. As demonstrated, the SPARTA system is capable of identifying the presence and composition of mixed heterogeneous particle populations, track serial functionalisation operations and monitor reactions occurring on the particle surface. In addition, for the first time, Raman spectroscopy was applied to size particles, directly held in the trap, while simultaneously acquiring their compositional spectrum.

In future studies, specifically focusing on the analysis of nanoformulations with SPARTA, a demonstration of drug loading heterogeneity is of interest. In particular, as a comprehensive analysis can be achieved by SPARTA, where the source of the heterogeneity may be directly traced back to changes in the core particle composition or differences in particle size.

5.2 SPARTA – future system development

In chapter 3, the further development of the SPARTA system into a dedicated SPARTA 2.0 setup was discussed, including six major improvements. A signal enhancement of up to 15-30 fold was achieved by using a more powerful laser and spectrograph. The spectral range was extended to allow simultaneous capture of the fingerprint and silent spectral regions. The use of a smaller pinhole fibre increased the confocality of the system and reduced background signal contamination. The laser stability and flexibility were improved by including an automated in-line shutter for laser trap disablement, as opposed to disabling the laser itself, and a current control box introduced straightforward tunability of the laser output power. Overall, the system stability and ease of use were improved by making it a dedicated system for SPARTA measurements only, as opposed to the first-generation system which was regularly converted between Raman imaging and trapping modes. Improvements to the operation process flow were also achieved through semi-automated calibration and enhanced spectral processing, by introducing a spectral response correction and flexible background solution signal subtraction.

The custom-built nature of the SPARTA platform makes it very flexible for further adaptation and improvement. Several factors, especially on the software side, can be identified to be addressed in future development.

Due to the versality of the system for different types of nanoparticles it can be challenging, especially for novice users, to determine the appropriate and moreover optimal measurement conditions for each sample and to assess the validity of their results. In particular, the particle concentration is of key importance for accurate and reliable trapping. To aid in this, the data processing scripts may be expanded to include assessment parameters of the data quality. This can be achieved by closer analysis of the iteration number at which the trapping was successful, which is recorded along with the spectrum (see Figure 2.6). This iteration number reflects the trapping chance and further analysis of the iteration number distribution may be used to inform on the optimum measurement concentration. The occurrence of a high number of traps at low iteration numbers, should reflect a concentration that is too high, providing adequate laser disabling times and thresholding.

Conversely, a distribution to the higher iteration number end, possibly in combination with repeated trap failure, could indicate a need to increase the particle concentration.

On the hardware side, further improvement may be gained by counteracting sample evaporation, which is currently impacting the maximum measurement time. The construction of an enclosed (environmental) measurement chamber or chip could be a means to resolve this, allowing better conservation of samples and extended measurement runs.

These improvements would greatly contribute to the user ease of use, by further automation and removal of user bias. This is important for the development of SPARTA into a full fledge accessible nanoparticle analysis tool, without the direct need for involvement of optics or Raman specialists.

5.3 SPARTA – EVs as cancer biomarkers

In the second half of chapter 3, the SPARTA 2.0 system was employed for the analysis of EVs to assess their potential as biomarkers, specifically in the context of breast cancer. By thorough analysis of the Raman spectrum obtained form an exemplary breast cancer EV type, the capability of Raman spectroscopy to give a detailed fingerprint of the composition of EVs was demonstrated. Three cell lines were selected as a subset and their EVs analysed. This was done as a preliminary study on the feasibility to distinguish cancer cell derived EVs from those derived of a healthy breast epithelial cell line. Using PCA and PLSDA modelling, cancerous *vs*. non-cancerous and inter-cancerous classification was be achieved with 100% sensitivity and specificity, mostly based on the difference in lipid content. The EV Raman spectra were compared to those derived from the lipid rich spectra of the parental cell lines and similar trends were observed in lipid/protein distributions, highlighting the composition reflection of the cell differences into their EVs.

The analyses were expanded to a full 11-EV panel, consisting of EVs from healthy and cancerous cell lines, including several receptor status subtypes as ER+, HER2+ and triple negative. The challenge in visual comparison of 11 Raman spectra simultaneously was met by construction of a novel visualisation approach, based on heat map representation of dimensionally reduced spectra. These dimensional reduction arrays allow for easy comparison of a high number of spectra, with clear colour-based distinction between differentiating spectral regions. PLSDA modelling was used to supplement this analysis, achieving sensitivities and specificity close to 100% for distinguishing between healthy and cancer cell derived EVs. The similarity between certain cell line – and thus EVs – cancerous origin was observed by overlap of their respective classification clusters in the PLSDA model.

Several previous studies were highlighted, such as those by Smith *et al.*[156] and more recently by Lee[175], Carney[196] and Kruglik *et al*[197]. These studies demonstrated initial forays into the use of Raman spectroscopy and optical trapping for the analysis of EVs, derived ranging from prostate cancer and platelets to urine and hepatocytes. The major advancements of the study presented here is the use of the SPARTA system, for automation, high-throughput and confocal accuracy combined with superior EV isolation and purification techniques. This allowed for the investigation and differentiation between, at first glance, highly similar EVs from a range of cancerous and non-cancers breast cancer cells.

The next major step for the research into EVs as cancer biomarkers, is the move from cancer cell line derived EVs to those found in patient blood plasma. In the isolation of EVs from blood plasma stringent purification techniques are even more paramount, due to the large amount of proteins and specifically similar sized lipoprotein particles present[263]. The use of SPARTA has a high potential to circumvent these issues. In part due to the single particle nature of the technique, EV spectra could be isolated post-measurement from those of contaminant particles. In addition, a high number of spectra and particles analysed will be required to enable the capture of a relevant fraction of the biological variation. This, in order to have a chance to pick up signatures from cancer derived EVs. The flexibility and automation of the SPARTA platform will be a key asset in this respect.

A prospective study design is shown schematically in Figure 5.1. EVs isolated from cultured cells, both of cancerous and non-cancerous origin can be analysed by SPARTA, as in the work presented here. This will inform to construct models both to identify cancerous *vs*. non-cancerous classifiers, as aid in the separation of EV spectra from those of possible contaminants in the plasma derived samples. EVs would also be isolated from blood plasma of healthy volunteers and cancer patients to be analysed by SPARTA. A combination of powerful statistical models will likely be required to isolate and classify the EV spectra and screen for the presence of abnormal, cancer derived ones. Together with the future system improvements of the SPARTA platform as mentioned above, this would allow SPARTA to be developed as a clinically applicable screening tool towards minimally invasive diagnostics.

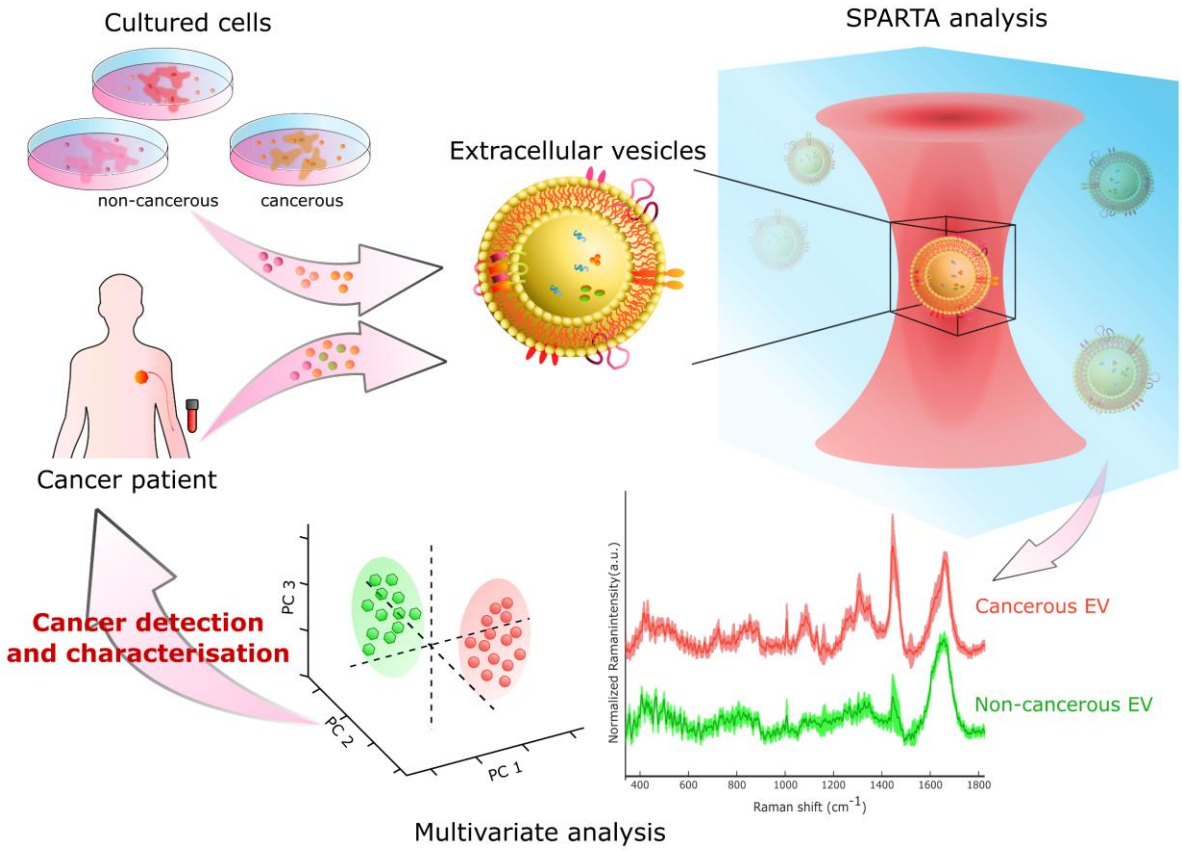

Figure 5.1 | SPARTA EVs as cancer biomarkers prospective study design. EVs are isolated from *in vitro* culture of cancerous and non-cancerous cell lines, as well as from the blood of cancer patients and healthy volunteers. The EVs are purified and analysed by SPARTA. Multivariate statistical analysis methods are applied to model the compositional differences of EVs from cancerous and non-cancerous origin. The overreaching aim is to detect and characterise cancer by EVs a blood borne biomarkers.

5.4 AuNC EV supraparticles and 3D FIB-SEM imaging

In chapter 4 the focus was shifted towards the study of EV-cell interactions, in particular the re-uptake of breast cancer cell derived EVs into their parent cells. The core difficulty of the detailed study of this, is the small size of EVs being below the typical optical diffraction limit and their similarity to the cellular background. To address these, a new analysis approach was developed using EM for superior resolution and introducing AuNCs to transform the EVs into trackable new entities, dubbed AuNC EV supraparticles. Hydrophobic AuNCs of 1-3 nm were synthesised, which self-assembled in the presence of saponin and EVs into AuNC EV supraparticles. These supraparticles were shown to have conserved EV protein markers, as well as no significant cell cytotoxicity. Self-assembly was also achieved in the absence of EVs and these AuNC supraparticles were utilised as a control system to analyse if the EV component specifically influenced the particle uptake by the EV parental cell line.

The visualisation of the EV-cell interactions and uptake was conducted using FIB-SEM serial sectioning. Image stacks were obtained which could be rendered into 3D models, showing the subcellular structure and locations of AuNC EV supraparticles at various time points. AuNC EV supraparticles could be tracked from early membrane interactions for uptake all through the endo-lysosomal system. A clear difference in uptake behaviour was observed for the AuNC supraparticles (in the absence of EVs), which exhibited the inability for integral uptake and were rapidly trafficked to the lysosomes. The presence and trafficking of the AuNCs was confirmed by the use of DF-STEM imaging and high resolution EDX analysis on cell lamellae. These lamellae were prepared *in-situ* using a FIB-SEM lift-out approach.

This study, being the first demonstration of combining nanoclusters and EVs into supraparticles and the first detailed study of EV uptake by FIB-SEM serial imaging, represents a powerful new step in visualising the intricate interplay of EV-cell interaction. The superior resolution compared to fluorescence microscopy approaches[251] allows for resolving single EVs. The resulting 3D models enable the study of full cells and the changes in their subcellular structure, compared to conventional TEM microtoming approaches[253].

As a future direction, apart from further investigation into the biological intricacies of EV uptake and trafficking, the combination of nanoclusters with EVs into supraparticles represents an interesting avenue into theranostic applications. Gold-based nanoclusters and supraparticles have previously been shown to have promising properties for radiation and photothermal therapy[223,224]. These properties could be leveraged and combined with those of EVs in AuNC EV supraparticles, to develop a potential combined diagnostic and therapeutic strategy.

5.5 Final remarks

This thesis explored new approaches for the characterisation of nanoformulations and extracellular vesicles, both on a single particle level and their interaction with cells. Nanomedicine is a complex field, dealing with interactions on the molecular, nano and micro scale which are revealed as being ever more intricate. To enable the development of new therapies and diagnostic tools, the methods used for their analysis equally need to advance. The SPARTA platform as presented in this thesis, represents a clear advance in single nanoparticle characterisation through its flexible, multimodal and above all automated approach. Compared to the state-of-the-art, the capability to trap hundreds of single particles in a controlled and automated fashion opens up a new level of detailed study of synthetic nanoformulations and complex EVs alike. In addition, the high level of detail achieved for the visualisation of EV-cellular interactions using 3D FIB-SEM, is a major step forward and will aid in elucidating their biological function and clinical application potential.

The methods presented here are envisioned to contribute directly to enable more in-depth single nanoparticle study, to tackle pressing issues in the analysis and application of a wide variety of nanoformulations and EVs.

6. References

6 References

1. Allen, T. M. & Cullis, P. R. Liposomal drug delivery systems: From concept to clinical applications. *Adv. Drug Deliv. Rev.* **65**, 36–48 (2013).
2. Hoffman, A. S. The origins and evolution of 'controlled' drug delivery systems. *J. Control. Release* **132**, 153–163 (2008).
3. Peer, D. *et al.* Nanocarriers as an emerging platform for cancer therapy. *Nat. Nanotechnol.* **2**, 751–760 (2007).
4. Meng, F., Zhong, Z. & Feijen, J. Stimuli-responsive polymersomes for programmed drug delivery. *Biomacromolecules* **10**, 197–209 (2009).
5. Wen, H., Jung, H. & Li, X. Drug Delivery Approaches in Addressing Clinical Pharmacology-Related Issues: Opportunities and Challenges. *AAPS J.* **17**, 1327–1340 (2015).
6. Barenholz, Y. Doxil® - The first FDA-approved nano-drug: Lessons learned. *J. Control. Release* **160**, 117–134 (2012).
7. Butt, H., Graf, K. & Kappl, M. *Physics and Chemistry of Interfaces*. (Wiley, 2003).
8. Bangham, A. D. & Horne, R. W. Negative staining of phospholipids and their structural modification by surface-active agents as observed in the electron microscope. *J. Mol. Biol.* **8**, 660–668 (1964).
9. Bangham, A. D., Standish, M. M. & Watkins, J. C. Diffusion of univalent ions across the lamellae of swollen phospholipids. *J. Mol. Biol.* **13**, 238–252 (1965).
10. Sessa, G. & Weissmann, G. Phospholipid spherules (liposomes) as a model for biological membranes. *J. Lipid Res.* **9**, 310–318 (1968).
11. Gregoriadis, G. & Ryman, B. E. Liposomes as carriers of enzymes or drugs: a new approach to the treatment of storage diseases. *Biochem. J.* **124**, (1971).
12. Immordino, M. L., Dosio, F. & Cattel, L. Stealth liposomes: review of the basic science, rationale, and clinical applications, existing and potential. *Int. J. Nanomedicine* **1**, 297–315 (2006).
13. Gulati, M., Grover, M., Singh, S. & Singh, M. Lipophilic drug derivatives in liposomes. *Int. J. Pharm.* **165**, 129–168 (1998).
14. Rahman, A. *et al.* Liposomal Protection of Adriamycin-induced Cardiotoxicity in Mice. *Cancer Res.* **40**, 1532–1537 (1980).

15. Akbarzadeh, A. *et al.* Liposome: Classification, preparation, and applications. *Nanoscale Res. Lett.* **8**, 1–8 (2013).

16. Ong, S. G. M., Chitneni, M., Lee, K. S., Ming, L. C. & Yuen, K. H. Evaluation of extrusion technique for nanosizing liposomes. *Pharmaceutics* **8**, (2016).

17. Discher, B. M. *et al.* Polymersomes: Tough vesicles made from diblock copolymers. *Science (80-.).* **284**, 1143–1146 (1999).

18. Najer, A. *et al.* Nanomimics of host cell membranes block invasion and expose invasive malaria parasites. *ACS Nano* **8**, 12560–12571 (2014).

19. Fariya, M., Jain, A., Dhawan, V., Shah, S. & Nagarsenker, M. S. Bolaamphiphiles: A pharmaceutical review. *Adv. Pharm. Bull.* **4**, 483–491 (2014).

20. Discher, D. E. *et al.* Emerging applications of polymersomes in delivery: From molecular dynamics to shrinkage of tumors. *Prog. Polym. Sci.* **32**, 838–857 (2007).

21. Bhattacharjee, S. DLS and zeta potential - What they are and what they are not? *J. Control. Release* **235**, 337–351 (2016).

22. Hassan, P. A., Rana, S. & Verma, G. Making sense of Brownian motion: Colloid characterization by dynamic light scattering. *Langmuir* **31**, 3–12 (2015).

23. Jans, H., Liu, X., Austin, L., Maes, G. & Huo, Q. Dynamic light scattering as a powerful tool for gold nanoparticle bioconjugation and biomolecular binding studies. *Anal. Chem.* **81**, 9425–9432 (2009).

24. Wright, M. Nanoparticle Tracking Analysis for the Multiparameter Characterization and Counting of Nanoparticle Suspensions. in *Nanoparticles in Biology and Medicine* (ed. Soloviev, M.) **906**, 511–524 (Humana Press, 2012).

25. Filipe, V., Hawe, A. & Jiskoot, W. Critical evaluation of nanoparticle tracking analysis (NTA) by NanoSight for the measurement of nanoparticles and protein aggregates. *Pharm. Res.* **27**, 796–810 (2010).

26. György, B. *et al.* Membrane vesicles, current state-of-the-art: Emerging role of extracellular vesicles. *Cell. Mol. Life Sci.* **68**, 2667–2688 (2011).

27. Kerr, J. F. R., Wyllie, A. H. & Currie, A. R. Apoptosis: A basic biological phenomenon with wide-ranging implications in tissue kinetics. *Br. J. Cancer* **26**, 239–257 (1972).

28. Raposo, G. & Stoorvogel, W. Extracellular vesicles: Exosomes, microvesicles, and friends. *J. Cell Biol.* **200**, 373 (2013).

29. Théry, C., Ostrowski, M. & Segura, E. Membrane vesicles as conveyors of immune responses. *Nat. Rev. Immunol.* **9**, 581–593 (2009).

30. Vlassov, A. V., Magdaleno, S., Setterquist, R. & Conrad, R. Exosomes: Current knowledge of their composition, biological functions, and diagnostic and therapeutic potentials. *Biochim. Biophys. Acta - Gen. Subj.* **1820**, 940–948 (2012).

31. Simons, M. & Raposo, G. Exosomes - vesicular carriers for intercellular communication. *Curr. Opin. Cell Biol.* **21**, 575–581 (2009).

32. Valadi, H. *et al.* Exosome-mediated transfer of mRNAs and microRNAs is a novel mechanism of genetic exchange between cells. *Nat. Cell Biol.* **9**, 654–659 (2007).

33. Al-Nedawi, K. *et al.* Intercellular transfer of the oncogenic receptor EGFRvIII by microvesicles derived from tumour cells. *Nat. Cell Biol.* **10**, 619–624 (2008).

34. Leblanc, P. *et al.* Retrovirus infection strongly enhances scrapie infectivity release in cell culture. *EMBO J.* **25**, 2674–2685 (2006).

35. Skog, J. *et al.* Glioblastoma microvesicles transport RNA and proteins that promote tumour growth and provide diagnostic biomarkers. *Nat. Cell Biol.* **10**, 1470–1476 (2008).

36. Mignot, G., Roux, S., Thery, C., Ségura, E. & Zitvogel, L. Prospects for exosomes in immunotherapy of cancer. *J. Cell. Mol. Med.* **10**, 376–388 (2006).

37. Théry, C. *et al.* Minimal information for studies of extracellular vesicles 2018 (MISEV2018): a position statement of the International Society for Extracellular Vesicles and update of the MISEV2014 guidelines. *J. Extracell. Vesicles* **7**, (2018).

38. Trams, E. G., Lauter, C. J., Norman Salem, J. & Heine, U. Exfoliation of membrane ecto-enzymes in the form of micro-vesicles. *BBA - Biomembr.* **645**, 63–70 (1981).

39. Pan, B. T. & Johnstone, R. M. Fate of the transferrin receptor during maturation of sheep reticulocytes in vitro: Selective externalization of the receptor. *Cell* **33**, 967–978 (1983).

40. Johnstone, R. M., Adam, M., Hammond, J. R., Orr, L. & Turbide, C. Vesicle formation during reticulocyte maturation. Association of plasma membrane activities with released vesicles (exosomes). *J. Biol. Chem.* **262**, 9412–9420 (1987).

41. Stoorvogel, W., Kleijmeer, M. J., Geuze, H. J. & Raposo, G. The biogenesis and functions of exosomes. *Traffic* **3**, 321–330 (2002).

42. Mathivanan, S., Ji, H. & Simpson, R. J. Exosomes: Extracellular organelles important in intercellular communication. *J. Proteomics* **73**, 1907–1920 (2010).

43. Raposo, G. *et al.* B lymphocytes secrete antigen-presenting vesicles. *J. Exp. Med.* **183**, 1161–1172 (1996).

44. Théry, C. *et al.* Molecular characterization of dendritic cell-derived exosomes: Selective accumulation of the heat shock protein hsc73. *J. Cell Biol.* **147**, 599–610 (1999).

45. Lamparski, H. G. *et al.* Production and characterization of clinical grade exosomes derived from dendritic cells. *J. Immunol. Methods* **270**, 211–226 (2002).

46. Cocucci, E., Racchetti, G. & Meldolesi, J. Shedding microvesicles: artefacts no more. *Trends Cell Biol.* **19**, 43–51 (2009).

47. Pizzirani, C. *et al.* Stimulation of P2 receptors causes release of IL-1β-loaded microvesicles from human dendritic cells. *Blood* **109**, 3856–3864 (2007).

48. Zhang, X. *et al.* Exosomes in cancer: Small particle, big player. *J. Hematol. Oncol.* **8**, 83 (2015).

49. Colombo, M., Raposo, G. & Théry, C. Biogenesis, Secretion, and Intercellular Interactions of Exosomes and Other Extracellular Vesicles. *Annu. Rev. Cell Dev. Biol.* **30**, 255–289 (2014).

50. Lehrich, B. M., Liang, Y., Khosravi, P., Federoff, H. J. & Fiandaca, M. S. Fetal Bovine Serum-Derived Extracellular Vesicles Persist within Vesicle-Depleted Culture Media. *Int. J. Mol. Sci.* **19**, 3538 (2018).

51. Théry, C., Amigorena, S., Raposo, G. & Clayton, A. Isolation and Characterization of Exosomes from Cell Culture Supernatants and Biological Fluids. in *Current Protocols in Cell Biology* **30**, 3.22.1-3.22.29 (John Wiley & Sons, Inc., 2006).

52. Cheruvanky, A. *et al.* Rapid isolation of urinary exosomal biomarkers using a nanomembrane ultrafiltration concentrator. *Am. J. Physiol. - Ren. Physiol.* **292**, F1657 (2007).

53. Böing, A. N. *et al.* Single-step isolation of extracellular vesicles by size-exclusion chromatography. *J. Extracell. Vesicles* **3**, 23430 (2014).

54. Nordin, J. Z. *et al.* Ultrafiltration with size-exclusion liquid chromatography for high yield isolation of extracellular vesicles preserving intact biophysical and functional properties. *Nanomedicine Nanotechnology, Biol. Med.* **11**, 879–883 (2015).

55. Mathivanan, S. *et al.* Proteomics analysis of A33 immunoaffinity-purified exosomes released from the human colon tumor cell line LIM1215 reveals a tissue-specific protein signature. *Mol. Cell. Proteomics* **9**, 197–208 (2010).

56. Koga, K. *et al.* Purification, characterization and biological significance of tumor-derived

exosomes. *Anticancer Res.* **25**, 3703–3707 (2005).

57. Van Der Pol, E. *et al.* Optical and non-optical methods for detection and characterization of microparticles and exosomes. *J. Thromb. Haemost.* **8**, 2596–2607 (2010).

58. Soo, C. Y. *et al.* Nanoparticle tracking analysis monitors microvesicle and exosome secretion from immune cells. *Immunology* **136**, 192–197 (2012).

59. Dragovic, R. A. *et al.* Sizing and phenotyping of cellular vesicles using Nanoparticle Tracking Analysis. *Nanomedicine Nanotechnology, Biol. Med.* **7**, 780–788 (2011).

60. Hoen, E. N. M. N. N.-'t *et al.* Quantitative and qualitative flow cytometric analysis of nanosized cell-derived membrane vesicles. *Nanomedicine Nanotechnology, Biol. Med.* **8**, 712–720 (2012).

61. van der Vlist, E. J., Nolte-'t Hoen, E. N. M., Stoorvogel, W., Arkesteijn, G. J. A. & Wauben, M. H. M. Fluorescent labeling of nano-sized vesicles released by cells and subsequent quantitative and qualitative analysis by high-resolution flow cytometry. *Nat. Protoc.* **7**, 1311–1326 (2012).

62. Tatischeff, I., Larquet, E., Falcón-Pérez, J. M., Turpin, P.-Y. & Kruglik, S. G. Fast characterisation of cell-derived extracellular vesicles by nanoparticles tracking analysis, cryo-electron microscopy, and Raman tweezers microspectroscopy. *J. Extracell. Vesicles* **1**, 19179 (2012).

63. Kleijmeer, M. *et al.* Reorganization of multivesicular bodies regulates MHC class II 11 antigen presentation by dendritic cells. *J. Cell Biol.* **155**, 53–63 (2001).

64. Février, B. & Raposo, G. Exosomes: Endosomal-derived vesicles shipping extracellular messages. *Curr. Opin. Cell Biol.* **16**, 415–421 (2004).

65. Chu, Z., Witte, D. P. & Qi, X. Saposin C-LBPA interaction in late-endosomes/lysosomes. *Exp. Cell Res.* **303**, 300–307 (2005).

66. Hurley, J. H. ESCRT complexes and the biogenesis of multivesicular bodies. *Curr. Opin. Cell Biol.* **20**, 4–11 (2008).

67. Buschow, S. I., Liefhebber, J. M. P., Wubbolts, R. & Stoorvogel, W. Exosomes contain ubiquitinated proteins. *Blood Cells, Mol. Dis.* **35**, 398–403 (2005).

68. Johnstone, R. M., Mathew, A., Mason, A. B. & Teng, K. Exosome formation during maturation of mammalian and avian reticulocytes: Evidence that exosome release is a major route for externalization of obsolete membrane proteins. *J. Cell. Physiol.* **147**, 27–36 (1991).

69. Gould, S. J., Booth, A. M. & Hildreth, J. E. K. The Trojan exosome hypothesis. *Proc. Natl. Acad. Sci. U. S. A.* **100**, 10592–10597 (2003).

70. Pelchen-Matthews, A., Raposo, G. & Marsh, M. Endosomes, exosomes and Trojan viruses. *Trends Microbiol.* **12**, 310–316 (2004).

71. Skehel, J. J. & Wiley, D. C. Receptor Binding and Membrane Fusion in Virus Entry: The Influenza Hemagglutinin. *Annu. Rev. Biochem.* **69**, 531–569 (2000).

72. Fuhrmann, G., Herrmann, I. K. & Stevens, M. M. Cell-derived vesicles for drug therapy and diagnostics: Opportunities and challenges. *Nano Today* **10**, 397–409 (2015).

73. Chen, X. *et al.* Characterization of microRNAs in serum: A novel class of biomarkers for diagnosis of cancer and other diseases. *Cell Res.* **18**, 997–1006 (2008).

74. Rabinowits, G., Gerçel-Taylor, C., Day, J. M., Taylor, D. D. & Kloecker, G. H. Exosomal microRNA: A diagnostic marker for lung cancer. *Clin. Lung Cancer* **10**, 42–46 (2009).

75. Nilsson, J. *et al.* Prostate cancer-derived urine exosomes: A novel approach to biomarkers for prostate cancer. *Br. J. Cancer* **100**, 1603–1607 (2009).

76. Escudier, B. *et al.* Vaccination of metastatic melanoma patients with autologous dendritic cell (DC) derived-exosomes: Results of the first phase 1 clinical trial. *J. Transl. Med.* **3**, 10 (2005).

77. Chaput, N. & Théry, C. Exosomes: Immune properties and potential clinical implementations. *Semin. Immunopathol.* **33**, 419–440 (2011).

78. Van Der Meel, R. *et al.* Extracellular vesicles as drug delivery systems: Lessons from the liposome field. *J. Control. Release* **195**, 72–85 (2014).

79. Vader, P., Mol, E. A., Pasterkamp, G. & Schiffelers, R. M. Extracellular vesicles for drug delivery. *Adv. Drug Deliv. Rev.* **106**, 148–156 (2016).

80. Kosaka, N. *et al.* Secretory mechanisms and intercellular transfer of microRNAs in living cells. *J. Biol. Chem.* **285**, 17442–17452 (2010).

81. Smith, E. & Dent, G. *Modern Raman Spectroscopy - A Practical Approach*. (John Wiley & Sons, Ltd, 2004).

82. Swain, R. J. & Stevens, M. M. Raman microspectroscopy for non-invasive biochemical analysis of single cells. *Biochem. Soc. Trans.* **35**, 544–549 (2007).

83. Movasaghi, Z., Rehman, S. & Rehman, I. U. Raman spectroscopy of biological tissues. *Appl. Spectrosc. Rev.* **42**, 493–541 (2007).

84. Krafft, C. Bioanalytical applications of Raman spectroscopy. *Anal. Bioanal. Chem.* **378**, 60–62 (2004).

85. Hedegaard, M. A. B., Bergholt, M. S. & Stevens, M. M. Quantitative multi-image analysis for biomedical Raman spectroscopic imaging. *J. Biophotonics* **9**, 542–550 (2016).

86. McCreery, R. L. Raman Spectroscopy for Chemical Analysis. *Meas. Sci. Technol.* **12**, 653–654 (2001).

87. Mozharov, S., Nordon, A., Littlejohn, D. & Marquardt, B. Automated cosmic spike filter optimized for process Raman spectroscopy. *Appl. Spectrosc.* **66**, 1326–1333 (2012).

88. Chew, W. Information-theoretic chemometric analyses of Raman data for chemical reaction studies. *J. Raman Spectrosc.* **42**, 36–47 (2011).

89. Li, S. & Dai, L. An improved algorithm to remove cosmic spikes in Raman spectra for online monitoring. *Appl. Spectrosc.* **65**, 1300–1306 (2011).

90. Brennan, J. F., Wang, Y., Dasari, R. R. & Feld, M. S. Near-infrared Raman spectrometer systems for human tissue studies. *Appl. Spectrosc.* **51**, 201–208 (1997).

91. Beier, B. D. & Berger, A. J. Method for automated background subtraction from Raman spectra containing known contaminants. *Analyst* **134**, 1198–1202 (2009).

92. Wold, S., Esbensen, K. & Geladi, P. Principal component analysis. *Chemom. Intell. Lab. Syst.* **2**, 37–52 (1987).

93. Wang, Z. L. Transmission electron microscopy of shape-controlled nanocrystals and their assemblies. *J. Phys. Chem. B* **104**, 1153–1175 (2000).

94. Amelinckx, S., Van Dyck, D., Van Landuyt, J. & Van Tendeloo, G. *Electron Microscopy*. *Electron Microscopy: Principles and Fundamentals* (Wiley, 1997).

95. Gopal, S. *et al.* Porous Silicon Nanoneedles Modulate Endocytosis to Deliver Biological Payloads. *Adv. Mater.* **31**, 1806788 (2019).

96. Midgley, P. A. & Weyland, M. 3D electron microscopy in the physical sciences: The development of Z-contrast and EFTEM tomography. in *Ultramicroscopy* **96**, 413–431 (2003).

97. Baumeister, W., Grimm, R. & Walz, J. Electron tomography of molecules and cells. *Trends in Cell Biology* **9**, 81–85 (1999).

98. Thompson, R. F., Walker, M., Siebert, C. A., Muench, S. P. & Ranson, N. A. An introduction to sample preparation and imaging by cryo-electron microscopy for structural biology. *Methods* **100**, 3–15 (2016).

99. Jung, M. K. & Mun, J. Y. Sample preparation and imaging of exosomes by transmission electron microscopy. *J. Vis. Exp.* **2018**, (2018).

100. Nixon, W. C. The General Principles of Scanning Electron Microscopy. *Philos. Trans. R. Soc. B Biol. Sci.* **261**, 45–50 (1971).

101. Villinger, C. *et al.* FIB/SEM tomography with TEM-like resolution for 3D imaging of high-pressure frozen cells. *Histochem. Cell Biol.* **138**, 549–556 (2012).

102. Reznikov, N., Almany-Magal, R., Shahar, R. & Weiner, S. Three-dimensional imaging of collagen fibril organization in rat circumferential lamellar bone using a dual beam electron microscope reveals ordered and disordered sub-lamellar structures. *Bone* **52**, 676–683 (2013).

103. Drobne, D. 3D Imaging of Cells and Tissues by Focused Ion Beam/Scanning Electron Microscopy (FIB/SEM). in *Nanoimaging* (eds. Sousa, A. A. & Kruhlak, M. J.) **950**, 275–292 (Humana Press, 2013).

104. Aronova, M. A., Sousa, A. A., Zhang, G. & Leapman, R. D. Limitations of beam damage in electron spectroscopic tomography of embedded cells. *J. Microsc.* **239**, 223–232 (2010).

105. Maugel, T. K. & Hayat, M. A. Principles and Techniques of Electron Microscopy: Biological Applications. *Trans. Am. Microsc. Soc.* **96**, 272 (1977).

106. Gopal, S. *et al.* Immunogold FIB-SEM: Combining Volumetric Ultrastructure Visualization with 3D Biomolecular Analysis to Dissect Cell-Environment Interactions. *Adv. Mater.* **31**, 1900488 (2019).

107. Kim, Y. J. *et al.* Morphological analysis of cells by scanning electron microscopy. *Jpn. J. Appl. Phys.* **47**, 1325–1328 (2008).

108. Guehrs, E. *et al.* Quantification of silver nanoparticle uptake and distribution within individual human macrophages by FIB/SEM slice and view. *J. Nanobiotechnology* **15**, 21 (2017).

109. Wierzbicki, R. *et al.* Mapping the Complex Morphology of Cell Interactions with Nanowire Substrates Using FIB-SEM. *PLoS One* **8**, e53307 (2013).

110. Adjei, I. M., Peetla, C. & Labhasetwar, V. Heterogeneity in nanoparticles influences biodistribution and targeting. *Nanomedicine* **9**, 267–278 (2014).

111. Mullen, D. G. & Banaszak Holl, M. M. Heterogeneous ligand-nanoparticle distributions: A major obstacle to scientific understanding and commercial translation. *Acc. Chem. Res.* **44**, 1135–1145 (2011).

112. Penders, J. *et al.* Single Particle Automated Raman Trapping Analysis. *Nat. Commun.* **9**, 4256 (2018).

113. Park, K. Controlled drug delivery systems: Past forward and future back. *J. Control. Release* **190**, 3–8 (2014).

114. Hibbert, C. Time to deliver. *Engineering* **249**, 36–37 (2008).

115. Domingos, R. F. *et al.* Characterizing manufactured nanoparticles in the environment: Multimethod determination of particle sizes. *Environ. Sci. Technol.* **43**, 7277–7284 (2009).

116. Chiang, C. K., Chen, W. T. & Chang, H. T. Nanoparticle-based mass spectrometry for the analysis of biomolecules. *Chem. Soc. Rev.* **40**, 1269–1281 (2011).

117. Kim, J. H., Bryan, W. W. & Lee, T. R. Preparation, characterization, and optical properties of gold, silver, and gold-silver alloy nanoshells having silica cores. *Langmuir* **24**, 11147–11152 (2008).

118. Zhang, Y. & Zhuo, R. Synthesis and in vitro drug release behavior of amphiphilic triblock copolymer nanoparticles based on poly (ethylene glycol) and polycaprolactone. *Biomaterials* **26**, 6736–6742 (2005).

119. Lebedew, P. Untersuchungen über die Druckkräfte des Lichtes. *Ann. Phys.* **311**, 433–458 (1901).

120. Ashkin, A. Acceleration and Trapping of Particles by Radiation Pressure. *Phys. Rev. Lett.* **24**, 156–159 (1970).

121. Ashkin, A. History of optical trapping and manipulation of small-neutral particle, atoms, and molecules. *IEEE J. Sel. Top. Quantum Electron.* **6**, 841–856 (2000).

122. Ashkin, A., Dziedzic, J. M., Bjorkholm, J. E. & Chu, S. Observation of a single-beam gradient force optical trap for dielectric particles. *Opt. Angular Momentum* **11**, 196–198 (2016).

123. Buehler, M. F., Allen, T. M. & Davis, E. J. Microparticle raman spectroscopy of multicomponent aerosols. *J. Colloid Interface Sci.* **146**, 79–89 (1991).

124. Cherney, D. P., Bridges, T. E. & Harris, J. M. Optical trapping of unilamellar phospholipid vesicles: Investigation of the effect of optical forces on the lipid membrane shape by confocal-Raman microscopy. *Anal. Chem.* **76**, 4920–4928 (2004).

125. Ichikawa, M. & Yoshikawa, K. Optical transport of a single cell-sized liposome. *Appl. Phys. Lett.* **79**, 4598–4600 (2001).

126. Chu, S., Hollberg, L., Bjorkholm, J. E., Cable, A. & Ashkin, A. Three-dimensional viscous confinement and cooling of atoms by resonance radiation pressure. *Phys. Rev. Lett.* **55**, 48–51 (1985).

127. Cohen-Tannoudji, C. N. Manipulating atoms with photons. *Rev. Mod. Phys.* **70**, 707–719 (1998).

128. Phillips, W. D. & Metcalf, H. Laser deceleration of an atomic beam. *Phys. Rev. Lett.* **48**, 596–599 (1982).

129. Phillips, W. D. Laser cooling and trapping of neutral atoms. *Rev. Mod. Phys.* **70**, 721–741 (1998).

130. Ketterle, W. When atoms behave as waves: Bose-Einstein condensation and the atom laser (nobel lecture). *ChemPhysChem* **3**, 736–753 (2002).

131. Ashkin, A. & Dziedzic, J. M. Optical trapping and manipulation of viruses and bacteria. *Science (80-.).* **235**, 1517–1520 (1987).

132. Ashkin, A., Dziedzic, J. M. & Yamane, T. Optical trapping and manipulation of single cells using infrared laser beams. *Nature* **330**, 769–771 (1987).

133. Ashkin, A. & Dziedzic, J. M. Internal cell manipulation using infrared laser traps. *Proc. Natl. Acad. Sci. U. S. A.* **86**, 7914–7918 (1989).

134. Smith, S. B., Cui, Y. & Bustamante, C. Overstretching B-DNA: The elastic response of individual double-stranded and single-stranded DNA molecules. *Science (80-.).* **271**, 795–799 (1996).

135. Block, S. M., Goldstein, L. S. B. & Schnapp, B. J. Bead movement by single kinesin molecules studied with optical tweezers. *Nature* **348**, 348–352 (1990).

136. Svoboda, K., Schmidt, C. F., Schnapp, B. J. & Block, S. M. Direct observation of kinesin stepping by optical trapping interferometry. *Nature* **365**, 721–727 (1993).

137. Delhaye, M. & Dhamelincourt, P. Raman microprobe and microscope with laser excitation. *J. Raman Spectrosc.* **3**, 33–43 (1975).

138. Thurn, R. & Kiefer, W. Observations of structural resonances in the Raman spectra of optically levitated dielectric microspheres. *J. Raman Spectrosc.* **15**, 411–413 (1984).

139. Thurn, R. & Kiefer, W. Raman-Microsampling Technique Applying Optical Levitation By Radiation Pressure. *Appl. Spectrosc.* **38**, 78–83 (1984).

140. Ashkin, A. & Dziedzic, J. M. Optical levitation by radiation pressure. *Appl. Phys. Lett.* **19**, 283–285 (1971).

141. Schweiger, G. Raman scattering on single aerosol particles and on flowing aerosols: a review. *J. Aerosol Sci.* **21**, 483–509 (1990).

142. Petrov, D. V. Raman spectroscopy of optically trapped particles. *J. Opt. A Pure Appl. Opt.* **9**, S139–S156 (2007).

143. Carls, J. C., Moncivais, G. & Brock, J. R. Time-resolved Raman spectroscopy from reacting optically levitated microdroplets. *Appl. Opt.* **29**, 2913 (1990).

144. Ajito, K. Combined near-infrared raman microprobe and laser trapping system: Application to the analysis of a single organic microdroplet in water. *Appl. Spectrosc.* **52**, 339–342 (1998).

145. Ajito, K. & Torimitsu, K. Single nanoparticle trapping using a Raman tweezers microscope. *Appl. Spectrosc.* **56**, 541–544 (2002).

146. Xie, C., Dinno, M. A. & Li, Y. Near-infrared Raman spectroscopy of single optically trapped biological cells. *Opt. Lett.* **27**, 249 (2002).

147. Ajito, K. & Torimitsu, K. Laser trapping and Raman spectroscopy of single cellular organelles in the nanometer range. in *Lab on a Chip* **2**, 11–14 (2002).

148. Sanderson, J. M. & Ward, A. D. Analysis of liposomal membrane composition using Raman tweezers. *Chem. Commun.* **10**, 1120–1121 (2004).

149. Palivan, C. G. *et al.* Bioinspired polymer vesicles and membranes for biological and medical applications. *Chem. Soc. Rev.* **45**, 377–411 (2016).

150. Cherney, D. P., Conboy, J. C. & Harris, J. M. Optical-Trapping Raman Microscopy Detection of Single Unilamellar Lipid Vesicles. *Anal. Chem.* **75**, 6621–6628 (2003).

151. Urlaub, E. *et al.* Raman investigation of styrene polymerization in single optically trapped emulsion particles. *Chem. Phys. Lett.* **231**, 511–514 (1994).

152. Schaefer, J. J., Crawford, A. C., Porter, M. D. & Harris, J. M. Confocal Raman microscopy for investigating synthesis and characterization of individual optically trapped vinyl-polymerized surfactant particles. *Appl. Spectrosc.* **68**, 633–641 (2014).

153. Houlne, M. P., Sjostrom, C. M., Uibel, R. H., Kleimeyer, J. A. & Harris, J. M. Confocal Raman microscopy for monitoring chemical reactions on single optically trapped, solid-phase support particles. *Anal. Chem.* **74**, 4311–4319 (2002).

154. Hardcastle, C. D. & Harris, J. M. Confocal Raman Microscopy for pH-Gradient Preconcentration and Quantitative Analyte Detection in Optically Trapped Phospholipid Vesicles. *Anal. Chem.* **87**, 7979–7986 (2015).

155. Stremersch, S. *et al.* Identification of individual exosome-like vesicles by surface enhanced raman spectroscopy. *Small* **12**, 3292–3301 (2016).

156. Smith, Z. J. *et al.* Single exosome study reveals subpopulations distributed among cell lines with variability related to membrane content. *J. Extracell. Vesicles* **4**, 28533 (2015).

157. Kolb, H. C., Finn, M. G. & Sharpless, K. B. Click Chemistry: Diverse Chemical Function from a Few Good Reactions. *Angew. Chemie - Int. Ed.* **40**, 2004–2021 (2001).

158. Lutz, J. F. & Zarafshani, Z. Efficient construction of therapeutics, bioconjugates, biomaterials and bioactive surfaces using azide-alkyne 'click' chemistry. *Adv. Drug Deliv. Rev.* **60**, 958–970 (2008).

159. Bridges, T. E., Houlne, M. P. & Harris, J. M. Spatially Resolved Analysis of Small Particles by Confocal Raman Microscopy: Depth Profiling and Optical Trapping. *Anal. Chem.* **76**, 576–584 (2004).

160. Cherney, D. P. & Harris, J. M. Confocal Raman Microscopy of Optical-Trapped Particles in Liquids. *Annu. Rev. Anal. Chem.* **3**, 277–297 (2010).

161. Ajito, K. & Torimitsu, K. Near-infrared Raman spectroscopy of single particles. *TrAC - Trends Anal. Chem.* **20**, 255–262 (2001).

162. Leitz, G., Fällman, E., Tuck, S. & Axner, O. Stress response in Caenorhabditis elegans caused by optical tweezers: Wavelength, power, and time dependence. *Biophys. J.* **82**, 2224–2231 (2002).

163. Yamakoshi, H. *et al.* Alkyne-tag Raman imaging for visualization of mobile small molecules in live cells. *J. Am. Chem. Soc.* **134**, 20681–20689 (2012).

164. Cai, D., Neyer, A., Kuckuk, R. & Heise, H. M. Raman, mid-infrared, near-infrared and ultraviolet-visible spectroscopy of PDMS silicone rubber for characterization of polymer optical waveguide materials. *J. Mol. Struct.* **976**, 274–281 (2010).

165. Yoo, B. K. & Joo, S. W. In situ Raman monitoring triazole formation from self-assembled monolayers of 1,4-diethynylbenzene on Ag and Au surfaces via 'click' cyclization. *J. Colloid Interface Sci.* **311**, 491–496 (2007).

166. Bazylewski, P., Divigalpitiya, R. & Fanchini, G. In situ Raman spectroscopy distinguishes between reversible and irreversible thiol modifications in l-cysteine. *RSC Adv.* **7**, 2964–2970 (2017).

167. Cho, E. J. *et al.* Nanoparticle characterization: State of the art, challenges, and emerging technologies. *Mol. Pharm.* **10**, 2093–2110 (2013).

168. Wei, H. & Wang, E. Nanomaterials with enzyme-like characteristics (nanozymes): Next-generation artificial enzymes. *Chem. Soc. Rev.* **42**, 6060–6093 (2013).

169. Todorova, N. *et al.* Surface presentation of functional peptides in solution determines cell internalization efficiency of TAT conjugated nanoparticles. *Nano Lett.* **14**, 5229–5237 (2014).

170. Almeida, C. S., Herrmann, I. K., Howes, P. D. & Stevens, M. M. Tailoring Cellular Uptake of Conjugated Polymer Nanoparticles Using Modular Amphiphilic Peptide Capping Ligands. *Chem. Mater.* **27**, 6879–6889 (2015).

171. Luongo, G. *et al.* Scalable High-Affinity Stabilization of Magnetic Iron Oxide Nanostructures by a Biocompatible Antifouling Homopolymer. *ACS Appl. Mater. Interfaces* **9**, 40059–40069 (2017).

172. Algar, W. R. *et al.* The controlled display of biomolecules on nanoparticles: A challenge suited to bioorthogonal chemistry. *Bioconjug. Chem.* **22**, 825–858 (2011).

173. Zhou, H. *et al.* Urinary exosomal transcription factors, a new class of biomarkers for renal disease. *Kidney Int.* **74**, 613–621 (2008).

174. Shin, H., Jeong, H., Park, J., Hong, S. & Choi, Y. Correlation between Cancerous Exosomes and Protein Markers Based on Surface-Enhanced Raman Spectroscopy (SERS) and Principal Component Analysis (PCA). *ACS Sensors* **3**, 2637–2643 (2018).

175. Lee, W. *et al.* Label-Free Prostate Cancer Detection by Characterization of Extracellular Vesicles Using Raman Spectroscopy. *Anal. Chem.* **90**, 11290–11296 (2018).

176. Lazaro-Pacheco, D., Shaaban, A. M., Rehman, S. & Rehman, I. Raman spectroscopy of breast cancer. *Appl. Spectrosc. Rev.* 1–37 (2019).

177. Auner, G. W. *et al.* Applications of Raman spectroscopy in cancer diagnosis. *Cancer Metastasis Rev.* **37**, 691–717 (2018).

178. Lieber, C. A., Majumder, S. K., Ellis, D. L., Billheimer, D. D. & Mahadevan-Jansen, A. In vivo nonmelanoma skin cancer diagnosis using Raman microspectroscopy. *Lasers Surg. Med.* **40**, 461–467 (2008).

179. Lui, H., Zhao, J., McLean, D. & Zeng, H. Real-time raman spectroscopy for in vivo skin cancer diagnosis. *Cancer Res.* **72**, 2491–2500 (2012).

180. Globocan. *The Global Cancer Observatory, Breast Cancer Fact sheet*. (2018).

181. Polyak, K. Heterogeneity in breast cancer. *Journal of Clinical Investigation* **121**, 3786–3788 (2011).

182. Ross, J. S. *et al.* The HER-2 Receptor and Breast Cancer: Ten Years of Targeted Anti-HER-2 Therapy and Personalized Medicine. *Oncologist* **14**, 320–368 (2009).

183. Freedman, D. A., Petitti, D. B. & Robins, J. M. On the efficacy of screening for breast cancer. *International Journal of Epidemiology* **33**, 43–55 (2004).

184. Warner, E. *et al.* Surveillance of BRCA1 and BRCA2 mutation carriers with magnetic resonance imaging, ultrasound, mammography, and clinical breast examination. *J. Am. Med. Assoc.* **292**, 1317–1325 (2004).

185. Pusztai, L. Molecular Classification of Breast Cancer: Limitations and Potential. *Oncologist* **11**, 868–877 (2006).

186. Ralbovsky, N. M. & Lednev, I. K. Raman spectroscopy and chemometrics: A potential universal method for diagnosing cancer. *Spectrochim. Acta - Part A Mol. Biomol. Spectrosc.* **219**, 463–487 (2019).

187. Lyng, F. M. *et al.* Discrimination of breast cancer from benign tumours using Raman spectroscopy. *PLoS One* **14**, e0212376 (2019).

188. Manoharan, R., Wang, Y. & Feld, M. S. Histochemical analysis of biological tissues using Raman spectroscopy. *Spectrochim. Acta Part A Mol. Biomol. Spectrosc.* **52**, 215–249 (1996).

189. Chaturvedi, D. *et al.* Different Phases of Breast Cancer Cells: Raman Study of Immortalized, Transformed, and Invasive Cells. *Biosensors* **6**, 57 (2016).

190. Talari, A. C. S., Evans, C. A., Holen, I., Coleman, R. E. & Rehman, I. U. Raman spectroscopic analysis differentiates between breast cancer cell lines. *J. Raman Spectrosc.* **46**, 421–427 (2015).

191. Paget, S. the Distribution of Secondary Growths in Cancer of the Breast. *Lancet* **133**, 571–573 (1889).

192. Hoshino, A. *et al.* Tumour exosome integrins determine organotropic metastasis. *Nature* **527**, 329–335 (2015).

193. Kaplan, R. N. *et al.* VEGFR1-positive haematopoietic bone marrow progenitors initiate the pre-metastatic niche. *Nature* **438**, 820–827 (2005).

194. Costa-Silva, B. *et al.* Pancreatic cancer exosomes initiate pre-metastatic niche formation in the liver. *Nat. Cell Biol.* **17**, 816–826 (2015).

195. Peinado, H. *et al.* Melanoma exosomes educate bone marrow progenitor cells toward a pro-metastatic phenotype through MET. *Nat. Med.* **18**, 883–891 (2012).

196. Carney, R. P. *et al.* Multispectral Optical Tweezers for Biochemical Fingerprinting of CD9-Positive Exosome Subpopulations. *Anal. Chem.* **89**, 5357–5363 (2017).

197. Kruglik, S. G. *et al.* Raman tweezers microspectroscopy of: Circa 100 nm extracellular vesicles. *Nanoscale* **11**, 1661–1679 (2019).

198. Rojalin, T., Phong, B., Koster, H. & Carney, R. P. Nanoplasmonic approaches for sensitive detection and molecular characterization of extracellular vesicles. *Front. Chem.* **7**, (2019).

199. Yan, Z. *et al.* A Label-free platform for identification of exosomes from different sources. *ACS Sensors* **4**, 488–497 (2019).

200. Gaigalas, A. K., Wang, L., He, H. J. & DeRose, P. Procedures for wavelength calibration and spectral response correction of CCD array spectrometers. *J. Res. Natl. Inst. Stand. Technol.* **114**, 1–14 (2009).

201. Wubbolts, R. *et al.* Proteomic and biochemical analyses of human B cell-derived exosomes: Potential implications for their function and multivesicular body formation. *J. Biol. Chem.* **278**, 10963–10972 (2003).

202. Gerlach, J. Q. & Griffin, M. D. Getting to know the extracellular vesicle glycome. *Mol. Biosyst.* **12**, 1071–1081 (2016).

203. Chen, I. H. *et al.* Analytical Pipeline for Discovery and Verification of Glycoproteins from Plasma-Derived Extracellular Vesicles as Breast Cancer Biomarkers. *Anal. Chem.* **90**, 6307–6313 (2018).

204. Vidavsky, N. *et al.* Mapping and Profiling Lipid Distribution in a 3D Model of Breast Cancer Progression. *ACS Cent. Sci.* **5**, 768–780 (2019).

205. Borland, D. & Taylor, R. M. Rainbow color map (still) considered harmful. *IEEE Comput. Graph. Appl.* **27**, 14–17 (2007).

206. Eddins, S. (MathWorks). Rainbow Color Map Critiques : An Overview and Annotated Bibliography. 1–18 (2014).

207. Joint ISO/CIE Standard. *Colorimetry -- Part 4: CIE 1976 L*a*b* Colour space*. *Iso 11664-4:2008 (Cie S 014-4/E:2007)* (2008).

208. Sperling, R. A., Rivera Gil, P., Zhang, F., Zanella, M. & Parak, W. J. Biological applications of gold nanoparticles. *Chem. Soc. Rev.* **37**, 1896–1908 (2008).

209. D. Howes, P., Rana, S. & M. Stevens, M. Plasmonic nanomaterials for biodiagnostics. *Chem. Soc. Rev.* **43**, 3835–3853 (2014).

210. de la Rica, R. *et al.* A designer peptide as a template for growing Au nanoclusters. *Chem. Commun.* **50**, 10648–10650 (2014).

211. Hembury, M. *et al.* Gold-silica quantum rattles for multimodal imaging and therapy. *Proc. Natl. Acad. Sci. U. S. A.* **112**, 1959–1964 (2015).

212. Klingberg, H. *et al.* Uptake of gold nanoparticles in primary human endothelial cells. *Toxicol. Res. (Camb).* **4**, 655–666 (2015).

213. Dykman, L. A. & Khlebtsov, N. G. Uptake of Engineered Gold Nanoparticles into Mammalian Cells. *Chem. Rev.* **114**, 1258–1288 (2014).

214. Glotzer, S. C. & Solomon, M. J. Anisotropy of building blocks and their assembly into complex structures. *Nat. Mater.* **6**, 557–562 (2007).

215. Wintzheimer, S. *et al.* Supraparticles: Functionality from Uniform Structural Motifs. *ACS Nano* **12**, 5093–5120 (2018).

216. Xia, Y. & Tang, Z. Monodisperse inorganic supraparticles: Formation mechanism, properties and applications. *Chem. Commun.* **48**, 6320–6336 (2012).

217. Velev, O. D., Furusawa, K. & Nagayama, K. Assembly of latex particles by using emulsion droplets as templates. 2. Ball-like and composite aggregates. *Langmuir* **12**, 2385–2391 (1996).

218. Manoharan, V. N. Colloidal matter: Packing, geometry, and entropy. *Science (80-.).* **349**, 1253751–1253751 (2015).

219. Duguet, E., Désert, A., Perro, A. & Ravaine, S. Design and elaboration of colloidal molecules: An overview. *Chem. Soc. Rev.* **40**, 941–960 (2011).

220. Piccinini, E., Pallarola, D., Battaglini, F. & Azzaroni, O. Self-limited self-assembly of nanoparticles into supraparticles: Towards supramolecular colloidal materials by design. *Mol. Syst. Des. Eng.* **1**, 155–162 (2016).

221. Wang, Y., He, J., Liu, C., Chong, W. H. & Chen, H. Thermodynamics versus kinetics in Nanosynthesis. *Angew. Chemie - Int. Ed.* **54**, 2022–2051 (2015).

222. Yang, F. *et al.* Multifunctional Self-Assembled Supernanoparticles for Deep-Tissue Bimodal Imaging and Amplified Dual-Mode Heating Treatment. *ACS Nano* **13**, 408–420 (2019).

223. Al Zaki, A. *et al.* Gold-Loaded Polymeric Micelles for Computed Tomography-Guided Radiation Therapy Treatment and Radiosensitization. *ACS Nano* **8**, 104–112 (2014).

224. Paterson, S., Thompson, S. A., Gracie, J., Wark, A. W. & De La Rica, R. Self-assembly of gold supraparticles with crystallographically aligned and strongly coupled nanoparticle building blocks for SERS and photothermal therapy. *Chem. Sci.* **7**, 6232–6237 (2016).

225. Shichibu, Y., Kamei, Y. & Konishi, K. Unique [core+two] structure and optical property of a dodeca-ligated undecagold cluster: Critical contribution of the exo gold atoms to the electronic structure. *Chem. Commun.* **48**, 7559–7561 (2012).

226. Teo, B. K., Shi, X. & Zhang, H. Pure Gold Cluster of 1:9:9:1:9:9:1 Layered Structure: A Novel 39-Metal-Atom Cluster [(Ph 3 P) 14 Au 39 Cl 6]Cl 2 with an Interstitial Gold Atom in a Hexagonal Antiprismatic Cage. *J. Am. Chem. Soc.* **114**, 2743–2745 (1992).

227. Harkness, K. M., Cliffel, D. E. & McLean, J. A. Characterization of thiolate-protected gold nanoparticles by mass spectrometry. *Analyst* **135**, 868–874 (2010).

228. Jadzinsky, P. D., Calero, G., Ackerson, C. J., Bushnell, D. A. & Kornberg, R. D. Structure of a thiol monolayer-protected gold nanoparticle at 1.1 Å resolution. *Science (80-.).* **318**, 430–433 (2007).

229. Zheng, J., Petty, J. T. & Dickson, R. M. High quantum yield blue emission from water-soluble Au8 nanodots. *J. Am. Chem. Soc.* **125**, 7780–7781 (2003).

230. Yang, Y. & Chen, S. Surface manipulation of the electronic energy of subnanometer-sized gold clusters: An electrochemical and spectroscopic investigation. *Nano Lett.* **3**, 75–79 (2003).

231. Wilcoxon, J. P. & Abrams, B. L. Synthesis, structure and properties of metal nanoclusters. *Chemical Society Reviews* **35**, 1162–1194 (2006).

232. Negishi, Y., Nobusada, K. & Tsukuda, T. Glutathione-protected gold clusters revisited: Bridging the gap between gold(I)-thiolate complexes and thiolate-protected gold nanocrystals. *J. Am. Chem. Soc.* **127**, 5261–5270 (2005).

233. Zhu, M., Lanni, E., Garg, N., Bier, M. E. & Jin, R. Kinetically controlled, high-yield synthesis of Au25 clusters. *J. Am. Chem. Soc.* **130**, 1138–1139 (2008).

234. Xie, X., Liao, J., Shao, X., Li, Q. & Lin, Y. The Effect of shape on Cellular Uptake of Gold Nanoparticles in the forms of Stars, Rods, and Triangles. *Sci. Rep.* **7**, (2017).

235. Favi, P. M. *et al.* Shape and surface chemistry effects on the cytotoxicity and cellular uptake of metallic nanorods and nanospheres. *J. Biomed. Mater. Res. - Part A* **103**, 3940–3955 (2015).

236. Pernodet, N. *et al.* Adverse effects of citrate/gold nanoparticles on human dermal fibroblasts. *Small* **2**, 766–773 (2006).

237. Penders, J., Stolzoff, M., Hickey, D. J., Andersson, M. & Webster, T. J. Shape-dependent antibacterial effects of non-cytotoxic gold nanoparticles. *Int. J. Nanomedicine* **12**, 2457–2468 (2017).

238. Zhang, Y., Shareena Dasari, T. P., Deng, H. & Yu, H. Antimicrobial Activity of Gold Nanoparticles and Ionic Gold. *J. Environ. Sci. Heal. - Part C Environ. Carcinog. Ecotoxicol. Rev.* **33**, 286–327 (2015).

239. Huang, X., El-Sayed, I. H., Qian, W. & El-Sayed, M. A. Cancer cell imaging and photothermal therapy in the near-infrared region by using gold nanorods. *J. Am. Chem. Soc.* **128**, 2115–2120 (2006).

240. Guo, J. *et al.* Gold nanoparticles enlighten the future of cancer theranostics. *Int. J. Nanomedicine* **12**, 6131–6152 (2017).

241. Krpetić, Ž. *et al.* Negotiation of intracellular membrane barriers by TAT-modified gold nanoparticles. *ACS Nano* **5**, 5195–5201 (2011).

242. Faulk, W. P. & Taylor, G. M. An immunocolloid method for the electron microscope. *Immunochemistry* **8**, 1081–3 (1971).

243. Koster, A. J. & Klumperman, J. Electron microscopy in cell biology: Integrating structure and function. *Nat. Rev. Mol. Cell Biol.* **4**, SS6-10 (2003).

244. Roth, J. The silver anniversary of gold: 25 years of the colloidal gold marker system for immunocytochemistry and histochemistry. *Histochem. Cell Biol.* **106**, 1–8 (1996).

245. Evergren, E. *et al.* A pre-embedding immunogold approach for detection of synaptic endocytic proteins in situ. *J. Neurosci. Methods* **135**, 169–174 (2004).

246. Yi, H., Leunissen, J. L. M., Shi, G. M., Gutekunst, C. A. & Hersch, S. M. A novel procedure for pre-embedding double immunogold-silver labeling at the ultrastructural level. *J. Histochem. Cytochem.* **49**, 279–283 (2001).

247. Hoenger, A. & McIntosh, J. R. Probing the macromolecular organization of cells by electron tomography. *Curr. Opin. Cell Biol.* **21**, 89–96 (2009).

248. Hohmann-Marriott, M. F. *et al.* Nanoscale 3D cellular imaging by axial scanning transmission electron tomography. *Nat. Methods* **6**, 729–731 (2009).

249. Zhang, X. *et al.* A unified deep-learning network to accurately segment insulin granules of different animal models imaged under different electron microscopy methodologies. *Protein and Cell* **10**, 306–311 (2019).

250. Sommer, C., Straehle, C., Kothe, U. & Hamprecht, F. A. Ilastik: Interactive learning and segmentation toolkit. in *2011 IEEE International Symposium on Biomedical Imaging: From Nano to Macro* 230–233 (IEEE, 2011).

251. Mulcahy, L. A., Pink, R. C. & Carter, D. R. F. Routes and mechanisms of extracellular vesicle uptake. *J. Extracell. Vesicles* **3**, 24641 (2014).

252. Buschow, S. I. *et al.* MHC II In dendritic cells is targeted to lysosomes or t cell-induced exosomes via distinct multivesicular body pathways. *Traffic* **10**, 1528–1542 (2009).

253. Denzer, K., Kleijmeer, M. J., Heijnen, H. F. G., Stoorvogel, W. & Geuze, H. J. Exosome: From internal vesicle of the multivesicular body to intercellular signaling device. *J. Cell Sci.* **113**, 3365–3374 (2000).

254. Fitzner, D. *et al.* Selective transfer of exosomes from oligodendrocytes to microglia by macropinocytosis. *J. Cell Sci.* **124**, 447–458 (2011).

255. Feng, D. *et al.* Cellular internalization of exosomes occurs through phagocytosis. *Traffic* **11**, 675–687 (2010).

256. Svensson, K. J. *et al.* Exosome uptake depends on ERK1/2-heat shock protein 27 signaling and lipid raft-mediated endocytosis negatively regulated by caveolin-1. *J. Biol. Chem.* **288**, 17713–17724 (2013).

257. Parolini, I. *et al.* Microenvironmental pH is a key factor for exosome traffic in tumor cells. *J. Biol. Chem.* **284**, 34211–34222 (2009).

258. Fuhrmann, G., Serio, A., Mazo, M., Nair, R. & Stevens, M. M. Active loading into extracellular vesicles significantly improves the cellular uptake and photodynamic effect of porphyrins. *J. Control. Release* **205**, 35–44 (2015).

259. Guo, G. *et al.* Self-assembly of transition-metal-oxide nanoparticle supraparticles with designed architectures and their enhanced lithium storage properties. *J. Mater. Chem. A* **4**, 16128–16135 (2016).

260. Belu, A. *et al.* Ultra-thin resin embedding method for scanning electron microscopy of individual cells on high and low aspect ratio 3D nanostructures. *J. Microsc.* **263**, 78–86 (2016).

261. Heymann, J. A. W. *et al.* 3D Imaging of mammalian cells with ion-abrasion scanning electron microscopy. *J. Struct. Biol.* **166**, 1–7 (2009).

262. Rabanel, J. M. *et al.* Nanoparticle heterogeneity: An emerging structural parameter influencing particle fate in biological media? *Nanoscale* **11**, 383–406 (2019).

263. Johnsen, K. B., Gudbergsson, J. M., Andresen, T. L. & Simonsen, J. B. What is the blood concentration of extracellular vesicles? Implications for the use of extracellular vesicles as blood-borne biomarkers of cancer. *Biochim. Biophys. Acta - Rev. Cancer* **1871**, 109–116 (2019).